Ultrasonic Guided Waves for Pitting Corrosion Monitoring of Reinforced Concrete Structures

Doctoral thesis

Submitted in partial fulfillment of the requirements for the degree of

Doctor of Philosophy

of the

Indian Institute of Technology, Bombay, India

and

Monash University, Australia

by

Rajeshwara chary Sriramadasu

Supervisors:

Sauvik Banerjee (IIT Bombay)

Ye Lu (Monash University)

The course of study for this award was developed jointly by
the Indian Institute of Technology, Bombay and Monash University, Australia
and given academic recognition by each of them.
The programme was administered by The IITB-Monash Research Academy

2019

This thesis is dedicated to my parents and elder sister

Acknowledgement

I thank the following people for their support in this academic endeavour of mine.

Mom and dad have always inspired and encouraged me to pursue higher studies. I hope they have realised their dreams through me. My younger siblings have taken the responsibility of parents and ensured a smooth running of the home. My special thanks to Ms Sukritee Bhaskar, who is with me all through my PhD. The interactions and discussion with her have invigorated my understanding of the contents of this thesis and enriched my knowledge on the electrochemistry. My stay at IIT Bombay could not be so pleasant and memorable without the association of many friends and juniors from IIT Bombay and Monash. Special thanks to Vijay and Nithya for suggesting edits this document.

Professor Sauvik Banerjee at IIT Bombay and Dr Ye Lu at Monash University have provided their inputs and suggestions at continuous and appropriate times. They have given me a free hand to learn various pieces of equipment and tools in the laboratory. I could finish the initial experiments on corrosion with the help of Long and Saravanan in the Civil laboratory of Monash. Michael Leach has helped me understand the safe operating procedures and coordinated my safety training. I was able to draft the risk assessment protocols for this work with their help. They helped me in setting up the corrosion research platform in the civil lab at both Monash University and IIT Bombay. Mr Pratap has aided me in material procurement and concrete beam related works. He has arranged for the testing of cubes and casting of beams.

I am grateful to the management of IITB-Monash academy who have funded this PhD topic and facilitated the administrative and financial matters, including my travel to Monash University. The staff at the Academy have always been helpful. They have assisted me in holding various seminars and presentations. I thank Sheba, who has edited most of my manuscripts.

I have benefited from interactions with my former colleagues at BHEL, especially Manimalini, Sandeep and Vijayaraju. They have encouraged me to start my dream research career. My teachers at IIT Roorkee, particularly Professor M. Parida and Professor KS Hariprasad have supported to rekindle my thoughts and ignite my passion for research. They have cooperated and recommended my application for graduate studies.

My sincere thanks to all my lab mates and friends for their constant support and advice.

Rajesh
IIT Bombay
Mumbai

Abstract

Recently, the development of sustainable reinforced concrete (RC) structures that last longer has become a matter of considerable interest. Corrosion poses a great threat to the ageing infrastructure in the world and researchers are seeking methods to monitor the corrosion in RC structures. Detection of corrosion at its embryonic stage has been an impending task in the non-destructive testing of materials. Several non-destructive testing methods such as half-cell potential, concrete resistivity, galvanostatic pulse and acoustic emission exist for assessing the presence of corrosion. The limitation of the current methods is that they either require measurement at several points or need a vast network of sensors. There is a necessity for effective structural health monitoring (SHM) tools, that warn of the potential distress in the material. The limitations posed by the traditional methods can be avoided by using the guided waves (GWs) to monitor RC structures. The GW-based techniques allow the scanning of a large area with fewer sensors; thus they are apt to perform SHM.

In the current study, corrosion in bare rebars is achieved by following the approaches of artificial scrapping of material and accelerated corrosion. Upon ascertaining the suitability of GWs for damage detection in rebars, the accelerated corrosion in embedded rebars is examined by using GWs that are actuated and detected by deploying contact transducers (CTs) and piezoelectric wafer transducers (PWTs).

The wave propagation in the artificially corroded bare rebar samples is explored by using the longitudinal waves. The pitting corrosion is simulated by reducing the diameter of the rebar over a certain length. The GW interaction with the pitting corrosion is numerically simulated by using finite element analysis, and the results are validated with experiments. The signal that is received contains several wave packets, which can be identified as various scattered modes that are generated from the edges of the corroded region. It is found that when the damage is placed at the centre of the rebar, several

scattered wave modes superimpose to form two distinct wave packets in the received signal. A damage index, DI, is proposed by using these two discrete wave packets. It is shown that the proposed DI can be used successfully to monitor the axial extent and intensity of pitting corrosion in rebars. However, for the pitting corrosion that is situated at an arbitrary position, a different methodology, which utilises the differential time of arrival of various scattered wave modes, is proposed to identify the location of the pitting corrosion. Finally, a non-dimensional parameter, namely the scatter coefficient (S_{coeff}), is defined to analyse the energy contributions of various scatter modes. It is found that this S_{coeff} gradually increases with the mass loss and the increment is pronounced when the corrosion pit is closer to the receiver location.

An accelerated corrosion setup that is based on the impressed current method is designed to erode the rebars. Inspection of corroded samples shows that the pits formed in real-life corrosion do not possess the sharp edges that are observed in the artificially corroded rebars. The corroded rebars are then studied by using the longitudinal wave modes that are generated by CTs and the flexural wave modes that are actuated by PWTs, to examine the suitability of GWs to assess corrosion. The damage index and scatter coefficient method developed to evaluate the artificially corroded rebars cannot be used for real-life corroded rebars. A careful examination of the GW signals show that the signal strength and group velocity vary with the changes in the diameter of the rebars. These findings are expected to help reconstruct the pitting corrosion in rebars embedded in concrete.

The process of corrosion in RC is more complicated than bare rebars. It leads to a reduction in diameter as well as debonding between concrete and rebars. Further studies have indicated that the current focus of research is on detecting the individual effect of corrosion and debonding of rebars in RC by artificially inducing damage. However, the two effects co-occur in the structures. In our study, the combined effect of corrosion and de-bonding on GW properties is examined. Numerical models are created to imitate the transition in the phase of corrosion in embedded rebars from the debonding to diameter-reduction. It is proposed that this transition might result in the zero-effect state in which the signal features of the corroded rebar are similar to that of pristine rebar. Numerical and experimental observations substantiate the hypothesised zero-effect state.

The GW propagation in rebars embedded in concrete is examined by deploying lon-

gitudinal modes that are generated and captured by using CTs. Theoretical dispersion curves are calculated using an approximate concrete model to recognise various modes. The validity of the approximate model is verified by its comparison with the full-scale numerical model. Multiple phases of corrosion, namely, corrosion initiation, corrosion progression and diameter reduction, are identified by assessing the changes in the signals. A novel corrosion classification method is proposed using a non-dimensional parameter, relative amplitude (RA), and group velocity extracted from wavelet analysis. The current study shows that the longitudinal GWs are suitable to recognise the incipient pitting corrosion in rebars.

CTs are not field-deployable as the ends of the rebars are generally not exposed. Present-day studies show that PWTs are embeddable in concrete; thus PWTs are apt to analyse corrosion. The GW signals actuated and detected by the PWTs that are affixed on rebar surfaces to probe in-situ pitting corrosion. PWTs induce both the longitudinal and flexural modes in RC among which the flexural mode is well-defined. The amplitude and group velocity of flexural mode develop distinctly in each phase of the corrosion. These measurements can characterise the nascent stage of corrosion. Another experiment is arranged to premeditate the rapid corrosion that creates the diameter reduction phase. The GW response of this phase is evaluated by defining a damage index, DI_{RC}.

In a nutshell, the DI and S_{coeff} defined in this study are useful to locate the damage and quantify the reduction in mass of rebars, wires and cables that are damaged due to pitting corrosion. The real-life corrosion in bare rebars can be estimated by observing the changes in the group velocity and amplitude of GWs. The zero-effect state that is propositioned and validated in this study emphasises the need for SHM of RC infrastructure. The approximate concrete model proposed in this study can accurately calculate the dispersion curves and efficiently replace the full-scale three-dimensional model. The CTs and PWTs encapsulate various phases of corrosion, in particular, the embryonic corrosion. The group velocity of longitudinal modes is more sensitive to corrosion initiation phase and damage reduction phase, while the group velocity of flexural mode is responsive to the debonding stage. It is recommended to use a hybrid-system that generates and evaluates the changes in both modes for corrosion classification. This work facilitates the development of an efficient health monitoring package, which can be deployed in the field with ease to identify corrosion in real-time.

Contents

Acknowledgement **ii**

Abstract **iv**

List of Figures **xi**

List of Tables **xi**

Nomenclature **xviii**

Declaration **xx**

1 Introduction **1**

1.1 Background and Motivation 1

1.2 Need for the study of corrosion in reinforced concrete 3

1.2.1 Effect of rebar corrosion on structural integrity 4

1.2.2 Utility of structural health monitoring 6

1.3 Scope of the study 8

1.4 Organisation of the thesis 8

2 Overview of corrosion detection in concrete **11**

2.1 Introduction 11

2.2 Mechanism of corrosion in concrete 12

2.2.1 Carbonation of concrete 14

2.2.2 Corrosion of rebars due to chloride ions 16

2.3 Current corrosion detection methods 17

2.3.1 Electrochemical methods 17

2.3.2 Mechanical methods 20
2.3.3 Other methods 26
2.4 Advantages of guided wave-based SHM 30
2.5 Concluding remarks 30

3 Literature review of guided wave-based corrosion monitoring 31
3.1 Introduction 31
3.2 Theory of wave propagation in plates 32
3.3 Theory of wave propagation in cylindrical bodies 36
3.4 Actuation and sensing 40
3.4.1 Transducers 40
3.4.2 Sensing method 46
3.5 Techniques for signal evaluation 48
3.5.1 GW parameters for damage detection 48
3.5.2 Advanced signal processing techniques 49
3.6 Damage detection in reinforced concrete using guided waves 50
3.6.1 Detection of surface defects in concrete 50
3.6.2 Detection of diameter reduction in rebars due to corrosion 52
3.6.3 Detection of rebar debonding 53
3.6.4 Detection of damages in retrofitted reinforced concrete structures . 54
3.7 Research gap 55
3.8 Concluding remarks 56

4 Methodologies for experimental and numerical analysis 57
4.1 Introduction 57
4.2 Preparation of samples 58
4.3 Guided wave testing 59
4.3.1 Selection of input signal and sensor arrangement 61
4.4 Corrosion setup 62
4.4.1 Bare rebar 62
4.4.2 Embedded rebars 64
4.5 Numerical modelling 69
4.5.1 Rebar corrosion model 69

4.5.2 Reinforced concrete corrosion model 70
4.6 Concluding remarks 72

5 Detection and assessment of pitting corrosion in rebars using scattering of ultrasonic guided waves 73
5.1 Introduction 73
5.2 Wave propagation in a corroded rebar 74
5.3 Numerical and experimental results 76
5.4 Damage index method to detect simulated corrosion of bare rebars 79
5.4.1 Assessment of corrosion in a rebar with varying corrosion intensity . 79
5.4.2 Assessment of corrosion in a rebar with varying axial extents of corrosion 82
5.4.3 Localisation of corrosion at an arbitrary location in the rebar 85
5.5 Evaluation of corrosion by using the energy of scattered wave modes 90
5.6 Suitability of guided waves for real-life corrosion detection in rebars 92
5.7 Concluding remarks 94

6 Sensitivity of longitudinal guided wave modes to pitting corrosion of rebars 96
6.1 Introduction 96
6.2 Numerical results 97
6.2.1 Corrosion of rebars in concrete 98
6.2.2 Debonding of rebars and steel 99
6.2.3 Zero effect state in corroded reinforced concrete structures 100
6.3 Theoretical modelling 103
6.3.1 Baseline validation 103
6.4 Results and discussion 104
6.4.1 Dispersion curves 104
6.4.2 Longitudinal guided waves for corrosion detection 109
6.4.3 Wavelet based feature extraction 113
6.5 Concluding remarks 117

7 Flexural guided waves for detecting the pitting corrosion of rebars 119

7.1 Introduction . . . 119

7.2 Experimental results . . . 120

7.2.1 Corrosion initiation phase . . . 120

7.2.2 Corrosion progression phase . . . 122

7.2.3 Diameter reduction and concrete cracking phase . . . 124

7.3 Mechanism of corrosion process . . . 125

7.4 Damage index for extreme corrosion . . . 130

7.5 Concluding remarks . . . 131

8 Summary and conclusions 133

8.1 Summary of work . . . 133

8.2 Conclusions . . . 135

8.3 Research contribution . . . 137

8.4 Future work . . . 138

8.5 Publications . . . 139

References 141

List of Figures

1.1 Rana plaza in Dhaka, Bangladesh (a) before collapse and (b) after collapse. Source: https://en.wikipedia.org/wiki/2013_Dhaka_garment_factory_collapse. 2

1.2 Bond strength variation with level of corrosion. Source: Coccia *et al.*, 2016. 5

2.1 Phase diagram of corrosion aided by chloride ions. 13

2.2 Typical damages in concrete (a) cracks, (b) intermediate corrosion and (c) extreme corrosion. 14

2.3 Phase diagram of carbonation in concrete. 15

2.4 Typical half-cell equiment and arrangement of test on concrete. 18

2.5 Galvanostatic pulse equipments used to test the corrosion of concrete specimens. Source: El-Dieb and El-Maaddawy, 2018. 20

2.6 AE system used for corrosion monitoring at IIT Bombay, Structural Health Monitoring and Retrofitting Lab that includes (a) controlling unit, (b) preamplifiers and (c) sensor arrangement on concrete beam. 22

2.7 Sensor arrangement for impact echo testing used for void detection in concrete at I l IT Bombay, Structural Health Monitoring and Retrofitting Lab. 23

2.8 Wavelet based reconstruction of voids in concrete using impact echo testing. 24

2.9 Damage localisation in a damaged (TSC 1) and an undamaged (TSC 2) cables using damage index method (DI) based on(a) vertical (DI_V) and (b) lateral (DI_L) modes of vibration ; and modal flexibility method (MF) based on (c) vertical (MF_V) and (d) lateral (MF_L) modes of vibration. Source: Wickramasinghe *et al.*, 2016. 25

2.10 Pitting corrosion in (a) a rebar sample and (b) corresponding strain measurements using FOS that indicate the location of corrosion. Source: Davis *et al.*, 2016. 27

3.1 Stresses acting on an infinitesimally small element in equilibrium. 32
3.2 Schematic diagram of a thin plate with thickness 2h. 35
3.3 Typical dispersion curves of an aluminium plate showing the relations between (a) frequency-wave number, (b) frequency-phase velocity and (c) frequency-group velocity. Source: Chang and Yuan, 2018. 37
3.4 Dispersion curves of a 3 mm-diameter rod, (a) Phase velocity (b) Group velocity. Source:Chaki and Bourse, 2009. 39
3.5 CTs of type Nano 30 and WDα (MISTRAS Group) that are used in GW testing. 41
3.6 GW-based monitoring using (a) angle beam and (b) angle beam array transducers. Source: Li and Rose, 2002 ©2002 IEEE. 42
3.7 Typical PWT with lead wires soldered. 42
3.8 Smart aggregate along with its component material used for crack monitroing. Source: Dumoulin *et al.*, 2012. 43
3.9 Process involved in manufacture of PVDF based piezoelectric sensor (a)–(e) from deposition of PVDF nano-fibres (NFs) to final PVDF sensor. Source: Khan *et al.*, 2018. 44
3.10 Illustration on the working principle of (a) the pulse echo method and (b) the pitch catch method. 46
3.11 Schematic of time reversal process in concrete specimen. Source: Mustapha *et al.*, 2014. 47

4.1 (a) Schematic diagram of RC beam, (b) transducer arrangement and (c) 60 kHz input signal. 61
4.2 Frequency response curve for the current experimental setup. 62
4.3 (a) Rebar samples used in the experiment. 63
4.4 Corrosion cell setup for steel bar. 64
4.5 Comparison of actual (gravimetric) and predicted (Faraday's law) mass loss for a 20 mm rebar. 65
4.6 Experimental setup with corrosion cell arrangement and data acquisition system (Monash University). 65
4.7 Electrolyte solution after five days and ten days of experiment. 66

4.8 RC beam used in the corrosion cell setup with electricals terminals marked (Monash University). 67
4.9 Experimental setup showing the accelerated corrosion and GW monitoring of corroded RC beam (IIT Bombay). 68
4.10 Schematic diagram of the RC beam that is used in study of corrosion and debonding. 71
4.11 Response of an undamaged structure at 100 kHz excitation frequency (a) Time History (b) 3D plot of signal using Gabor wavelet. 72

5.1 Reflection and transmission pattern in damaged rebar. 75
5.2 A typical rebar used as a baseline, and a rebar with corrosion. 76
5.3 (a) Comparison of baseline signal from experiment and FEA and, (b) comparison of energy envelope of baseline signal from experiment and FEA. . . 77
5.4 Group velocity dispersion curves for a 20 mm rebar. 78
5.5 Comparison of FEA and experiment signal of rebar with 100 mm-wide corrosion located at the centre. 78
5.6 Comparison of the signal from a corroded rebar with baseline signal by using FEA. 80
5.7 Comparison of energy envelopes of the signal from corroded rebar with baseline signal by using FEA. 81
5.8 Discretisation in a typical rebar for damage index calculation, and path of the signal in case of damage at the node, k. 81
5.9 Damage index of steel bars with various intensities of corrosion located at the centre (FEA). 82
5.10 Comparison of the signal from rebars with various intensities of corrosion by using experiments. 83
5.11 Damage index plots for rebars with various levels of corrosion by using experiments. 84
5.12 Damage index plot for various lengths of damage located at the centre by using FEA. 85
5.13 Damage index plot for various lengths of damage located at the centre by using experiments. 85
5.14 Response of a rebar with corrosion located at 200 mm from the actuator. . 86

5.15 Schematic diagram displaying the path followed by various scattered wave modes. 87
5.16 Scattered wave modes, with paths identified, for a damage located at 200 mm from actuator end from (a) FEA and (b) experiment. 89
5.17 Localisation plot showing the relationship between the location of the damage and the scatter coefficient. 91
5.18 Mass loss plot showing the relationship between mass loss and scatter coefficient for axial extent 100 mm. 91
5.19 Baseline signal of rebar sample 20R2. 92
5.20 Figure 4 Comparison of GW response of the rebars with different levels of corrosion (Sample 20R2). 93
5.21 Variation of group velocity of $F(1,\ 1)$ with mass loss (Sample 20R2). . . . 93

6.1 Comparison of (a) signals and (b) energy envelopes of an undamaged specimen and a corroded specimen. 99
6.2 Variation of amplitude of $L(0,\ 1)$ mode with (a) corrosion along the length and (b) mass loss in pitting type of corrosion in the rebar. 99
6.3 Variation of (a)amplitude and (b) group velocity of $L(0,\ 1)$ mode with increase in debond between steel and concrete. 100
6.4 Comparison of energy envelops for various damage scenarios, in order to identify the zero state effect for damage that is located at the centre of the rebar. 102
6.5 Approximation of RC beam made for the purpose of dispersion curve generation and verification 104
6.6 Comparison of baseline signals from, (a) experimental and numerical models, (b) numerical and reduced numerical models, and (c) numerical model generated in Abaqus for reduced numerical simulations. 105
6.7 GW signals at various frequencies (50 kHz, 60 kHz and 75 kHz) showing the dispersion behaviour in RC beam 106
6.8 Group velocity dispersion curves of (a) a 12 mm diameter bar, and (b) a 10 mm diameter rebar embedded in concrete. 107
6.9 Wave modes in the experimental baseline signal with input frequency of 60 kHz. 108

6.10 GW mode shapes extracted from theoretical dispersion relations and numerical simulations. 109
6.11 Comparison of numerical baseline with a 40-mm-long debond and corrosion with a 2 mm (depth) x 100 mm (length) reduction in material. 110
6.12 Comparison of normalised $L(0,\ 1)$ mode and baseline for various level of corrosion. 112
6.13 Comparison of normalised $L(0,\ 3)$ mode and baseline for various level of corrosion. 113
6.14 Comparison of normalised $L(0,\ 4)$ mode and baseline for various level of corrosion. 114
6.15 Magnitude scalogram of signal on the (a) initial day (baseline), (b) sixth day, (c) ninth day, and (d) twelfth day; showing the CWT amplitude versus time, and the frequency of corroded bars. 115
6.16 Relative amplitude curves of $L(0,\ 3)$ and $L(0,\ 4)$ modes with an increase in corrosion of rebars. 118
6.17 Variation of the group velocity of (a) $L(0,\ 4)$ mode, (b) $L(0,\ 1)$ mode and (c) $L(0,\ 3)$ mode with increase in corrosion of rebars. 118

7.1 Baseline signal obtained from undamaged concrete specimen excited with 5 cycle hanning pulse at 75 kHz. 121
7.2 Schematic diagram of corrosion in RC structures, triggered by the impressed current. 122
7.3 GW signals recorded using piezoelectric transducers attached to the rebar after various days in corrosive solution. 123
7.4 Energy envelope of the GW signals recorded using piezoelectric transducers attached to the rebar in the initial phase of corrosion. 123
7.5 Split RCC beam showing the bonding between reinforcement and concrete (a) at the intact portion and, (b) corroded portion. 124
7.6 Energy envelope of the GW signals recorded using piezoelectric transducers attached to the rebar in the corrosion progression phase. 125
7.7 Cracked concrete beam and the pulled-out rebars after twelve days of corrosion. 126

7.8 Energy envelope of the GW signals recorded using piezoelectric transducers attached to the rebar in the final phase. 127
7.9 Variation in the amplitude of $F(1,\ 1)$ mode with the progress of corrosion. 127
7.10 Impressed current observed in the power supply for the constant voltage across the terminals. 128
7.11 Variation of group velocity of flexural mode with the progress of corrosion for sample 20C1 129
7.12 Various phases of corrosion recognised from the changes in the amplitude with corrosion of sample 12C2. 130
7.13 Variation in the damage index ($\mathrm{DI}_R C$) with the number of days in corrosive solution. 132

List of Tables

2.1 Threshold limits of chloride contents (ACI 318). 17
2.2 Probability of corrosion based on half-cell potential values (ASTM C876-15). 18
2.3 Probability of corrosion based on concrete resistivity measurements (RILEM TC-154). 19
2.4 Various techniques to detect corrosion along with their advantage and limitation. 29

4.1 Mix design for M25 grade concrete. 58
4.2 Cube strength results for concrete specimens. 59
4.3 Details of experimental samples. 60
4.4 Material properties of concrete and rebar. 69

5.1 Scattered wave modes and their arrival times at the sensor. 75
5.2 Estimation of damage length using damage index plot for a 100 mm-wide corrosion damage in rebar (FEA). 82
5.3 Estimation of corrosion length from damage index plots by using experimental signals. 83
5.4 Estimation of corrosion length using damage index plot for damage that is equidistant from transducers. 84
5.5 Location estimation by using the time of arrival of damage edge scattered wave packets. 88

Nomenclature

ϵ_{ij}	Strain on a plane perpendicular to i in the direction j
$\lambda,\ \mu$	Lam*é* Parameters
ν	Poisson's Ratio
ω	Frequency
ρ	Density
σ_{ij}	Stress on a plane perpendicular to i in the direction j
C_L	Longitudinal wave speed
C_T	Shear wave speed
DI_{RC}	Damage index for diameter reduction phase in RC
G	Shear Modulus
k	Wave Number
S_{coeff}	Scatter Coefficient
Δ_i	Pulse duration of the input signal
[C]	Stiffness matrix
[S]	Compliance matrix
CFRP	Carbon Fibre Reinforced Polymer
CT	Contact Transducer

CWT	Continuous Wavelet Transform
DI	Damage Index
FBG	Fibre Bragg Grating
FEM	Finite Element Method
FFT	Fast Fourier Transform
FOS	Fibre Optic Sensor
FRP	Fiber Reinforced Polymer
GW	Guided Wave
NDE	Non-destructive Evaluation
PSO	Particle Swarm Optimization
PVDF	Polyvinyldiene flouride
PWT	Piezoelectric Wafer Transducer
PZT	Lead (Pb) Zirconium (Zr) Titanate (Ti)
RA	Relative Amplitude
RC	Reinforced Concrete
Rebar	Reinforcement Bar
SAFE	Semi Analytical Finite Element
SEM	Spectral Element Method
SEM	Spectral Element Method
SHM	Structural Health Monitoring
ToF	Time of Flight

Declaration

I declare that this written submission represents my ideas in my own words and where others' ideas or words have been included, I have adequately cited and referenced the original sources. I also declare that I have adhered to all principles of academic honesty and integrity and have not misrepresented or fabricated or falsified any idea/data/fact/source in my submission. I understand that any violation of the above will be cause for disciplinary action by the Institute and can also evoke penal action from the sources which have thus not been properly cited or from whom proper permission has not been taken when needed.

Student Name: Rajeshwara chary Sriramadasu

IITB ID: 144044004

Monash ID: 26856921

Chapter 1

Introduction

1.1 Background and Motivation

The United Nations' report on the world cities estimates that the urban population would experience a whopping 20 percent growth by the year 2030 from its present level in year 2019. The infrastructure in cities is getting over strained and there is a need for augmentation of this infrastructure to support the anticipated growth. The developing nations will have a major share of this worldwide trend of urbanisation and population growth [United Nations, 2018]. The purpose of civil infrastructure is to provide a safe environment to its users pertaining to strength and serviceability requirements. The deficiencies in quality of construction practices, external environment and operating conditions affect the performance of the structures. Poor construction practices including the design errors are categorised as defects in structure. The presence of defects in structures lead to reduction in the desired performance level. The defects are often the breeding ground for the deterioration of the infrastructure. The structures dilapidate due to ageing, environmental effects and operating conditions. Deterioration can be arrested with the help of periodic maintenance. Prior knowledge of defects in the structures helps in understanding the deterioration mechanism and subsequent maintenance. The compounding effects of defects and deterioration lead to damages in the structural components. It is imperative to control these deficiencies for the safe operation of the infrastructure at the desired performance level [Aktan *et al.*, 1996].

Ready availability of constituent materials, like cement, aggregates and water, and ease of moulding into desired shape are the defining characteristics of concrete that make it the widely used construction material in the civil infrastructure across the world, in

(a) (b)

Figure 1.1: Rana plaza in Dhaka, Bangladesh (a) before collapse and (b) after collapse. Source: https://en.wikipedia.org/wiki/2013_Dhaka_garment_factory_collapse.

bridges, buildings, nuclear power plant structures, chimneys, cooling towers, dams and the like. India and china are the top producers of the cement and these two countries are centres of the growth in human capital. Thus, the future construction in the world will be made of reinforced concrete (RC). The design standards prescribe that the structure shall withstand the maximum load without collapse and also satisfy the serviceability requirements such as deflections and cracking throughout the service life. Several quality control measures are taken at the design and construction stages to ensure safety of the structures. Deficiency in quality control systems and environmental factors lead to defects, deterioration and damages. They cause reduction in performance level, subsequently. Typical defects in RC structures are poor compaction, inadequate reinforcement detail, improper materials and so on. The inception of microcracks, ingress of acidic chemicals, growth of algae and such others fall in the deterioration domain. Typical damages in RC structures which cause a significant reduction in the performance are corrosion of reinforcement steel bars (rebars), cracking and spalling of concrete, and loss of bond at the interface of rebars and concrete (debonding). The poor maintenance and continued usage of the structures at reduced capacity lead to catastrophic failure which can result in loss of numerous lives and enormous wealth.

A case of Rana plaza in Dhaka, Bangladesh is represented in Figure 1.1. It is build as a eight storey residential complex which is later modified as commercial shopping complex. The building looked magnificent from its outer appearance and is praised for its commercial activity as it housed many businesses. All appeared well, until it collapsed catastrophically in the year 2013, resulting in an enormous loss. News reports express

that more than 1200 people lost their lives in this incident. Subsequent expert studies suggest that the disaster is engendered as a consequence lapses in routine maintenance and overlooking of distress signals [Sinkovics *et al.*, 2016]. Many such mishaps occur across the world on regular basis. Frequent checks and repairs are indispensable to ensure integrity and longevity of the structures. Continuous monitoring of the infrastructure with an aim to detect the signs of deterioration and damage using a set of online sensors, data acquisition, signal processing system and damage detection algorithms is termed as structural health monitoring (SHM). Therefore, it is incumbent on the structural safety authorities to enforce the SHM of each structure.

1.2 Need for the study of corrosion in reinforced concrete

Concrete is a composite material consisting of cement, coarse aggregates (CA), sand, admixtures and water. The construction codes prescribe several quality control tests and measures to test the suitability of locally available aggregates, sand and water for their use in concrete. Indian standard, IS 383 prescribes the acceptance criteria for the CA and sand (also called as fine aggregate (FA)). Potable water in general is considered suitable for mixing of concrete. Water shall not contain high levels of acids, alkalis, salts and other substances which cause the deterioration of concrete or rebar. IS 3025 contains the procedure for various tests and the permissible limits of solids in water. For example, part 32 of IS 3025 prescribes that the chlorides in water shall be less than 500 mg/l when it is used in RC construction. The water used in the curing stage shall be clean and shall also meet the above standards. Commonly used ordinary Portland cement (OPC) is manufactured from clay and limestone and the final product contains tricalcium silicate (C_3S), dicalcium silicate (C_2S), tricalcium aluminate (C_3A) and tetracalcium aluminoferrite (C_4AF). C_3S and C_2S are responsible for the strength of the OPC. Portland pozzolana cement (PPC) consists of OPC and pozzolanic material such as fly-ash, calcined clay, volcanic ash and silica fumes. IS 1489 (part 1) and IS 1489 (part 2) specify the standards for fly-ash and calcined clay based PPC , respectively. Admixtures in powder or liquid form are used to improve workability, reduce setting-time, increase strength, and prevent corrosion . IS 9103 specifies that the admixtures shall not alter the durability of the concrete and

not react with the constituent material to form hazardous products. In RC construction, rebars are embedded in concrete to improve its performance. They provide the necessary strength in tension and increase the load carrying capacity. Steel bars are also used as tendons to provide the necessary stress in the pre-tensioned or post-tensioned beams. The high yield strength rebars which are generally used in RC shall conform to IS 1786. The above quality checks on materials ensure that RC structures are made durable and resilient. However, they are observed to deteriorate due to defects and environmental conditions. It is necessary to detect, quantify and arrest the damages and to retrofit the structures to ensure their safe operation. Early detection of the corrosion process could have the advantage to limit the location and extent of necessary repairs and replacement and can reduce the cost which is necessary for rehabilitation work.

1.2.1 Effect of rebar corrosion on structural integrity

Deterioration of concrete due to corrosion caused by carbonation and chloride-ions leads to damages and structural degradation. The parameters to evaluate durability such as sectional area, ductility, bonding and strength alter as a result of corrosion. The stresses get redistributed due to the damages and affect the deformation and failure patterns. These changes cause a reduction in the service life of the structure [Vu and Stewart, 2000]. The influence of corrosion on durability of concrete is summarised in this section.

In the composite system of RC the stress transfer between concrete and steel happens mainly through friction and to a small extent through bearing due to undulation on surface. Thus, the bonding between steel and concrete is very crucial. Pull-out tests are used to calculate the bond strength of rebars in RC. Simple method of pulling out by application of force with the use of universal testing machine (UTM) is deployed traditionally to estimate bond strength as per international standard ASTM C234 (which is now obsolete). This setup caused compression on concrete as the packing presses against it to create tension in the rebar [Cabrera, 1996]. This limitation is bypassed by introducing tension pull-out test. The tension pull-out test is successful in eliminating the undue concrete compression, yet it induces the issue of spaced splices and as a result the crack orientation and rate are far from the actual. It is important to select the procedure and setup for the bond strength estimation that ensures the test conditions closely resemble the state of actual structural members. Improvements are proposed by

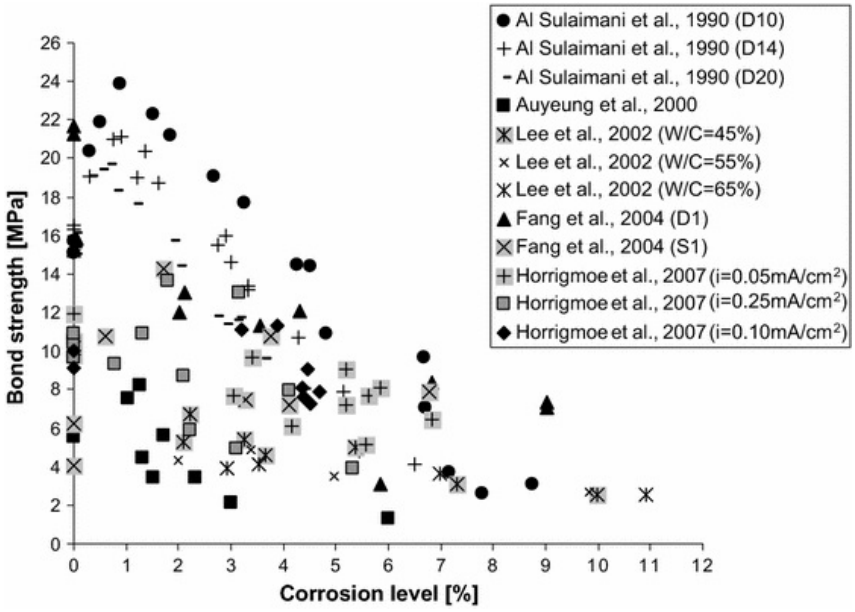

Figure 1.2: Bond strength variation with level of corrosion. Source: Coccia *et al.*, 2016.

researchers in the form of the simple beam test, modified beam tests and cantilever beam test arrangements which try to mimic the actual beam loading and stress conditions thus closely represent the flexural beam behaviour.The latest bond strength test using the cantilever beam model has a great advantage over the previous methods as the flexural behaviour, tensile strains and strain variations are comparable to the field conditions. This test introduces the shear and bending stresses as intended and the setup provides the flexibility to achieve the desired crack pattern. The latest international standard ASTM A944 is based on this type test arrangement. The standard suggest that these tests shall be used to compare the relative bond strength of rebars with varying physical properties but the values predicted shall not be used for RC design as they are higher than the actual values [Kemp *et al.*, 1968]. Experimental studies using pull-out tests show that the corrosion adds to the bond strength in its initial stage [Fang *et al.*, 2006; Bilcik and Holly, 2013]. The results of bond strength tests compiled from the literature Al-Sulaimani *et al.* [1990]; Auyeung [2001]; Lee *et al.* [2002]; Fang *et al.* [2004]; Horrigmoe *et al.* [2007] is presented in the Figure 1.2.

Studies indicate that this increase is prominent for corrosion up to 4 per cent [Almusallam *et al.*, 1996]. The reason behind this phenomenon is small expansive mechanical pressure that is applied by the corrosion product on surrounding concrete. This action restrains the rebar from sliding by increasing the mechanical interlocking. This

phenomenon gets reversed upon initiation of cracks due to excess pressure which occurs around 5 per cent corrosion. The bond strength reduces at very rapid pace from this level of corrosion with reduction up to 70 per cent when the corrosion level reaches 8 per cent. It is worthwhile to note that this reduction in bond strength is predominant only in the corrosion level 5 to 8 per cent. Subsequently, up to 80 per cent corrosion causes further reduction of 20 per cent in the bond strength. The initial corrosion of 5 per cent is thus very critical in structural health monitoring and retrofitting of concrete structures to avoid catastrophic failure. Further investigations by Almusallam, 2001 on the corroded steel bars show that the mechanical properties of residual steel and pristine rebar are same. The stress-strain curves plotted using the nominal diameter of corroded rebars show that tensile stress at the ultimate load. Corrosion causes a reduction in the diameter of rebars; thus, the value of ultimate load reduces with increase in the corrosion level. Mechanical-failure behaviour of rebars at the ultimate load changes to brittle mode of failure when the corrosion level is greater than 13 per cent. Brittle failure is dangerous as it leads to an abrupt collapse rather that yielding which show sufficient warning signs.

The reduction in rebar area due to corrosion causes reduction in the flexural strength of RC beams. Apart from reduction in the flexural strength corrosion also modifies the mode of failure in RC beams. The load tests on pristine RC beams indicate flexure mode of failure whereas the corroded RC beams fail in shear; thus, corrosion reduces the shear strength of the beams considerably [Rodriguez *et al.*, 1997]. Cracking of beams due to corrosion is studied by several researchers [Cabrera, 1996]. Crack distribution in corroded beams changes to concentrated instead of scattered mode, resulting in excess penetration of chlorides in limited area [Wei-liang and Yu-xi, 2001]. Appearance of initial cracks due to corrosion gets expedited in loaded RC beams [Maaddawy *et al.*, 2005].

1.2.2 Utility of structural health monitoring

The emphasis on safety, durability and integrity of structures has led to extensive research in non-destructive testing (NDT). The breakthroughs in sensor technology, material science, electronic packaging and signal processing have led to revamping of traditional damage detection techniques. With the current methods, it is possible to detect the damage at an early stage and remedial steps can be taken to save the economy and human life. SHM is a system to detect the damage in a structure by real-time monitoring of the

component features. It is achieved by exciting the structure with actuators, collecting the signal using sensors and processing signal data in a digital computer. The scholarly interest for structural health related issues has been relentlessly increasing in recent years. The increasing interest of the community in damage prognosis is driven by the fact that, it helps in detecting the damage at an early stage, assists in maintenance operations and aids in estimating the residual lifespan of the structure for safe operation [Raghavan and Cesnik, 2007]. SHM of RC structures can be achieved in two ways, active sensing and passive sensing. The passive sensing methods based on vibration characteristics such as frequency and mode shape involve low frequencies. The range of damage detection is short as they employ low frequencies. A dense array of sensors is required for evaluating the entire structure using these methods. Passive sensing methods like acoustic emission involve high frequencies but they rely on the internal loading such as cracks or external loading such as impact which are uncontrolled. These methods require the sensors and the sensing system to function continuously, which generate enormous data, consume a huge electric power and involve a hefty operating cost. The active sensing methods require controlled loading thus can be operated at conveniently spaced time intervals. The sensing system need not be operative during the occurrence of any damage event. Active sensing arrangement captures the state of structural members post any damage event. Till date the NDT methods for RC have used low frequency but they have low sensitivity to the damages and they can not be used for qualitative and quantitative assessment of damages with small dimensions and intensity. Guided wave (GW) based technique is an active sensing technology and deploys higher frequencies ranging between 20 kHz to 20 MHz and hence can effectively be used to detect damage of small size located in a wider range. The challenge in testing of concrete using high frequency is that the microstructure noise and loss of energy in concrete medium becomes predominant at the high frequencies. The microstructure noise can mask the actual damage signals thus focussed wave generation coupled with robust signal processing techniques need to be developed [Song and Saraswathy, 2007; Wu and Chang, 2006a].

1.3 Scope of the study

The objective of present study is to evaluate the corrosion damage in rebars by deploying numerical and experimental studies. GWs are promising alternative to the existing techniques thus their utility in corrosion detection is explored. Scope of the study is outline as below.

1. Investigation of the mechanism of GW propagation in the corroded rebars by artificially scrapping the material and recognise sensitive features of GW signals that respond to the changes in intensity, location and length of corrosion. Explore the possibility to utilise the GW characteristics to develop damage indices that can quantify unknown defect in the rebar.

2. Identification of GW modes produced and acquired by contact transducers (CTs) and embeddable piezoelectric wafer transducers (PWTs) in the frequency range of 20 kHz to 150 kHz.

3. Creation of an experimental setup that can simulate the accelerated corrosion in embedded rebars at desired location.

4. Development of numerical and theoretical model to identify GW modes, to explore damages like debonding and diameter reduction on GW characteristics, and to decipher various phases of corrosion indicated by changes in GW signals.

5. Demonstration of the universal applicability of GW based monitoring by considering rebars of two different diameters (20 mm and 12 mm).

1.4 Organisation of the thesis

Pertaining to the scope, this thesis is organised into eight chapters. The scheme of each chapter is explained below.

- **Chapter 1** begins with the background and motivation, which elucidate the urge of author to pursue the current research. Later, the need to detect corrosion is discussed along with its effect on the strength of structural members. The chapter further explains the importance of prognosis that is better achieved by adopting

the system of structural health monitoring. The objective and scope of the current study is demarcated by enumerating the various investigations that are planned. The chapter is concluded by presenting the organisation of this thesis.

- An elaborate description of various causes and types of corrosion along with their mechanism in concrete is presented in **Chapter 2**. The existing methods to detect corrosion are presented and the reasons for adopting the current method are described later.

- The course of this research is decided by carrying out extensive literature review, that is presented in **Chapter 3**, with an aim to identify the research gap. Mechanics of GW propagation is presented to understand their interaction with wave guides and defects. Research gap is identified by studying the current developments in corrosion detection using GWs along with their limitations.

- **Chapter 4** enlightens various experimental, numerical and theoretical investigations that are performed using GWs generated by a range of piezoelectric sensors to decipher the corrosion in its initial stages. The experiments are designed to closely represent the actual corrosion in RC structures. Two basic methods of GW generation and sensing using CTs and PWTs are used to understand GW characteristics in bare and embedded rebars. Theoretical dispersion curves are generated to identify modes of propagation. The process of numerical simulation adopted to uncover the defect influenced features in the response signal is presented in detail.

- To understand the complex problem of corrosion in concrete it is important to study its simplified version in bare rebars. **Chapter 5** outlines the damage detection strategy to recognise corrosion in bare rebars. This chapter critically examines the suitability of contact and PWTs to detect in-situ corrosion of bare rebars. The experiments adopt two methods to simulate the corrosion namely, artificial scrapping of material and impressed current method. Features of the GW response signal are deciphered using the theoretical dispersion curves and numerical simulations. This knowledge is utilised to develop a damage index method.

- The feasibility of longitudinal GWs to detect corrosion is presented in **Chapter 6**. presents the GW based method using CTs to estimate corrosion in rebars embedded

in concrete. The numerical studies throw light on a peculiar situation in which GWs signals from corroded rebars show similarity with that of pristine rebars embedded in concrete. The ability of CTs to generate dominant longitudinal GW modes is exploited, to study the interaction of GWs with corrosion features. The sensitivity of different wave modes to commencement of rust formation, debonding and reduction in rebar diameter is presented based on their mode shapes which are calculated using the theoretical dispersion relations. A damage identification scheme with the help of non-dimensional parameter called relative amplitude (RA) and group velocities of higher longitudinal wave modes is then presented.

- **Chapter 7** addresses the issue of corrosion detection by adopting GWs generated by embeddable PWTs. The chapter highlights that continuous monitoring can demystify the confusion regarding status of corrosion as it can be used to ascertain various phases of corrosion.

- **Chapter 8** concludes the thesis with summary of work and contributions made by the author to establish structural health monitoring with the aid of GWs as a tool in prognosis of rebar corrosion. The implications of research work and the future work are presented at the end.

Chapter 2

Overview of corrosion detection in concrete

2.1 Introduction

RC structures are intended to function throughout their service life satisfactorily without any collapse of structural members. Few reasons such as improper design and construction, growth of algae and plants, cracking or spalling of concrete, and corrosion of rebars cause the premature failure in the structure and affect the service life. Corrosion of rebars is recognised as the major cause of damage in RC structures. Several non-destructive testing (NDT) methods exist to detect corrosion. Commonly used tests include visual inspection, chemical tests like half-cell potential methods and mechanical test like ultrasonic pulse velocity. However, these tests are limited in their capacity as they require multiple measurements, can not quantify the damage and are expensive to deploy on large structures. This chapter reviews mechanism of corrosion and various quality tests that are prescribed by current codes of practice for RC construction. A careful examination of the literature reveals that inception of corrosion and its subsequent progress are yet to be unveiled. Corrosion is a gradual phenomenon thus the mode of testing shall have ability to distinguish minute changes. Non-destructive evaluation (NDE) or structural health monitoring (SHM) is adopted in such cases. Literature is reviewed in this chapter to examine a range of health monitoring techniques that are currently in development. Among these, guided wave based methods are promising to uncover the incipient corrosion.

2.2 Mechanism of corrosion in concrete

Corrosion is an electrochemical process in which the metal (Iron) returns to its stable form in nature by oxidation. It is driven by the difference in the electrical potential of various rebars in an RC structure. The corrosion process generally involves the combination of the anodic dissolution of the steel and cathodic reduction of the oxidants like dissolved Oxygen, chloride or sulphates in the aqueous solution. Depending upon arrangement of the anode and cathode where the oxidation of metal and the reduction of the oxidant occur respectively , corrosion can be termed as uniform corrosion and pitting corrosion. Carbonation of concrete causes microcell corrosion in which a numerous number of small corrosion cells are formed over a large length of rebar. This effect causes the cross section of rebar to reduce in a large length of rebar. This type of corrosion is termed as uniform corrosion. This type of corrosion is often slow and can be detected and controlled easily. Low chloride concentration often results in the formation of macro-cell corrosion in rebars. In this type of corrosion, a small portion of the rebar with high negative potential acts as anode and rest of the rebar acts as a cathode. Corrosion of the rebar occurs at the anodic site and cross section of this portion gets reduced due to the formation of rust. This type of corrosion is termed as localised corrosion or pitting type of corrosion [Ji *et al.*, 2013]. This type of corrosion can occur and propagate at a faster rate and is recognised to be more dangerous because the cross section of the rebar is reduced to a point at which the load-carrying capacity of the rebar is completely diminished and a catastrophic failure of the structure is enforced [Ahmad, 2003]. In the both type of corrosion the pore solution acts as the electrolyte by facilitating the movement of electrons. The general chemical reaction at the anode in steel involve the formation of Fe_2O_3 and more stable hydrated product $Fe_2O_3 \cdot (H_2O)_x$. The phase diagram of corrosion process is shown in Figure 2.1 and the electrochemical reactions that occur at the anodic site are summarised in Equation 2.1 to Equation 2.4.

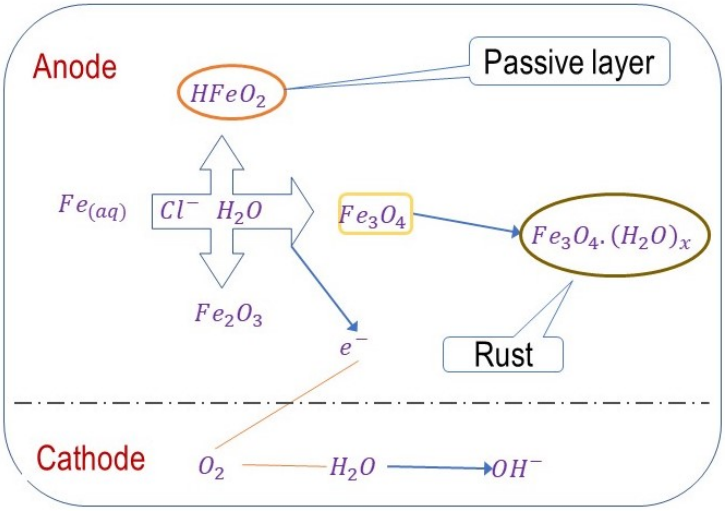

Figure 2.1: Phase diagram of corrosion aided by chloride ions.

$$3\,\mathrm{Fe} + 4\,\mathrm{H_2O} \longrightarrow \mathrm{Fe_3O_4} + 8\,\mathrm{H^+} + 8\,\mathrm{e^-} \tag{2.1}$$

$$2\,\mathrm{Fe} + 3\,\mathrm{H_2O} \longrightarrow \mathrm{Fe_2O_3} + 6\,\mathrm{H^+} + 6\,\mathrm{e^-} \tag{2.2}$$

$$\mathrm{Fe^+}\,2\,\mathrm{H_2O} \longrightarrow \mathrm{HFeO_2} + 3\,\mathrm{H^+} + 2\,\mathrm{e^-} \tag{2.3}$$

$$\mathrm{Fe} \longrightarrow \mathrm{Fe_2}^+ + 2\,\mathrm{e^-} \tag{2.4}$$

The cathodic reactions involve the reduction of dissolved oxygen in aqueous medium hence this reaction is driven by their availability (Equation 2.5).

$$2\,\mathrm{H_2O} + \mathrm{O_2} + 4\,\mathrm{e^-} \longrightarrow 4\,\mathrm{OH^-} \tag{2.5}$$

Studies suggest that the corrosion occur in three different phases which are initiation depassivation and propagation [Valipour *et al.*, 2014; Reis *et al.*, 2005]. Visual signs corrosion damage in the form of cracking, rust formation and rebar diameter reduction are shown in Figure 2.2 The concrete cover provides protection against the external environment to the rebars. The pH of pore solution is generally in the range 12.5 to 13.5. High alkalinity level of the pore solution protects steel from corrosion by forming a protective passive-layer. Maintaining the low water cement ratio of concrete results in lower permeability and thus ensures that the voids in concrete are unconnected. This reduces the diffusion of corrosive agents is reduced in such impermeable structures. The alkaline pore solution provides the chemical barrier whereas the sound concrete offers the mechanical protection against corrosion. These factors contribute to the natural ability of the concrete to resist corrosion

(a) (b)

(c)

Figure 2.2: Typical damages in concrete (a) cracks, (b) intermediate corrosion and (c) extreme corrosion.

thus structures should function without deterioration if they are designed, constructed and maintained properly. However, these conditions are not met in the real structures and corrosion of rebars has become a normal phenomenon. High porosity of the concrete, concentration of the acidic agents in the exterior environment and moisture contribute to the diffusion of corrosion causing agents such as carbon-dioxide, sulphur and chloride. The Carbonation (Section 2.2.1) and ingress of chloride-ions (Section 2.2.2) contribute to the corrosion in majority of structures thus they are described in the following sections.

2.2.1 Carbonation of concrete

A good quality concrete prevents the inception of corrosive agents from environment. The carbon-dioxide (CO_2) in the atmosphere can deteriorate the condition of the concrete. CO_2 on its own does not affect the condition of concrete but when it combines with moisture carbonic acid (H_2CO_3) is formed and it reduces the alkalinity of the con-

crete (Equation 2.6) and add to the probability of rebar deterioration due to corrosion. The sources of CO_2 in mainly the atmospheric air, in urban environment and in tunnels its concentration is sufficient to cause deterioration. Carbonation also alter the internal structure and porosity of the hydration products of cement by formation of calcium carbonate (Equation 2.7). Excess availability of CO_2 and H_2O worsens the situation as they react with $CaCO_3$ to form $Ca(HCO_3)_2$ (bicarbonate) which is water soluble unlike $CaCO_3$ (Equation 2.8). This causes further drop in pH and leaching of concrete. The complete phase transformation of carbonation in concrete is represented in Figure 2.3

$$CO_2 + H_2O \longrightarrow H_2CO_3 \overset{\text{Aq. Medium}}{\rightleftharpoons} 2\,H^+ + {CO_3}^{2-} \tag{2.6}$$

$$CaO + H_2CO_3 \longrightarrow CaCO_3 + H_2O \tag{2.7}$$

$$CaCO_3 + H_2O + CO_2 \longrightarrow Ca(HCO_3)_2 \tag{2.8}$$

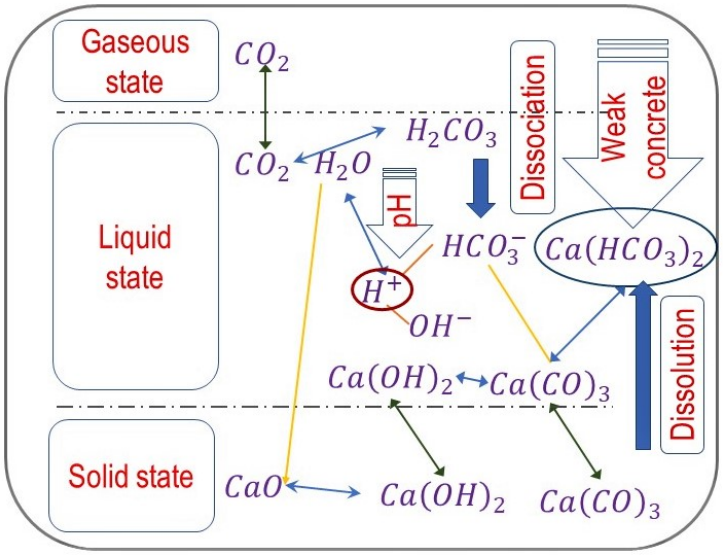

Figure 2.3: Phase diagram of carbonation in concrete.

The extent of carbonation in a good quality concrete is limited to a few millimetre in depth of external surface. But, in a poor quality concrete the carbonation depth could extend to complete cover-depth. The causes of this deterioration are mainly high water-cement ratio and improper curing. Concrete with low cement quantity have a high permeability as air voids become predominant and connected after the hardening. Generally, carbonation is slow process and proceeds with a rate up to 1.0 mm per year.

Carbonation also highly depends on relative humidity of the concrete. Buildings which are unprotected from rain, covered from sunlight and have low cover thickness are highly susceptible to carbonation. Reduction of pH below 9.5 commences corrosion and passive layer is disintegrated when the pH approaches 8.0. Severe corrosion cases are observed when the pH falls below 7.0 which is acidic range. A simple test of the concrete cores or extracted samples with the phenolphthalein indicator can uncover the extent of carbonation. Sound concrete samples which are highly alkaline render a purple-red colour to the indicator whereas carbonated zones remain uncoloured. Studies show that the discolouration of the indicator in the above method occur for a pH up to 9.5 although the rebar corrosion may have effected when pH of pore solution is less than 11. Thus, this method shall be seen as an approximate measure of rebar corrosion.

Detailed studies on the pore solution of the concrete extracted after the carbonation have confirmed that the free alkali metal content gets decreased. Besides deterioration of the concrete quality the microscopic studies on the carbonation products have reported that they show a significant increase in the chloride and sulphur concentrations [De Weerdt *et al.*, 2019].A carbonated concrete is susceptible to corrosion as the threshold value of chloride ion required to corrode steel is loared due to carbonation of concrete.

2.2.2 Corrosion of rebars due to chloride ions

Chloride ions are the main reason for corrosion of rebars in concrete across the world. These are classified into internal chlorides which enter during the preparation stage and external chlorides which diffuse or seep through the outside medium. Major sources of internal chlorides are chemical admixtures, water used in mixing and curing, reactive aggregates and the external chlorides are due to de-icing salt, sea water or air in the onshore or near shore structures. The pores in concrete provide the necessary path for the chloride diffusion. Thus, a sound concrete with less air voids is naturally protected against corrosion whereas a poor quality concrete with sufficient connected air voids is extremely susceptible to corrosion. The carbonation process which increases the pH contribute to the fast migration of the chloride ions inside the pore solutions. The literature is focussed on the chloride induced corrosion due to two major factors, firstly, abundance of chloride containing substances and secondly, their ability to de-passivate the passive layer. Chloride induced damages in concrete become noticeable when their concentration exceeds

Table 2.1: Threshold limits of chloride contents (ACI 318).

Type of structure	Maximum allowable chloride (% by weight of cement)
Prestressed concrete	0.06
RC exposed to moisture with access to external chloride	0.15
RC exposed to moisture without access to external chlorides	0.30
RC (Dry) covered from moisture	1.00

a certain threshold which is 0.6 kg per cubic metre of concrete as per IS 456. Relevant limits of chloride content recommended for USA building code ACI 318 are mentioned in the table 2.1 Chloride ions initiate the corrosion by destabilising the passive layer around the steel and the concentration required for this initiation process depends on the pH of pore solution. Apart from the chloride ion concentration, the rate of corrosion depends on several factors such as Oxygen availability, electrical resistivity,pH , temperature and relative humidity.

2.3 Current corrosion detection methods

The importance of damage prognosis is recognised by various enforcing agencies. The change in physical properties during corrosion are utilised to develop various NDT methods. These can be broadly categorised as electrochemical and mechanical methods.

2.3.1 Electrochemical methods

Half-cell potential measurement

Half-cell potential method is the widely used in civil industry to estimate the tendency of rebars to corrode. In this method, susceptibility of of embedded rebar to corrosion is estimated by measuring their potential relative to a reference half-cell placed on the concrete and electrically connected to the rebar. Reference half-cell is generally copper in copper sulfate solution or silver in silver chloride solution which have positive potential of +314 mV and +199 mV respectively, when measured with standard hydrogen electrode. The values of predicted potential depend upon the reference half-cell thus the results shall be interpreted after applying necessary corrections. In the test process, the pore solution

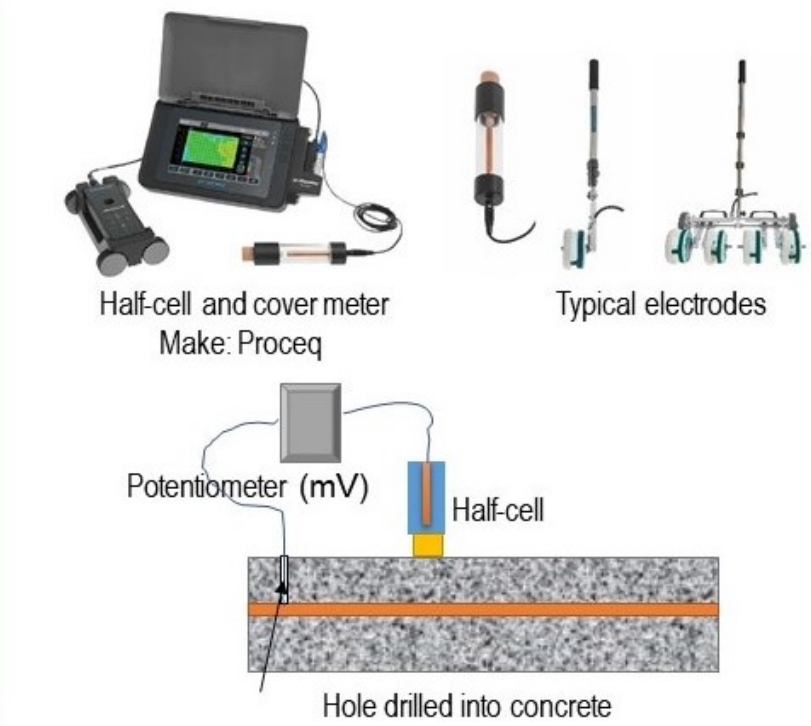

Figure 2.4: Typical half-cell equiment and arrangement of test on concrete.

Table 2.2: Probability of corrosion based on half-cell potential values (ASTM C876-15).

Value of potential measured with $Cu/CuSO_4$ electrode	Probability of corrosion
< -350 mV	90 % or high probability
-350 mV to -200 mV	50 % or uncertain
> -200 mV	10 % or low probability

serves as electrolyte. Concrete is wetted with diluted soap water to increase the electrical connection. Another lead wire is connected directly to the rebar cage by drilling a hole. Proceq make half-cell testing equipment and schematic diagram of testing is shown in Figure 2.4. For the accurate measurement of potentials the rebars shall have the unbroken electrical connectivity. The connectivity is checked with the help of multimeter and the resistance between remote points shall be less than 1Ω. Multiple connecting points at the rebar shall be used to test the same slab if the rebars lack the continuous electrical connection. ASTM C876 includes the standard protocol for half-cell measurements. The measured potentials can be interpreted to estimate the probability of corrosion as below in Table 2.2. This method is widely used for its simplicity and its capability to indicate the structural members prone to corrosion. Limitation of this method is that it cannot suggest the extent and stage of corrosion.

Concrete resistivity measurement

Electrical resistivity of a material is its property to inhibit the charge transfer. The materials with higher resistivity exhibit lower current for same voltage condition. Porosity, saturation of the pores, characteristics of poresolution and temperature determine the resistivity of concrete. The anodic and cathodic currents depend on the resistivity thus it plays an important role in determining in the rate of reaction [Hornbostel *et al.*, 2013]. The RILEM-standard recommends to use four probe method instead of two probe method for the calculation of resistivity. RILEM is an international union that provides recommendations for various standards in construction. The values of resistivity shall be interpreted as in Table 2.3 to estimate the corrosion potential of a member. Four probe resistivity measurements are used by Fu and Chung, 1997 to explore the relationship between the bond strength and resistivity of corroded RC specimens. The bond strength shows an initial increase with corrosion followed by rapid reduction whereas the contact resistivity measurements show a consistent increase with corrosion. Thus, they can not be used to estimate corrosion accurately.

Table 2.3: Probability of corrosion based on concrete resistivity measurements (RILEM TC-154).

Value of concrete resistivity (Ωm)	Probability of corrosion
< 100	high
100 to 500	moderate
500 to 1000	low
> 1000	negligible

Linear polarisation resistance measurement

As mentioned above, the half potential and concrete resistivity measurements can only indicate the probability of corrosion and do not reckon its actual rate. Linear polarisation resistance (LPR) measurement is used to estimate the instantaneous corrosion rate. It is carried out by applying a small electrochemical perturbation to the steel reinforcement with the help of an auxiliary electrode placed on the surface of concrete. A small DC potential change , δE, around 20 mV is applied to the steel as perturbation. The resulting current (δI) is measured after a suitable time typically 30 to 300 seconds. Polarisation resistance (Rp) is calculated using the relation between potential and current, Rp= δE/δI.

Instantaneous rate of corrosion that depends on the steel area, concrete cover resistance is then determined and used to calculate loss of rebar thickness per year [Pradhan and Bhattacharjee, 2009]. This method requires access to the rebars which is generally provided by drilling a hole. Recent improvements include use of combined four point resistivity and LPR method in which the direct exposure of reinforcement is not necessary [Sadowski, 2012]. LPR measurements are correlated to the mass loss in embedded rebars subjected to chloride corrosion and carbonation. The results show that LPR method overestimates the mass loss values Law *et al.* [2004].

Galvanostatic pulse method

Galvanostatic pulse method also measures the polarisation resistance like LPR technique. Their working differs essentially in the procedure of measuring the resistance value. In this method, an electric current pulse is applied and the resultant transient potential drop is used to calculate the polarisation resistance. Duration of testing in this method is lower as the pulse duration in the range of 5 to 10 seconds. However, this method overestimate the potentials compared to LPR [Tang, 2002]. Figure 2.5 shows the commercial Galva Pulse GP-5000 equipment deployed to test corrosion potential of concrete specimens.

Figure 2.5: Galvanostatic pulse equipments used to test the corrosion of concrete specimens. Source: El-Dieb and El-Maaddawy, 2018.

2.3.2 Mechanical methods

The mechanical properties of the material such as strain, displacement, mode shapes are used to quantify damage in the structure.

Acoustic emission

Elastic waves are generated when structural components undergo irreversible changes due to internal factors like corrosion or external factors like loading, machine induced vibration and earthquake. This transient stress wave generation mechanism is termed as acoustic emission (AE). AE monitoring equipment includes an extensive network of sensors and preamplifiers which are controlled by a controlling unit as shown in Figure **??**. Typical sources of AE are crack initiation and propagation, microfracture in the materials, plastic deformation, failure or collapse etc. This method is developed as a monitoring system for the composite materials used in the aerospace industry [Robinson *et al.*, 2016]. Recently there is trend in application of this method to detect the damages in concrete structures Mangual *et al.* [2011]; Noorsuhada [2016]. The AE sensors listen to all the stress waves near their vicinity and record them in real-time. In a corroded RC, the stress waves generated during the corrosion initiation process which creates microcracks and propagation in which the micro-cracks develop into macro-cracks. The analysis of AE data is carried in two ways by analysing the basic parameters of signals and complete signal analysis which are termed as parametric analysis and waveform analysis, respectively. The basic parameters used in the parametric analysis are time of arrival amplitude, frequency, rise time and count.

Recently, AE is successfully deployed to detect the real-time deterioration caused by corrosion related concrete cracking. Intensity of AE signals is correlated with the progress of corrosion damage in prestressing strands by researchers. The results are promising for their relation to mass loss characterised by the loss of steel section. In the volume expansion stage of corrosion the number of AE activity is higher [Mangual *et al.*, 2013]. The influence of various stages of pitting corrosion on the structural behaviour of RC beams is evaluated using AE during the accelerated corrosion experiments and load tests [Di Benedetti *et al.*, 2012; Sharma *et al.*, 2018]. The analysis of AE data shows distinct trends for relative amplitude (RA) value, average frequency (AF) and b-value for different corrosion levels. These trends aid in interpreting various stages of the damage from the microcracking to ultimate failure. AE is also used to monitor the crack pattern and orientation in corroded beams. AE can estimate the change in failure pattern due to corrosion of RC beams from flexure mode to shear mode. The load tests on the beams

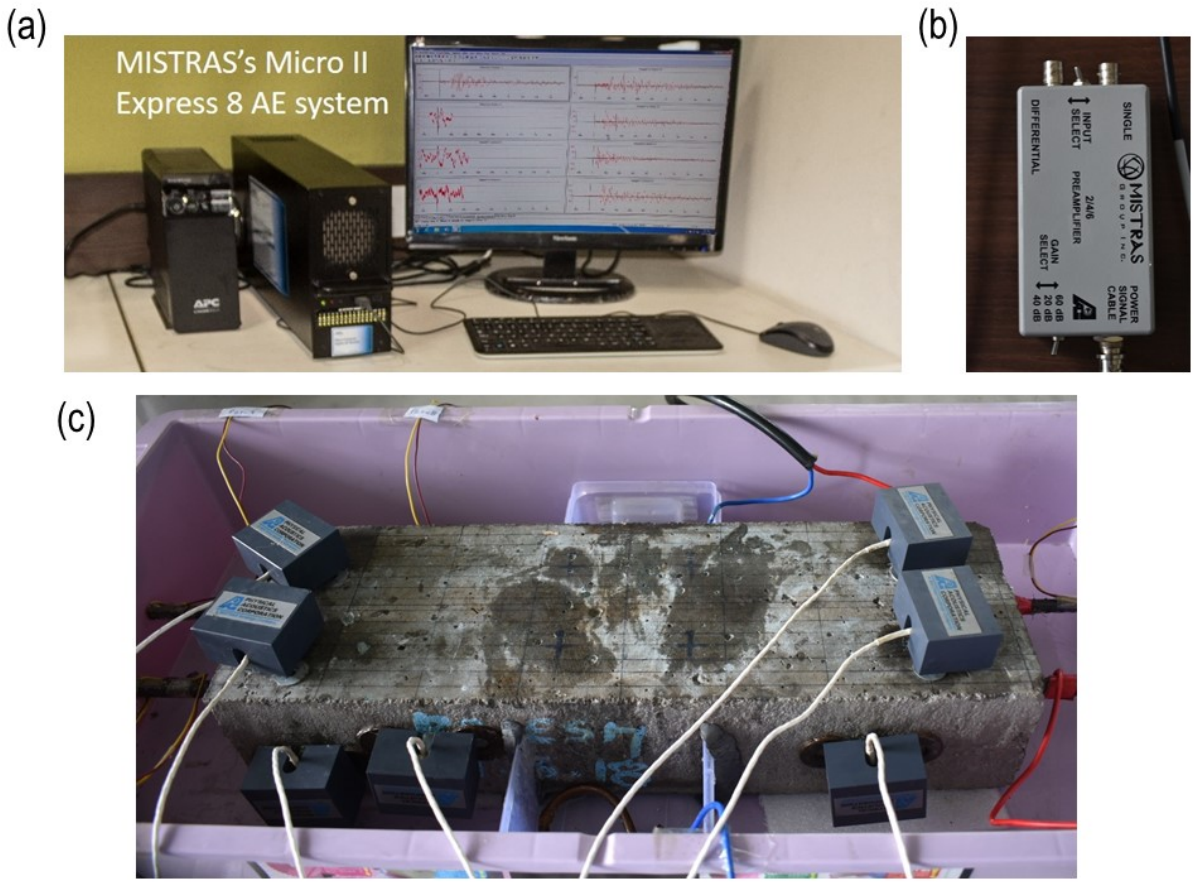

Figure 2.6: AE system used for corrosion monitoring at IIT Bombay, Structural Health Monitoring and Retrofitting Lab that includes (a) controlling unit, (b) preamplifiers and (c) sensor arrangement on concrete beam.

are performed using a combination of load-controlled and displacement-controlled three-point bending tests to study the changes in residual strength. Upon the study of the AE data acquired during the static loading, the damage is classified and quantified based on the time-driven parametric approach [Zaki *et al.*, 2017].

Impact echo

Impact echo method is widely used for pile integrity testing and concrete imaging. In this method, a small transient point load is applied on concrete surface with a calibrated hammer to generate waves and the response is accumulated with sensors. These signals are analysed in time domain and frequency domain to monitor the arrival times and frequency of vibrational resonance peaks [Zhu and Popovics, 2007]. Currently research is in progress to detect defects in concrete using impact echo method. A distributed sensor array network, as shown in Figure 2.7, is deployed to develop the detect voids in concrete.

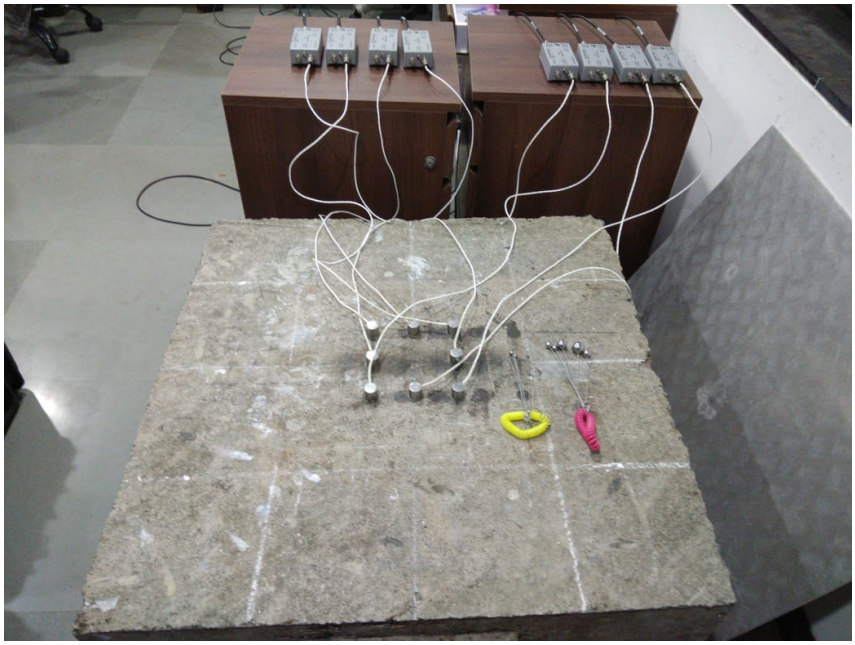

Figure 2.7: Sensor arrangement for impact echo testing used for void detection in concrete at I l IT Bombay, Structural Health Monitoring and Retrofitting Lab.

The impact stress wave characteristics are analysed for variety of voids and an algorithm is developed to reconstruct the voids by using time-frequency analysis. Figure 2.8shows the profile of void in concrete estimated using the wavelet transform coefficients. The circular wave front observed in the plot indicates that the wave propagating with spherical wave fronts. The high intensity white patch from the distance 175 mm to 200 mm represents the reflection of the wave at the void depth of 175 mm. And the patch nearer to 350mm indicates the reflection of the wave from the bottom surface. The central location of the white patch in X-axis indicates that the void is located at the centre.

Vibration data

Vibration properties of the structure such as frequency, mode shapes, damping, sensitivity and flexibility are used to detect the presence of damage as it reduces the stiffness, shifts natural-frequencies, and changes frequency response function and mode shapes. In this method, the structure is excited to induce vibration and the response is captured with accelerometers. In case of an undamaged structure, the imparted energy is fully utilised for vibration whereas presence of damage causes dissipation of energy. Damping characteristics are thus used to study degree of corrosion in beams . Structures with corrosion damages show high damping in second and third mode compared to the undam-

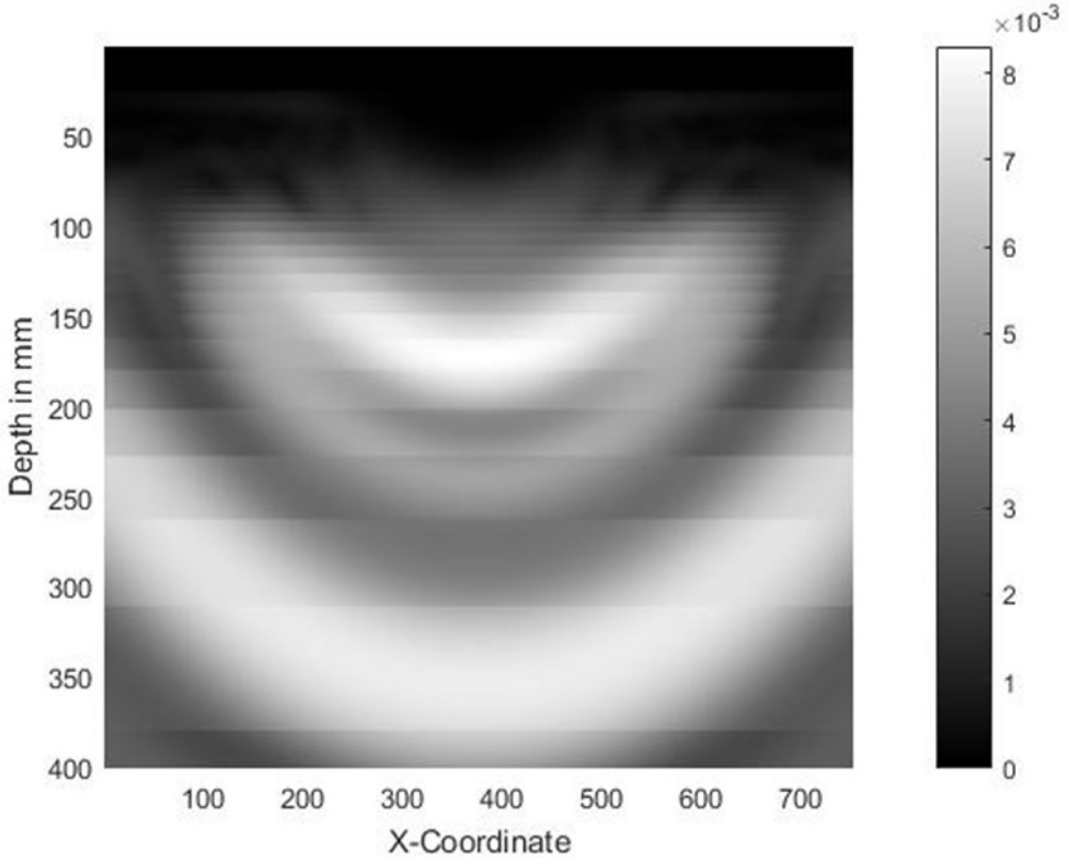

Figure 2.8: Wavelet based reconstruction of voids in concrete using impact echo testing.

aged one [Razak and Choi, 2001]. Damping and natural frequencies provide the global behaviour of the structures and cannot be used in localisation of damage. Uncertainty in estimation of damping and ambient noise are challenges in this method [Cao *et al.*, 2017]. Damage index methods are developed using modal flexibility Pandey and Biswas [1994] and mode-shape data with a constantly updating baseline to localise crack formation in RC members [Wahalathantri *et al.*, 2015]. Damage index plots to assess the corrosion of cables in suspension bridges are shown in Figure 2.9. Modes with dominant vertical vibration are effective in detecting the corrosion damage.

Electromechanical impedance

Damages and defects alter the mechanical impedance of the structure. These changes can be estimated with the use of smart piezoelectric or macro fibre composite transducers that are integrated inside the structure. These broadband transducers are excited with an input sinusoidal pulse covering a large frequency band. Condition of the structure

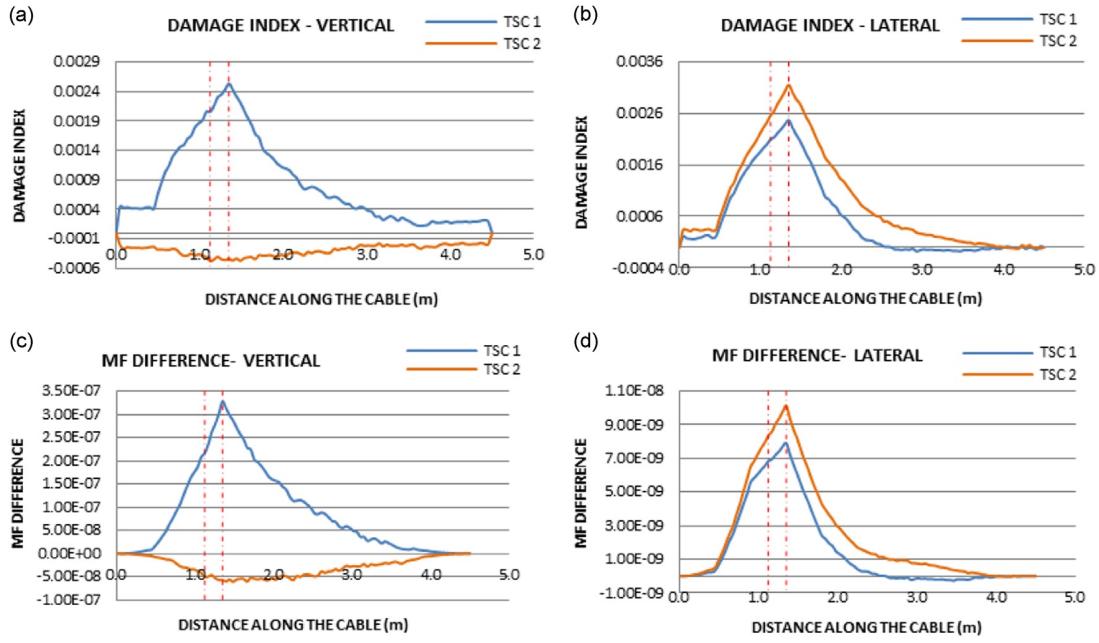

Figure 2.9: Damage localisation in a damaged (TSC 1) and an undamaged (TSC 2) cables using damage index method (DI) based on(a) vertical (DI_V) and (b) lateral (DI_L) modes of vibration ; and modal flexibility method (MF) based on (c) vertical (MF_V) and (d) lateral (MF_L) modes of vibration. Source: Wickramasinghe *et al.*, 2016.

is assessed by monitoring the impedance of smart transducers. Establishing a baseline signature is necessary to recognise the later changes due to corrosion or cracks. The baseline response consists spectral peaks corresponding to sensor material. Alteration and appearance of new peaks in the later life of structure represent the deterioration of structural components. It is reported that this method can detect damages located up to 2 m from the sensor location. Frequency of testing coincides with the ultrasonic range (20 kHz to 500 kHz) thus the response is affected by the structural vibrations.

Elastic waves

Wave propagation is extensively used to study the mechanical behaviour of materials. The changes in mechanical properties affect the propagation characteristics of various wave modes, and this property is extensively used for damage identification.Elastic waves can propagate in concrete and NDT methods are developed based on their propagation characteristics. These waves travel faster in denser medium and slower in sparse medium. This principle is used to assess the quality of concrete in ultrasonic pulse velocity measurements. In structures with thickness comparable to wavelength the elastic waves are guided by the boundaries and a number of wave modes exist. Interaction of these waves

with damage results in scattering and mode conversion. Defect features can be accurately detected by analysing the wave signals. The major components of GW based SHM are transducers, sensor network, signal processing and analysis techniques. Its use is becoming more common in industry because of tremendous advances in the field of wave propagation with focus on mechanics, mathematics, electronics and sensors. Advent of high performance computing has led to the detailed understanding of wave propagation in waveguides with or without damages. These advances have allowed the research community to understand their propagation characteristics in complex waveguides and composite materials like embedded pipes, RC and FRP repaired RC. While health monitoring systems based on guided waves for structures made of steel, aluminium and carbon fibre-based composites are well established, the non-destructive evaluation (NDE) of RC structures is yet to be established. Bulky and inhomogeneous nature of RC poses challenges as they induce highly dissipative waves. Proper interpretation of stress-waves signals and wave modes is necessary for practical application of these waves for damage detection.

2.3.3 Other methods

Apart from the aforementioned techniques several other methods exist that use thermal, electrical and magnetic properties of the materials to detect damages in concrete. Several studies exploit the changes to characteristics of light in fibre optic sensors (FOS) to assess the damages. FOS yield sophisticated information about the strain, temperature, cracks, delamination and chloride concentration [Maalej *et al.*, 2004; Barrias *et al.*, 2016]. Strain measurements show that composite action is not achieved at the provided development length in corroded rebars due to debonding of rebars and concrete. The peaks in strain measurements indicate hidden pitting (Figure 2.10). Distributed sensor networks are deployed to achieve a better sensing range and the installation of these sensors is labour intensive. Major challenge in FOS based detection method is the loss of contact between sensor and rebars due to corrosion. This problem is addressed by application of water proof sealant and 2-part marine epoxy [Davis *et al.*, 2016]. Shift in the wavelength of fibre Bragg grating (FBG) is used to assess corrosion by researchers. The sensitivity of FBG sensors is improved by using coating of Polydimethyl Siloxane layer [Tan *et al.*, 2016]. Self sensing devices are developed using FOS that function as both sensor and reinforcing material in concrete [Lau, 2004].

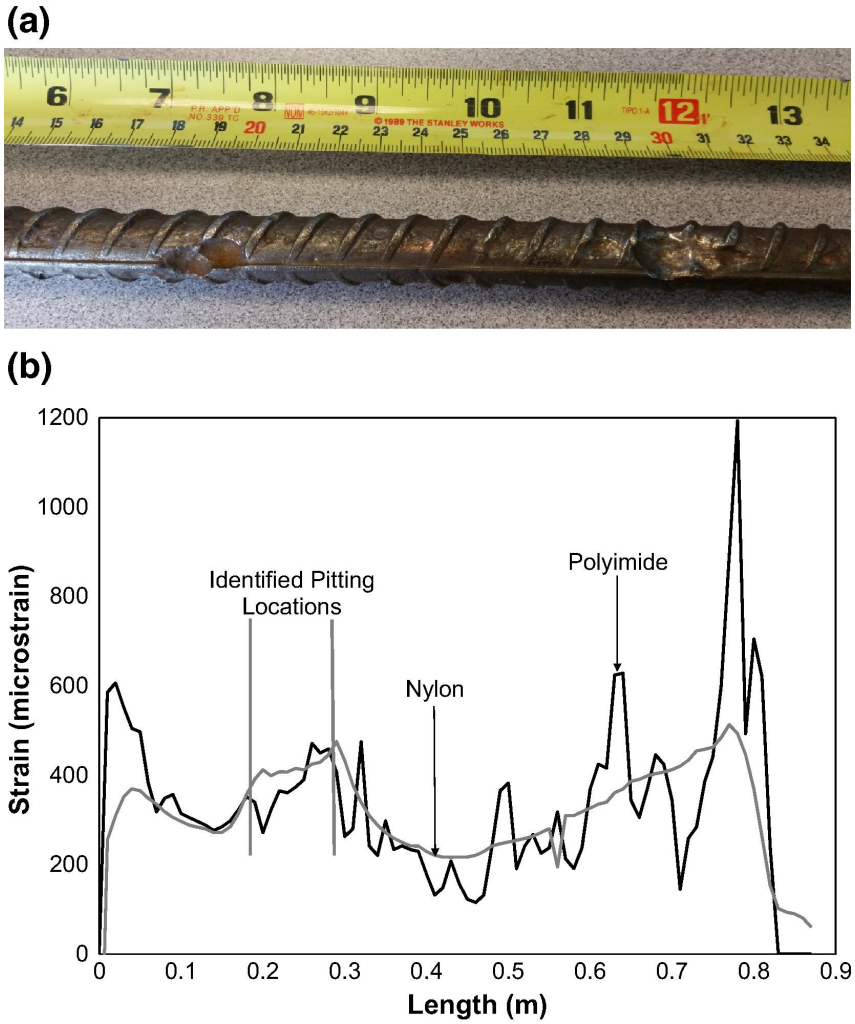

Figure 2.10: Pitting corrosion in (a) a rebar sample and (b) corresponding strain measurements using FOS that indicate the location of corrosion. Source: Davis *et al.*, 2016.

Recent focus of the studies is three dimensional imaging of concrete using the temperature distribution, ultrasonic signals and electrical potentials. Studies show that infrared thermography (IRT) has potential to detect the defects in concrete. The thermal properties of the material such as conductivity and heat capacity are altered due to flaws. Thermal images captured by infrared cameras are investigated for qualitative evaluation of various damages. Delamination and subsurface defects in bridge decks are detected by thermal inertia measurements [Del Grande and Durbin, 2003]. The temperature difference depends on the defect dimensions. Defects closer to surface result in quicker achievement of peak-temperature difference and the increase in defect area increases the temperature difference [Cheng *et al.*, 2008]. Defects in concrete slabs are quantified by calculating the calibration curves of temperature difference that are functions of material properties [Maierhofer *et al.*, 2006]. Ultrasonic tomography is a recent technique to visualise dam-

ages. Phased arrays of ultrasonic transducers are used in commercial imaging systems like MIRA and EYECON. Bulk waves are generated in concrete medium using the focussed ultrasound and the images are reconstructed using synthetic aperture focussing technique (SAFT) and reverse time migration (RTM) [Beniwal and Ganguli, 2015, 2016]. Electrical resistance tomography (ERT) is used to reconstruct the three dimensional image of RC cylinders. In this method, electrical current is injected and the voltage is measured at several points on the boundary. Theoretical diffusive models are used to estimate the distribution of electric current that is a dependent of conductivity and admittance of constituent materials of RC [Karhunen *et al.*, 2010].

Eddy current testing is an emerging technology in NDE of metallic structures. In this method, eddy current is induced by an excitation coil and presence of flaws is sensed by change in the electromagnetic field [Frankowski, 2011; Minesawa and Sasaki, 2014]. Pulsed eddy current (PEC) method uses a broadband excitation signal with multiple frequencies typically a rectangular wave pulse [Lebrun *et al.*, 1997]. The signals are compared with a reference signal that is obtained from an undamaged specimen. Time series analysis of differential signal calculated by subtracting defective signal from reference signal gives information on defect depth and location. The peak value of differential signal gives defect depth and, arrival time of peak gives information on the location. Principal component analysis based feature extraction is used by researchers to minimise noise and to normalise the errors that occur when using different sensors of the same type. Multiple PEC sensor system offers the advantage of 3D defect reconstruction [Tian *et al.*, 2005; Tian and Sophian, 2005]. Eddy current is also used for electromagnetic heating of the RC slabs through induction and subsequently infrared thermography is performed on the slabs for thermal imaging and damage detection. Loss of rebar mass due to corrosion is directly proportional to the temperature gradient. However, in the initial stage of corrosion the temperature gradient decreases due to formation of rust. Several other factors such as concrete cover cause non linear change in the temperature gradient hence further studies are necessary to adopt this method [Kwon *et al.*, 2011; Zhu *et al.*, 2016].

Table 2.4: Various techniques to detect corrosion along with their advantage and limitation.

S No.	Name	Advantage	Limitation
1	Visual inspection	Quick estimation.	In accurate and subject to errors.
2	Half-cell potential	Estimation of probability.	No information of actual corrosion.
3	Concrete resistivity	Indicate the corrosion risk.	Influenced by several other factor apart from corrosion.
4	Linear polarisation resistance	Determine rate of corrosion.	Overestimation of corrosion current and unreliable due to inconsistency in measurements.
5	Galvanostatic pulse	Faster measurements compared to other electrochemical techniques.	Quantification is not possible.
6	Acoustic emission	External source or trigger not required.	High power requirement as sensors need to be engaged continuously.
7	Impact echo	Quantification of subsurface defects.	Low sensitivity, labour intensive and time consuming.
8	Vibration data	Evaluate the global damage parameters.	Multi-modal, expensive and low sensitivity
9	Electromechanical impedance	Better sensitivity due to high frequency of testing.	Latest method and corrosion is not quantified.
10	Fibre optic sensors	Estimate multiple structural parameters such as strains, crack width and temperature.	High cost of installation.
11	Thermal imaging	Three-dimensional visualisation of damage	High energy requirement to heat the structural members
12	Eddy current testing	High sensitivity to surface defects	Difficulty in assessing structures with low conductivity like concrete

2.4 Advantages of guided wave-based SHM

The traditional NDT techniques to estimate corrosion such as visual inspection, ultrasonic pulse velocity and half-cell potential measurements do not corroborate the extent of corrosion in the RC structures. A comparison of different methods is presented in Table 2.4. Advantages of GW based damage detection method are:

1. A single sensor can be used to study a long testing subject and acquire all the data. The sensor need not moved to each location to scan the entire area.

2. Owing to the high frequencies deployed for testing, this method can give an accurate picture of test subject as it is sensitive to damages with smaller sizes.

3. Damage quantification and localisation is possible with this technique

4. It can be deployed for the damage detection in inaccessible and concealed spaces like structure under water, coating , encapsulated inside a different structure.

5. For inspection of structures such as pipeline, this method offers possibility to scan the damages with minimal removal of insulation thus saving time and cost.

6. Damages in composite structures and multilayered structures can be detected using this method by utilising damage sensitive frequencies and modes of propagation.

2.5 Concluding remarks

The major cause of failure in RC structures is recognised as corrosion. The factors that contribute to the inception of corrosion are discussed in this chapter. The mechanism of corrosion caused by carbonation and chloride ions is explained in detail. Existing literature is studied to understand the current damage detection methods in RC. The literature study enlightens that several methods exist to detect corrosion, yet they are not capable to foresee its commencement. Among the latest methods, elastic wave based methods are least invasive and have the potential to decipher corrosion inception.

Chapter 3

Literature review of guided wave-based corrosion monitoring

3.1 Introduction

The propagation of energy in a body with the aid of particle movement in the body can be described as wave propagation. It depends on the mechanical properties of medium and boundaries. The characteristics of waves are affected when there is change in the medium thus waves are used to study the materials. Understanding the mechanism of wave propagation is important for devising reliable and robust SHM techniques. In a large structure like a block of concrete the waves travel in the bulk of material away from the boundaries hence these are called bulk waves. In thin structures the waves are channelled by the boundaries thus they are termed as GWs (GWs). GW propagation is associated with bounded media and the actual boundary conditions determine the type and mode of the wave that propagates. The early research in the field of GW propagation originated from the work of Lord Raleigh. He has investigated the propagation of stress waves in elastic solids with finite thickness comparable to wavelength [Rayleigh, 1885]. Horace Lamb has established theoretical fundamentals of waves that can propagate in plate like structures with free surfaces [Lamb, 1917]. These waves are called Lamb waves.

GWs in natural waveguides such as plates,multilayered composites, rails, rods and pipes are considered for their use in SHM in the recent years. GWs follow the boundaries and propagate along them. In a beam the waves travel along its longitudinal axis, in a plate, they are guided by upper and lower surfaces. Several analytical, semi analytical and finite element based methods have been employed to simulate the GW propaga-

tion. These numerical models aid in better understanding of the experimental results in complex structures. This chapter summarises theoretical fundamentals of GWs and the currents developments in the application of GWs to corrosion detection. GW generation, sensing, mechanism of propagation and signal evaluation methods are covered in the literature survey. Latest developments in defect localisation using this method are studied to recognise the lacuna in modern research.

3.2 Theory of wave propagation in plates

The equations of motion pertaining to a three dimensional deformable solid with density (ρ) can be derived by considering equilibrium of an infinitesimally small size element with stresses (Figure 3.1) and body force $\{\mathbf{f}= [f_x\ f_y\ f_z]\}$.

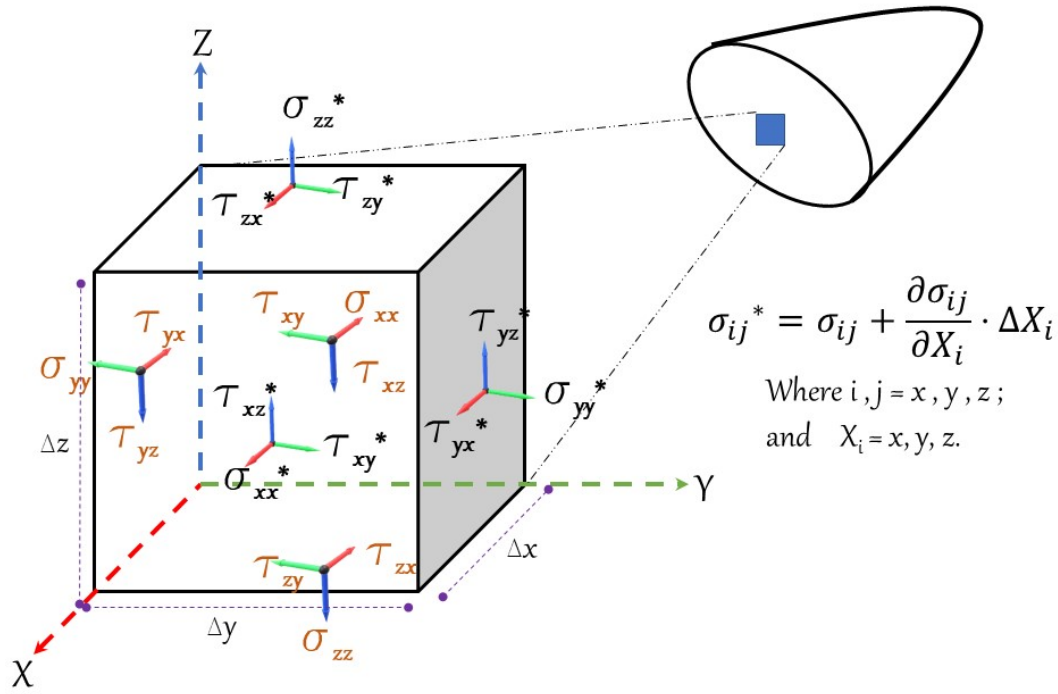

Figure 3.1: Stresses acting on an infinitesimally small element in equilibrium.

Applying Newton's second law of motion for this element, the equilibrium of all the forces in each of the three orthogonal axes lead to three equations (3.1a–3.1c) and equi-

librium of moments show that $\tau_{xy} = \tau_{yx}$, $\tau_{yz} = \tau_{zy}$ and $\tau_{zx} = \tau_{xz}$.

$$\frac{\partial \sigma_{xx}}{\partial x} + \frac{\partial \tau_{yx}}{\partial y} + \frac{\partial \tau_{zx}}{\partial z} + \rho f_x = \rho \frac{\partial^2 u_x}{\partial t^2} \tag{3.1a}$$

$$\frac{\partial \tau_{xy}}{\partial x} + \frac{\partial \sigma_{yy}}{\partial y} + \frac{\partial \tau_{zy}}{\partial z} + \rho f_y = \rho \frac{\partial^2 u_y}{\partial t^2} \tag{3.1b}$$

$$\frac{\partial \tau_{xz}}{\partial x} + \frac{\partial \tau_{yz}}{\partial y} + \frac{\partial \sigma_{zz}}{\partial z} + \rho f_z = \rho \frac{\partial^2 u_z}{\partial t^2} \tag{3.1c}$$

In tensor notation, all the equations of equilibrium can be represented by set of relations in Equation 3.2 where $i, j = (x, y, z)$ *or* $(1, 2, 3)$. The number of unknowns in these three equations is six thus additional information is required to solve them.

$$\begin{aligned} \boldsymbol{\sigma_{ji,i}} + \rho \boldsymbol{f_i} &= \rho \ddot{\boldsymbol{u}}_{\boldsymbol{i}} \\ \boldsymbol{\tau_{ij}} &= \boldsymbol{\tau_{ji}} \end{aligned} \tag{3.2}$$

The stress-strain relations that describe the behaviour of material and boundary conditions provide these additional equations. The relationship between stress ($\boldsymbol{\sigma}$) and strain ($\boldsymbol{\epsilon}$) for an elastic body based on Hooke's law for is given by 3.3. The strains are expressed in terms of actual displacements $\{\mathbf{U}= [u_1 \ u_2 \ \ u_3]\}$ along the axes 1,2 and 3 by Equation 3.4.

$$\begin{bmatrix} \sigma_{11} \\ \sigma_{22} \\ \sigma_{33} \\ \sigma_{12} \\ \sigma_{23} \\ \sigma_{31} \end{bmatrix} = \begin{bmatrix} C_{1111} & C_{1122} & C_{1133} & C_{1112} & C_{1123} & C_{1131} \\ C_{2211} & C_{2222} & C_{2233} & C_{2212} & C_{2223} & C_{2231} \\ C_{3311} & C_{3222} & C_{3333} & C_{3312} & C_{3323} & C_{3331} \\ C_{1211} & C_{1222} & C_{1233} & C_{1212} & C_{1223} & C_{1231} \\ C_{2311} & C_{2322} & C_{2333} & C_{2312} & C_{2323} & C_{2331} \\ C_{3111} & C_{3122} & C_{3133} & C_{3112} & C_{3123} & C_{3131} \end{bmatrix} \begin{bmatrix} \epsilon_{11} \\ \epsilon_{22} \\ \epsilon_{33} \\ \epsilon_{12} \\ \epsilon_{23} \\ \epsilon_{31} \end{bmatrix} \tag{3.3}$$

$$\textit{or} \qquad \boldsymbol{\sigma_{ij}} = \boldsymbol{C_{ijkl}} \boldsymbol{\epsilon_{kl}}; \quad i, j, k, l = 1, 2, 3$$

$$\boldsymbol{\epsilon_{kl}} = \frac{\mathbf{1}}{\mathbf{2}} \left(\boldsymbol{u_{k,l}} + \boldsymbol{u_{l,k}} \right) \tag{3.4}$$

The constitutive relations can be written $[\boldsymbol{\epsilon}] = [\boldsymbol{S}][\boldsymbol{\sigma}]$ alternatively in which the compliance matrix $[\boldsymbol{S}]$ is the inverse of stiffness matrix $[\boldsymbol{C}]$. For an anisotropic and orthotropic material the compliance matrix $[\boldsymbol{S}]$contains 21 and 9 independent constants, respectively. An isotropic material has same properties in all the directions thus it requires only two

constants among the modulus of elasticity (E), shear modulus (G) and Poisson's ratio (ν). The constitutive relations for an isotropic material are summarised in (Equation 3.5)

$$\begin{bmatrix} \epsilon_{11} \\ \epsilon_{22} \\ \epsilon_{33} \\ \epsilon_{12} \\ \epsilon_{23} \\ \epsilon_{31} \end{bmatrix} = \begin{bmatrix} \frac{1}{E} & -\frac{\nu}{E} & -\frac{\nu}{E} & 0 & 0 & 0 \\ -\frac{\nu}{E} & \frac{1}{E} & -\frac{\nu}{E} & 0 & 0 & 0 \\ -\frac{\nu}{E} & -\frac{\nu}{E} & \frac{1}{E} & 0 & 0 & 0 \\ 0 & 0 & 0 & \frac{1}{2G} & 0 & 0 \\ 0 & 0 & 0 & 0 & \frac{1}{2G} & 0 \\ 0 & 0 & 0 & 0 & 0 & \frac{1}{2G} \end{bmatrix} \begin{bmatrix} \sigma_{11} \\ \sigma_{22} \\ \sigma_{33} \\ \sigma_{12} \\ \sigma_{23} \\ \sigma_{31} \end{bmatrix} \tag{3.5}$$

The Stress σ_{11} can be expressed alternatively as

$$\sigma_{11} = \frac{E}{1+\nu}\epsilon_{11} + \frac{E\nu}{(1+\nu)(1-2\nu)}(\epsilon_{11} + \epsilon_{22} + \epsilon_{33}) \tag{3.6}$$

$$\sigma_{11} = 2\mu\epsilon_{11} + \lambda(\epsilon_{11} + \epsilon_{22} + \epsilon_{33}) \tag{3.7}$$

$$where \quad \mu = G = \frac{E}{2(1+\nu)} \qquad and \qquad \lambda = \frac{E\nu}{(1+\nu)(1-2\nu)} \tag{3.8}$$

A similar manipulation can be carried out to express the other stress strain relations in terms of μ and λ. These are summarised in tensor notation as

$$\begin{aligned} \boldsymbol{\sigma_{ij}} &= \lambda\boldsymbol{\epsilon_{kk}}\boldsymbol{\delta_{ij}} + 2\mu\boldsymbol{\epsilon_{ij}} \\ \delta_{ij} &= \begin{cases} 1 \; if \; i = j \\ 0 \; if \; i \neq j \end{cases} \end{aligned} \tag{3.9}$$

The equations of equilibrium (3.2), stress-strain (Equation 3.9) and strain-displacement(Equation 3.4) relations can be combined to derive a set of governing differential equations of motion in Cartesian coordinates for an elastic-isotropic solid that are given by Equation 3.10.

$$\begin{aligned} (\lambda+\mu)\,\nabla\nabla\cdot\mathbf{U} + \mu\nabla^2\mathbf{U} + \rho\mathbf{f} &= \rho\ddot{\mathbf{U}} \\ \nabla &= \frac{\partial}{\partial x_1}\hat{x}_1 + \frac{\partial}{\partial x_2}\hat{x}_2 + \frac{\partial}{\partial x_3}\hat{x}_3 \\ \nabla^2 &= \frac{\partial^2}{\partial x_1^2} + \frac{\partial^2}{\partial x_2^2} + \frac{\partial^2}{\partial x_3^2} \end{aligned} \tag{3.10}$$

The equations of motion 3.10 are highly complex to solve thus it is simplified by using Helmholtz's decomposition of the displacement vector by introducing scalar potential ϕ

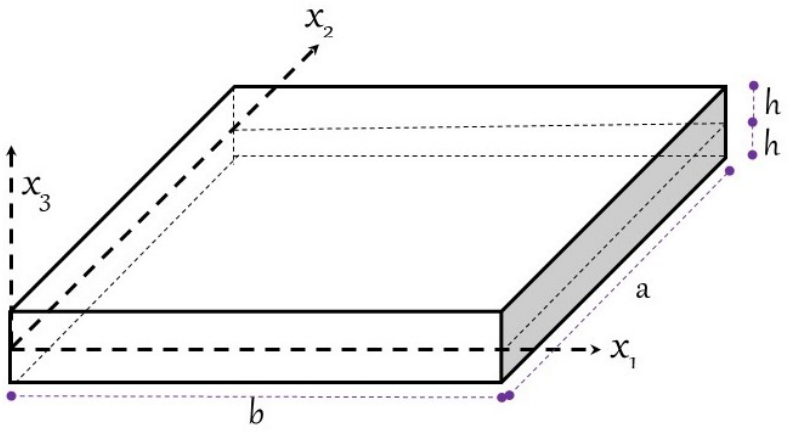

Figure 3.2: Schematic diagram of a thin plate with thickness 2h.

and vector potential $\mathbf{H}$ such that $\mathbf{U} = \nabla\phi + \nabla \times \mathbf{H}$ and $\nabla \cdot \mathbf{H} = 0$. The body force can also be expressed as $\mathbf{f} = \nabla F + \nabla \times \mathbf{B}$ and $\nabla \cdot \mathbf{B} = 0$. The simplified governing differential equation is

$$\nabla \left\{ (\lambda + 2\mu) \nabla^2 \phi + \rho F - \rho \ddot{\phi} \right\} + \nabla \times \left\{ \mu \nabla^2 \mathbf{H} + \rho \mathbf{B} - \rho \ddot{\mathbf{H}} \right\} = 0 \tag{3.11}$$

The solution to this equation exist when both the terms in curly brackets are equal to zero that is

$$(\lambda + 2\mu) \nabla^2 \phi + \rho \mathbf{F} - \rho \ddot{\phi} = 0 \tag{3.12}$$

$$\mu \nabla^2 \mathbf{H} + \rho \mathbf{B} - \rho \ddot{\mathbf{H}} = 0 \tag{3.13}$$

In the absence of body forces ($F = \mathbf{B} = 0$), the simplified equations are

$$\nabla^2 \phi = \frac{1}{{C_L}^2} \ddot{\phi} \quad \text{and} \quad \nabla^2 \mathbf{H} = \frac{1}{{C_T}^2} \ddot{\mathbf{H}} \tag{3.14}$$

where $C_L = \sqrt{\frac{\lambda+\mu}{\rho}}$ and $C_T = \sqrt{\frac{\mu}{\rho}}$. Boundary conditions shall be specified to obtain the particular solution of the governing equations for finite media. These boundary conditions are known displacement or traction or mixed. The governing equations are further simplified by assuming plane strain condition to solve wave propagation problem in thin plates (see Figure 3.2). Assuming plane strain in x_1x_3-plane, the displacements are given

by

$$\begin{aligned} u_1 &= \frac{\partial \phi}{\partial x_1} + \frac{\partial H}{\partial x_3} \\ u_2 &= 0 \\ u_3 &= \frac{\partial \phi}{\partial x_3} + \frac{\partial H}{\partial x_1} \end{aligned} \tag{3.15}$$

Substitution of Equation 3.15 in Equation 3.14 leads to the following general solution

$$\phi = [A_1 \sin(px_3) + A_2 \cos(px_3)] \,.\, \exp(i(kx_1 - \omega t)) \tag{3.16}$$

$$H = [B_1 \sin(qx_3) + B_2 \cos(qx_3)] \,.\, \exp(i(kx_1 - \omega t)) \tag{3.17}$$

where $p^2 = \frac{\omega^2}{{C_L}^2} - k^2$ and $q^2 = \frac{\omega^2}{{C_T}^2} - k^2$. Upon applying boundary conditions relations 3.18 and 3.19 are obtained for symmetric and antisymmetric modes, respectively.

$$\frac{\tan(qh)}{\tan(ph)} = -\frac{4k^2pq}{(k^2 - q^2)^2} \qquad \textit{Symmetric mode} \tag{3.18}$$

$$\frac{\tan(qh)}{\tan(ph)} = -\frac{(k^2 - q^2)^2}{4k^2pq} \qquad \textit{Antisymmetric mode} \tag{3.19}$$

The value of wave number, k, can be calculated for a given frequency ω from the aforementioned Raleigh-Lamb frequency relations which are also called dispersion relations. In general the modes in a plate are classified as symmetric, antisymmetric and shear-horizontal [Su and Ye, 2009; Rose, 2014; Graff, 1975]. The theoretical formulation and solutions described in this section are derived in the nineteenth century yet the frequency spectrum and behaviour of higher modes are understood after recent developments in the computer-aided solution strategies. Typical dispersion curves for an aluminium plate that are calculated using experiments are plotted in Figure 3.3. These plots shows number of possible modes increase with the increase in frequency-thickness product.

3.3 Theory of wave propagation in cylindrical bodies

GWs are also used to detect damages in cylindrical-structural components like rods and pipes. The equations of motion can be derived in cylindrical coordinates (r θ z) by applying transformation of coordinates to the equations of plate. The equilibrium equations

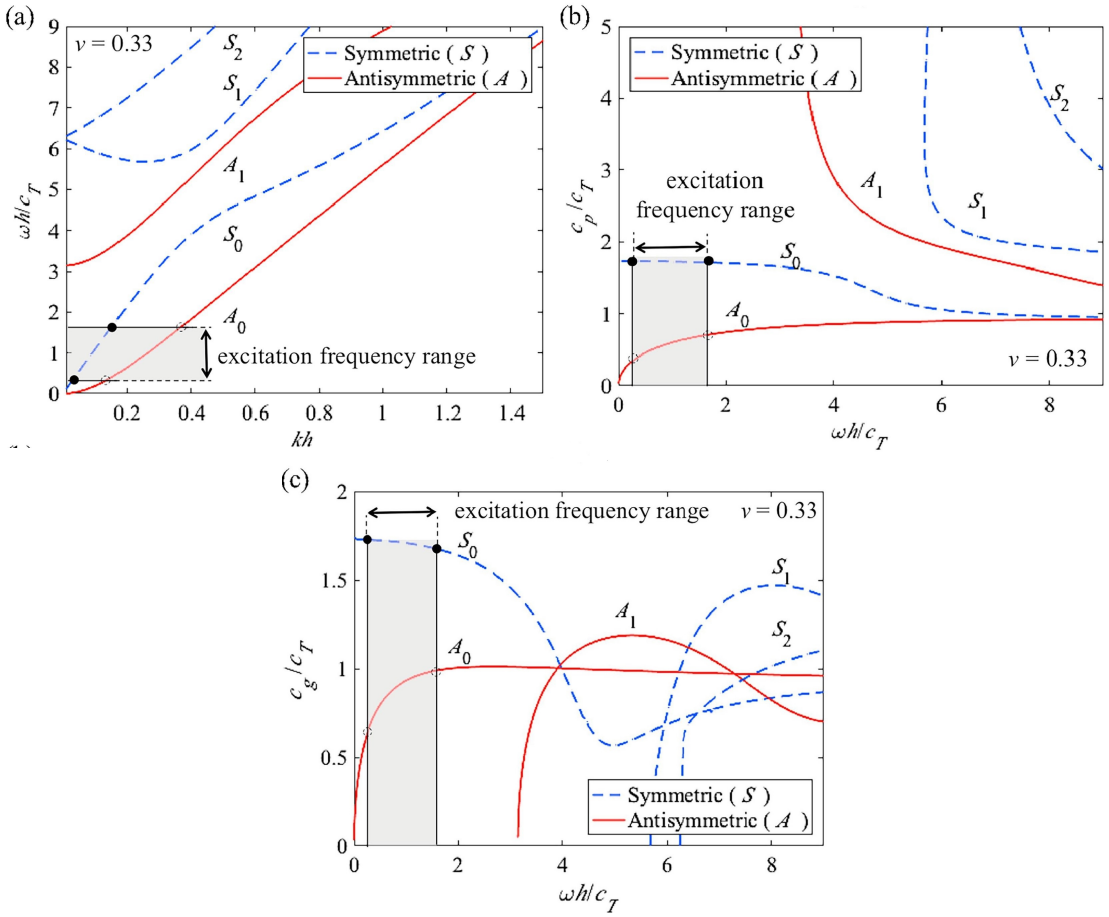

Figure 3.3: Typical dispersion curves of an aluminium plate showing the relations between (a) frequency-wave number, (b) frequency-phase velocity and (c) frequency-group velocity. Source: Chang and Yuan, 2018.

for an elastic-isotropic solids are given by

$$\nabla^2 u - \frac{u}{r^2} - \frac{2}{r^2}\frac{\partial v}{\partial \theta} + \frac{1}{1-2\nu}\frac{\partial \Delta}{\partial r} = \frac{1}{{C_T}^2}\frac{\partial^2 u}{\partial t^2} \tag{3.20a}$$

$$\nabla^2 v - \frac{v}{r^2} - \frac{2}{r^2}\frac{\partial u}{\partial \theta} + \frac{1}{1-2\nu}\frac{\partial \Delta}{\partial \theta} = \frac{1}{{C_T}^2}\frac{\partial^2 v}{\partial t^2} \tag{3.20b}$$

$$\nabla^2 w + \frac{1}{1-2\nu}\frac{\partial \Delta}{\partial z} = \frac{1}{{C_T}^2}\frac{\partial^2 w}{\partial t^2} \tag{3.20c}$$

where Laplacian operator ∇^2 and the first invariant of strain (dilation) Δ are expressed as

$$\nabla^2 = \frac{\partial^2}{\partial r^2} + \frac{1}{r}\frac{\partial}{\partial r} + \frac{1}{r^2}\frac{\partial^2}{\partial \theta} + \frac{\partial^2}{\partial z^2} \tag{3.21}$$

$$\Delta = \frac{\partial u}{\partial r} + \frac{1}{r}\left(\frac{\partial v}{\partial \theta} + u\right) + \frac{\partial w}{\partial z} \tag{3.22}$$

The displacements are represented in terms of scalar (φ) and vector ($\boldsymbol{\psi}$) potentials by

$$\begin{aligned} u =& \frac{\partial \varphi}{\partial r} + \frac{1}{r}\frac{\partial \psi_z}{\partial \theta} - \frac{\partial \psi_\theta}{\partial z} \\ v =& \frac{1}{r}\frac{\partial \varphi}{\partial \theta} + \frac{\partial \psi_r}{\partial z} - \frac{\partial \psi_z}{\partial r} \\ w =& \frac{\partial \varphi}{\partial z} + \frac{1}{r}\frac{\partial \left(r\psi_\theta\right)}{\partial r} - \frac{1}{r}\frac{\partial \psi_r}{\partial \theta} \end{aligned} \tag{3.23}$$

The scalar and vector potentials shall satisfy the simplified governing equations motion,

$$\begin{aligned} \frac{\partial^2 \varphi}{\partial r^2} + \frac{1}{r}\frac{\partial^2 \varphi}{\partial r} + \frac{1}{r^2}\frac{\partial^2 \varphi}{\partial \theta^2} + \frac{\partial^2 \varphi}{\partial z^2} &= \frac{1}{{C_L}^2}\frac{\partial^2 \varphi}{\partial t^2} \\ \nabla^2 \psi_r - \frac{\psi_r}{r^2} - \frac{2}{r^2}\frac{\partial \psi_\theta}{\partial \theta} &= \frac{1}{{C_T}^2}\frac{\partial^2 \psi_r}{\partial t^2} \\ \nabla^2 \psi_\theta - \frac{\psi_\theta}{r^2} + \frac{2}{r^2}\frac{\partial \psi_r}{\partial \theta} &= \frac{1}{{C_T}^2}\frac{\partial^2 \psi_\theta}{\partial t^2} \\ \nabla^2 \psi_z &= \frac{1}{{C_T}^2}\frac{\partial^2 \psi_z}{\partial t^2} \end{aligned} \tag{3.24}$$

Traction free boundary conditions at outer surface of the rod (radius, r=a) are

$$\begin{aligned} \tau_{rr} =& \lambda\Delta + 2\mu\frac{\partial u}{\partial r} = 0 \\ \tau_{r\theta} =& \mu\left[\frac{1}{r}\left(\frac{\partial u}{\partial \theta} - v\right) + \frac{\partial v}{\partial r}\right] = 0 \\ \tau_{rz} =& \mu\left(\frac{\partial u}{\partial z} + \frac{\partial w}{\partial r}\right) = 0 \end{aligned} \tag{3.25}$$

The initial form of solutions to φ, ψ_r, ψ_θ and ψ_z are presented in [Gazis, 1959] as

$$\begin{aligned} \varphi = f(r)\cos\left(m\theta\right)e^{i(kz-\omega t)} \quad \psi_r = h_r(r)\sin\left(m\theta\right)e^{i(kz-\omega t)} \\ \psi_\theta = h_\theta(r)\cos\left(m\theta\right)e^{i(kz-\omega t)} \quad \psi_z = h_z(r)\sin\left(m\theta\right)e^{i(kz-\omega t)} \end{aligned} \tag{3.26}$$

The dispersion relations result upon substituting Equation 3.26 in the governing differential equation (Equation 3.24). In this solution longitudinal and torsional modes exist for $m = 0$. Longitudinal modes are given by

$$\frac{2\alpha}{a}(\beta^2 + k^2)J_1(\alpha a)J_1(\beta a) - (\beta^2 - k^2)J_0(\alpha a)J_0(\beta a) - 4k^2\alpha\beta J_1(\alpha a)J_0(\beta a) = 0 \tag{3.27}$$

where $\alpha^2 = \frac{\omega^2}{{C_L}^2} - k^2$ and $\beta^2 = \frac{\omega^2}{{C_T}^2} - k^2$. Torsional modes exist when the circumferential displacement (u_θ) are assumed non-zero. The dispersion relation for torsional mode are given by

$$\beta a J_0(\beta a) = 2J_1(\beta a) \tag{3.28}$$

For non-zero values of m flexural modes are possible in which all the displacements exist. Few researchers consider that Gazis solution is not correct for torsional modes thus an alternative solution that is proposed by Sun *et al.*, 2005 that can be used to estimate longitudinal as well as torsional modes as

$$\begin{aligned} \varphi &= f(r)e^{(im\theta)}e^{i(kz-\omega t)} \quad & \psi_r &= h_r(r)e^{(im\theta)}e^{i(kz-\omega t)} \\ \psi_\theta &= h_\theta(r)e^{(im\theta)}e^{i(kz-\omega t)} \quad & \psi_z &= h_z(r)e^{(im\theta)}e^{i(kz-\omega t)} \end{aligned} \tag{3.29}$$

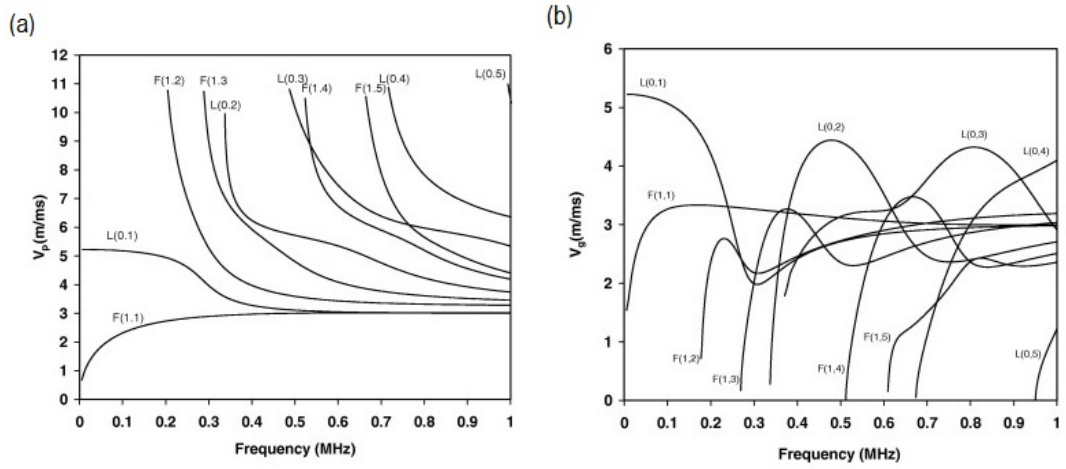

Figure 3.4: Dispersion curves of a 3 mm-diameter rod, (a) Phase velocity (b) Group velocity. Source:Chaki and Bourse, 2009.

The case of GW propagation in hollow cylindrical structures is widely studied. In such structures, the modes with high circumferential order have small amplitude thus their influence can be ignored while constructing the energy distribution of wave group. However, the contribution of modes depends on the nature of loading. For a small circumferential loading the higher order modes have a higher amplitude thus they must be included in the GW analysis. In order to obtain a smooth angular profile in a hallow pipe the loading length shall be increased as it will excite fewer modes.

3.4 Actuation and sensing

GW technique is an active sensing method thus it requires external stimulus by an actuator to generate GWs. A variety of transducers are used that include piezoelectric material like lead zirconium titanate (PZT), polyvinyldiene fluoride (PVDF) and macro fibre composites (MFC), electromagnetic acoustic transducers (EMAT), optical fibres in the form of Fibre Bragg Gratings (FBG), carbon nanotubes and laser vibrometer. The popular piezoelectric sensors are made of lead based material thus novel sensors are sought. This section enlists commonly used sensors and sensing mechanism for GW-based damage detection.

3.4.1 Transducers

Piezoelectric materials have the ability to convert the mechanical stress to electrical energy also the conversely electric field to mechanical deformation. These properties make them suitable to use as transducers. Same patch can be used either as an actuator or sensor. They are preferred due to their low cost, high resonant frequencies, energy efficiency, low impedance and availability in several forms.

Contact transducers

Compactly packed piezoelectric transducers commonly referred as contact transducers (CTs) are used in acoustic wave sensing applications. They have single crystal of piezoelectric material encased in a protective casing. They are designed for field and industrial application on rough surfaces. These are deployed in GW studies to selectively generate and capture longitudinal waves. These transducers can be used to generate GWs. They can be used in rebars with small diameters and in plates coupled with wedge transducers for GW generation. Another variant of CTs with dual crystal are available. These type of transducers deploy separate piezoelectric element for actuation and sensing that can be used in pulse echo type of sensing [Wu and Chang, 2006a]. Typical transducers are shown in Figure 3.5. A number of factor such as contact pressure, coupling agent and surface profile of the test specimen affect the strength of signals measured by contact transducers thus correction coefficients are proposed by researchers to reduce the errors in measurements Treiber *et al.* [2009].

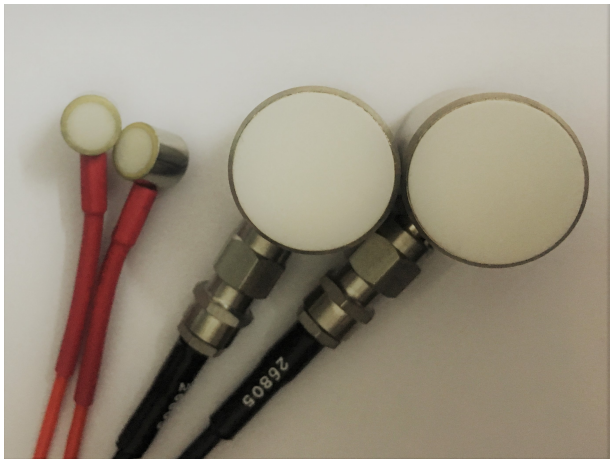

Figure 3.5: CTs of type Nano 30 and WDα (MISTRAS Group) that are used in GW testing.

Angle beam

Angle beam transducers are used to generate GWs by oblique incidence in thin structures. They focus the refracted shear waves generated by piezoelectric transducers affixed to a wedge with adjustable angle. The wedge is arranged with non-reflecting material that eliminate the internal reflections. The arrangement of wedge for damage detection is illustrated in Figure 3.6(a). These transducers are used for selective excitation of GW modes based on the phase velocity calculations. An array of multiple transducers is used for circumferential defect detection in pipes (Figure 3.6(b)). Angle beam have great potential for damage detection in concrete as the desired modes that are sensitive to specific damage feature can be excited [Na *et al.*, 2003].

Piezoelectric wafer transducers

Piezoelectric patches in can be easily cast in desired shapes and sizes. Piezoelectric wafer transducers (PWTs) consist of piezoelectric material cast in between conducting metal strips such as copper (Figure 3.7). The orthotropic behaviour of these material can be used to set the poling direction aligned to desired sensing path. Surface bonded PWTs are deployed to study defects such as corrosion and debonding by researchers [Lu *et al.*, 2013; Mustapha *et al.*, 2014]. Embeddable piezoelectric sensors attached to rebar, which are installed during the construction phase, have proven to be durable and effective tools in assessing corrosion [Talakokula and Bhalla, 2015].

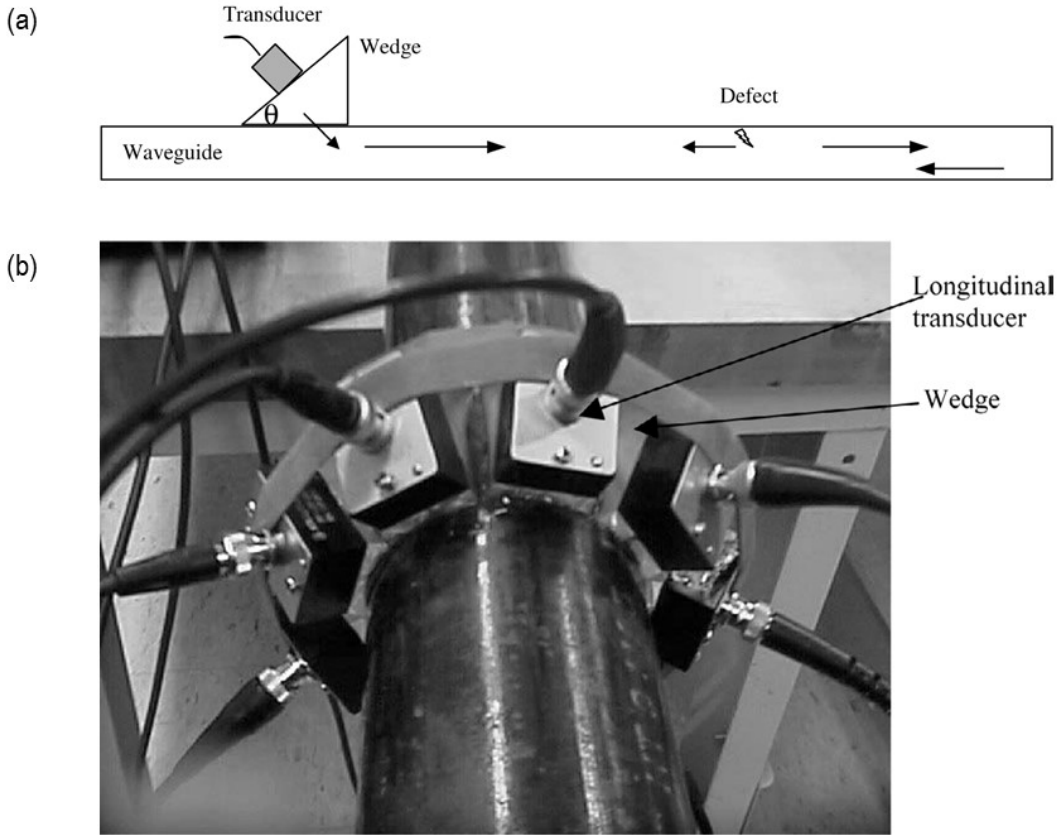

Figure 3.6: GW-based monitoring using (a) angle beam and (b) angle beam array transducers. Source: Li and Rose, 2002 ©2002 IEEE.

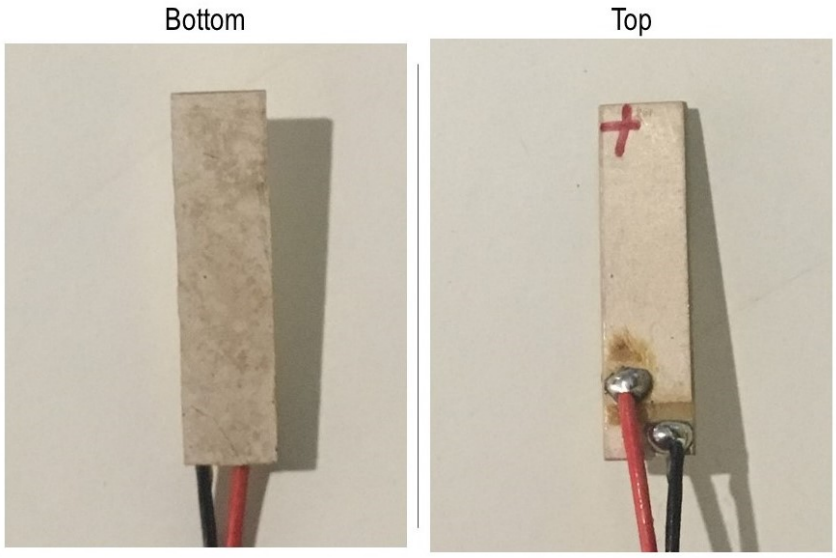

Figure 3.7: Typical PWT with lead wires soldered.

Embeddable smart sensors

In order to achieve better damage sensitivity, the sensors shall be embedded inside the concrete. The sensors get damaged due to the rough environmental condition if they are embedded without protective treatment. Several investigators have prepared and tested smart aggregate to sustain the aggressive setting. Smart aggregates are low cost multifunctional devises which can be used to monitor several stages of RC like curing, chloride inception, early strength, impact and structural health. The sensors consist PWT coated with a water proof layer, electrical insulation and cast into cement mortar. Dumoulin et al., have used embedded smart aggregates (details shown in Figure 3.8) as transducers to monitor concrete beams from crack initiation phase and progressive evaluation as the crack propagation takes place. The size of the transducers used is

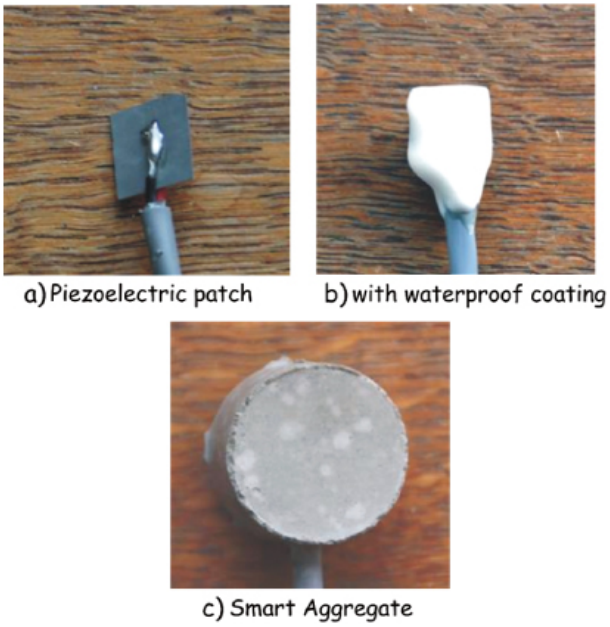

Figure 3.8: Smart aggregate along with its component material used for crack monitroing. Source: Dumoulin *et al.*, 2012.

comparable to the size of larger size aggregates and this could be a concern as the strength of transducer is less compared to the overall strength of concrete could provide a potential point for crack initiation. Recently, embeddable piezoelectric patches are successfully tested to detect and quantify uniform corrosion in RC structures [Talakokula *et al.*, 2014]. The effectiveness of embeddable vibration sensors and PWT are studied and it is found that both these sensors can detect various stages individually and in combination. Hughi, D. et al have used embedded PZT sensor to generate bulk wave and effectively monitor

crack width in RC beams. The estimated results are compared with the crack gauge measurement [Hughi and Marzouk, 2015].

Piezoelectric polymers

PZT based sensors that are discussed above are not flexible thus the bonding between sensors and structure cannot be ascertained in case of curved structures. Also, PZT material is carcinogenic due to presence of lead thus scientists are working to replace them with eco-friendly elements. Piezoelectric polymers have found their application in varied fields due to mechanical flexibility and low cost of manufacture compared to ceramic based material. Polymer material such as polyvinyldiene flouride (PVDF) is sensitive to damages and is flexible. The manufacturing process of PVDF sensor is illustrated in Figure 3.9.

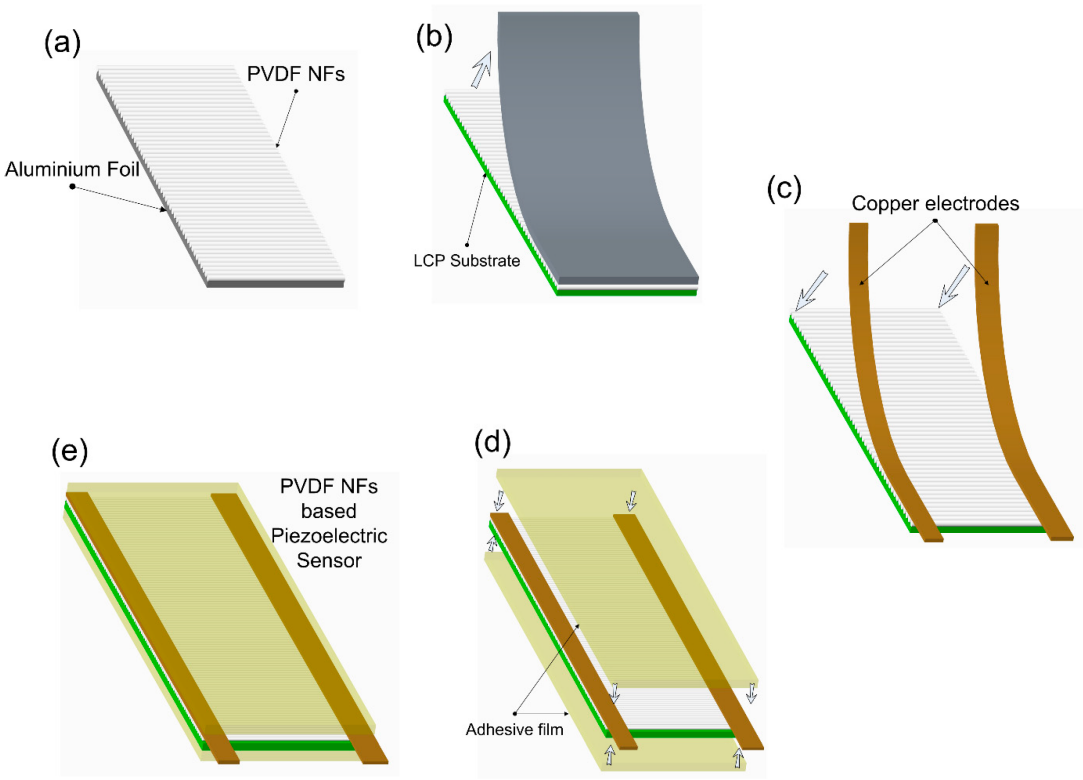

Figure 3.9: Process involved in manufacture of PVDF based piezoelectric sensor (a)–(e) from deposition of PVDF nano-fibres (NFs) to final PVDF sensor. Source: Khan *et al.*, 2018.

PVDF sensors are used to detect the impact loading on a cantilever beam [Dung and Sasaki, 2016]. The sensor responses are predicted accurately by the numerical models that are useful in determining the optimum size and location of the sensors [Brown and

Mason, 1996]. The mechanical performance of PVDF sensors alters with the temperature hence it shall be compensated using calibration methods. PVDF sensors are used to manufacture wireless smart-sensors. The performance of PVDF based wireless sensors is evaluated with dynamic strain gauges. They measure vibrations effectively with good repeatability [Gu *et al.*, 2005]. The damages in form of holes and corrosion in the bridges can be estimated from changes in the first and second order frequencies of vibration that are measured by using PVDF sensors [Yu *et al.*, 2013].

Other sensors

Apart from the piezoelectric based transducers, several other sensors are in use to actuate and sense GWs. Joule and Villari effects on ferromagnetic materials are utilised to develop the magnetostrictive sensors. The ferromagnetic magnetic materials respond to the application of magnetic flux and cause mechanical strain, conversely change in the mechanical strain causes change in the magnetic flux. These effects are used to generate and sense the GWs [Kwun and Teller, 1994; Kim and Kwon, 2015]. Researchers have used crossed-coil magnetostrictive sensors to generate torsional modes in pipes with an improved sensitivity to circumferential notches [Kim *et al.*, 2011]. Electromagnetic acoustic transducers (EMATs) can generate GWs with electromagnetic field based on Lorentz force mechanism. The advantage of EMATs is that they do not required direct contact with the test specimen. A combination of piezoelectric transducer for actuation and EMAT for sensing is proposed as an effective way to monitor the debonding damage in embedded rebars [Na and Kund, 2003]. EMATs that are improved by periodic permanent magnets are used to generate T(0,2) mode for pipe inspection [Nurmalia *et al.*, 2017]. Hybrid techniques are devised to identify cracks in aluminium plates and delamination damage in composite plates by using GWs that are generated by PWT patches and the wave field images that are captured by scanning laser doppler vibrometer (SLDV) [Yu and Tian, 2013; Sohn *et al.*, 2011]. FOS and FBG are used to sense the GWs that are generated by piezoelectric transmitter [Melle *et al.*, 1992; Guo and Yang, 2015]. Doppler effect-based fibre optic sensors (FOD) are attached to CFRP plates and they are found to capture the damage signals emanating from multiple directions with improved sensitivity in comparison to FBG [Li *et al.*, 2009].

3.4.2 Sensing method

The sensors shall be arranged optimally to scan the complete structure. Two basic modes of sensing pulse echo and pitch catch are possible to capture the signal. In recent years, time reversal method is developed. These methods are described in explicit detail below.

Pulse echo

In the pulse echo method, the wave energy is imparted to the test surface by a signal transmitter. The wave propagates through the medium and is reflected (echo) when it interacts with the defect, interface and boundaries. A transducer is placed on the surface to captures the reflected signal (3.10 (a)). Signal emanated by damage is estimated by subtracting the boundary induced signals. Location of the damage is estimated from the time of flight and velocity of wave. Single mode and dual mode transducers are available for pulse echo testing. The single mode transducers have only one crystal which functions both as an actuator and a sensor. The dual mode transducers include two piezoelectric crystal in a single casing in which one transmits the signal and the other receives the signal.

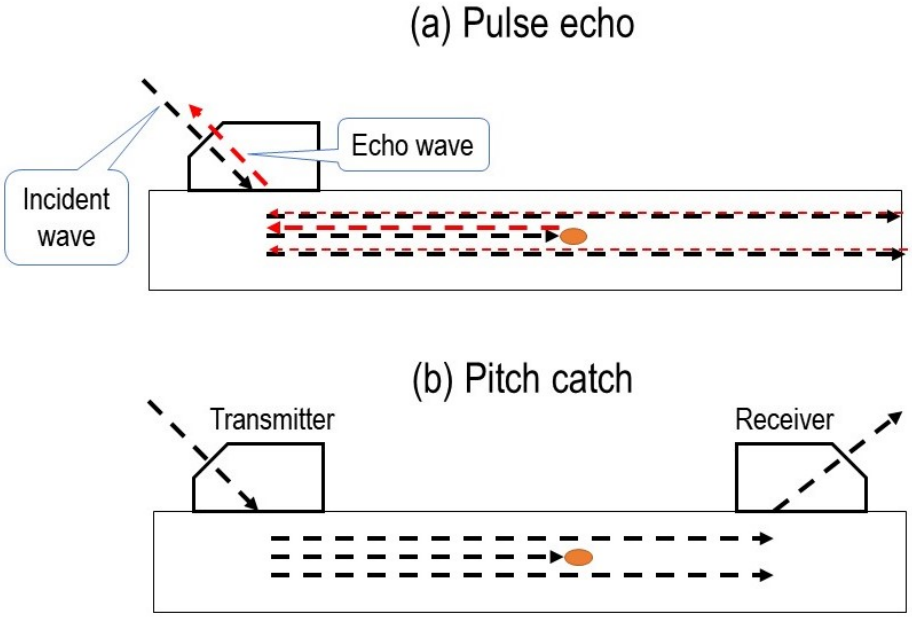

Figure 3.10: Illustration on the working principle of (a) the pulse echo method and (b) the pitch catch method.

Pitch catch

In the pitch catch method, the actuator-sensor pair are arranged away from each other. The ultrasonic waves that are generated by actuator travel in the test specimen and are received by the sensor (3.10 (b)). The features of the signal such as time of flight, amplitude, frequency and mode are altered due to the flaws.

Time reversal method

Time reversal process is extensively used in medical, bioengineering, underwater imaging and lithotripsy and has found its application in non-destructive testing. Time reversal method is a new mode of GW testing that uses a series of wave generation and detection to evaluate the damage. Studies have shown that time reversal method can be used to understand the wave interaction with a different kind of damage in concrete and FRP repaired concrete [Park *et al.*, 2009; Kudela *et al.*, 2007]. The working principle of this

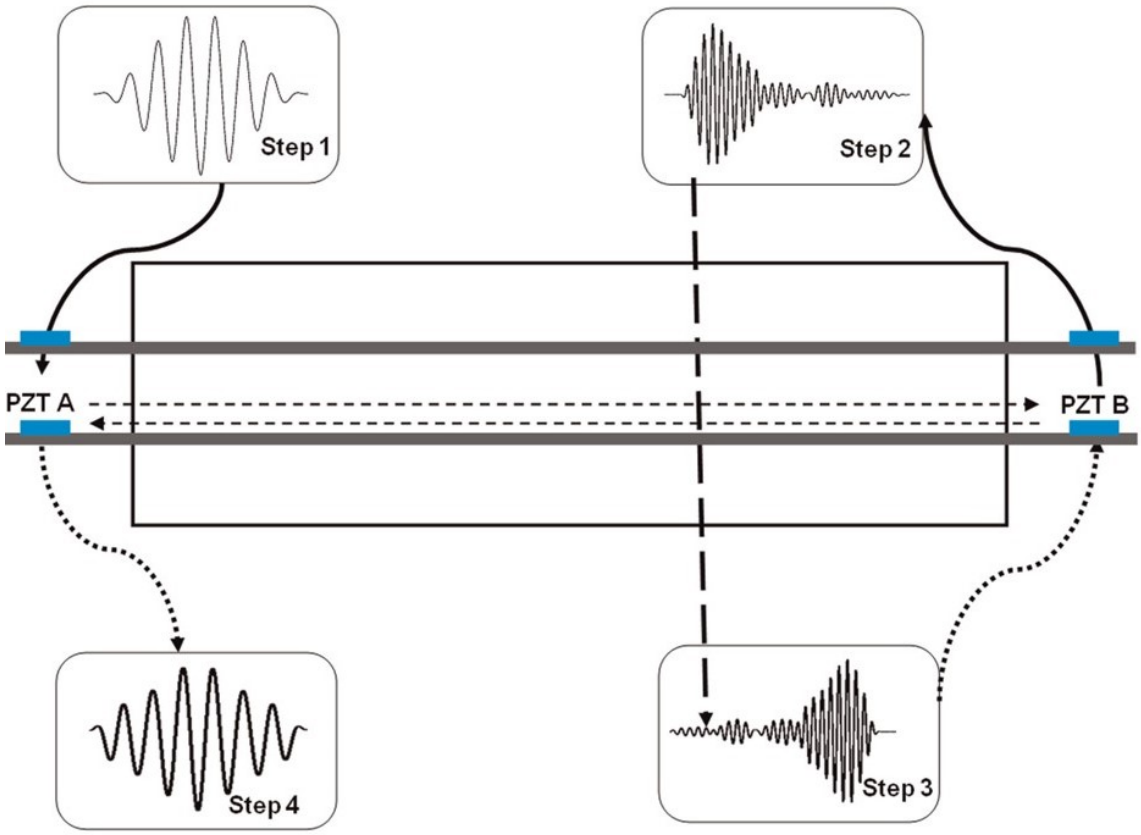

Figure 3.11: Schematic of time reversal process in concrete specimen. Source: Mustapha *et al.*, 2014.

method is based on the reciprocity of wave propagation. Figure 3.11 provides an illustration of the methodology followed in this process. Initially, a wave pulse is input by the transducer PZT A that triggers GWs in the specimen (Step 1). The wave signals are captured by PZT B that is located at the far end of the specimen (Step 2). The received signals are time reversed and the specimen is actuated by PZT B with the time reversed pulse (Step 3). The response of the specimen for the input pulse in Step 3 is captured by PZT A (Step 4). In an intact specimen that is devoid of any damage, the input pulse in Step 1 (original signal) and the response signal in Step 4 (time reversed signal) shall have same shape. However, presence of a damage in the specimen distorts the response signal and results in the poor correlation in the shape of the original signal and time reversed signal [Kim and Sohn, 2006; Park *et al.*, 2009; Zhang *et al.*, 2017; Li *et al.*, 2017].

3.5 Techniques for signal evaluation

3.5.1 GW parameters for damage detection

Signal strength

One method of monitoring corrosion in concrete is by measuring the amplitude of the reflected wave signals at sensors placed at suitable locations. Such an approach leads to erroneous data and is not suitable for continuous monitoring of the structures for an extended duration of time. The bond between sensor and concrete weakens over time and this, in turn, would affect the recorded signal.

Time of flight

GW modes propagate at different speeds. Studies recommend that the sensor and actuator shall be spaced at sufficient distance to avoid the near field effect. If the sensor and actuator are nearby the seperation between various wave group will not be clear hence it is difficult to distinguish them and to estimate the time of arrivals.

Frequency content

Frequency of excitation is an important factor and it has to be chosen appropriately to excite specific modes. In case of a linear response, the frequency of received signal is same

as excitation frequency. However, non-linear response from damage generates multiple frequencies. Limited number of studies are done on frequency based analysis of corrosion.

3.5.2 Advanced signal processing techniques

Measuring the electrical potential of the PZT elements attached to concrete or rebars is the conventional method for detecting damage. The amplitude and time of flight based damage detection techniques require the signal data obtained for the test case to be noise free. The wave modes that arise due to boundary reflections shall be separated from those due to damage. Signal processing techniques are used to correlate the captured time-reversed signal with the original wave pulse. Damage index, which indicates the dissimilarity between two wave signals, is established to determine the extent of damage in the structure. Damage indices such as root mean square deviation and cross-correlation coefficient are thus formulated based on the electrical potential measurements [Park and Inman, 2007]. The disadvantage of these methods is that they can predict the existence of damage but cannot estimate the change in structural properties. The damage indices are defined based on energy-based evaluation (EEI) and root mean square deviation (RMSD) to evaluate the debonding in concrete filled steel tubes. It is found that RMSD is more sensitive to debonding [Xu *et al.*, 2013].

Advanced techniques such as genetic algorithms, artificial neural networks, simulated annealing and particle swarm optimisation are used to diagnose the damage. Multiple damage data and modal decomposition can be used to establish the type and severity of anomalies. Spectral element method (SEM) has been used exclusively for non-linear wave propagation problems that require higher-order finite element approaches. SEM approaches are generally based on Lagrange polynomials through Gauss–Lobatto–Legendre (GLL) or Chebyshev–Gauss–Lobatto (CGL) points [Willberg *et al.*, 2015]. Scientists have used spectral element method for numerical modelling of de-bond between FRP layer and concrete. They proposed and tested an ensemble method based on the standard PSO algorithm and developed an adaptive algorithm to increase the performance of the proposed strategy concerning the identification of the damage location using impedance measurements [Sun *et al.*, 2015]. Use of wireless sensors and equipment can augment the current research. MICA mote and MICAZ mote are the two most popular platforms for wireless sensor deployment. Such sensors require low energy and a standard AA type of battery

is sufficient to provide the electric energy for up to ten years. These systems use dynamic power management and auto-shutdown techniques to conserve energy. Integration of piezoelectric-based sensing systems to wireless technology is the latest speciality of SHM [Gu *et al.*, 2005; Yu *et al.*, 2013].

3.6 Damage detection in reinforced concrete using guided waves

3.6.1 Detection of surface defects in concrete

Surface cracking in concrete occurs due to the collective result of reinforcement corrosion, excessive loading, temperature variations and weathering of material. The defect may be a sizeable local crack or numerous small cracks distributed over an area. Relatively less attention is paid to detecting the cracks in concrete using PZT transducers. Surface bonded piezoelectric patches are used to generate surface waves in concrete. These studies encompassed numerical simulations and experimental testing.

Numerical models using finite difference method and experiments using the ultrasonic transmitters and miniature accelerometers on a concrete slab show that notch type of damage can be detected. Wavelet transform coefficient of lamb wave signals can quantify the depth of surface cracking in concrete [Yang *et al.*, 2009]. Numerical simulations on a concrete beam using time reversal process have shown promising results in the detection of cracks [Yang *et al.*, 2015]. Markovic *et al.*, 2015 have developed a three dimensional model of the smart aggregate actuator. The displacement from this model is used as an input for actuating wave propagation in concrete. They have compared the results of these for various crack length and hole diameter with the experiments.

Several numerical studies created finite element models in ANSYS software. The reflection at the boundaries is inhibited by deploying boundary condition that has only transmitting capabilities which are achieved by inhibiting the reflections. This type of boundary is termed transmitting, or non-reflecting or absorbing boundary. It helps in minimising the time of computation and analysis of the signals. The transmitting boundary is designed by adding a free field boundary element to the main concrete model. Researchers adopt a combination of free field and viscous boundaries. Energy absorption

at such boundaries depends on density (ρ), longitudinal and shear wave speeds (C_L and C_T), normal velocity and tangential velocities of the nodes at the edges of concrete(v_n and v_t) and the influence area (A). It is given by Equation 3.30.

$$\begin{aligned} F_n &= -\rho C_L(v_n^m - v_n^c)A \\ F_t &= -\rho C_T(v_t^m - v_t^c)A \end{aligned} \tag{3.30}$$

The concrete part of the numerical model is assigned with SOLID45 element, which allows three mechanical degrees of freedom at each of its eight nodes. Three-dimensional solid element (SOLID5) used for piezoelectric transducers. This element has six degrees of freedom at each node, and the additional degrees of freedom are assigned for the electrical parameter. To account for the damped nature of concrete, Raleigh damping model with mass damping factor α and stiffness damping factor β are used. The effect of damping on sensors output is also studied. It is found that an increase in damping factor, β, affects the sensor response and the sensor response has dropped dramatically at high frequency. The contribution of α to the total damping is found to be negligible. The study has demonstrated that the transmitting type of boundary minimises the contamination of the propagating wave due to reflection from the boundaries of the waveguide. It is also reported that this type of boundary reduces the computation time remarkably. Excitation by a source ($Q(\omega)$) in concrete slabs generates GW modes. The weight factor(w^n) defines the contribution and the transfer function ($H^n(\omega, x)$) define the dispersion behaviour for each of the n possible mode of the propagating wave ($G(\omega, x)$).

$$G(\omega, x) = \sum_n [w^n H^n(\omega, x) Q(\omega)] \tag{3.31}$$

Ultrasonic waves get reflected and transmitted at the interface between two materials. The amplitude of reflected and transmitted waves is a function of their impedances. Cracks in concrete introduce a discontinuity in the form of air-gap. Thus, the interface consists of solid and air. In a cracked concrete specimen, the reflected waves dominate as the impedance of air is much lower than that of concrete. It is demonstrated that surface bonded transducers can be used to generate surface waves and have the potential to detect surface damage. The group velocity dispersion curves of surface waves are plotted by varying the input frequency and measuring the time of arrivals. Studies reported the

effect of microstructure needs to be considered to eliminate the difference in the numerical and experimental signals[Song *et al.*, 2008].

Piezo-ceramic sensors are embedded in concrete and excited with a wide band frequency sweep between 20–120 kHz. Crack width index (CWI) is defined using the embedded sensor measurements, which is the measure of the deviation of amplitude of signal after application of load from that before the application of load. Strain sensors are also attached on the beam on either side of the probable cracking region and the strain in concrete is measured with loading. The relation between strain and CWI values is derived for two stages of before and after crack initiation. These equations are translated to existing empirical crack width relations to obtain the crack widths in terms of CWI values. The values of crack widths predicted by these equations match closely with the actual measurements and are useful to detect and assess the distress signals in RC [Hughi and Marzouk, 2015]. An important observation is made on the durability of piezo-ceramics is these studies. The sensors are found to withstand the heat of hydration and concrete dead loads with simple epoxy and encasement protection.

3.6.2 Detection of diameter reduction in rebars due to corrosion

Amjad *et al.*, 2015 have shown that time of flight obtained by using the cross-correlation technique can be used to detect the existence of damage in a rebar. They have compared the difference in time of flight of an undamaged bar and damaged bar of the same length and established that the time of flight (TOF) varies with the diameter of the bar. ToF obtained from various wavelet transforms has been used to detect uniform corrosion. The differential ToF of $L(0,\ 1)$ mode from undamaged rebar and corroded rebar has been used to identify the corrosion state in various uniformly corroded rebar samples. It is reported that the differential ToF increases with the intensity of the corrosion in the rebar. The pitting corrosion in pipelines is widely studied in the literature by correlating the reflection characteristics of GWs with the damage sizes Wang *et al.* [2010]; Tse and Wang [2013]; Carandente *et al.* [2012]. Demma *et al.*, 2004 have investigated the dependence of reflection coefficient on circumferential extent and depth of defect in pipelines by using torsional $T(0,\ 1)$ mode and have proposed reflection maps to quantify unknown defects in pipelines. Miller *et al.*, 2013 have measured the time of flight in loaded beams with bars of various corrosion level and correlated TOF data to the level of corrosion. The time of flight

data of different rebars can be used to detect the corroded rebars in a structure. From the experiments on corrosion, it is observed that the process of corrosion is complicated, and it can not be equated to a simple reduction in rebar diameter. Study of accelerated corrosion in rebars is the focus of research in recent years. CTs that are attached to the ends of the rebars are used by researchers to generate GW in rebar [Sharma and Mukherjee, 2010; Sharma *et al.*, 2018]. Very few studies are available to quantify the reduction in the rebar cross-section with PWT measurements.

3.6.3 Detection of rebar debonding

Debonding causes a significant reduction in the bond strength. Various researchers have used finite element analysis (FEA) to study the debonding of rebars. The most popular strategy applied in numerical modelling is untying the rebar and concrete at the interface. Numerical simulations show that the strength of the GW in rebar increases and time of flight decreases for with debonding [Wu *et al.*, 2014]. The GWs are concentrated in the rebar as the debonding occurs. Rebars have higher wave speed and lower damping compared to concrete. Instead of calculating the wave displacements in the time domain, few researchers have used frequency and wave-number domain analysis [Yu and Tian, 2013]. Such studies transform the time domain wave equations into the frequency domain using Fourier transform or a wavelet transform. Spectral finite element method has become popular due to low computational cost as interpolation functions closely represent the displacements thus require a low level of discretisation. One dimensional spectral elements are deployed to study the changes in the interface between concrete and rebar [Wang *et al.*, 2009]. The effective properties, elastic modulus (E_{eq}), density (ρ_{eq}) and viscous damping ratio (η_{eq}) which depend on the material properties of steel and concrete are used in the formulation. The intensity of debonding is defined by a reduction in the active concrete area used in the spectral element formulation. Damage identification parameters are proposed based on the reflected and transmitted wave amplitude and time of flight measurements. These parameters can distinguish the location, length and intensity of the debonding. Piezoelectric sensors are used to detect single debond and multiple debonds in embedded rebars. Damage indices and wave attenuation are proposed to asses the effect of debonding length and location. The damage indices that are based on the wavelet packet transform are sensitive to both the location and length of the damage [Xu

et al., 2013].

GWs generated with different configurations of transducers arrangements such as angle beam, spherical-conical coupler and direct contact. Debonding is simulated by separating the rebar and concrete with the use of a PVC pipe sleeve. The length of pipe is varied to achieve 25 per cent, 50 per cent and 75 per cent debonding. The above three samples along with a sample without any debonding are used in the study. In these experiments, transducers are excited at a set of frequencies comprising of 50 kHz, 150 kHz and 1 MHz. It is concluded in these studies that spherical-conical coupler type of transducers excited at 1 MHz frequency shows high sensitivity towards debonding damage. However, angle beam type of arrangement placed on the concrete surface and excited at 50 kHz can be used for damage detection when the rebars are not accessible for transducer placement. These studies indicated that the contact transducers show high scattering at low frequency. The modes generated due to the spherical conical type of sensors are predicted to be higher order flexural modes [Na *et al.*, 2003]. These studies show that higher order flexural modes are sensitive to debonding and lower order longitudinal modes generated with CTs cannot efficiently detect debonding. The dispersion modes of the RC specimen are not studied to explain the reason behind the scattering observed for lower frequencies. Embedded piezoelectric discs are used as transducers for damage detection in concrete beams. They have established a baseline data for a typical beam of same dimensions cast under similar conditions and compared the signal data obtained for other beams to establish a correlation between signal strength and de-bond size [Wu and Chang, 2006b,a].

3.6.4 Detection of damages in retrofitted reinforced concrete structures

Retrofitting the damaged concrete with FRP layers extends the service life of RC structures. However, de-bonding at concrete and FRP interface decreases the anticipated service life and may lead to catastrophic failure of structural components. Hence, a reliable and extensive SHM system is required to detect these damages at their embryonic stage and to monitor their growth over the lifespan of the structure. This process involves the manual application of adhesive on a concrete surface and is prone to de-bonding. Experimental studies have established that the GWs can detect the debonding between

in CFRP sheet and RC beam [Luangvilai *et al.*, 2003]. The time reversal process is used to identify the damage, and the reconstructed signals are used to develop a damage index based on cross-correlation technique [Lu *et al.*, 2014]. A spectral plate finite element is designed to analyse elastic wave propagation in a composite plate for various orientations and relative volume fractions of reinforcing fibres [Kudela *et al.*, 2007]. A non-reflecting boundary condition using dashpot elements is used in order to reduce the reflections of the Lamb waves at boundaries [Hosseini *et al.*, 2013].

3.7 Research gap

Corrosion leads to a reduction in the diameter of rebars and debonding at the concrete-steel interface. The literature review elucidates that the inception of corrosion is not ascertained to date. GW-based SHM is a multidisciplinary approach that draws expertise from signal processing, material science, sensor technology and mechanics. GWs that are generated by PWTs are used in the SHM of aerospace and mechanical structures. PWTs are cheap and easy to install. The recent studies show that they can be embedded in concrete. GWs have the potential to identify damage in concrete. Very little work is done to identify corrosion in concrete using PWTs. The difficulties associated with the GW-based health monitoring are the presence of multiple wave modes which renders the received signal at sensors a complex form; reflections from boundaries that may conceal the wave modes scattered by the damage and possible noise in the signal due to interference from microstructure interaction.

In recent studies, it has been expressed that the diameter reduction and debonding have a complementary effect on the wave characteristics. An increase in the corrosion level increases the surface roughness of the rebar, which would result in energy dissipation to surrounding material, thus resulting in decreased amplitude whereas de-bonding has the opposite effect that. It is proposed to identify the zero-effect state, in which the effect of de-bonding and corrosion would result in a state of the signal, which would be the same as that of intact rebar. Appropriate methods to identify and distinguish states in the corrosion process will be devised.

The GW propagation in plates with damages is well studied, whereas knowledge of waves in corroded cylindrical bodies it is limited. The current studies calculate the GW

dispersion curves is based on approximate models such as bare rebar or rebar embedded in the infinite concrete medium. These models lead to incorrect estimation of GW modes. There is a need to understand GW characteristics in concrete with appropriate numerical and experimental analysis. Baseline identification in concrete is difficult due to the composite nature of the concrete material. The signal varies within the concrete of the same composition. Hence, it is imperative to develop a baseline free method of NDE. This research proposal aims to identify the inception of corrosion in rebars that are embedded in concrete and develop damage indices to estimate corrosion.

3.8 Concluding remarks

In this chapter, GW-based technique for identification of damages in concrete is investigated in detail. The theory of GW propagation in plates and rods is discussed. Dispersion relations in rods are derived by considering an isotropic homogeneous solid. Various transducers used for GW generation and detection are enlisted. Three basic methods of GW testing the pulse echo, pitch catch and time reversal techniques are explored. Current advances in the detection of surface cracking, rebar corrosion, rebar debonding and FRP delamination are surveyed. The literature review presented in this chapter is concluded by presenting the gap in the literature.

Chapter 4

Methodologies for experimental and numerical analysis

4.1 Introduction

This chapter outlines experimental and numerical methods deployed to study the corrosion in rebars. It includes a detailed description of GW generation and sensing along with various instruments. Two basics methods of GWs generation and detection using piezoelectric sensors in the form of compact acoustic CTs and surface bonded PWTs are explored. A baseline signal is collected on undamaged bare rebar and concrete specimens using the pitch catch method. Artificial corrosion in bare rebars is created by mechanically scrapping material and the GW signals are noted. Numerical simulations are used to calculate the dispersion curves and identify the modes. The GW signals are exploited to calculate damage indices for various cases of corrosion. In the real-life, corroded rebar does not possess the sharp edges at the corrosion site that appear due to mechanical scrapping hence the bare rebar is corroded with help of accelerated corrosion setup and the results are compared with the previous case.

Literature review reveals that corrosion in embedded rebars involves increase in the bond, debonding and reduction in diameter. These phenomenon have complimentary effect on wave characteristics. Several numerical cases are assessed to identify the case of zero effect case. Numerical and experimental studies are then performed on concrete specimens that conform to M25 grade embedded with rebar of various diameters. Corrosion in rebars achieved with accelerated corrosion setup is monitored using GWs. The wave modes are calculated using the dispersion curves which are validated by numerical and

experimental studies on baseline model. Numerical simulations are deployed to confirm the state of rebar which includes the loss of diameter and weakening of the bond.

4.2 Preparation of samples

High yield strength reinforcement bars are used in this study for experiments. These bars are thermo-mechanically treated and have yield strength of 500 GPa. Diameters of the rebars used in this study are 20 mm and 12 mm. The ends of the rebars are ground to have a plain surface. This ensures the proper contact for transducers attached on end surface for longitudinal wave excitation. The rebars are are prepared with sufficient slot for the attachment of PWTs. Concrete beams are cast using the mix proportions which are designed as per IS 10262-2009. A M25 grade concrete is designed with minimum slum of 100 mm for workability. Cement corresponding to OPC-53 grade is used. Fine aggregate used is Zone-1 sand with moisture content 1.3 % and course aggregates (CAs) are 10 mm and 20 mm size crushed gravel in proportion 40:60. Potable water is used with a water cement ratio of 0.5:1 and for the purpose of mix design air voids are assumed to be 2 % of the volume of concrete. The final mix design is mentioned in table 4.1. The concrete is mixed in mechanical mixer with capacity of 100 kg.A total of 18 samples are cast in three batches. Concrete is placed after inserting the rebars into moulds with dimensions (102 mm $\times$ 152 mm $\times$ 502 mm). Test cubes (150 mm $\times$ 150 mm $\times$ 150 mm) are cast to ascertain the compressive strength of the set concrete. The test results show that the twenty-eight day strength of concrete satisfies the requirement of IS 456 (Table 4.2). Beams are cured in curing tank for initial three days and are later transferred to humid room and covered with moisture retaining sacks. These are allowed wet curing for twenty-eight days. The projected ends of the reinforcement are protected from corrosion during the curing process by applying sufficient amount of grease.

Table 4.1: Mix design for M25 grade concrete.

Material	Water	Cement	Sand	CA (10 mm)	CA (20 mm)
Weight (kg)	170	340	756	440	720

Table 4.2: Cube strength results for concrete specimens.

Batch No.	Sample No.	Weight (kg)	Load (kN)	Strength (MPa)
1	1	8.537	883.4	39.00
	2	8.508	857.1	38.09
	3	8.585	889.0	39.50
2	4	8.570	840.0	37.33
	5	8.576	857.1	37.96
	6	8.560	889.0	40.53
3	7	8.490	883.4	36.72
	8	8.400	857.1	34.97
	9	8.485	861.2	38.28

4.3 Guided wave testing

An RC beam as shown in Figure 4.1(a) with a width of 100 mm, depth of 150 mm and length of 500 mm is used to study the corrosion of rebars that are embedded in concrete. High yield strength deformed (HYSD) reinforcement bars with a diameter of 20 mm and length of 700 mm are used this study. The compressive strength of the concrete cubes, when tested after twenty-eight days, is 25 MPa. The tensile strength of the rebars, when measured using the universal testing machine (UTM), is 500 MPa. Two rebars are embedded in concrete with clear cover maintained as 30 mm. The bottom rebar is wetted with corrosive solution and impressed current is applied to it whereas the top rebar is uncorroded. The rebar ends are prepared, and piezoelectric sensors are attached to the reinforcement bar. The transducer on one end is used for actuation whereas the transducer on the opposite end of the same rebar is used for sensing. The details of specimens used in the studies are summarised in Table 4.3. The designation sample follows the order [Rebar Diameter (mm)] [Rebar condition] [Type of sensor]. Rebar condition is denoted by letters A, R and C, where A is bare rebar that corroded artificially, R is bare rebar that is corroded using accelerated corrosion setup, C is rebar embedded in concrete. The type of sensor is denoted by numerals 1 and 2 to denote contact transducer and PWT, respectively. For example, 20A1 means a 20 mm-diameter rebar that is corroded artificially and tested using a contact type of transducer.

GWs are actuated and sensed by two methods in this study. First, the longitudinal mode by CTs. Second, the flexural mode by PWTs. In order to attach the CTs, the ends of these samples are flattened and uniform-contact condition is ensured with the help of

Table 4.3: Details of experimental samples.

Designation	Rebar size	Sensor	Corrosion method	Place	Quantity
Bare rebar					
20A1	20 mm	CT	Artificial	Monash	6
20R1	20 mm	CT	Accelerated	Monash	1
20R2	20 mm	PWT	Accelerated	Monash	1
12R1	12 mm	CT	Accelerated	IIT Bombay	1
12R2	12 mm	PWT	Accelerated	IIT Bombay	1
RC Beam					
20C1	20 mm	PWT	Accelerated	Monash	3
12C1	12 mm	CT	Accelerated	IIT Bombay	3
12C2	12 mm	PWT	Accelerated	IIT Bombay	3

a transducer guide that maintains the position as well as pressure as shown in Figure 4.1(b). The transducer guide consists of an epoxy-based sealant which is cast-in-situ and a steel ball to hold the transducer in position and to ensure proper contact. The excitation using PWTs generates a dominant flexural mode of vibration in the sample. Several GW modes get generated due to the complexity of geometry in RC beams. The surface of the steel bar at each end is flattened to attach PWTs, supplied by PI Ceramic, with material conforming to PIC 151. PWT at one of the ends is marked for actuation and another end is marked for sensing. The GW response of the beam is collected at regular intervals to evaluate the change in wave characteristics with an increase in corrosion of the rebars. The input signal is generated by an arbitrary function generator, AFG 3102, and then amplified by an amplifier, EPA 104. The central frequency for signal actuation is selected based on the frequency modulation curves. These curves are plotted for each rebar and transducer pair.

The type of CTs and oscilloscope put-upon use at Monash University and IIT Bombay are different. At Monash University, contact type transducers, Accusan-S 12.5 mm-diameter (supplied by Olympus), are used for actuation and sensing of GWs. The response signal is collected by the receiving transducer with a sampling frequency of 10 MHz by a digital oscilloscope, DPO4034B, which is controlled by a PC using LabVIEW. To minimise the noise, the response signal is averaged over 512 cycles by using an inbuilt function that is available in the oscilloscope. At IIT Bombay, CTs PAC Nano-30 that are supplied by Mistras group are used. The signal is collected with a Keysight make oscilloscope,

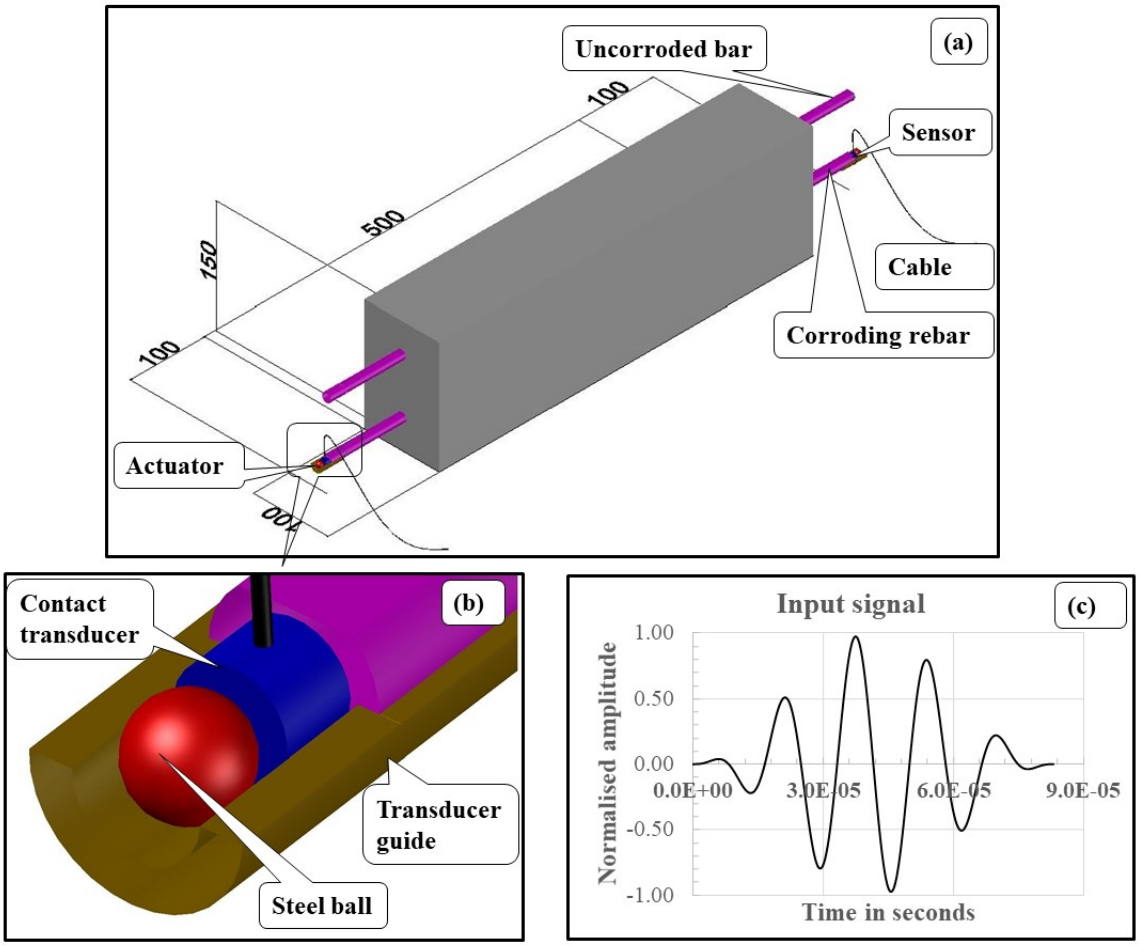

Figure 4.1: (a) Schematic diagram of RC beam, (b) transducer arrangement and (c) 60 kHz input signal.

DSOX2014A. The sampling frequency of 2.5 MHz is used along with the averaging function. The GW response is collected at regular intervals of 12 hrs for twelve days until the visible cracks appeared on the concrete.

4.3.1 Selection of input signal and sensor arrangement

A broadband signal ensures the precise excitation at the intended frequency; however, the output signal can be clearly interpreted if the input signal is narrow-band. To strike a balance between the two, a five-cycle sine pulse in the Hanning window is chosen as the input signal (Figure 4.1(c)). The efficiency of transducers depends upon the distance between the actuator-sensor pair and the frequency of excitation in a given structural system. To determine the optimum frequency of excitation in the current case, a parametric study of the responses in various excitation frequencies of PWTs is conducted. The fre-

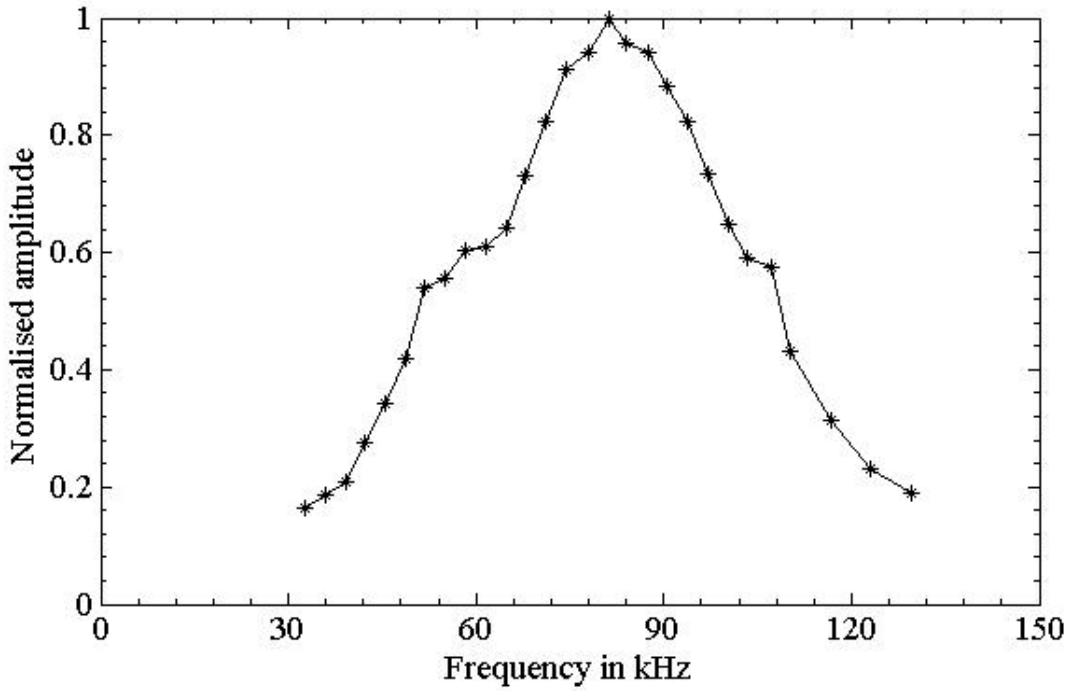

Figure 4.2: Frequency response curve for the current experimental setup.

quency response curve of sample 20C1, which indicates the peak signal strength for each frequency of excitation, is plotted in Figure 4.2. The study shows that the optimum response is obtained for the frequencies in range 70 kHz to 90 kHz. The frequency of 75 kHz is chosen in the current study. Similiar study is conducted for the other specimens listed in Table 4.3. It is found that GWs can be excited with less dispersion at 100 kHz and 60 kHz for 20 mm and 12 mm bare rebars, respectively. The peak response is obtained at 75 kHz and 60 kHz for 20 mm and 12 mm rebars embedded in concrete, respectively.

4.4 Corrosion setup

4.4.1 Bare rebar

Corrosion is slow in the natural environment and, generally, takes a long period of time. Two type of corrosion strategies are followed to corrode the rebars. First type, the corrosion in the rebar samples is achieved by scrapping off the material from the surface of these samples. Rebar samples, such as those that are shown in Figure 4.3 with various corrosion intensities, axial extents, and locations are used in experiments.

Second type, pitting corrosion in rebar is achieved by initiating an electro-chemical

Figure 4.3: (a) Rebar samples used in the experiment.

reaction in the steel bar. The electrolyte used for this electrolysis process is a 3.5%-NaCl solution. A constant current of 0.31 Ampere is applied across the terminals by a DC power supply. The corrosion current density of 100 mA/cm^2 can be achieved in the circular steel bar with diameter of 20 mm with the applied current. The chloride concentration and corrosion current density are sufficient to initialise corrosion process in the steel bar. The positive terminal of the power supply is attached to the reinforcement bar, which makes it the anode, and the negative terminal is attached to a copper bar which acts as the anode. The copper bar is immersed in the solution along with a part of steel bar which is selected for the corrosion.

The corrosion setup of steel bar is shown in Figure 4.4. A plastic box is used to contain the electrolyte and the bar is inserted by making a circular hole. The gap around the bar is sealed with a silicone sealant which can be easily removed. The bar is removed from the setup and cleaned to measure weight at frequent intervals and resealed using the same procedure. The corrosion product, $Fe(OH)_3$, which is commonly known as rust, is formed as a result of the reactions at the anode. The amount of mass loss by anode during the corrosion process can be estimated using Faraday's law given by Equation 4.1. M is atomic mass which is 55.845 g for Iron, i is the current in Ampere, t is the time in seconds, z is ionic charge which is 2 for Iron and F is Faraday's constant which is 96500 ampere/second.

$$Massloss\ in\ gram: \quad m = \frac{(Mit)}{(zF)} \tag{4.1}$$

The amount of mass loss for a 20 mm diameter steel bar is plotted in Figure 4.5. The mass loss observed in experiments is in close agreement with the mass loss curve plotted using the Faraday's law. The linear relationship between mass loss and corrosion current

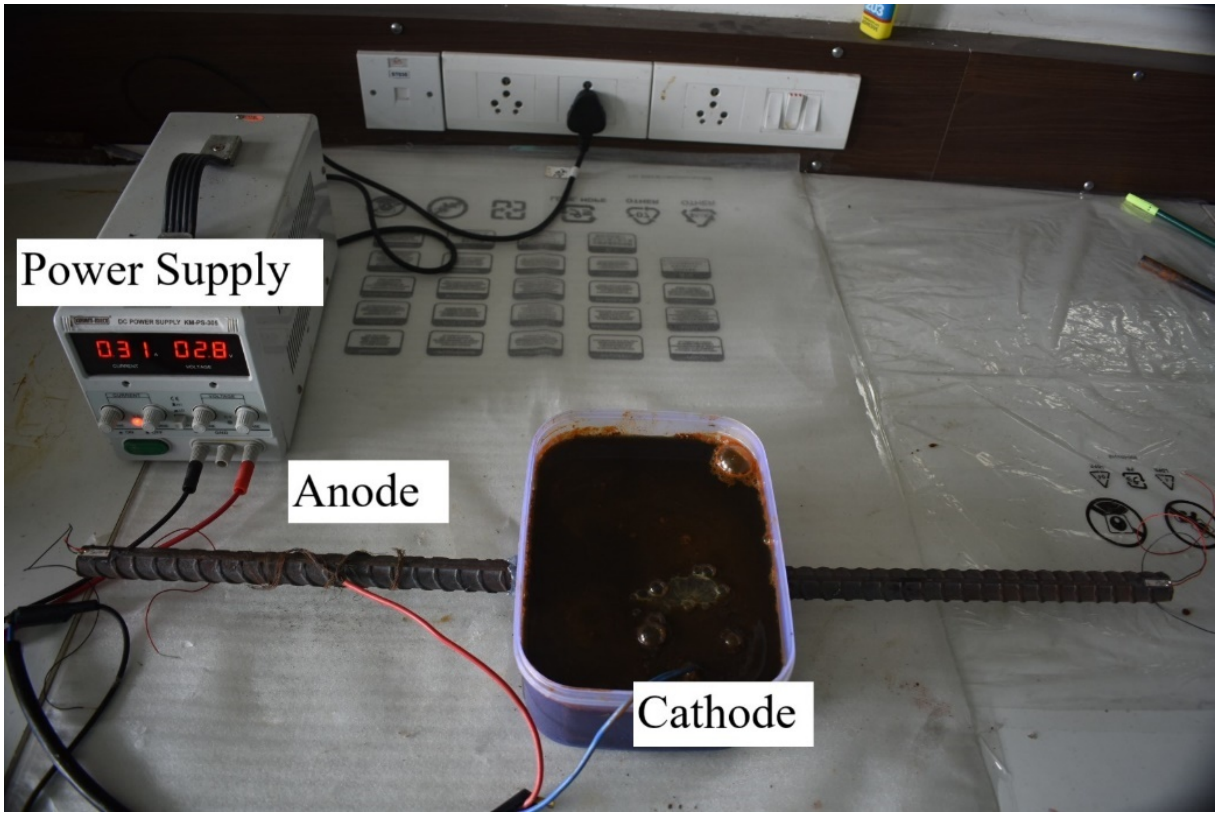

Figure 4.4: Corrosion cell setup for steel bar.

can be utilised to estimate the loss of mass at an unknown time. This relationship can also be applied for corrosion of steel bars embedded in concrete.

4.4.2 Embedded rebars

Corrosion process in concrete is much intricate and generally takes very long duration. Also, the location of corrosion cannot be controlled in natural environment. The corrosion process is accelerated in the laboratory by exposing the concrete beam to chloride environment. Pitting corrosion in rebar is achieved by initiating the electro-chemical reaction in it. The electrolyte for this electrolysis process is chosen as 9% NaCl w/v solution for 20 mm diameter rebars and 5% NaCl w/v solution for 12 mm diameter rebars. The experiments in Monash University used a constant voltage of 25 Volts is applied across the terminals using a DC power-supply. The positive terminal of the power supply is attached to the reinforcement bar making it as anode and negative terminal is attached to a galvanised wire mesh which is immersed in the solution along with concrete beam. The experimental setup with signal generation and acquisition that are used at Monash University are shown in Figure 4.6. To achieve pitting type of corrosion in rebars, the

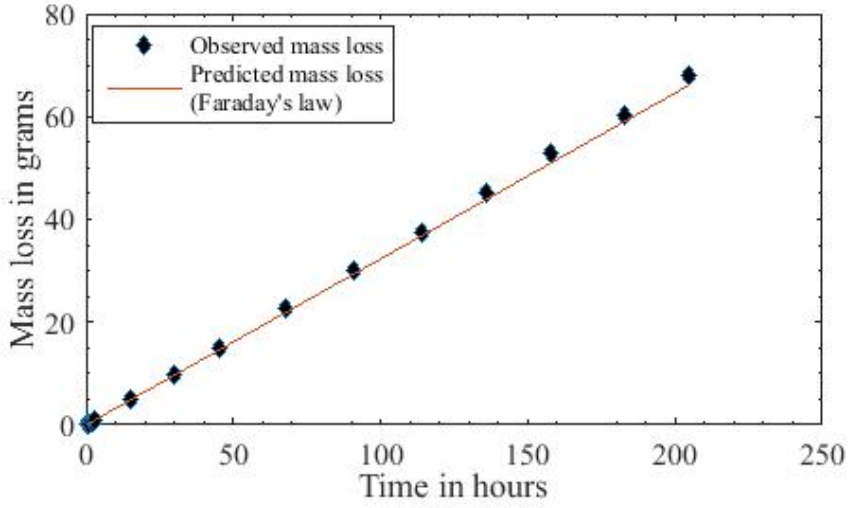

Figure 4.5: Comparison of actual (gravimetric) and predicted (Faraday's law) mass loss for a 20 mm rebar.

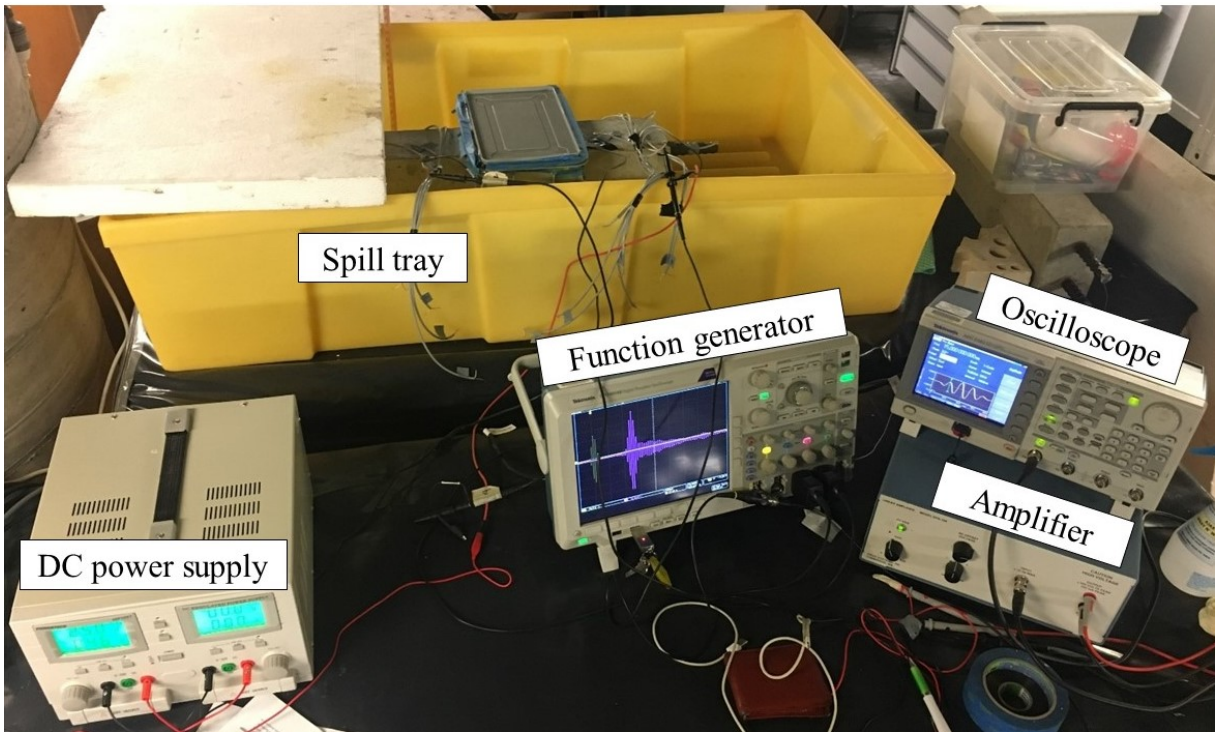

Figure 4.6: Experimental setup with corrosion cell arrangement and data acquisition system (Monash University).

portion of concrete wetted with the corrosive solution is restricted to 150 mm. The initial pH of NaCl is found to be 6.45. The pH of the solution is monitored continuously, and it is found that the pH has increased with the time. The pH of the the solution after ten days of corrosion is found to be 12. This indicates the increase in the alkalinity of the solution due to dissociation of H_2O molecules. The electrolyte is devoid of any colour

initially. The rust formed during the corrosion process is brownish in colour. This corrosion product gets leached into the electrolyte through the pores and through the cracks in concrete created by advancement of corrosion. The colour of the solution has changed to pale brown after five days and to dark brown after ten days. The change in colour of the electrolyte as shown in Figure 4.7 confirms the corrosion of rebars in the concrete.

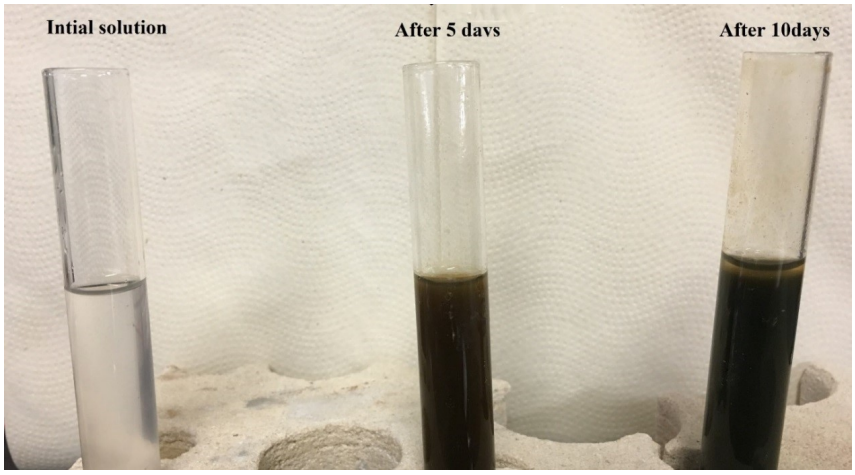

Figure 4.7: Electrolyte solution after five days and ten days of experiment.

The RC beam used in the study with typical anode and cathode is shown in Figure 4.8. The experimental setup that is shown Figure 4.9 is used at IIT Bombay to induce and monitor the localised corrosion of the rebars. The electrolyte used is a 5% NaCl solution, the anode is a copper bar and the rebar is cathode. A DC-power-supply equipment is used provide a constant electric current to bottom rebar which is made to corrode whereas the top rebar is kept uncorroded. An equivalent corrosion current density of 88.2 A/cm2 is maintained in the rebar. The complete setup of corrosion experiment and GW monitoring is outlined in the Figure 4.9. The inception of cracks after several days in corrosion can also be seen in the figure.

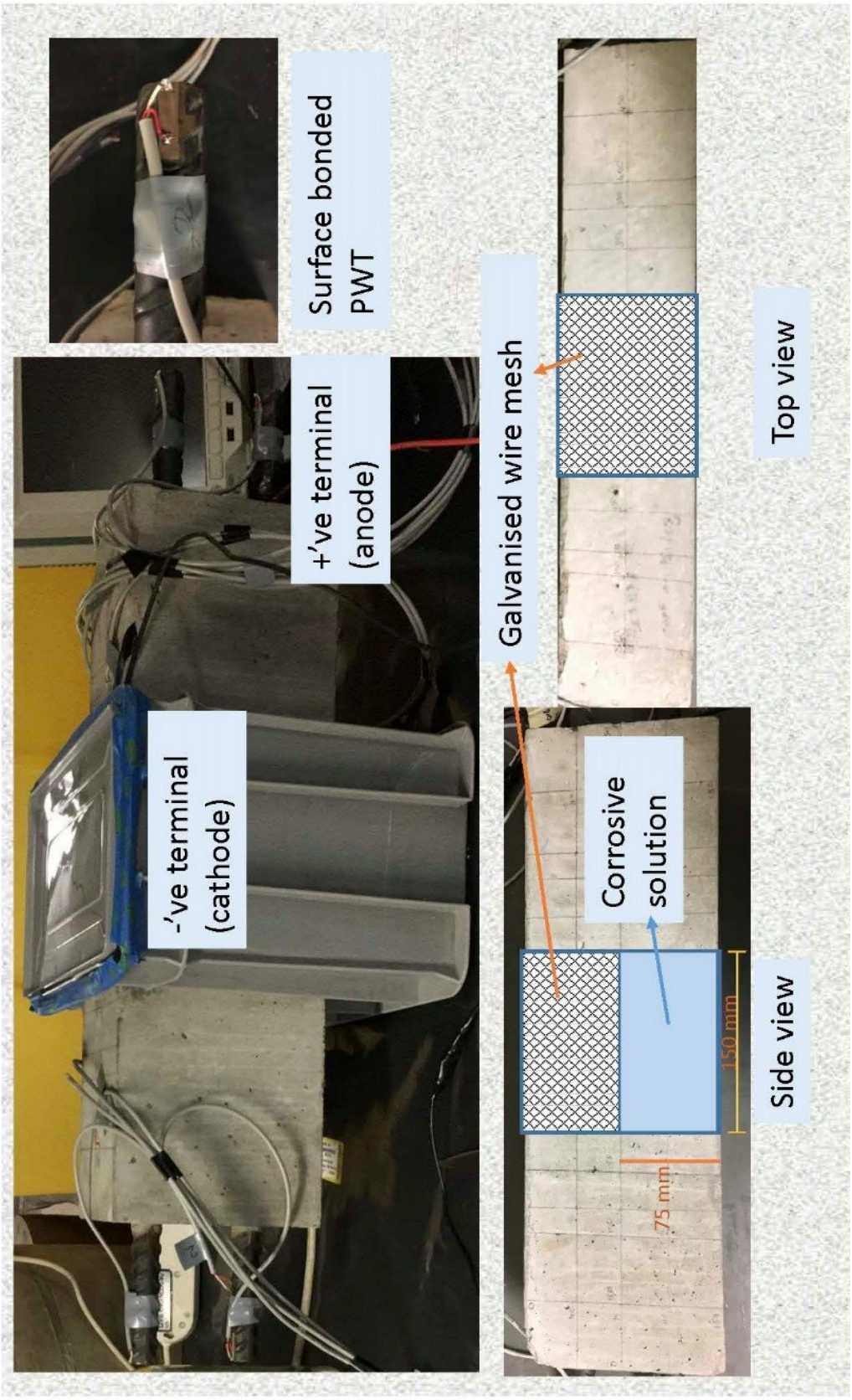

Figure 4.8: RC beam used in the corrosion cell setup with electricals terminals marked (Monash University).

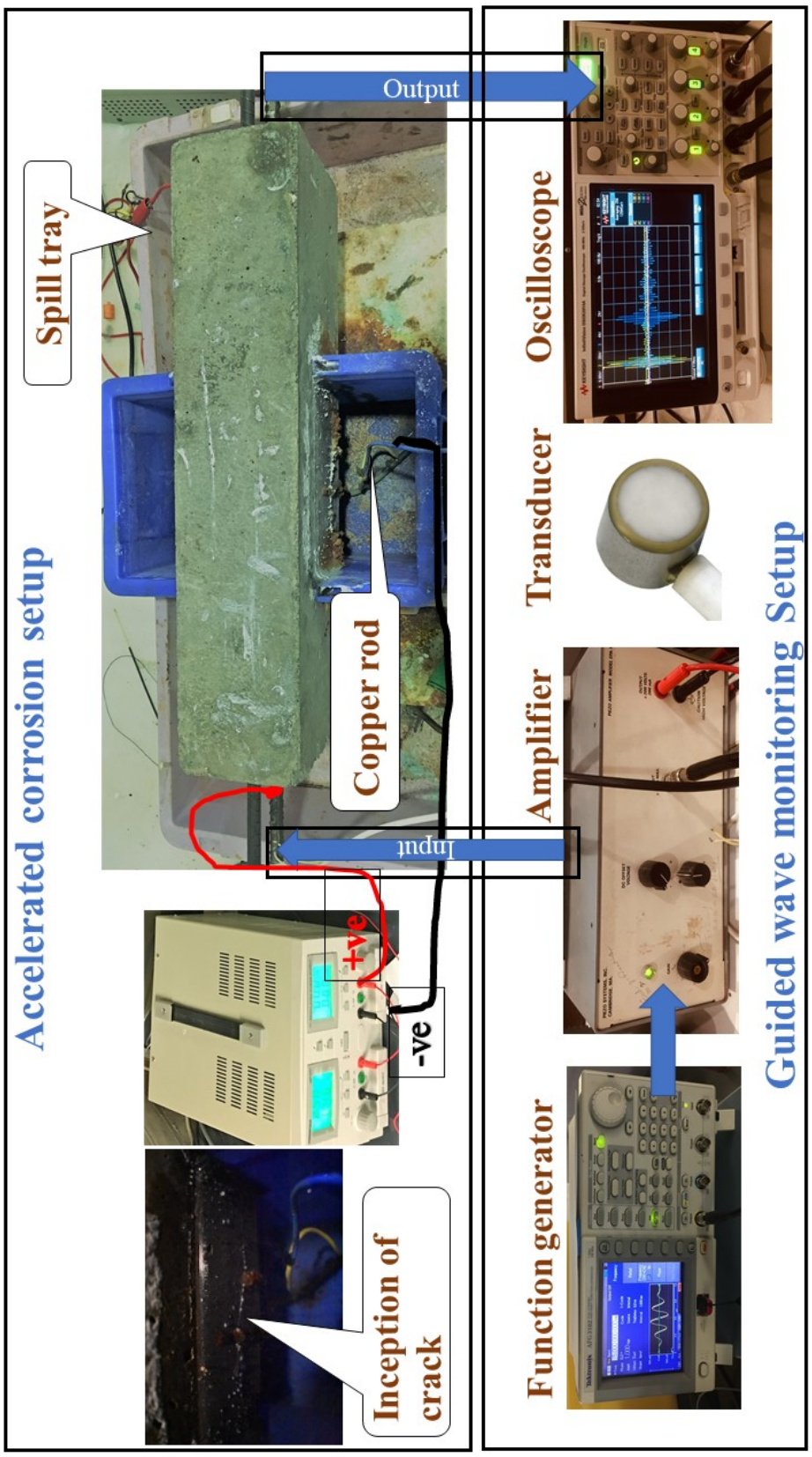

Figure 4.9: Experimental setup showing the accelerated corrosion and GW monitoring of corroded RC beam (IIT Bombay).

4.5 Numerical modelling

4.5.1 Rebar corrosion model

A numerical model of rebar with a simply supported boundary condition is developed in Abacus/CAE 6.14, a finite element analysis (FEA) software. The length and diameter of the rebars are 600 mm and 20 mm, respectively. Material properties of the rebar are listed in Table 4.4. A mesh size of 2 mm and time increment of 1X10-7 sec are used to satisfy the Courant–Friedrich–Levy condition [Courant *et al.*, 1967]. Corrosion is simulated in rebar by reducing the diameter of the selected portion while keeping all the other modelling parameters unchanged. A five-cycle Hanning pulse at 100 kHz is applied at one end of the rebar to generate longitudinal waves.

Table 4.4: Material properties of concrete and rebar.

Material	Density (kg/m3)	Youngs modulus (GPa)	Poisson ratio
Concrete	2238	19.00	0.15
Rebar	7850	205.00	0.29
Rust	3925	102.00	0.15

The effect of ribs on rebar has been studied by a few researchers and the key finding of their research is that the presence of ribs do not affect the signal when the ratio of the wavelength to the dimension of the ribs is high [Ervin *et al.*, 2006; Beard, 2002; Lu *et al.*, 2014]. The typical rib dimension for a 20 mm rebar is in the range of 1.25 mm to 1.35 mm. The frequency of the testing that is used in this study is 50-150 kHz. The wavelength-to-rib dimension is estimated to be greater than 2, which indicates that the ribs have a limited effect on wave characteristics. Therefore, a simplified solid rebar model is used instead of ribbed rebar for simulation.

For CT excitation the input pulse is applied in the form of pressure and the output signal is collected in the form of longitudinal displacements. For the PWT excitation and reception,the inbuilt ability of the software to simulate electrical excitation and mechanical wave propagation simultaneously is utilized in this study. Explicit code is used to model the RC, and the implicit code is used to model the PWT. These two codes are executed simultaneously using standard-explicit co-simulation, which is available in the software.

4.5.2 Reinforced concrete corrosion model

Wave propagation in RC is complex due to the composite nature of concrete. In order to simplify the analysis, concrete is assumed to be isotropic and elastic. The presence of two different materials, namely, concrete and reinforcement steel make it impossible to calculate the wave characteristics analytically; therefore, numerical modelling is adopted. For the current study, commercial finite element software, Abaqus/CAE 6.13, is used. The properties of material used in the study are mentioned in Table 4.4

Longitudinal excitation

A numerical model of the concrete beam is generated using commercially available finite element method (FEM) software, Abaqus/CAE. Concrete and rebar are created as separated parts with material properties mentioned in Table 4.4 and they are assembled and tied using TIE constraint, which keeps the displacements at the interface equal. The ribs are found to have less effect on the wave properties hence the rebar is modelled devoid of ribs [Ervin *et al.*, 2006; Beard, 2002]. In the tie constraint, the rebar surface is selected as master surface and the concrete surface is selected as slave. A dynamic explicit type of analysis is selected with a maximum time increment of 0.1 μs and a mesh size is chosen to satisfy the convention that at least 10 elements shall exist per wavelength [Courant *et al.*, 1967]. A pressure pulse, which is a Hanning windowed sine pulse with five cycles, is applied at one end of the rebar in an area equal to CT to generate longitudinal GWs. The response of the structure is analysed for a total time of 1 ms and the longitudinal displacements at the other end of the same rebar are plotted to compare with the transducer response. The numerical model is modified to study the effect of pure corrosion and debonding in RC beam. The rebar is portioned to include a damage in a part of the rebar. The damage size is changed to study the effect of the damage. For a debonding type of damage the rebar is untied from the concrete along with a very fine reduction in diameter which equals 0.01 mm. The diameter is reduced to avoid the interaction of the rebar and concrete during the wave propagation. For a corrosion type of damage, the rebar cross-section is reduced, and rust is added to the rebar substituting the reduced volume of the rebar.

Excitation by piezoelectric wafer transducers

A three-dimensional finite element model of an RC beam is developed using an explicit method in Abaqus software in order to study GW propagation that is generated by embedded PWT. Corrosion in rebar is simulated by reducing the diameter of the rebar, and debonding is simulated by untying the concrete and the rebar. The dynamic-implicit method is used to simulate piezoelectric material. The implicit and explicit models are co-executed using standard-explicit co-simulation. The two complementary effects of corrosion and disbond on wave features, which results in a zero-effect state, are studied in detail. For the current study, the electro-mechanical properties that correspond to SP-5H PWTs are used, as presented in reference Sikdar *et al.*, 2016. A concrete beam that has the dimensions, 150 mm x 100 mm x 500 mm, is embedded with a rebar of a length of 1.5m. PWTs are attached to the surface of rebars at each end. A schematic representation of the model is shown in Figure 4.10. A narrowband five-cycle hanning pulse is used

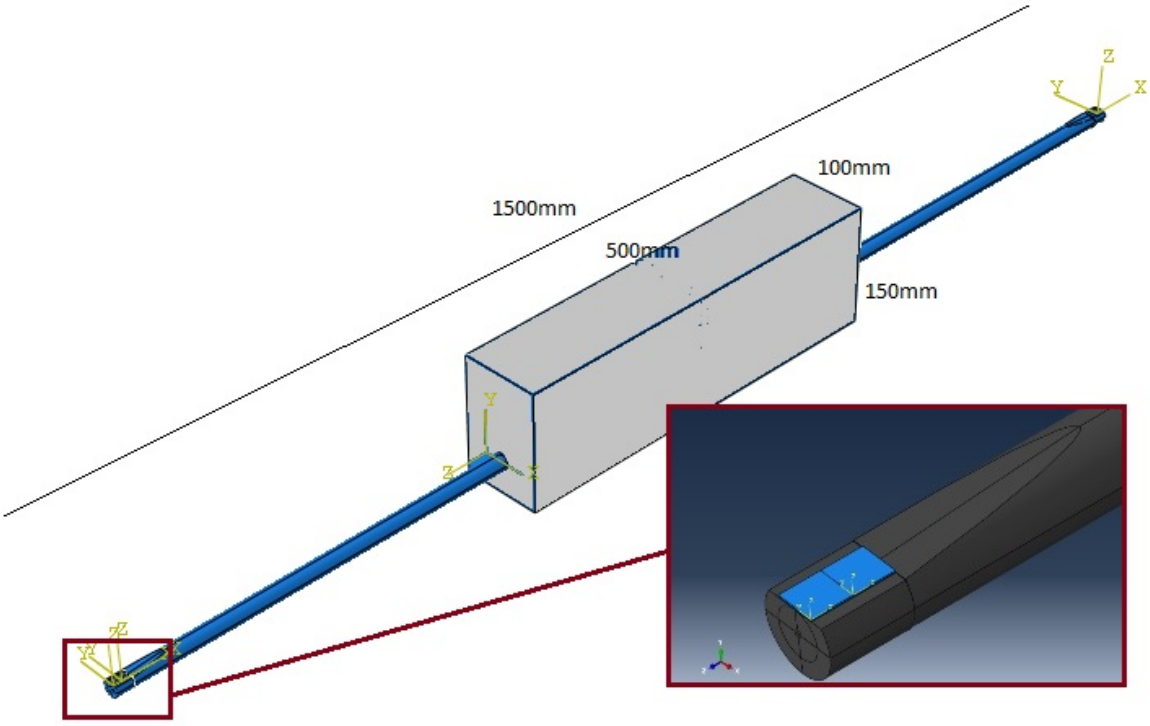

Figure 4.10: Schematic diagram of the RC beam that is used in study of corrosion and debonding.

as input for wave generation. The response of the structure is shown in Figure 4.11a. It is analyzed by using Gabor Wavelet, the wavelet coefficients of which are plotted in Figure 4.11b. It is observed that the given excitation results in two wave modes and these are

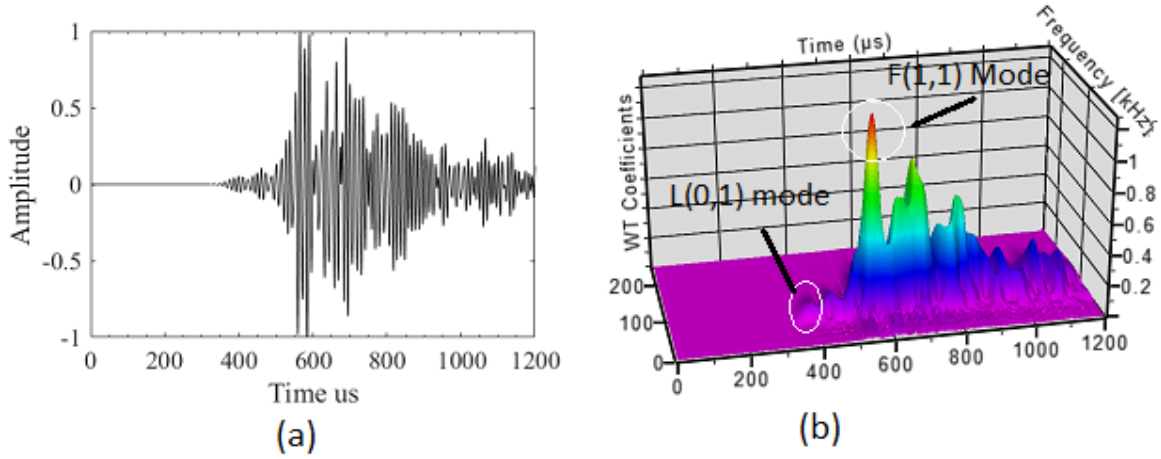

Figure 4.11: Response of an undamaged structure at 100 kHz excitation frequency (a) Time History (b) 3D plot of signal using Gabor wavelet.

recognized as the longitudinal mode $L(0,\ 1)$ and the flexural mode $F(1,\ 1)$ where the flexural mode has dominant energy.

4.6 Concluding remarks

This chapter discussed the experiments and numerical simulations performed to assess corrosion in detail. The experimental specimens include the concrete samples that are embedded with the rebars of various diameters. Piezoelectric sensors in the form of wafers and compact barrels are used to generate and sense the GWs in two basic ways by using the CTs and PWTs. The section, corrosion setup, introduces to the accelerated corrosion setup which is used for the sustained corrosion of the bare and embedded rebars. The details of the numerical modelling using finite element method software, Abaqus/CAE is outlined in the section numerical modelling.

Chapter 5

Detection and assessment of pitting corrosion in rebars using scattering of ultrasonic guided waves

5.1 Introduction

Literature study indicates that corrosion needs to be detected and arrested at its inception as it reduces structural integrity. Corrosion of embedded rebars is more complex than simple rebars hence it is important to understand corrosion in bare rebars before it is studied in embedded rebars. Corrosion in rebars can be classified into uniform corrosion and pitting corrosion. In uniform corrosion, the reduction in diameter is identical throughout the length of the rebar. This type of corrosion is often slow and can be detected and controlled easily. Recently, embeddable piezoelectric patches are successfully tested to detect and quantify uniform corrosion in RC structures [Talakokula *et al.*, 2014]. In the pitting type of corrosion, the corrosion is limited to a specific portion of the rebar, and such damage can occur and propagate at a faster rate. It is recognised to be more dangerous because the cross section of the rebar is reduced to a point at which the load-carrying capacity of the rebar is completely diminished and a catastrophic failure of the structure is enforced [Cao and Cheung, 2014; Regier and Hoult, 2015]. However, the dominant change in the ToF and the amplitude of wave modes, which is observed due to uniform corrosion, could not be witnessed in the case of pitting corrosion. Hence, the methods that are developed for uniform corrosion do not hold good for pitting corrosion.

Detection and assessment of pitting corrosion in rebars by using ultrasonic GWs is an impending task in this study. The longitudinal GW mode, $L(0,\ 1)$, is excited by using CTs that are attached to the ends of the rebar. The variation in amplitude measurements

due to bonding between the transducer and the structure is eliminated by normalising the signal with respect to the peak amplitude of the $L(0,\ 1)$ mode. The response of the rebar with pitting corrosion is analysed and various wave modes in the signal are identified. Corrosion is simulated artificially by scraping the material which creates the scattered modes that are generated due to the presence of damage can imitate the damage intensity and boundaries. The characteristics of the scattered waves are predicted by testing rebars at various corrosion levels. Damage index (DI) methods act as efficient tools in the visualising of structural health monitoring data [Wandowski *et al.*, 2015].

5.2 Wave propagation in a corroded rebar

The existence of corrosion in reinforcement leads to contamination of the received signal due to scattering at the damage edges. The change in the geometric properties of the reinforcement necessitates a change in the group velocity in the damaged area. Hence, a change in the ToF can be observed in that area. However, this change in the ToF cannot result in an appreciable change in the ToF of the initially transmitted signal of the entire structure. Depending upon the location and relative size of damage, with respect to the rebar, an infinite number of modes are possible. The prevalence of any particular mode depends on the incident wave energy and reflection coefficients. A few basic transmission and reflection modes that occur due to the front and rear edges of damage are shown in Figure 5.1. A part of the initial signal is unaffected by the damage and arrives at the sensor at a time, T. The times of flight for various portions of the rebar are indicated by t_1, t_2 and t_3. Arrival times for various damage-scattered modes are listed in Table 5.1. These modes are numbered from 1 to 10. The mode number 1 is the directly transmitted signal, and mode number 2 is the boundary reflected signal. The modes from 3 to 10 are the damage edge scattered signals. The arrows indicate the path followed by each of these modes which is referred as reflection and transmission pattern. In order to calculate the total time of flight of each of the modes the rebar is divided into three parts, the first part is the undamaged portion of the rebar near the actuator, the second part is the damaged portion of the rebar and the third part is the undamaged portion near the sensor. The time of arrival of each of these three parts is indicated by t_1, t_2, and t_3 in Figure 5.1. The time of arrival for a damaged scattered mode is calculated by totalling the times taken by

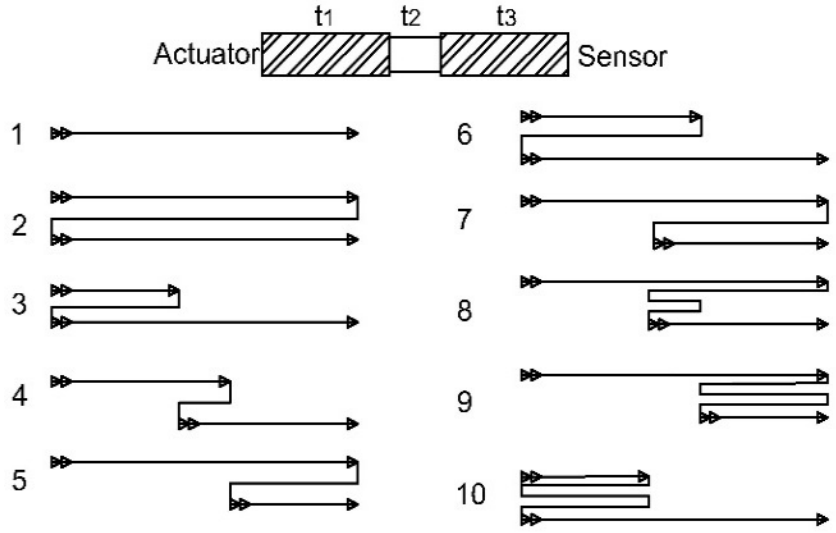

Figure 5.1: Reflection and transmission pattern in damaged rebar.

the wave mode in each of these three parts. The arrival time for various damage-scattered modes numbered from 1 to 10 is listed in Table 5.1.

Table 5.1: Scattered wave modes and their arrival times at the sensor.

Mode No.	Time of arrival at sensor	Mode No.	Time of arrival at sensor
1	T	6	$T+2*t_1+2*t_2$
2	3T	7	$T+2*t_2+2*t_3$
3	$T+2*t_1$	8	$T+4*t_2+2*t3$
4	$T+2*t_2$	9	$T+4*t_3$
5	$T+2*t_3$	10	$T+4*t_1$

The received signal takes a simplified form when the damage is located equidistant from the actuator and sensor (that is, $t_1=t_3$). In such a case, the scattered wave modes 3 and 5 arrive at the same time. Simillarly, two sets of scattered wave modes (6, 7) and (9, 10) also arrive at the same time. Thus, in the received signal, these two sets of scattered wave packets form two distinct peaks, which are observed in the numerical simulations and experiments. In this study, the effect of rebar corrosion on the characterstics of various scattered wave packets is analysed.

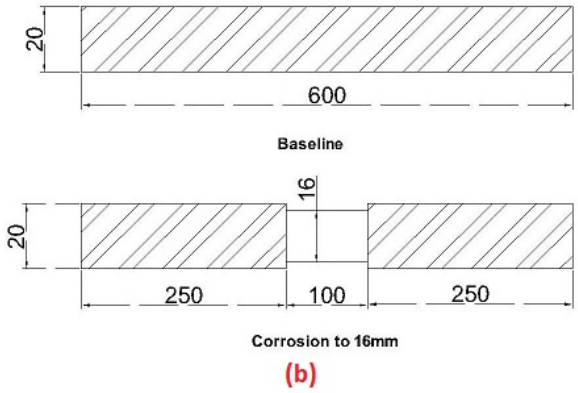

Figure 5.2: A typical rebar used as a baseline, and a rebar with corrosion.

5.3 Numerical and experimental results

A rebar without damage is used as a baseline. The baseline signal shows a clear transmission signature at a time, 'T', and boundary echo after time, '3T'. A schematic diagram of a pristine rebar and a rebar with corrosion damage that is located at the centre, with an axial extent of 100 mm, is shown in Figure 5.2.

The responses of an undamaged specimen that is collected using simulation and experiments are compared in Figure 5.3(a). The direct transmitted signal and the boundary reflected signal could be recognised from the energy envelopes of the signals by using the Hilbert coefficients [Feldman, 2011], as shown in Figure 5.3(b). The input frequency of 100 kHz results in a dominant $L(0,\ 1)$ mode, which has an arrival time of 129.5 μs in the simulation. Additionally, it is comparable to the arrival time (125.2 μs) of the direct transmitted signal that is observed in the experiments. Dispersion curves for a rebar with a diameter of 20 mm are plotted by using DISPERSE software [Pavlakovic and Lowe, 2005]. The group velocity is obtained from numerical results for each of the frequencies of excitation by dividing the length of the rebar with ToF, which is calculated by the differential time from the peak input to the peak output. These dispersion curves, as shown in Figure 5.4, are verified by using group velocities that are obtained through experiments on the undamaged rebar.

Figure 5.5 shows a typical comparison of FEA and experimental signals for a 100 mm-wide corrosion of rebar with a diameter reduction to 16 mm diameter from 20 mm diameter. The response of rebars with corrosion damage shows the wave packets that are generated due to scattering from damage edges, which are like the simulation results. This

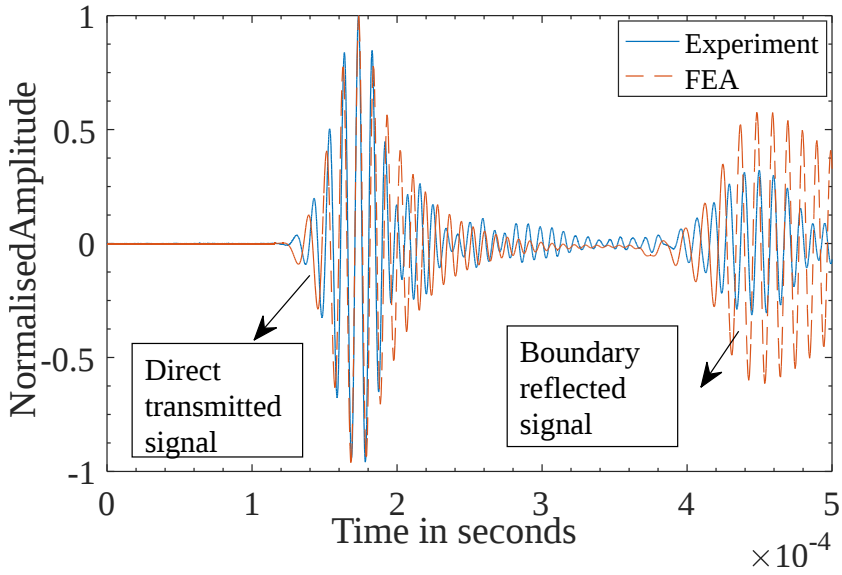

(a) Signal

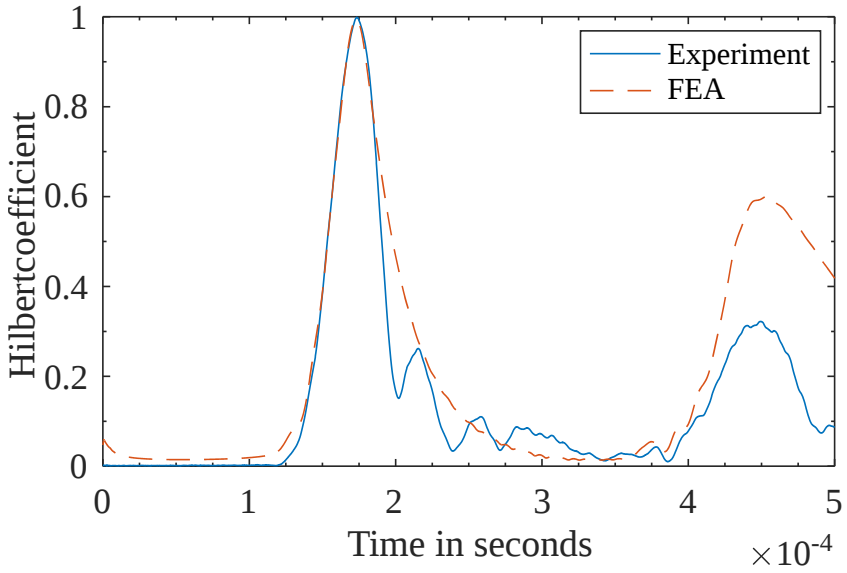

(b) Envelope

Figure 5.3: (a) Comparison of baseline signal from experiment and FEA and, (b) comparison of energy envelope of baseline signal from experiment and FEA.

damage-scattered signal can be utilised to study the effect of a change in the intensity, axial extent and location of pitting corrosion, which will be addressed in section 5.4. In the rebar in which the corrosion is located at the centre, two distinct wave packets can be observed in the signal, as will be explained in section 5.4.1 and section 5.4.2. These wave packets are analysed in order to develop a damage index method. In the rebar in which the damage located away from the centre, more than two packets are observed, as will be explained in section 5.4.3, four of which are significant and are used to identify

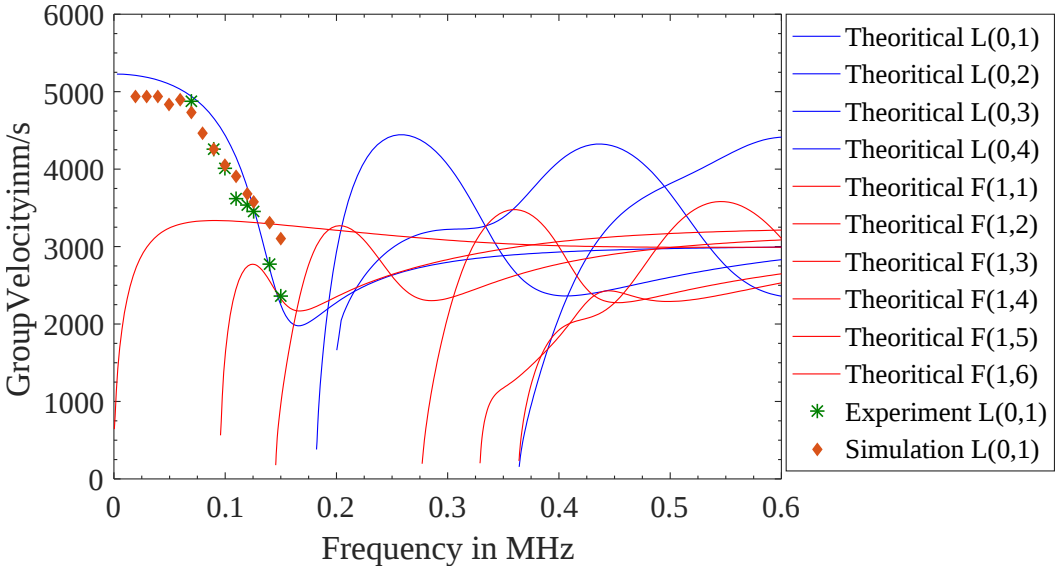

Figure 5.4: Group velocity dispersion curves for a 20 mm rebar.

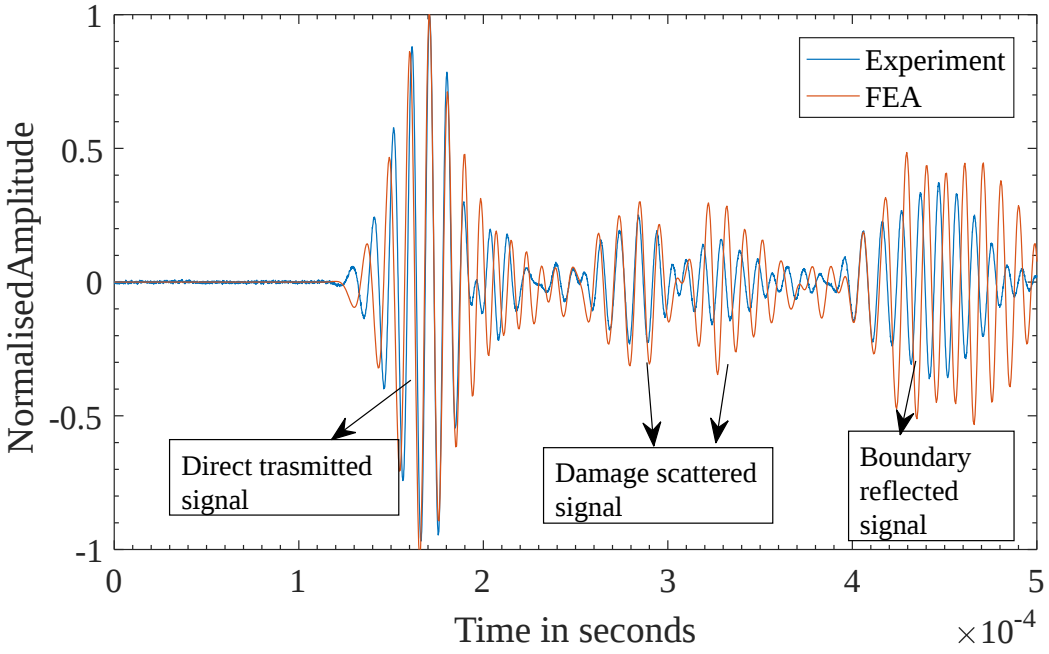

Figure 5.5: Comparison of FEA and experiment signal of rebar with 100 mm-wide corrosion located at the centre.

the damage.

5.4 Damage index method to detect simulated corrosion of bare rebars

From numerical studies and experiments, it is observed that the presence of damage results in scattering of wave energy. The wave packets that are generated due to scattering are examined in this study in order to develop a method to ascertain the progress of the damage. Three types of variations in corrosion are examined. First, the intensity of corrosion is varied for a fixed axial extent of corrosion at the centre by reducing the diameter of rebar in the corroded region. The radial profile of the pitting corrosion is maintained as circular for computational simplicity. Second, the axial extent of corrosion is varied for a fixed reduction in diameter at the centre. Third, the location of corrosion is varied while maintaining the intensity and axial extent of corrosion as constant.

5.4.1 Assessment of corrosion in a rebar with varying corrosion intensity

In order to examine the effect of corrosion, rebars with various intensities of corrosion are modelled and the results are compared with the baseline signal. Figure 5.6 shows the comparison between signals with and without a 100 mm-wide corrosion that is located at the centre with a diameter reduction to 16 mm. Figure 5.7 shows the energy envelope that is plotted using a Hilbert transform of the signals. Two distinct peaks can be observed in the signal of the corroded sample, and this effect can be attributed to the scattering from the edges of the damage. It is further observed that an increase in corrosion of the rebar results in an increase in the amplitude of scattered wave packets. The differential time of arrival of the two wave packets has a direct correlation with the boundaries of the damage. A damage index is developed by using the reflection pattern that occurs due to the pitting type of the corrosion that is located at the centre of the rebar. In this method, the rebar is discretised into n elements with n+1 nodes, as shown in Figure 5.8. The boundary of the damage is assumed to exist at each of the nodes, and the damage index is calculated. The path that is followed by the scattered wave for a damage boundary that is located at the kth node is shown in Figure 5.8. DI is the measure of the relative amplitude of the scattered wave with respect to that of the directly transmitted signal.

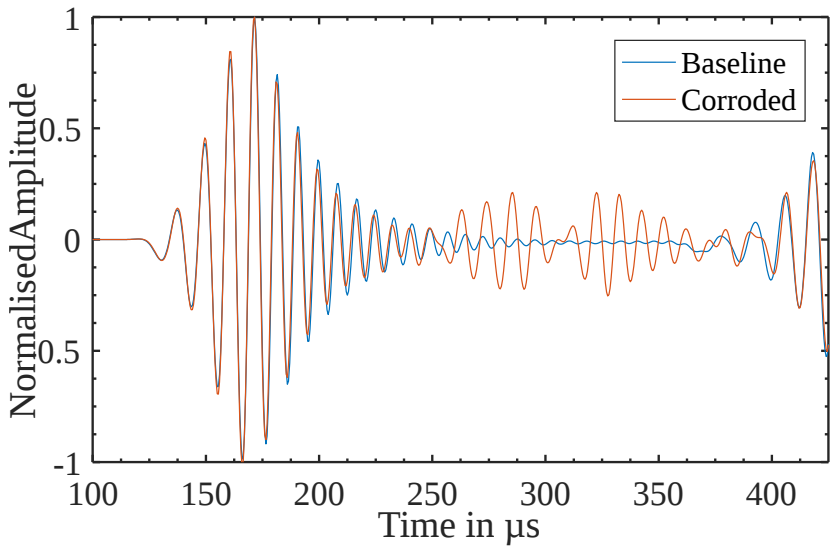

Figure 5.6: Comparison of the signal from a corroded rebar with baseline signal by using FEA.

Typically, if there is no damage the value of the damage index will be zero. The damage index at each node is defined by the following equation:

$$DI(x) = \sqrt{\int_{t_1}^{t_2} (S - B)^2 dt} \tag{5.1}$$

where t_1= (L+2∗x)/V, t_2=t1+ Δ_i , V is the velocity of the specific mode. L is the length of rebar, and x is the distance of a node from the sensor. Δ_i is the pulse duration of the input pulse (50μs for 100 kHz). S is the signal from the specimen with damage. B is the baseline signal.

In the current case, the length of the damage is maintained at 100 mm, and the diameter of the corroded portion is reduced. The damage index of various corroded rebar samples, which is calculated by using FEA signal, is shown in Figure 5.9. It can be observed from the figure that the value of the damage index increases with an increase in the level of corrosion. The front and rear edges of the damage have a high damage index, which can be used to monitor the progress of the corrosion in the rebar. In the detail, the peak in the damage index plot indicates the location of the damage edge, while the area under the curve for each case of damage can be used in order to estimate the intensity of corrosion. An estimate of the axial length of corrosion, which is obtained from the peak-to-peak distance in the damage index plot, is listed in Table 5.2.

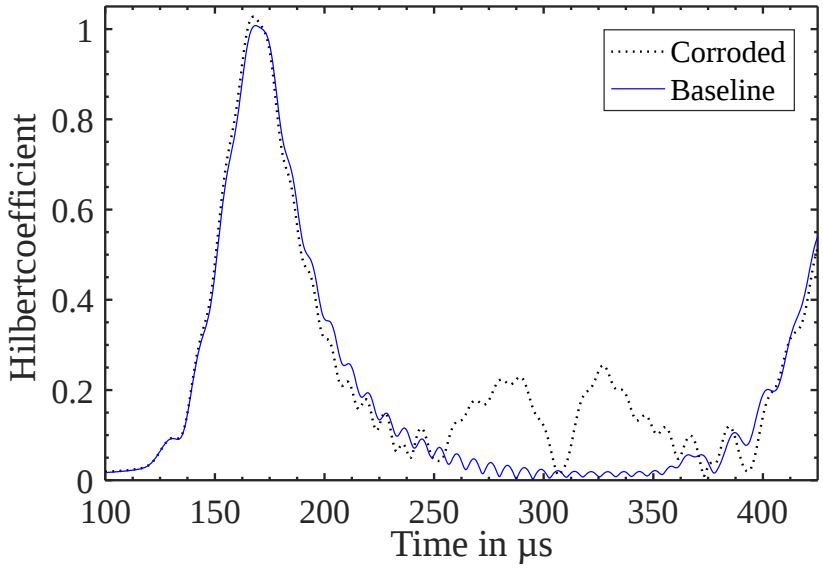

Figure 5.7: Comparison of energy envelopes of the signal from corroded rebar with baseline signal by using FEA.

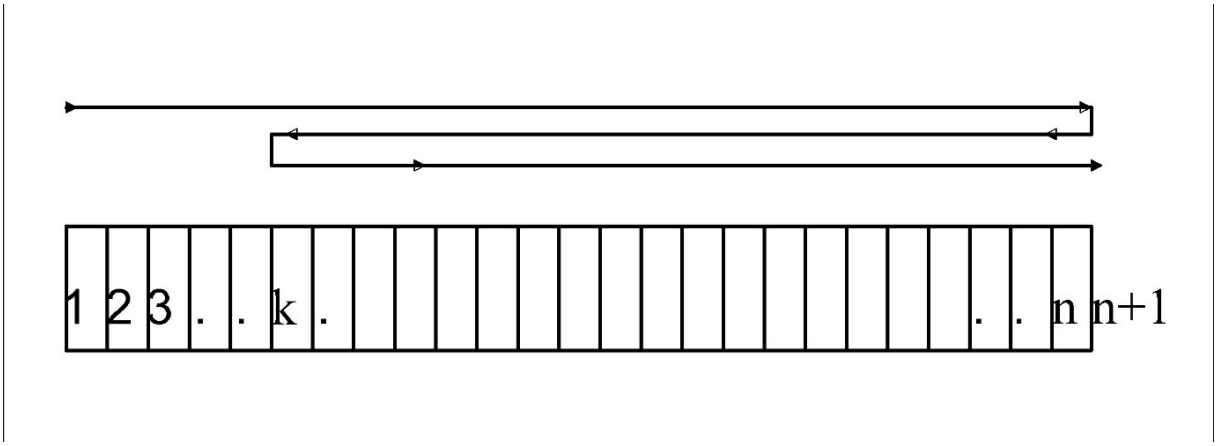

Figure 5.8: Discretisation in a typical rebar for damage index calculation, and path of the signal in case of damage at the node, k.

The results of the simulation are verified with experimental results in a few cases. A comparison of the signal of the corroded rebars with the baseline that is obtained from experiments is shown in Figure 5.10. In line with the simulation results, the signal from a corroded rebar has scattered wave packets, which form two distinct wave packets. The damage index is calculated by using the experimental signals and it is plotted against each of the discretised nodes. The value of DI is equal to zero at an undamaged node as there is no scattered wave that arrives at the corresponding arrival time. The value of DI increases with the damage and the maximum value is more than 1 as the definition of DI does not include the normalisation. It can also be observed that the increase in the

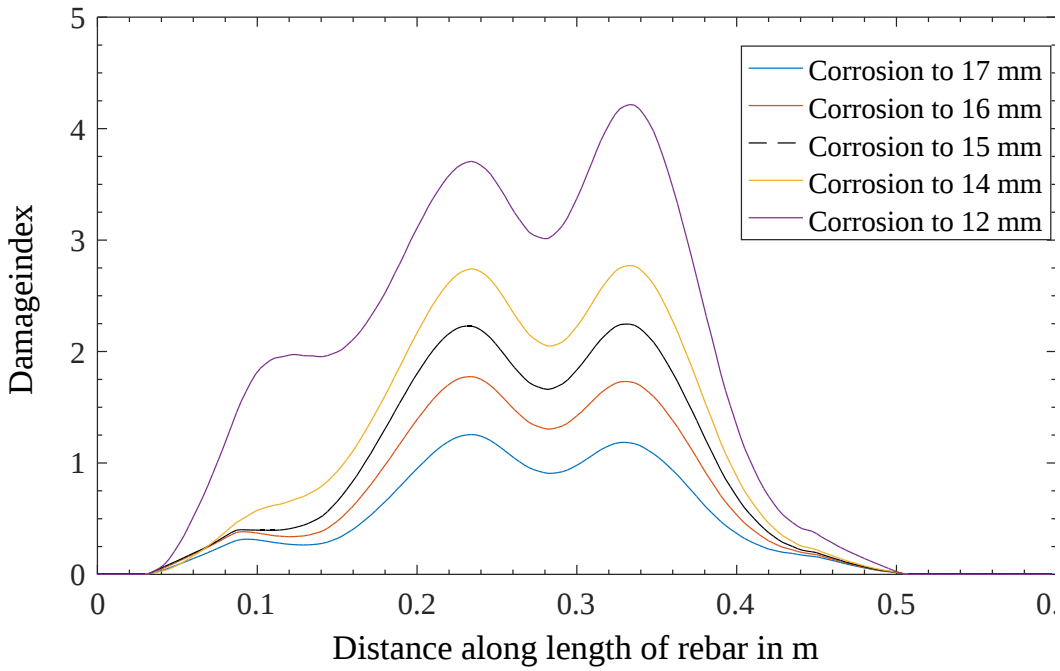

Figure 5.9: Damage index of steel bars with various intensities of corrosion located at the centre (FEA).

Table 5.2: Estimation of damage length using damage index plot for a 100 mm-wide corrosion damage in rebar (FEA).

Reduced diameter (mm)	First peak (mm)	Second peak (mm)	Damage size (mm)	Error in length estimation (%)
17	234	330	96	4 %
16	234	330	96	4 %
15	231	333	102	2 %
14	234	333	99	1 %
12	231	333	102	2 %

corrosion intensity results in an increase in the damage index, as shown in Figure 5.11. Hence, the progression of the corrosion due to the change in the intensity can be monitored by using the current method. The estimation of the length of the corroded portion by using the damage index is presented in Table 5.3 for a few experimental specimens.

5.4.2 Assessment of corrosion in a rebar with varying axial extents of corrosion

The corrosion in a rebar can also progress due to an increase in the length of the corroded portion. Hence, various rebars with the varying axial extents of corrosion for the same reduction in diameter are studied by using FEA and experiments. It is observed that

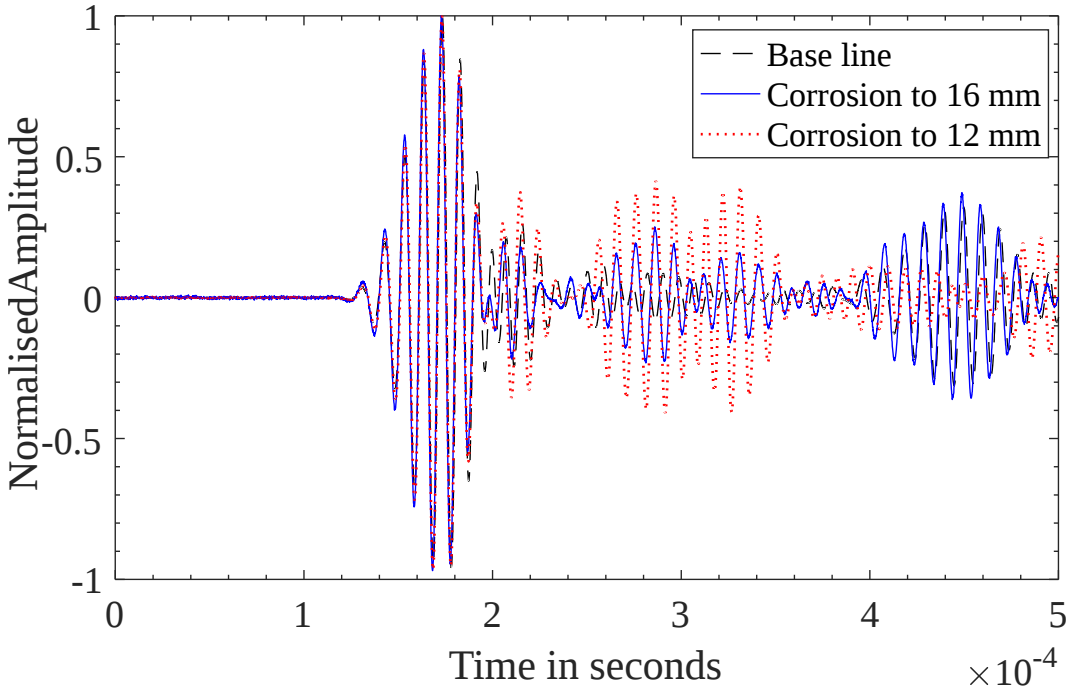

Figure 5.10: Comparison of the signal from rebars with various intensities of corrosion by using experiments.

Table 5.3: Estimation of corrosion length from damage index plots by using experimental signals.

Corroded rebar diameter (mm)	First peak (mm)	Second peak (mm)	Damage size (mm)	Error in length estimation (%)
16	246	342	96	4 %
12	255	345	90	10 %

the differential time of arrival of the scattered wave packets increases with the increase in the length of the corroded portion. The damage index that is similar and is defined in section 4.3.1 can be used to monitor this category of pitting corrosion progression in the rebar. Damage index that is calculated by using FEA signals in a few cases of corrosion with different lengths of corrosion is shown in Figure 5.12. In the figure, the damage index that is obtained for corrosion cases of the axial extents of 100 mm, 150 mm and 200 mm clearly shows the edges of corrosion damage. Hence, the pitting corrosion can be monitored when its progress is along the axial direction. The lengths of the corroded portion that is calculated for the FEA signals by using the damage index plots are listed in Table 5.4. The simulation results are verified by using damage index plots of the signal from experiments, as shown in Figure 5.13. The length of the damage, which is estimated from experiments, is in agreement with simulation results that are presented in Table 5.4.

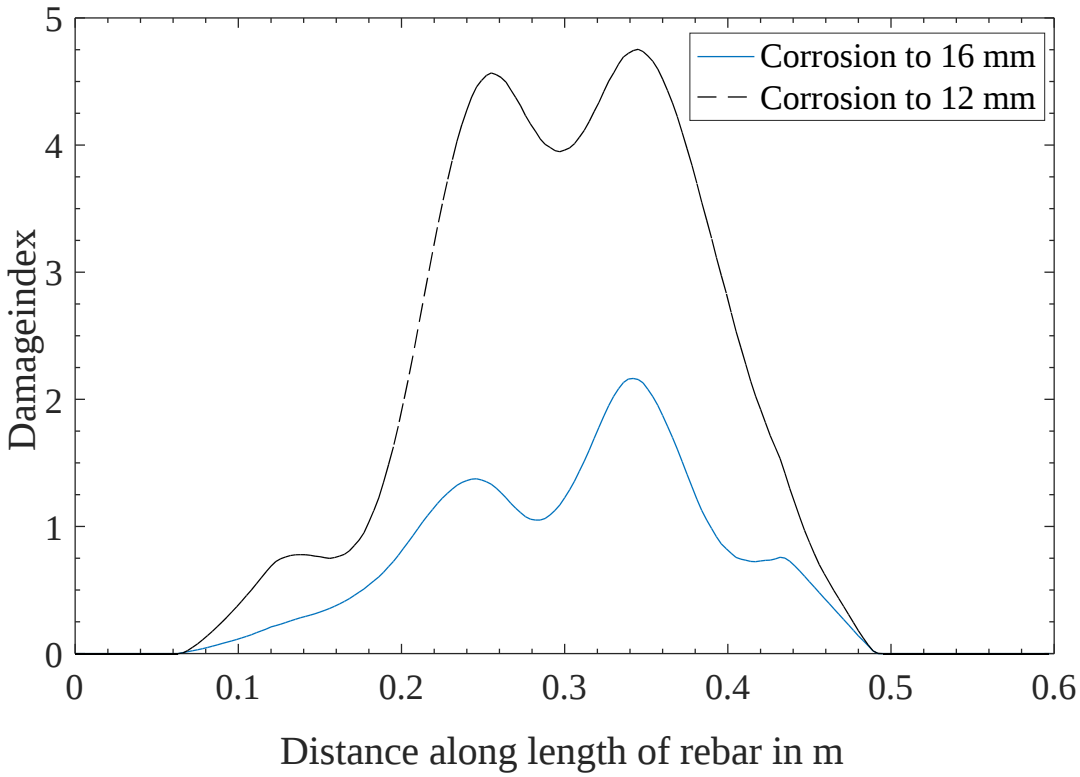

Figure 5.11: Damage index plots for rebars with various levels of corrosion by using experiments.

Table 5.4: Estimation of corrosion length using damage index plot for damage that is equidistant from transducers.

Corrosion length (mm)	Damage size (Simulation) (mm)	Error (%) (Simulation)	Damage size (Experiment) (mm)	Error (%) (Experiment)
50	102	100 %	-	-
100	99	4 %	96	4 %
150	129	14 %	132	12 %
200	178	11 %	192	4 %

On the other hand, in the case of the corrosion with an axial extent of less than a cut-off length, it is observed that damage could not be quantified by using the damage index that is defined in this study. This is because the distinct peaks in received signal could only be observed when the damage is larger than the cut-off length. Numerical models with various lengths of damage are analysed, and the cut-off length for the current case is 70 mm. As can be observed in the pitting corrosion that has an axial extent of 50 mm, the damage index method results in a large error in Table 5.4. A different approach shall be followed in order to decompose the superimposed signal so that damage can be quantified in such cases.

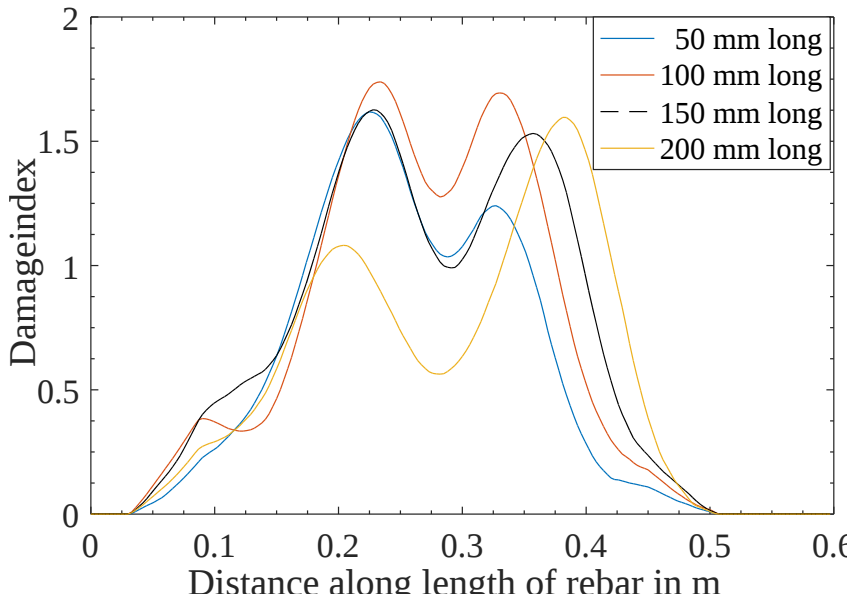

Figure 5.12: Damage index plot for various lengths of damage located at the centre by using FEA.

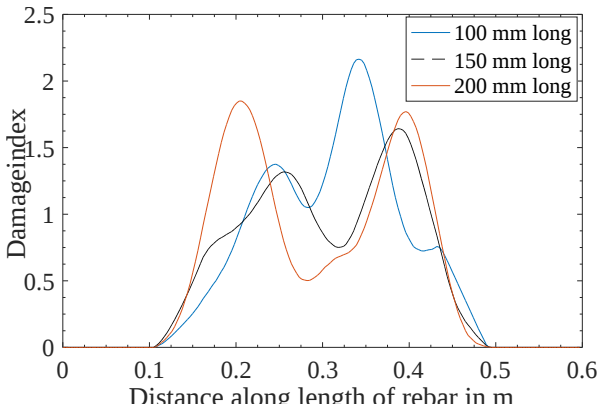

Figure 5.13: Damage index plot for various lengths of damage located at the centre by using experiments.

5.4.3 Localisation of corrosion at an arbitrary location in the rebar

In the previous two sections, the damage is maintained at the central location of the rebar. This configuration causes the various scattered waves to arrive at a similar time. Thus, the wave modes are superimposed and result in two distinct wave modes that could be used to develop a damage index. In this section, the location of the pitting corrosion is varied and its effect on the wave characteristics is examined. For this study, an axial extent of 100 mm, and a reduced diameter of 16 mm are chosen for the corrosion. A typical signal in the simulation for the pitting corrosion that is located at a distance

200 mm from the actuator is shown in Figure 5.14. Unlike the corrosion that is located equidistant from the actuator and the sensor, the asymmetric corrosion results in multiple wave packets. Typically, four dominant wave packets can be observed due to scattering. These four wave packets are due to reflections from structure boundaries and the damage edges, as shown in Figure 5.15. The arrival time of each of these wave packets depends upon the location and the axial extent of the damage. Hence, an estimate of the damage can be made by using these scattered waves.

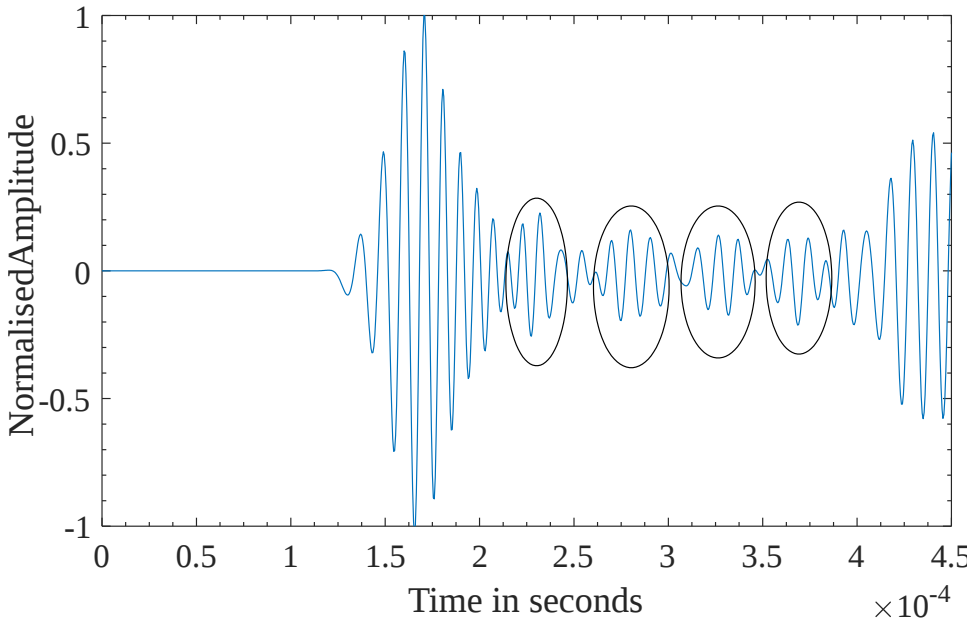

Figure 5.14: Response of a rebar with corrosion located at 200 mm from the actuator.

Contrary to the previous cases, in the present case, the arrival time of the scattered waves is not superimposed. Hence, for the damage that is located at an arbitrary location, a different approach is required to estimate the damage. The scattered wave packets that are obtained from the FEA and experimental results for a typical damage that is located at 200 mm from the actuator end are highlighted in Figure 5.16. The front edge of the damage can be reconstructed by using the first and fourth wave packets, and rear edge can be estimated by using the second and third wave packets. Let T_1, T_2, T_3 and T_4 be the arrival times of each of the wave packets. The location of the front edge of the damage from the actuator end can then be obtained as $x_1 \cong 0.5 \times [L - 0.5 \times (T_4 - T_1) \times V]$, and the location of the rear edge of the damage from the actuator end can be estimated as $x_2 \cong 0.5 \times [L - 0.5 \times (T_3 - T_2) \times V]$. The location and the extent of corrosion that

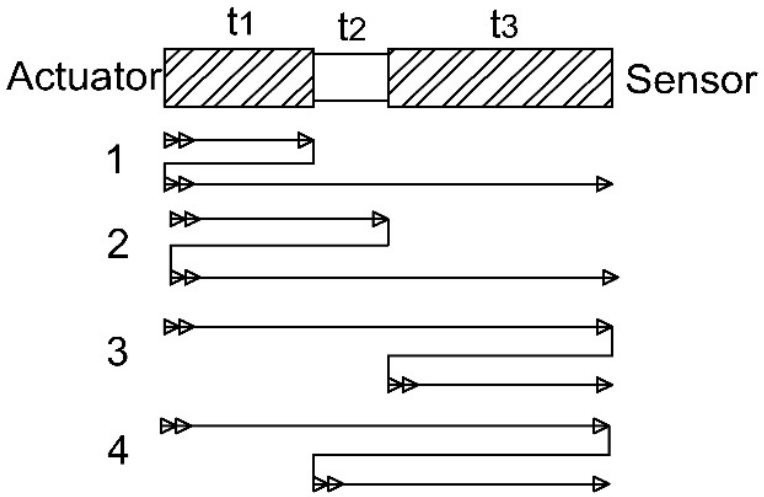

Figure 5.15: Schematic diagram displaying the path followed by various scattered wave modes.

are estimated by this method for various cases are tabulated in Table 5.5. It is observed that the current method could be applied with considerable accuracy to the detection of damage location. The observed error can be attributed to the difference in the wave velocity in the corroded and intact portions of the rebar, which is not taken into account in the present study. In addition, the possible overlap of the scattered signal with boundary reflections contributes to the shifting of peaks, which results in the error in the length estimation.

Table 5.5: Location estimation by using the time of arrival of damage edge scattered wave packets.

Sample No.	T_1 (x10-6 s)	T_2 (x10-6 s)	T_3 (x10-6 s)	T_4 (x10-6 s)	x_1 (mm)	x_2 (mm)	Damage location (mm)	Actual location (mm)	Error (%)
FEA results									
1	215.5	262.5	350.0	398.0	108	208	158	150	6 %
2	225.0	273.5	329.0	376.0	141	242	192	200	4 %
3	253.5	300.5	350.0	389.0	158	248	203	240	15 %
Experiment results									
1	212.4	271.7	337.0	371.8	133	231	182	200	9 %
2	220.6	264.6	310.0	352.6	161	252	207	250	17 %

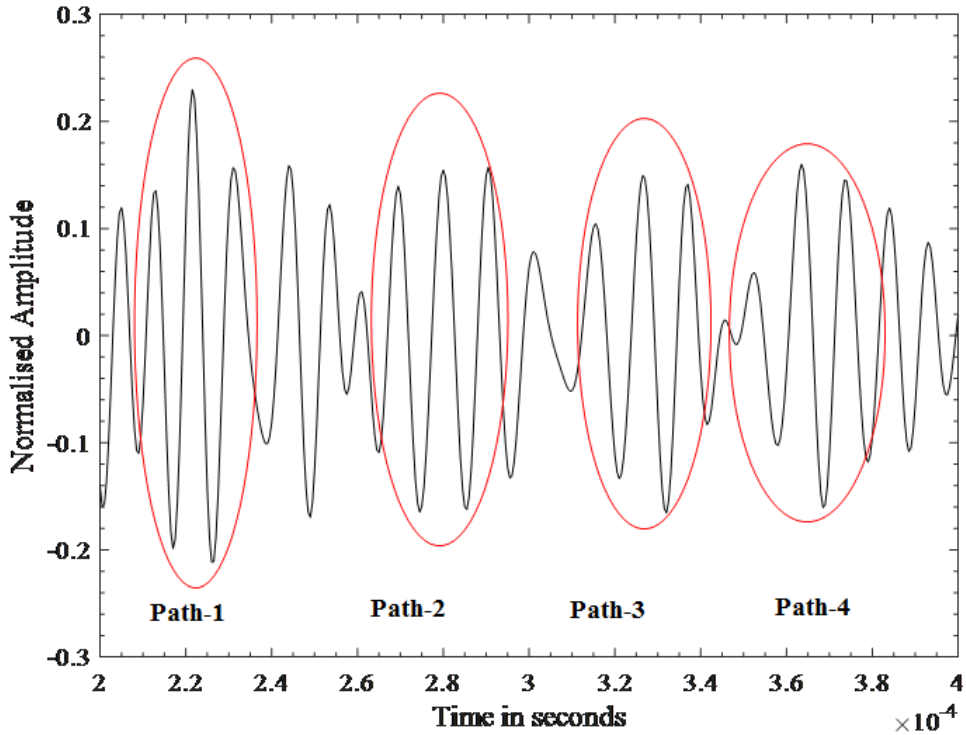

(a)

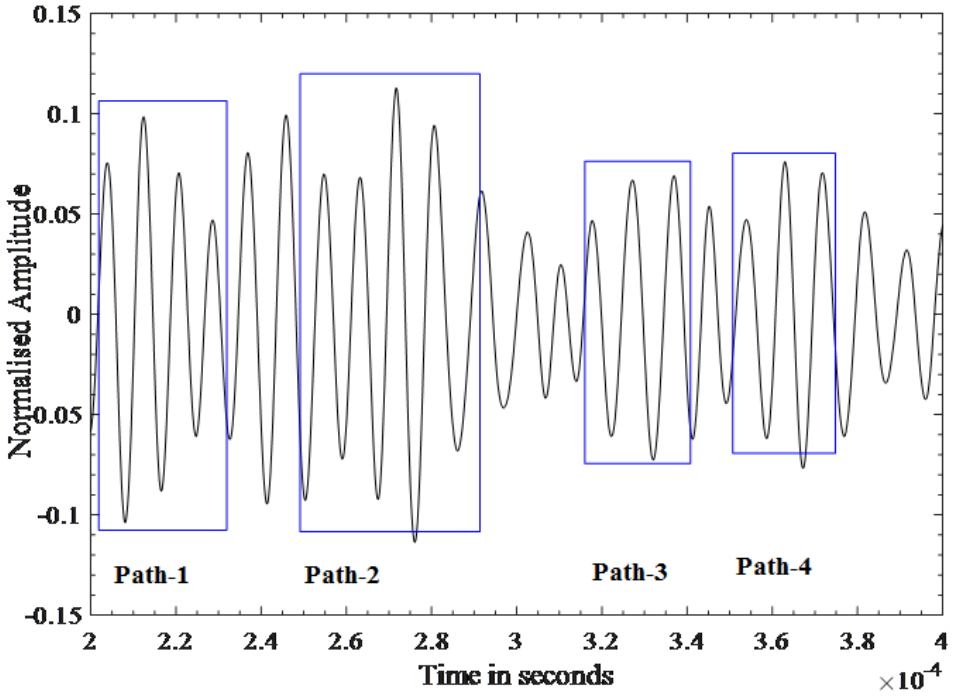

(b)

Figure 5.16: Scattered wave modes, with paths identified, for a damage located at 200 mm from actuator end from (a) FEA and (b) experiment.

5.5 Evaluation of corrosion by using the energy of scattered wave modes

From the previous studies, it is observed that intensity of damage has a direct correlation with the energy of the scattered wave modes. In this section, the factors that affect the scattered energy are studied. A non-dimensional parameter, scatter coefficient (S_{coeff}), is defined as the ratio of the energy of the scattered wave modes of a specimen to the energy of the direct transmitted wave. The total energy of all the wave modes that occur before the arrival of the boundary reflected signal is considered to define this parameter.

$$S_{coeff} = \sqrt{\frac{\int_0^{3T}(S-B)^2 dt}{\int_0^{3T}(B)^2 dt}} \tag{5.2}$$

where Time arrival, V is the group velocity; L is the length of the rebar; S is the signal from the specimen with damage; and B is the baseline signal. The scatter coefficient of corroded rebars with a fixed axial extent and intensity is calculated for various locations of damage. The damage that is closer to the sensor results in a higher scatter than that of a damage that is away from the sensor. This observation concurs with the findings that the reflection coefficients diminish with the increase in the distance between the sensor and the damage [40]. Figure 5.17 shows the variation of scatter coefficients with the location in the various axial extents of corrosion, with diameter reduction to 16 mm. From this localisation plot, it can be predicted that the increment in the axial extent of corrosion is likely to cause an increase in the scatter coefficient. In order to define a corrosion damage intuitively, it is essential to quantify it in terms of mass loss. The percentage of mass loss is defined as the weight of material loss due to corrosion in a rebar with respect the initial weight of the rebar. Mass loss in the current case is achieved by reducing the diameter of the rebar for a given axial extent of corrosion. It is observed that scatter coefficient increases with the loss of mass, as shown in Figure 5.18, which depicts the variation of the scatter coefficient against the mass loss in a rebar that has a 100 mm-long pitting corrosion. It is understood that the scatter coefficient is affected by the change in the location, axial extent and intensity of corrosion. Therefore, the axial extents of corrosion can be estimated by using the differential ToF of various scattered wave modes, while the

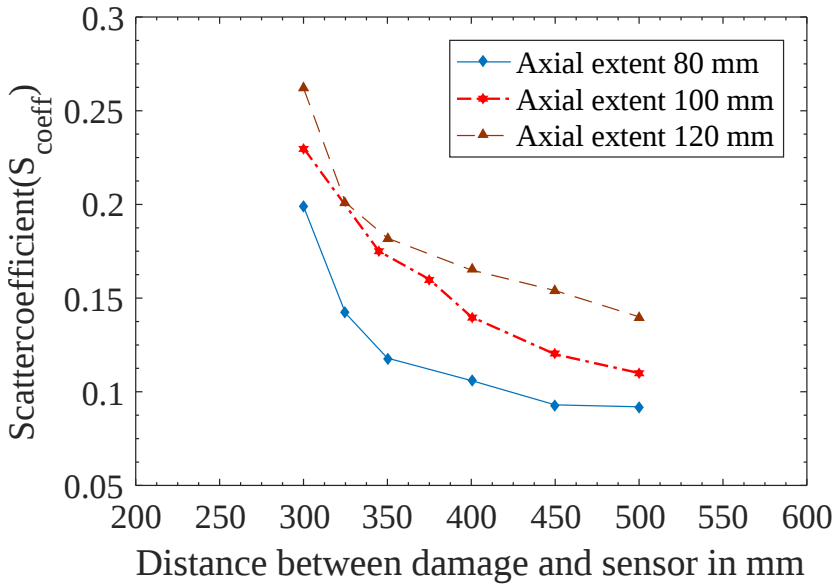

Figure 5.17: Localisation plot showing the relationship between the location of the damage and the scatter coefficient.

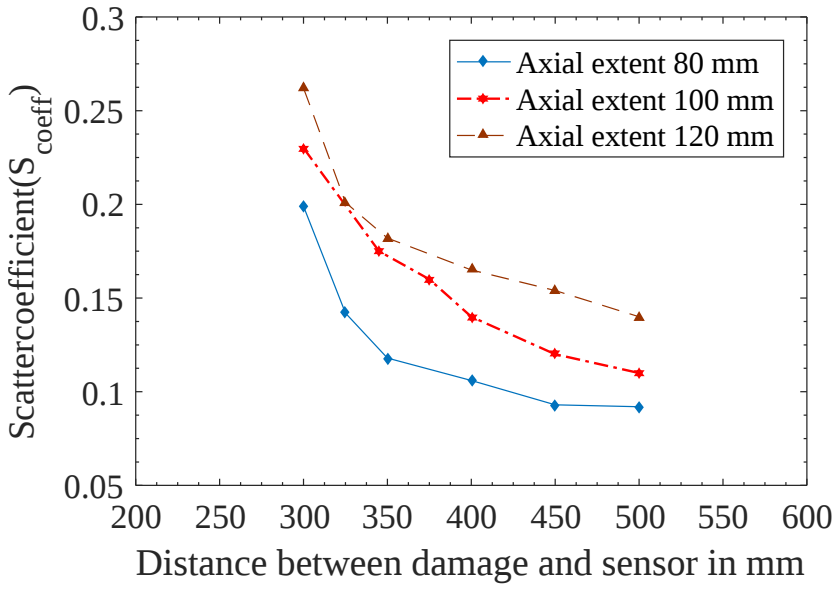

Figure 5.18: Mass loss plot showing the relationship between mass loss and scatter coefficient for axial extent 100 mm.

empirical plots for localisation and mass loss, which are presented in this section, can be used to estimate location and intensity of an arbitrary damage.

5.6 Suitability of guided waves for real-life corrosion detection in rebars

In the above section, GW signals include the damage reflected wave packets that can be used to identify, locate and quantify the defects. In real-life, corroded rebars do not have the sharp vertical edges at the corrosion location. In this section, the applicability of previously defined damage indices is examined. The rebar samples 20R1 and 12R1 are tested with CTs. The signals from intact specimen show that the dominant mode is $L(0,\ 1)$. The rebars are corroded as per the procedure outlined in section 4.4.1. The response signal is collected at a regular interval and compared with the baseline signal. It is observed that the amplitude and group velocity of $L(0,\ 1)$ mode vary with the corrosion. The GW signals do not show any discrete wave packets. PWT sensors are then used to detect real-life corrosion in rebar samples 20R2 and 12R2. The initial response of the rebar 20R2 without any corrosion is considered as a baseline signal and is shown in Figure 5.19. The signals with various levels of corrosion are compared using this baseline signal. After the cross talk at the beginning, the baseline signal shows two modes of GWs, that is $L(0,\ 1)$ and $F(1,\ 1)$ with the group velocity of 4473 m/s and 3014 m/s, respectively. The boundary reflected signals of these two modes can also be recognised in the received

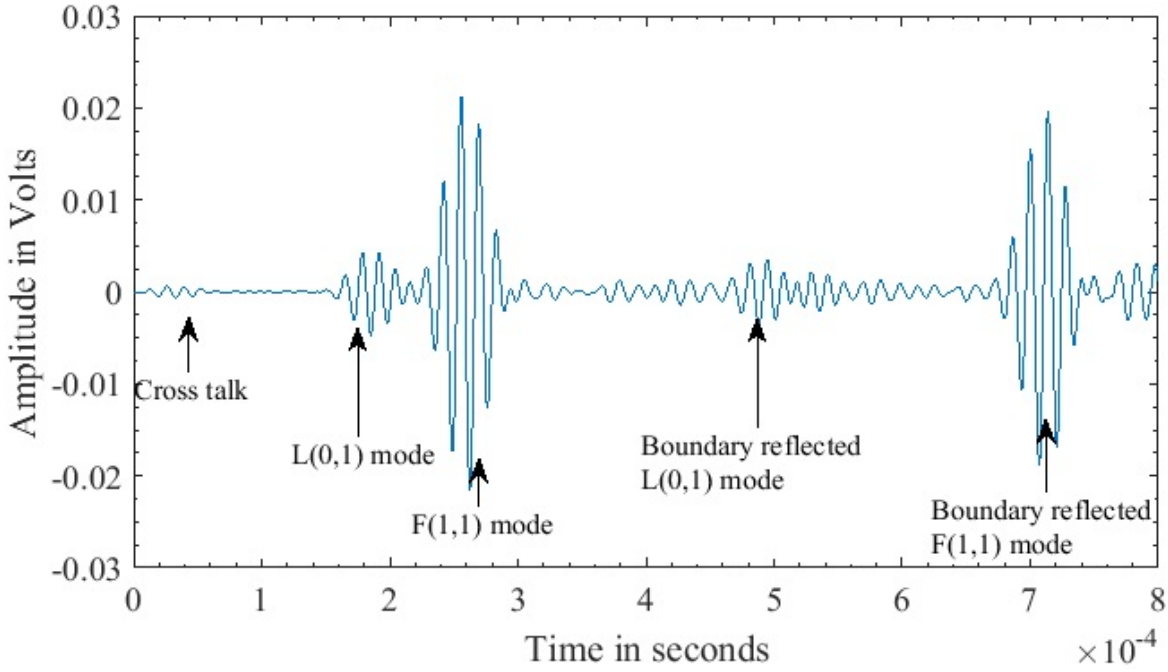

Figure 5.19: Baseline signal of rebar sample 20R2.

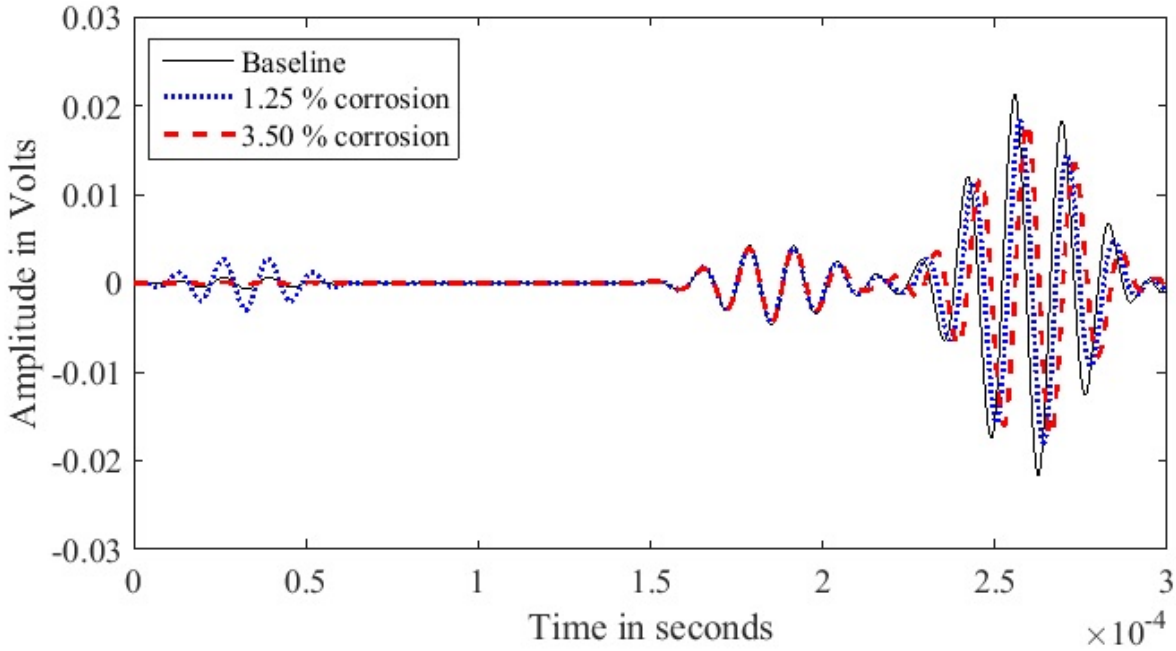

Figure 5.20: Figure 4 Comparison of GW response of the rebars with different levels of corrosion (Sample 20R2).

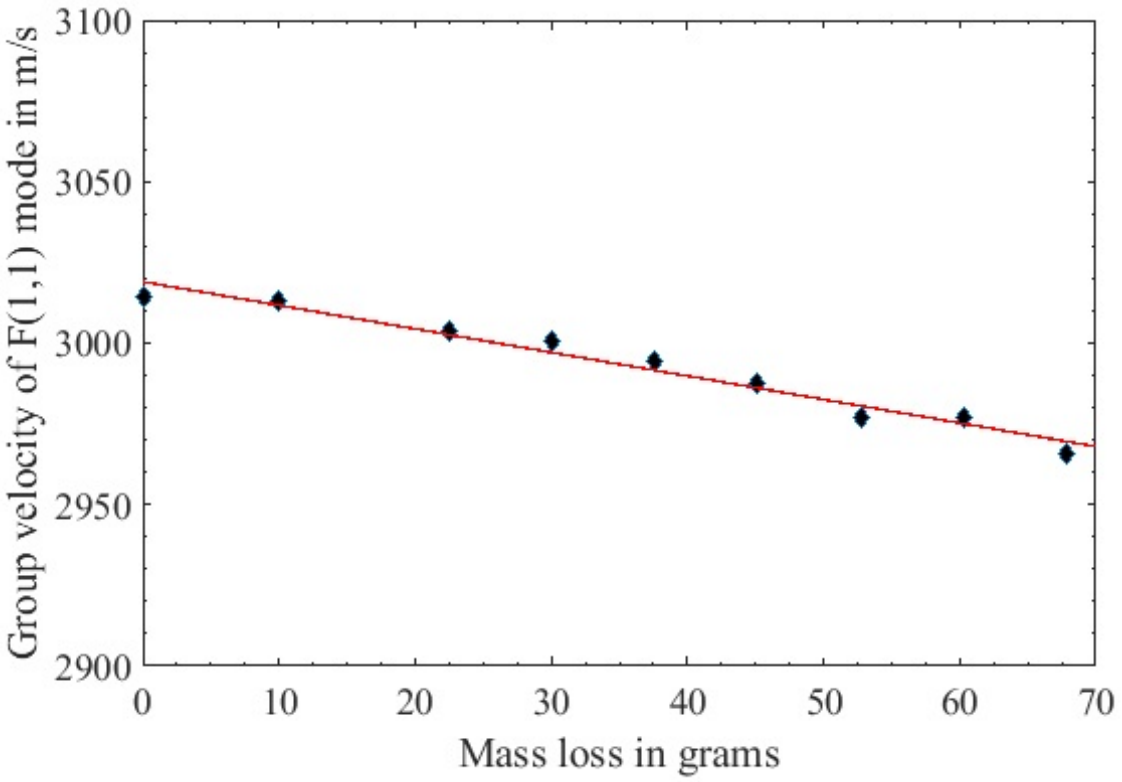

Figure 5.21: Variation of group velocity of $F(1,\ 1)$ with mass loss (Sample 20R2).

signal.

During the process of corrosion as elaborated above, the mass of steel is lost; thus, the

effective diameter of the bar decreases. Figure 5.20 shows the comparison of signals for rebar with various levels of corrosion. It can be observed that the corrosion of rebar has very less effect on the $L(0,\ 1)$ mode compared to $F(1,\ 1)$ mode. The change in amplitude and TOF of $L(0,\ 1)$ mode is very less. In contrast, the $F(1,\ 1)$ mode is observed to be very sensitive to the corrosion damage. Corrosion of the steel bar has caused a decrease in the group velocity 5.21 and also decrease in the peak amplitude of the $F(1,\ 1)$ mode.

5.7 Concluding remarks

In this chapter, the behaviour of GWs in corroded rebars is investigated. Pitting corrosion of bare rebars is examined in the current study by using longitudinal GWs. The response of various corroded bars is studied in order to discern the changes in signal due to corrosion. It is observed that a direct transmitted signal is not affected much by pitting corrosion; hence, it could not be used to identify damage, which, however, can be highlighted by various damage-scattered wave modes. For damage that is located equidistant from the actuator and the sensor, scattered wave modes are superimposed and two distinct wave packets can be observed. A damage index method is thus developed using these two wave packets for assessment. In order to identify arbitrary pitting corrosion that is located away from the centre, a method is developed by utilising the energy and the time of arrival of scattered wave modes. The arrival time of dominant scattered wave modes is utilised to trace the front and rear edges of the damage. The factors that affect the scattered energy in a corroded rebar are explored by defining a scatter coefficient. It is found that the scatter coefficient gradually increases with the mass loss, and the increment is pronounced when the pitting corrosion is closer to the receiver location. The scatter coefficient when used in conjunction with the localisation method is found to be promising in the assessment of pitting corrosion in rebars. The current progress in wave propagation mechanism and damage index methods would further help in evaluating the corrosion status of the embedded rebars in concrete.

Experiments are then performed to achieve real-life corrosion accelerated by impressed current. GW signals that are generated and sensed by CTs and PWTs are used to analyse corrosion. In contrast to the signals of artificial corrosion case, in which the sharp edges have resulted in distinct wave packets due to scattering, the signals of real-life corrosion

samples do not contain these distinct wave packets. In the real-life corrosion case, the changes in the amplitude and group velocity of the GW mode show considerable change with the damage. A small mass loss of 0.4 percent causes 1.14 percent change in the change in group velocity of $F(1,\ 1)$. The clear diminishing trend in the amplitude and group velocity observed for this slight change corrosion levels is promising to apply GW for corrosion detection in complex case of damages in RC structures.The GWs excited by CTs generate the predominant $L(0,\ 1)$ mode. The amplitude and group velocity of $L(0,\ 1)$ mode decrease with the increase in the corrosion level. Actuating the rebar with PWTs generates both $L(0,\ 1)$ and $F(1,\ 1)$ modes among which the $F(1,\ 1)$ mode is dominant. The changes in amplitude and group velocity of the $F(1,\ 1)$ mode are suitable to detect corrosion.

Chapter 6

Sensitivity of longitudinal guided wave modes to pitting corrosion of rebars

6.1 Introduction

In the previous chapter it is demonstrated that GWs are useful in identification and quantification of pitting corrosion in bare rebars. Corrosion in bare rebars was efficiently located and estimated using longitudinal GWs, with the help of DI method. In this chapter, longitudinal mode is used to study corrosion in embedded rebars. This mode is generated and sensed by deploying CTs.

GWs are sensitive to the changes in the properties of materials, the geometry and the interface conditions, and can be used to detect debonding, corrosion and cracks in concrete [Gaul *et al.*, 2012]. The generating and the sensing of dominant longitudinal GW modes can be achieved using CTs. Feature extraction and analysis are simplified when CTs are used because the flexural modes are not present in the signal. Studies show that CTs can be used to detect the corrosion and debonding of rebars. The amplitude of the GWs decreases with the increase in the corrosion level and increases with an increase in the level of debonding damage [Na *et al.*, 2003; Miller *et al.*, 2002]. The study of accelerated corrosion in rebars has been the focus of research in recent years [Miller *et al.*, 2013; Sharma *et al.*, 2018; Talakokula *et al.*, 2014]. Sharma and Mukherjee, 2013 have named the $L(0,\ 1)$ mode that is generated at 100 kHz the surface seeking mode, and the $L(0,\ 7)$ mode that is generated at 1 MHz the core seeking mode. These two modes have shown preferential interaction with a specific type of damage each; hence, these modes were expected to decipher the corrosion status. Amplitude values can be influenced by a

sensor and by the structure bonding. To overcome this issue, a few researchers have used the change in the time of flight as an indicator of damage. These values were measured on beams with and without loading have been correlated to assess corrosion damage [Miller *et al.*, 2013]. This study is motivated by the need to develop an effective pitting corrosion identification strategy using longitudinal GWs that are generated and captured by CTs.

Studies have revealed that the corrosion process results in an increase in the bond, debonding and diameter reduction, and their effect on wave characteristics was found to be complementary to each other [Ervin and Reis, 2008]. Numerical simulations are performed to indicate that presence of both damage during corrosion process may lead to a concealed damage state. This effect is termed zero-effect state. The effect of pitting corrosion on the wave modes is experimentally assimilated and corrosion is accelerated using an impressed-current-based technique. Unlike previous investigations, the theoretical model that is used in the calculation of dispersion curves considers the finite dimensions of RC. These GW modes are then verified with full-scale three dimensional finite element analysis model. Numerical simulations are deployed to confirm the state of the rebar, including the loss of diameter and weakening of the bond. The influence of longitudinal wave modes on various phases of pitting corrosion is examined in detail. For this purpose, a non-dimensional coefficient that is termed relative amplitude (RA) is designed for comparison of the peak amplitudes of the wave modes that are extracted from the wavelet analysis. The changes in the RA and the group velocity of a longitudinal wave mode are used to propose a pitting corrosion identification strategy.

6.2 Numerical results

The individual effects of deterioration in RC structures in the form of loss of rebar mass and loss of bonding are well studied in the literature. However, the combined effect of these damages is not established. In this section, numerical simulations are used to calculate the change in guided wave features due to loss in the rebar mass and loss of bonding between steel and concrete and the concealed damage state arising out of their simultaneous presence is illustrated. To this effect,a co-simulation model of RC beam and piezoelectric sensors is developed in commercial finite element software, Abaqus/CAE. The modes arising from guided wave propagation are recognised as L(0,1) and F(1,1).

The characteristics of L(0,1) mode are studied in detail as it is the fastest mode.

6.2.1 Corrosion of rebars in concrete

Corrosion causes decrease in the mass, alters the dimensions of the intact rebar and results in the formation of rust. In the numerical simulations, the gap leftover by changes in the intact rebar dimensions is filled by rust. The contact between the rust that is formed during corrosion and the intact rebar is achieved by tying them. The properties of concrete, rebar and rust are mentioned in 4.4. The effect of a typical corrosion damage on guided wave signals is shown in Figure 6.1a by comparing the signal from undamaged specimen and a corroded specimen. The energy envelops of these signals are shown in Figure 6.1b. The guided wave amplitude of the corroded sample is less than that of the undamaged one. The increase in the mass loss can be either due to localised decrease in the rebar diameter or due to increase in the axial extent. In order to analyse the changes in amplitude due to corrosion, parametric studies are carried out by creating damage at the centre of the rebar in two different ways, first, by increasing the axial extents of corrosion and second, by reducing the diameter of the rebar. In the first case, the reduction in diameter is kept unchanged at 16 mm while the length of corrosion is varied from 100 mm to 400 mm. In the second case, the length of corroded rebar is maintained constant at 200 mm while the diameter is reduced from 20 mm to 16 mm. The influence of corrosion on the wave amplitudes of the $L(0,\ 1)$ mode is studied by plotting the peak amplitude. The changes in peak amplitude for first case of corrosion are shown in Figure 6.2a and the corresponding changes for second case are depicted in Figure 6.2b. Both the ways of corrosion show a decrease the amplitudes of $L(0,\ 1)$ mode with the increase in the corrosion level. Also, the speed of the wave is observed to be lower than that of an undamaged rebar. More energy is leaked into the surroundings as the bar gets corroded thus the observed energy is considerably lower than that of an intact specimen. The results of parametric study show a quadratic decreasing trend in the wave amplitude of the guided wave mode.

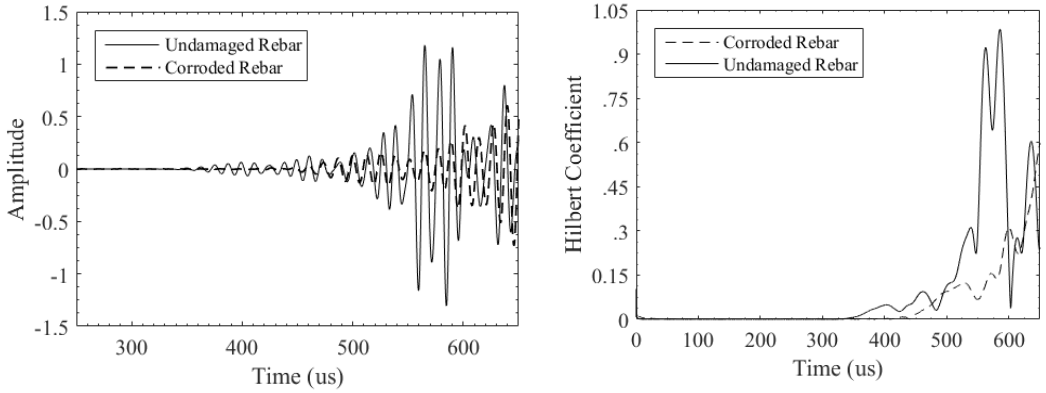

(a) (b)

Figure 6.1: Comparison of (a) signals and (b) energy envelopes of an undamaged specimen and a corroded specimen.

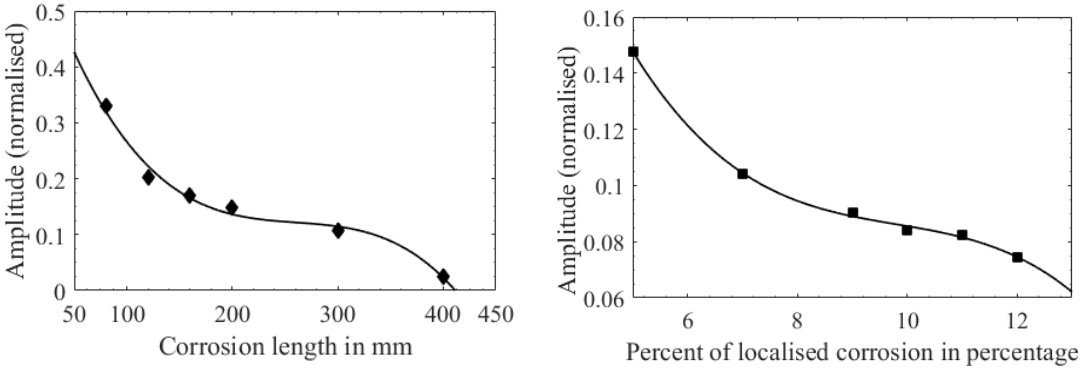

(a) (b)

Figure 6.2: Variation of amplitude of $L(0,\ 1)$ mode with (a) corrosion along the length and (b) mass loss in pitting type of corrosion in the rebar.

6.2.2 Debonding of rebars and steel

Debonding is simulated by untying the rebar and the concrete at the interface. The variations in the wave amplitude and the group velocity with the debond length are plotted in Figure 6.3a and Figure 6.3b . It is observed that the amplitude of the received signal increases exponentially with the increase in the debond length (Figure 6.3a). This can be attributed to the fact that with an increase in the debond length, the loss of energy to the surrounding concrete medium is less, and the wave energy is more focused in the rebar. The observed exponential trend in the parametric study conforms to the study by Wu *et al.*, 2015. For the debonded specimen, the group velocity of the $L(0,\ 1)$ mode is faster than that of an undamaged specimen. Also, as shown in Figure 6.3b , the wave velocity rises with the increase in the debond length and finally attains the wave speed

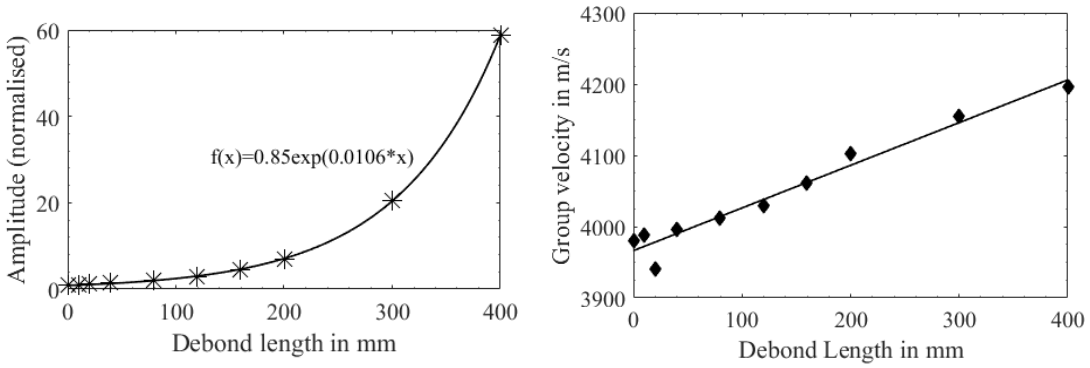

(a) (b)

Figure 6.3: Variation of (a)amplitude and (b) group velocity of $L(0,\ 1)$ mode with increase in debond between steel and concrete.

in a bare rebar.

6.2.3 Zero effect state in corroded reinforced concrete structures

In a typical RC structure, the damages of debonding and corrosion occur simultaneously. A rebar that is subjected to prolonged corrosion will develop rust. As this rust separates from the host rebar, it leads to debonding. From the discussion in the preceding sections, it is observed that these two kinds of damages have complementary effects on wave characteristics. Hence, it is an impending task to study these two damages together. An undamaged concrete beam, which is subjected to the corrosive environment, is considered in the study. With the onset of corrosion, the diameter of the intact rebar reduces gradually, and rust develops along the perimeter of the rebar. As the volume of the corrosion product becomes bulkier, it leads to the scaling of rust, resulting in separation between the layers of the intact rebar and rust, which can be termed as debonding. Based on this premise, the $L(0,\ 1)$ mode was chosen and numerical investigations were carried out for various cases of damage to find the zero effect state.

Curve "0" in Figure 6.4 shows the energy envelope of response that was obtained in an undamaged rebar. Corrosion damage that is 80 mm wide is simulated at the center of the rebar. It is observed from curve "1" that the amplitude and the velocity of the signal are reduced with the corrosion of the rebar. On the other hand, from curve "2" a sudden jump in amplitude and velocity is observed when a debond is initiated between the rebar

and the concrete. As the rebar is allowed to corrode further (Curves 3, 4 and 5) along with a uniform reduction in the diameter, the amplitude of the signal gradually approaches to that of the undamaged specimen. An important inference can be drawn from Figure 6.4; with the onset of debonding in the rebar that is subjected to corrosion, due to the separation of the rust, a sudden rise in amplitude and velocity of $L(0,\ 1)$ mode can be observed. As the corrosion progresses from this stage, the wave characteristics gradually approach that of an undamaged stage. In fact, such a zero state effect is independent of the initial damage. A similar phenomenon in which, a damaged rebar that shows wave characteristics that are equivalent to an undamaged rebar can, therefore, be expected from a rebar that has initial debond and is subjected to corrosion at a later stage.

The study is repeated with different lengths of damage and it is found that the zero-effect state can be located for damage of any size. The possibility of a zero-effect state for varying damage sizes makes it impossible to identify an abrupt change in the wave characteristics due to the onset of debonding or corrosion. Further study is required to ascertain the observed phenomenon experimentally and to establish methods to identify and distinguish the damages.

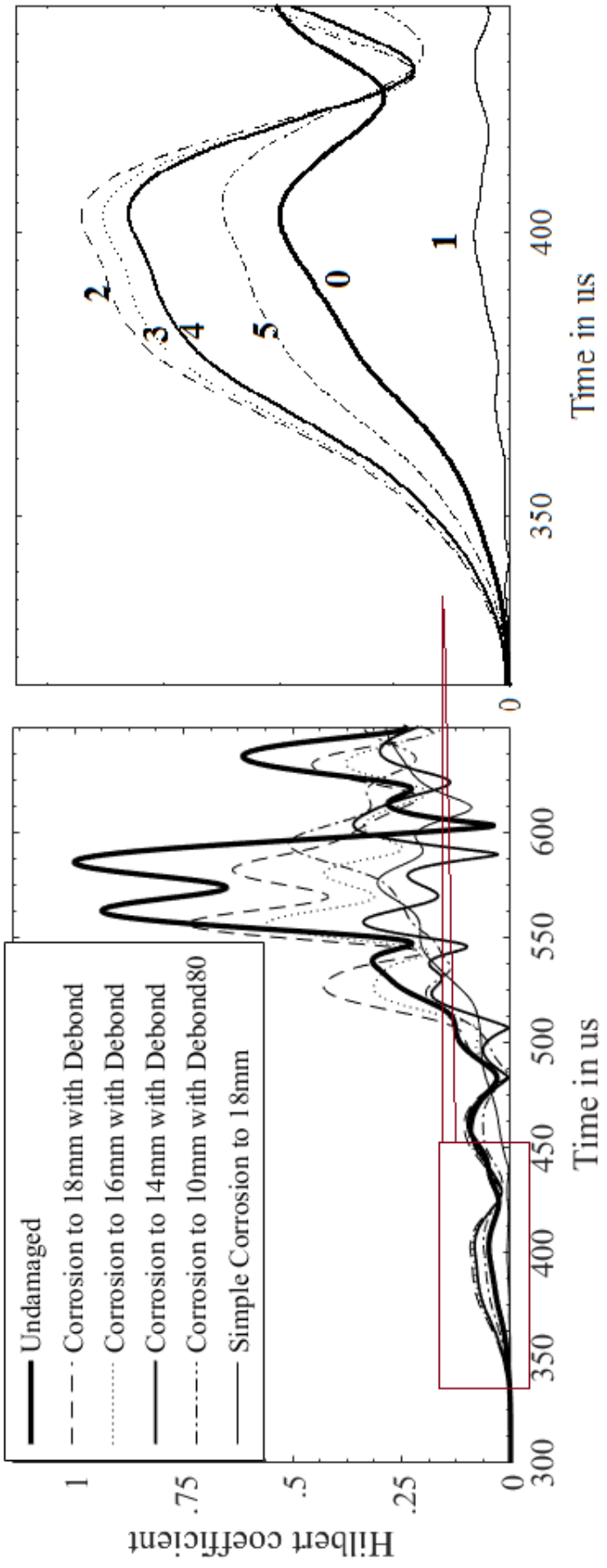

Figure 6.4: Comparison of energy envelops for various damage scenarios, in order to identify the zero state effect for damage that is located at the centre of the rebar.

6.3 Theoretical modelling

The solution to the governing equation of wave propagation in a cylindrical wave guide has also been studied extensively in the literature. The solutions of the equation result in a set of transcendental equations, and the roots of this set of equations result in various modes of wave propagation. Curves depicting variation in the characteristics of the wave, such as energy velocity, phase velocity and attenuation with frequency, are known as dispersion curves. Various researchers have developed software packages to calculate the dispersion curves for plates and cylinders that are in vacuum or embedded in a medium. The calculation of dispersion curves for an RC beam is complex because the rebar and beam are of different geometric shapes. Previous studies have used the approximation of bare rebar or rebars embedded in an infinite concrete medium to estimate the dispersion behaviour of embedded rebars Na *et al.* [2003]; Sharma and Mukherjee [2010]. However, the dimension of the concrete in an RC beam is finite in practice; hence, the approximations above may lead to erroneous results.

In the current study, an approximation is made to reduce the cuboidal concrete geometry to a cylindrical one, with an effective radius, Re, surrounding the rebars with radius, Rr. The value of Re is the smallest width and depth of the concrete. In the current case, the width is 100 mm, hence, the radius, Re, is maintained as 50 mm in calculations. The material properties of the concrete and steel, which are listed in Table 4.4, are used in dispersion curve calculations. The multi-layered waveguide approximation that is shown in Figure 6.5 is used to generate the dispersion curves. The group velocity dispersion curves are calculated using PCdisp, a MATLAB package [Seco and Jiménez, 2012].

6.3.1 Baseline validation

The specification of a baseline model is necessary for a non-destructive evaluation of structural members. An RC beam without any damage is chosen as the baseline experimental model. In numerical simulations, the baseline model is an RC beam with complete bonding and without any change in the diameter of the rebar. The number of wave modes generated due to dispersion is found to be the same, and the arrival times are close to each other in experiments and in numerical simulations, as shown in Figure 6.6(a). In the theoretical modelling, an approximate model of the concrete beam is used to calculate

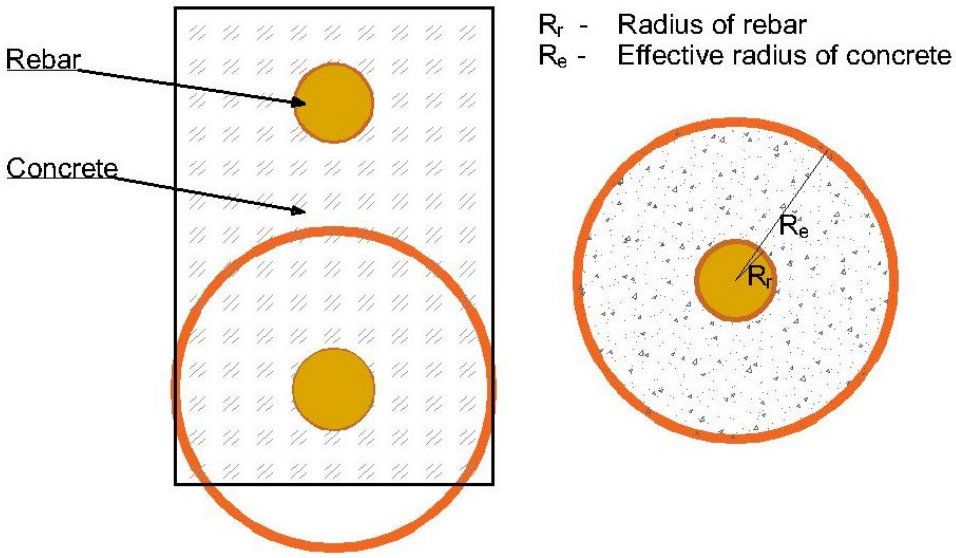

Figure 6.5: Approximation of RC beam made for the purpose of dispersion curve generation and verification

dispersion curves. The validity of this model is checked by a numerical model of the beam, which has an effective radius. The FEA model is shown in Figure 6.6(c), and the time history of the longitudinal displacement (Uz) of this model is compared with that of the full-scale model (Figure 6.6(b)). The results show that the approximation is valid, because the time histories of displacement from both the models are in close agreement.

6.4 Results and discussion

6.4.1 Dispersion curves

The theoretical and numerical models are used to study the effect of various parameters on the dispersion behaviour of GWs in RC beams. It is found that the thickness of concrete plays an important role in the dispersion of GWs. The addition of concrete layer over the rebar in the numerical model results in the attenuation of the energy that flows through the rebars and a reduction in the group velocities. It is also found that the addition of a concrete layer contributes to the increased dispersion, and several wave modes appear even at frequencies lower than 100 kHz.

Figure 6.7 shows GW signals that were collected from experiments on the RC beam that comprised a rebar of a diameter of 12 mm, excited by input pulses with central

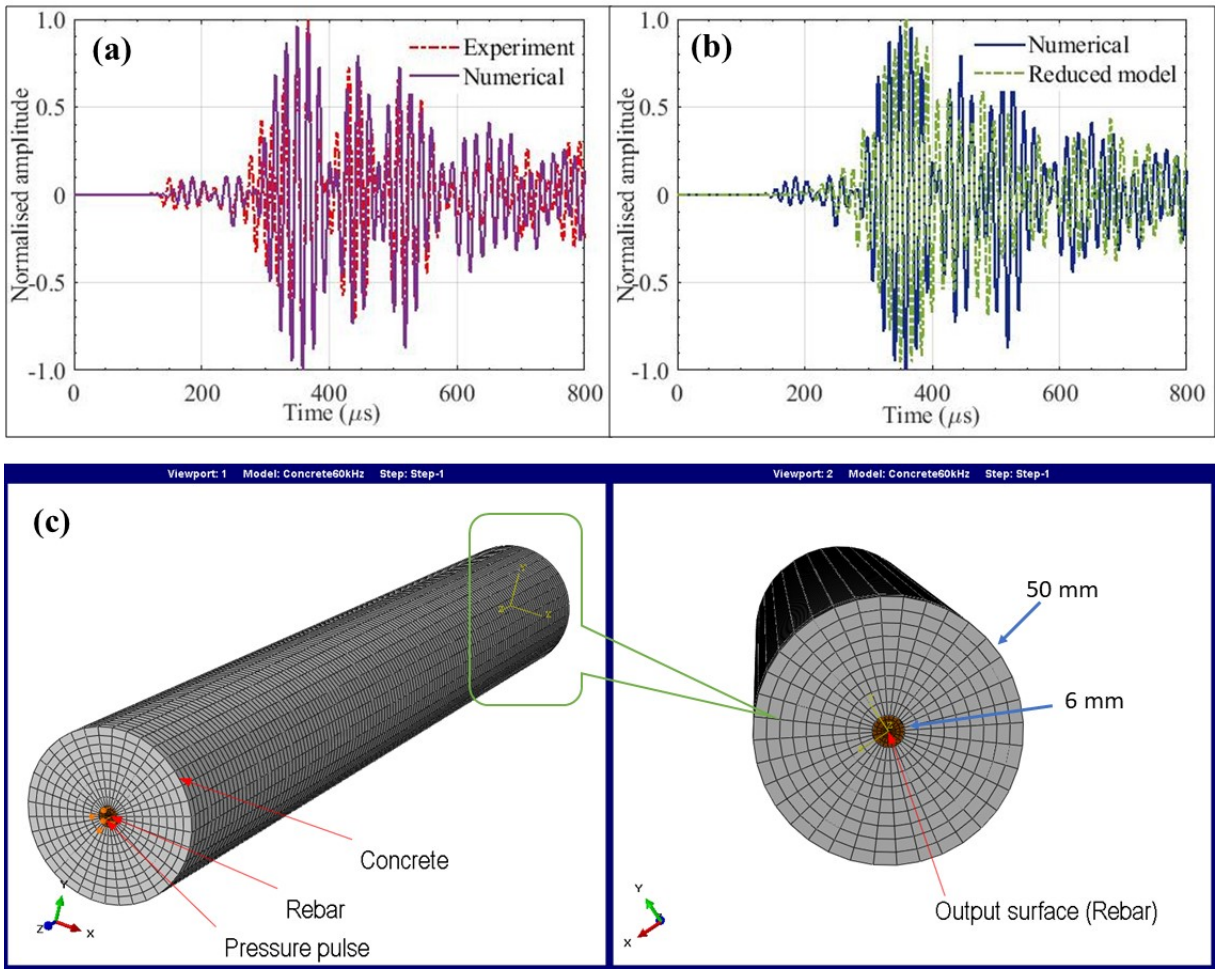

Figure 6.6: Comparison of baseline signals from, (a) experimental and numerical models, (b) numerical and reduced numerical models, and (c) numerical model generated in Abaqus for reduced numerical simulations.

frequencies of 50 kHz, 60 kHz and 75 kHz. These signals are analysed to understand the effect of excitation frequency on the response of the specimens. It is found that the number of modes increases with the increase in the excitation frequency. The dispersion curves for rebars with diameters of 12 mm and 10 mm embedded in the concrete of an effective radius of 50 mm are shown in Figures 6.8(a) and 6.8(b), respectively. These figures illustrate the dispersion behaviour as the number of possible wave modes and their corresponding energy velocity changes with the change in frequency. Dispersion curves for 12 mm embedded rebar show that three wave modes, $L(0,\ 1)$, $L(0,\ 2)$ and $L(0,\ 3)$ exist for 50 kHz excitation. Altering the excitation frequency to 60 kHz changes the number of possible modes to four longitudinal modes, which are $L(0,\ 1)$, $L(0,\ 2)$, $L(0,\ 3)$ and $L(0,\ 4)$. Further examination of the dispersion curves shows that shifting the excitation frequency to 75 kHz increases the number of possible modes to five which are $L(0,\ 1)$,

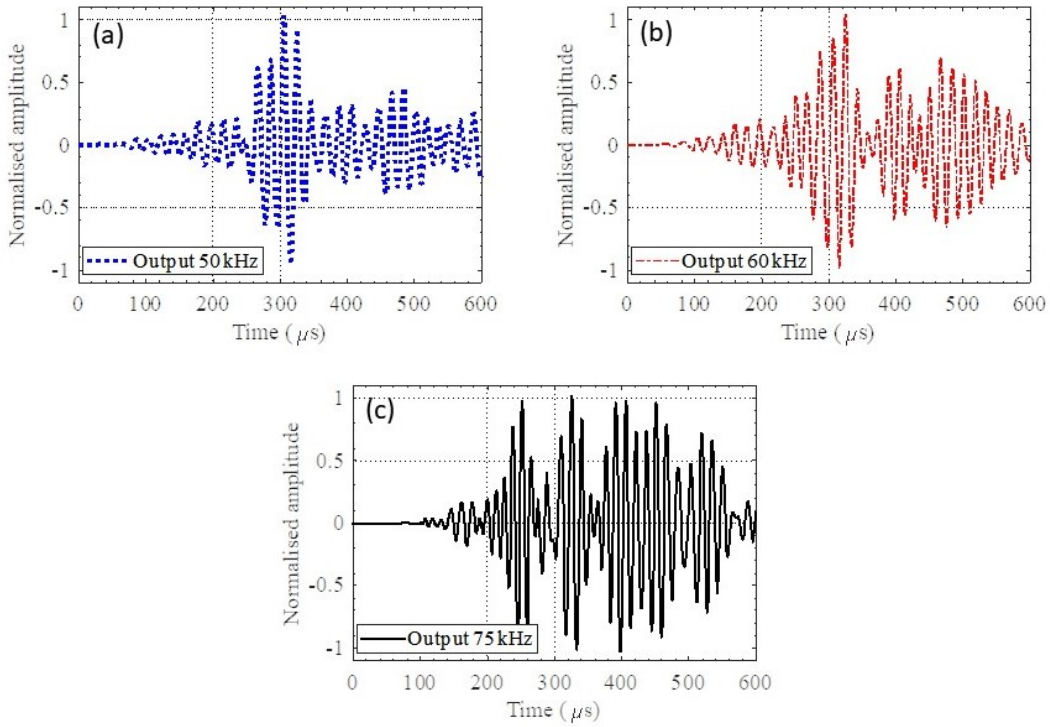

Figure 6.7: GW signals at various frequencies (50 kHz, 60 kHz and 75 kHz) showing the dispersion behaviour in RC beam

$L(0,\ 2)$, $L(0,\ 3)$, $L(0,\ 4)$ and $L(0,\ 5)$. The results of numerical simulations in Figure 6.7 illustrate the dispersion behaviour. It can be observed that the number of wave packets and arrival time of the wave packets change with the excitation frequency. It is observed that the reduction in the diameter of a 12 mm rebar to a 10 mm one affects the energy flow and causes a change in the group velocity. For example, the group velocity of the $L(0,\ 2)$ mode at 60 kHz changes from 2830 m/s to 2660 m/s with the change in diameter from 12 mm to 10 mm. Such variations at the time of flight or group velocity may be used to identify corrosion.

In the current model, the dominant mode of excitation and sensing is longitudinal. The received signal is carefully studied to recognise the modes of wave propagation, which are longitudinal. In the experimental baseline signal, four distinct wave packets are observed, which are identified as various wave modes that are based on their group velocities (Figure 6.9). The first (fastest) mode arrives at 220 μs, and it is recognised as the $L(0,\ 2)$ mode, the second mode is $L(0,\ 3)$ with an arrival time of 350 μs, the third mode is $L(0,\ 1)$ with an arrival time of 450 μs and the fourth (slowest) mode is $L(0,\ 4)$ with an arrival time of 550 μs.

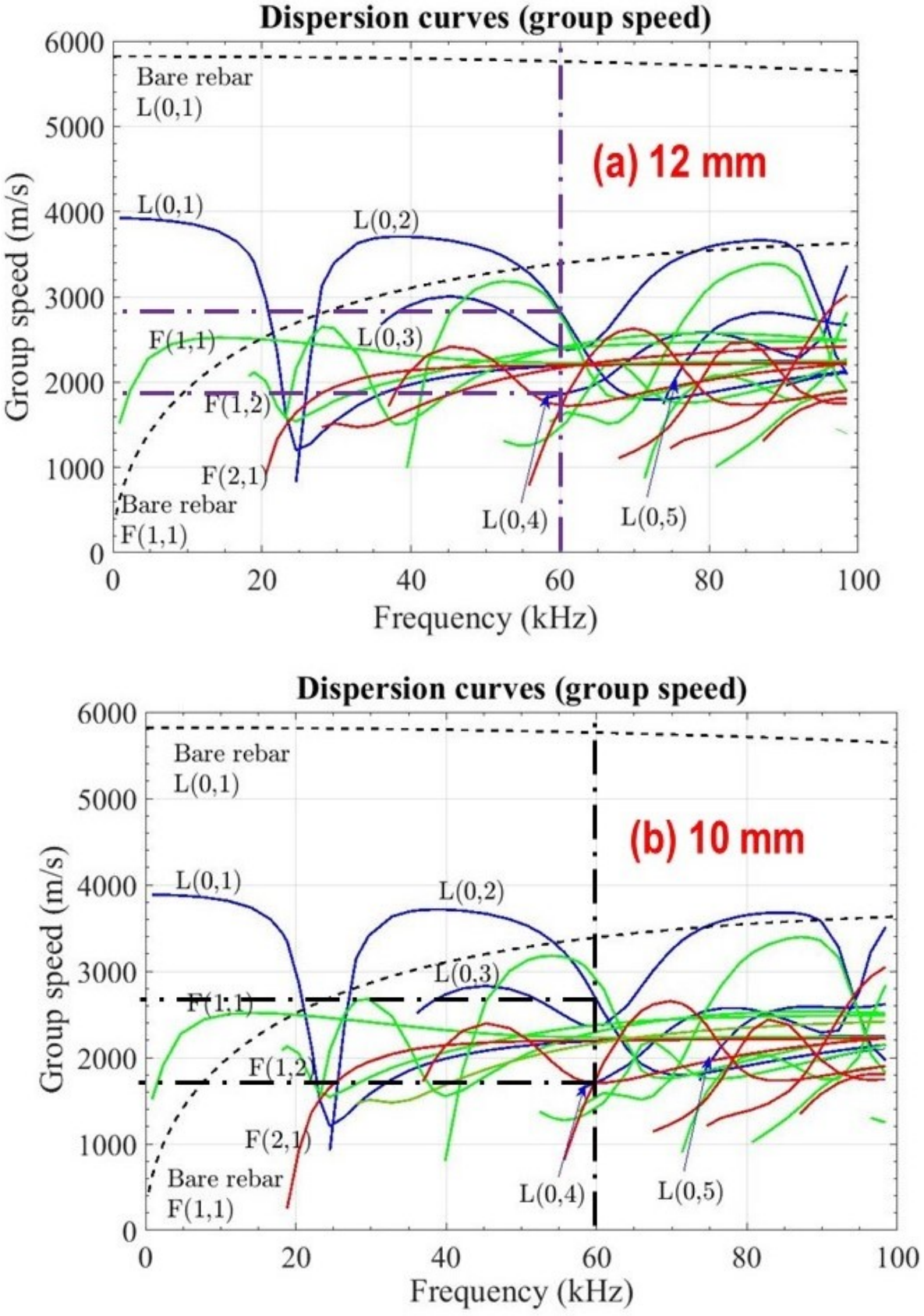

Figure 6.8: Group velocity dispersion curves of (a) a 12 mm diameter bar, and (b) a 10 mm diameter rebar embedded in concrete.

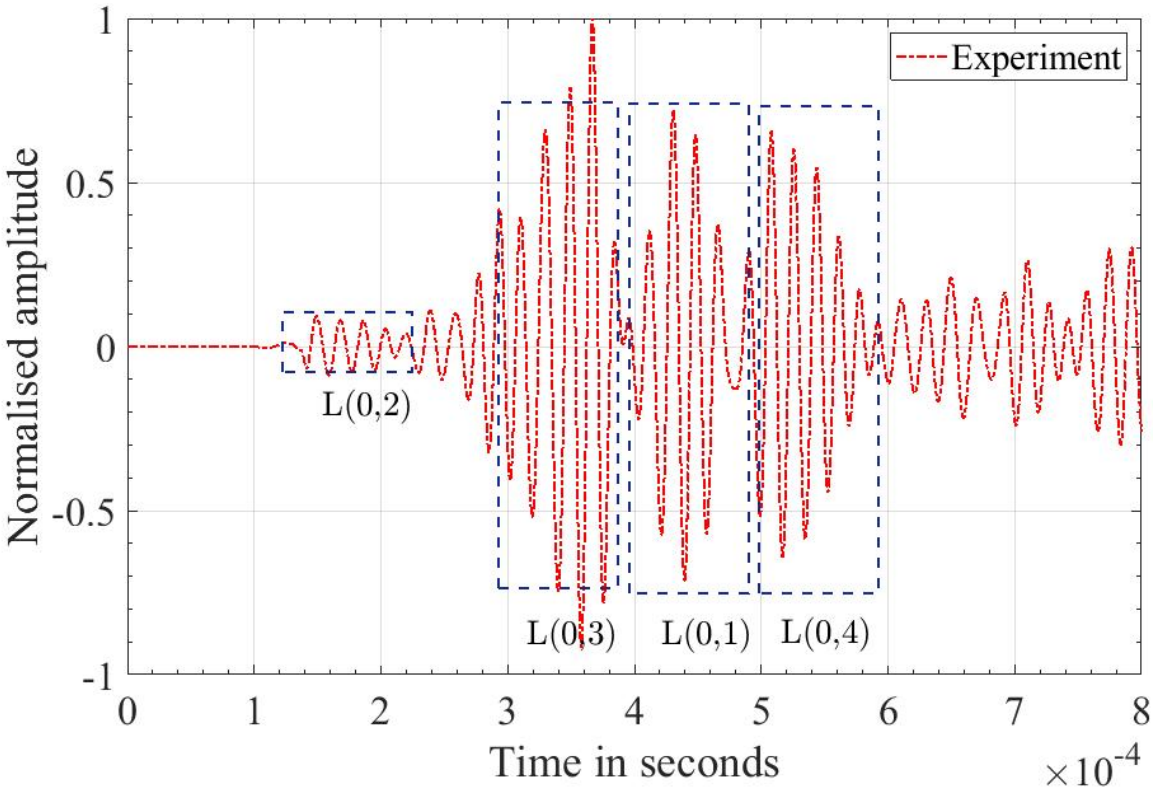

Figure 6.9: Wave modes in the experimental baseline signal with input frequency of 60 kHz.

The numerical displacements of the RC beam in the longitudinal direction (U_z) at a distance of 100 mm from the sensor are analysed. The theoretical mode shapes and normalised displacements, U_z, are plotted in Figure 6.10 as the function of distance from the centre of the rebar. The numerical displacements show good correlation with the theoretical mode shapes. This result confirms that the wave packets that are observed are different wave modes and not internal reflections. The GW modes, $L(0,\ 1)$ and $L(0,\ 2)$, show that they have less energy in the core of the rebar. The $L(0,\ 2)$ mode has a slight peak in the interface region. Therefore, it is predicted $L(0,\ 2)$ mode will be sensitive to corrosion initiation and debonding. In the $L(0,\ 3)$ mode, more energy is concentrated in the core of the rebar as well as in the interface region of the rebar and the concrete. Hence, $L(0,\ 3)$ mode is expected to show a pronounced variation in all three phases of corrosion. In the $L(0,\ 4)$ mode, the energy is concentrated in the core of the rebar, and the energy decreases as the interface region approaches. Therefore, this mode is expected to show dominant change when there are changes in the core of the rebar.

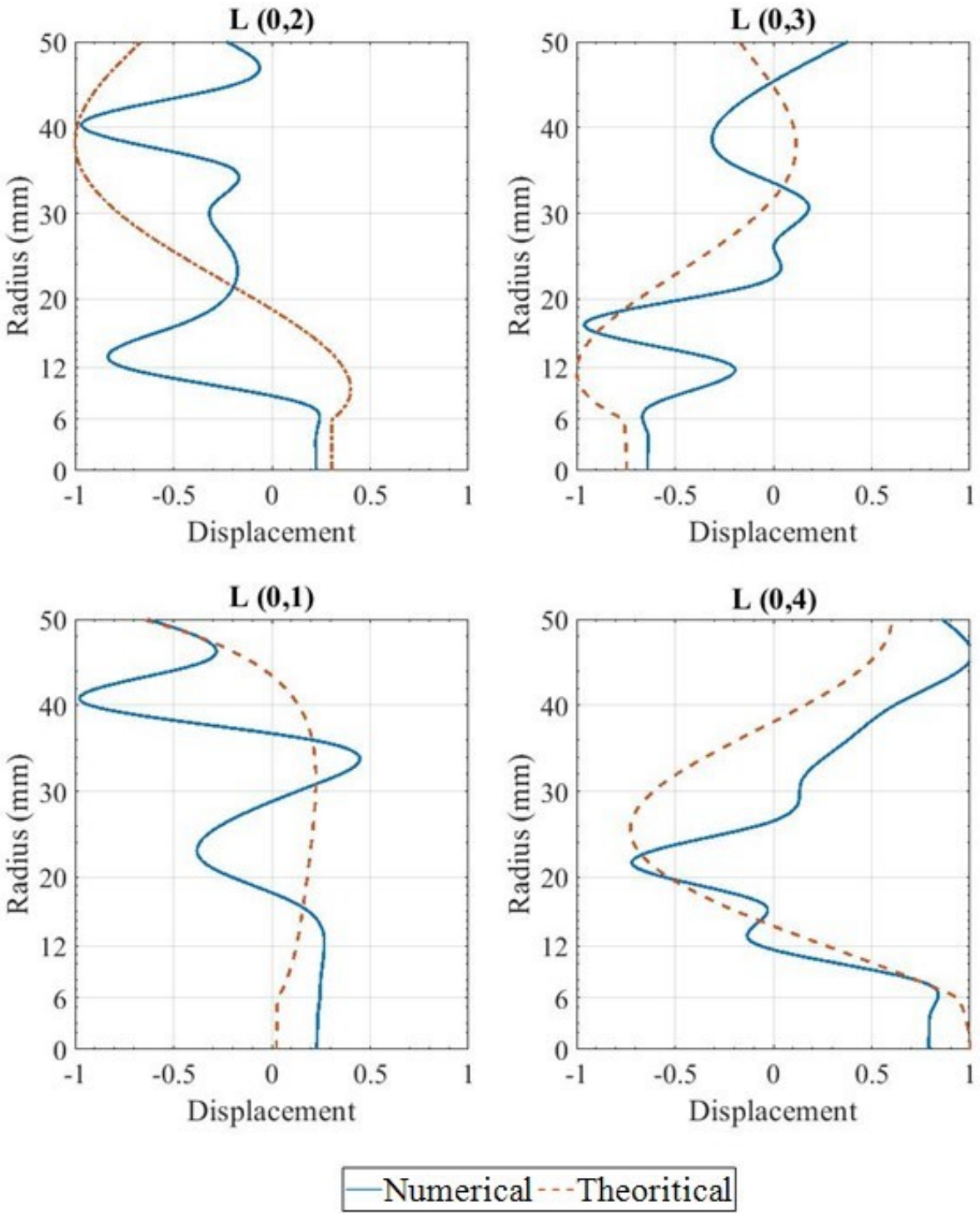

Figure 6.10: GW mode shapes extracted from theoretical dispersion relations and numerical simulations.

6.4.2 Longitudinal guided waves for corrosion detection

The individual effects of pure corrosion along with a simple reduction in the rebar cross-section and pure debonding when there is a loss of bond between concrete and steel are

studied to assess their impact on the GW signals. Figure 6.11 shows a comparison of the signal that is obtained from numerical simulations of an intact beam, corrosion which is 100 mm long and has a reduction of 2 mm in diameter, and debonding which is 40 mm long and which is located in the middle of the beam. It is observed that the debonding increases the amplitude of the signal and decreases the time of arrival because more energy is concentrated inside the rebar; whereas, a reduction in the rebar diameter results in a reduction of amplitude and the group velocity of the signal. The findings are consistent with the dispersion curves, showing that the group velocity of the modes decreases with the reduction in diameter.

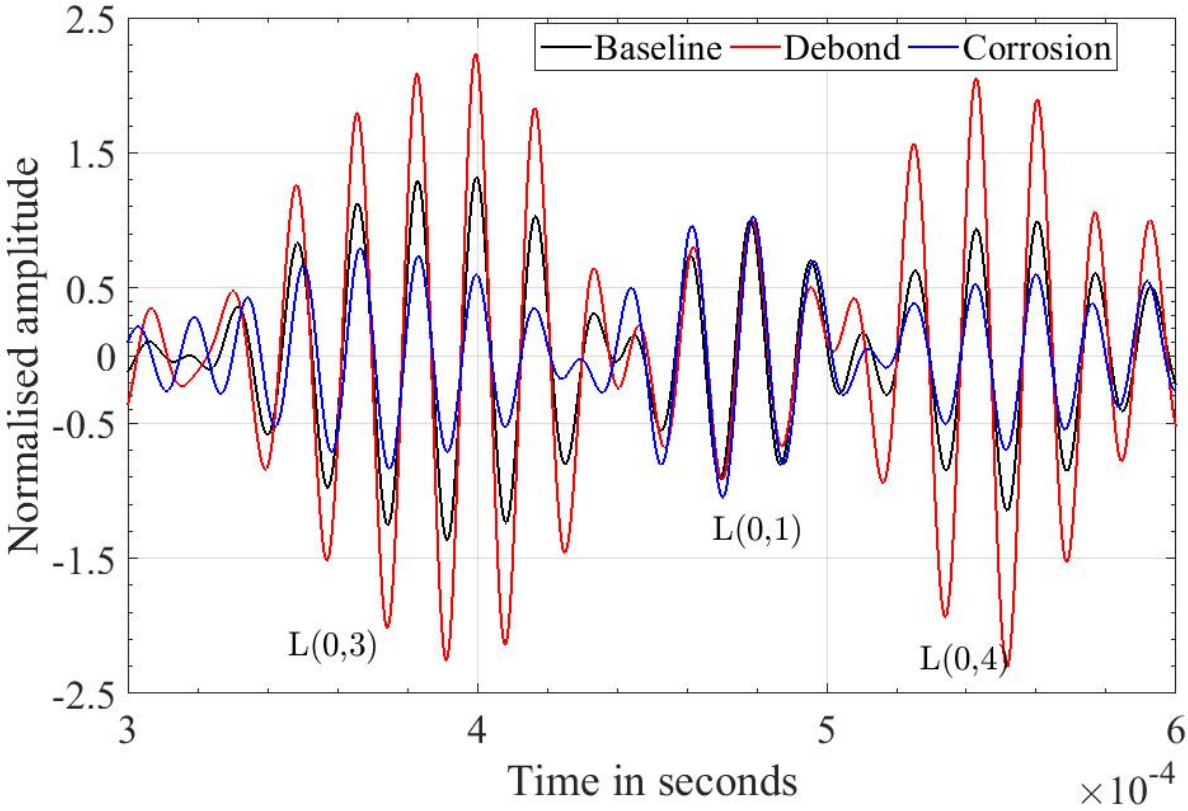

Figure 6.11: Comparison of numerical baseline with a 40-mm-long debond and corrosion with a 2 mm (depth) x 100 mm (length) reduction in material.

Unlike the simple reduction in the rebar diameter or debonding in simulation, corrosion of embedded rebars in the real world is intricate. Corrosion is initiated when the passive layer around the rebar is de-passivated by the chloride ions in the experimental setup. In this process, the chloride ions oxidise the iron (Fe) atoms to form the oxidation products ($Fe_2O_3 \cdot (H_2O)x$) termed rust. These products are much bulkier than pristine Fe, due to which they exert internal pressure and increase the bonding between the rebar and the

concrete in the initial stage. This process increases the energy leakage into the concrete from the rebars. As corrosion progress, the rust products get separated from the rebar and there will be debonding between steel and concrete. The GW modes that have vibration concentrated in the rebar may show an increase in the energy, whereas the GW modes with energy concentrated in the interface region show a decrease in the amplitude. In the final phase, the diameter of the rebar is reduced further due to corrosion, and the wave modes with energy concentrated inside the rebar are affected further.

To this end, the RC beam (Sample 12C1) was corroded with a constant current supply, as outlined in section 4.4.2 on the corrosion setup. The experiment was stopped after twelve days, because the beam showed signs of premature failure in the form of visible cracks and excess seepage of corrosion products. The signals were then compared with the baseline to measure the variation caused by the corrosion and to track the changes in specific modes due to corrosion. The $L(0,\ 2)$ mode is the fastest mode, but the amplitude of this mode is very low. Hence, this mode is not used in damage identification. Amongst the remaining three modes, the amplitude of the $L(0,\ 1)$ mode remained unaltered under corrosion. This observation is in congruence with the study on the mode shape of this mode, which shows small displacements in the rebar and at the interface, indicating the negligible influence of corrosion on this mode. The peak-to-peak amplitude of the $L(0,\ 1)$ mode is used to normalise the signal each day, corresponding to different corrosion levels. In this process, the peak-to-peak amplitude of the $L(0,\ 1)$ mode is equated to ± 1 in all the signals. This process eliminates the influence of the bonding condition of the rebar and the sensors because relative signal strength values of various modes are used in the analysis instead of actual measurements. The normalised $L(0,\ 1)$ mode for multiple days of corrosion is extracted and compared with the $L(0,\ 1)$ mode of the baseline in Figure 6.12. The $L(0,\ 1)$ mode shows a slight increase in the group velocity in the initial five days, which can be attributed to seepage of electrolyte. The decrease in velocity after that is attributed to corrosion pressure. However, the range of variation is small; hence, this is not useful for corrosion detection.

Similarly, the $L(0,\ 3)$ mode is extracted from the normalised signal, and its variation from various levels of corrosion is shown in Figure 6.13. It is observed that the amplitude of this mode shows a decrease till the sixth day. After the sixth day, the amplitude begins to increase until the ninth day and, finally, the amplitude begins to decrease again. The

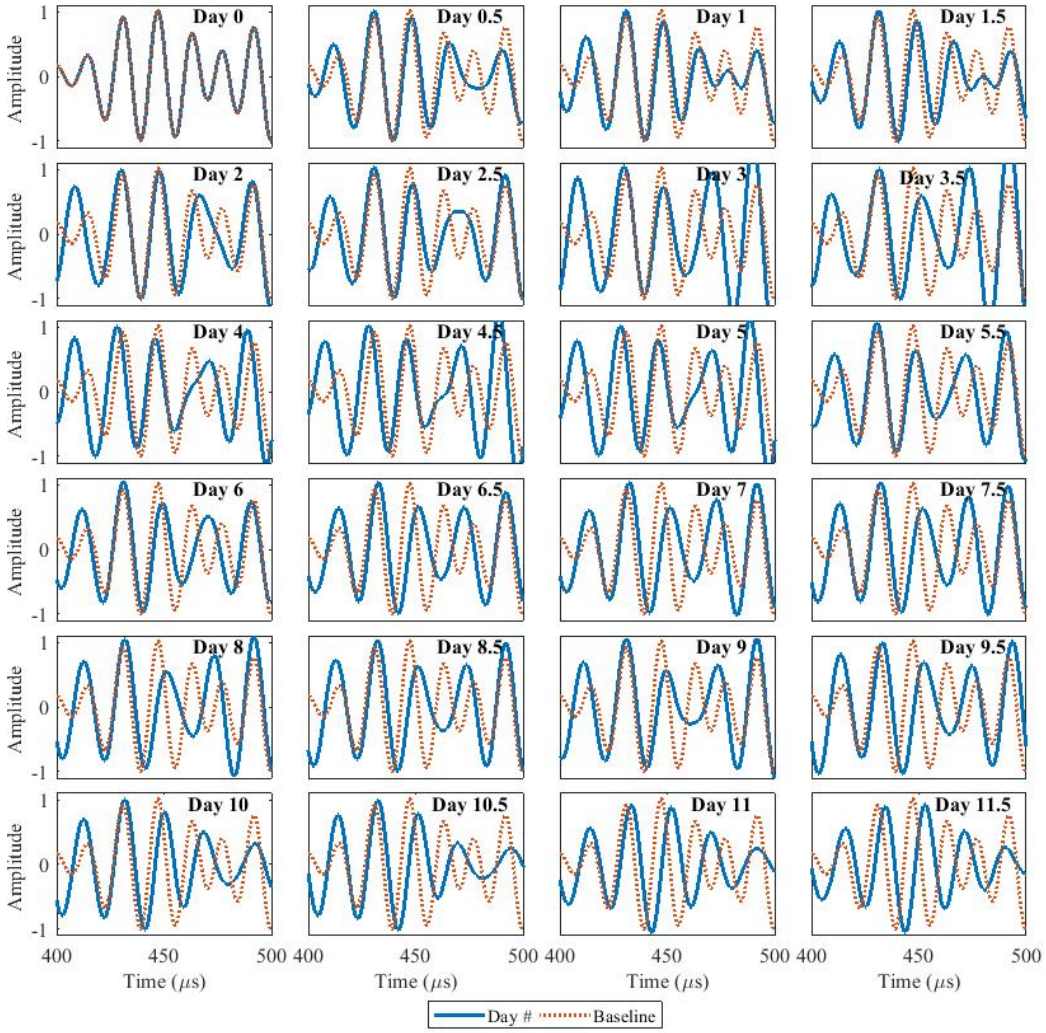

Figure 6.12: Comparison of normalised $L(0,\ 1)$ mode and baseline for various level of corrosion.

variation in the group velocity of this mode is insignificant; hence, it is not useful in corrosion identification. The $L(0,\ 4)$ mode is extracted from the response signal, and its variation from various levels of corrosion is shown in Figure 6.14. The amplitude and the velocity of the $L(0,\ 4)$ mode are marginally affected until the ninth day and show a rapid change thereafter. It is therefore concluded that $L(0,\ 3)$ can be used in continuous monitoring of corrosion because three different phases of corrosion are clearly observed in the feature change in the $L(0,\ 3)$ mode. $L(0,\ 4)$ can be used to distinguish between the corrosion initiation phase and the diameter loss phase, because the $L(0,\ 3)$ mode decreases in both phases, but $L(0,\ 4)$ decreases only in the latter phase.

The comparison of normalised GW signals can serve as a preliminary step to corrosion analysis because the various phases can be estimated. However, the method relies on the

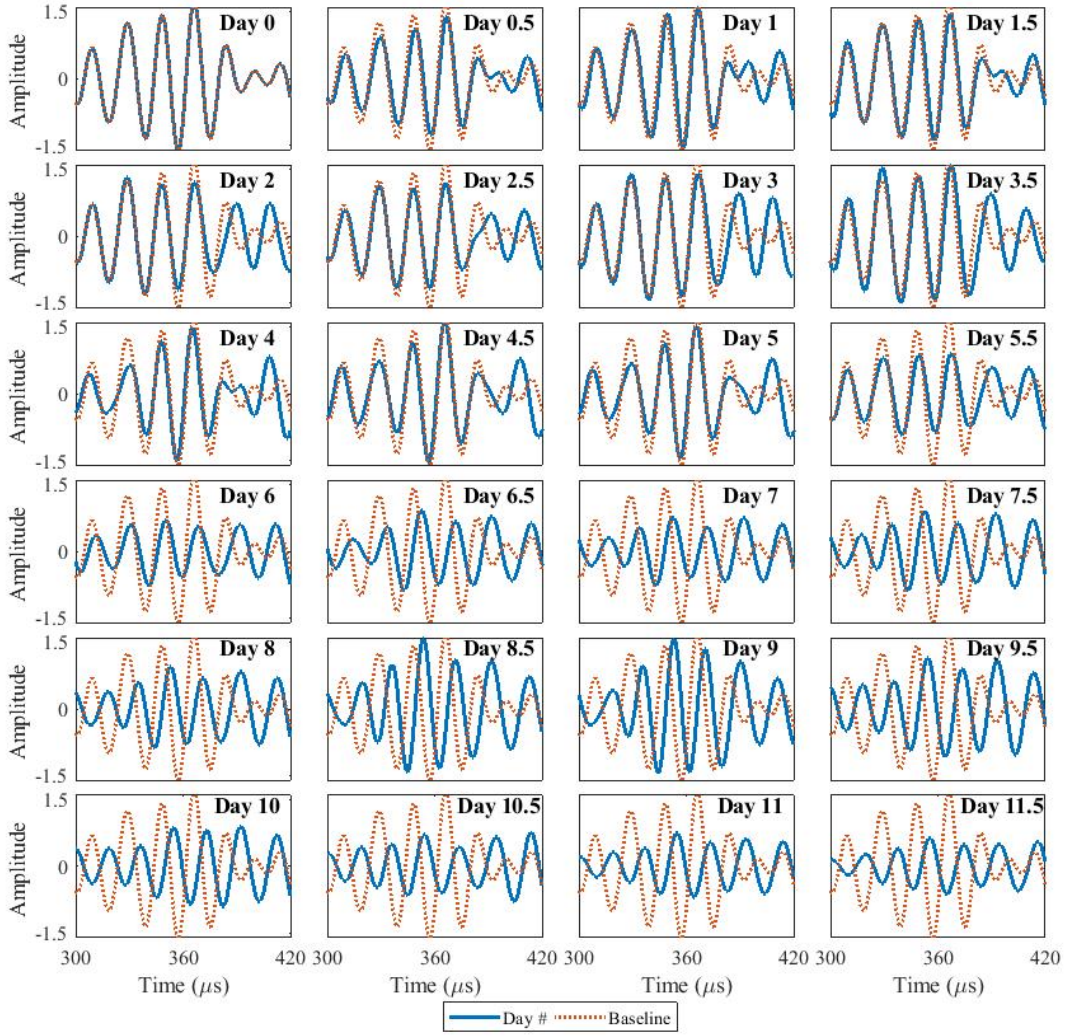

Figure 6.13: Comparison of normalised $L(0,\ 3)$ mode and baseline for various level of corrosion.

capturing of the local maxima of discrete data and does not account for the attenuation in the cycles of each of the modes. It is essential to compare the total change in the mode rather than only the peak amplitude with the baseline. A new method that defines a non-dimensional parameter is proposed in the following section to capture the overall change in each of the modes.

6.4.3 Wavelet based feature extraction

The study of the time-dependent amplitude variation of a signal is termed time series analysis. This type of analysis completely ignores the intrinsic frequency content of the structure. The fast Fourier transform (FFT) is often used to represent the signal in the frequency domain. However, the FFT of a signal does not give information about the

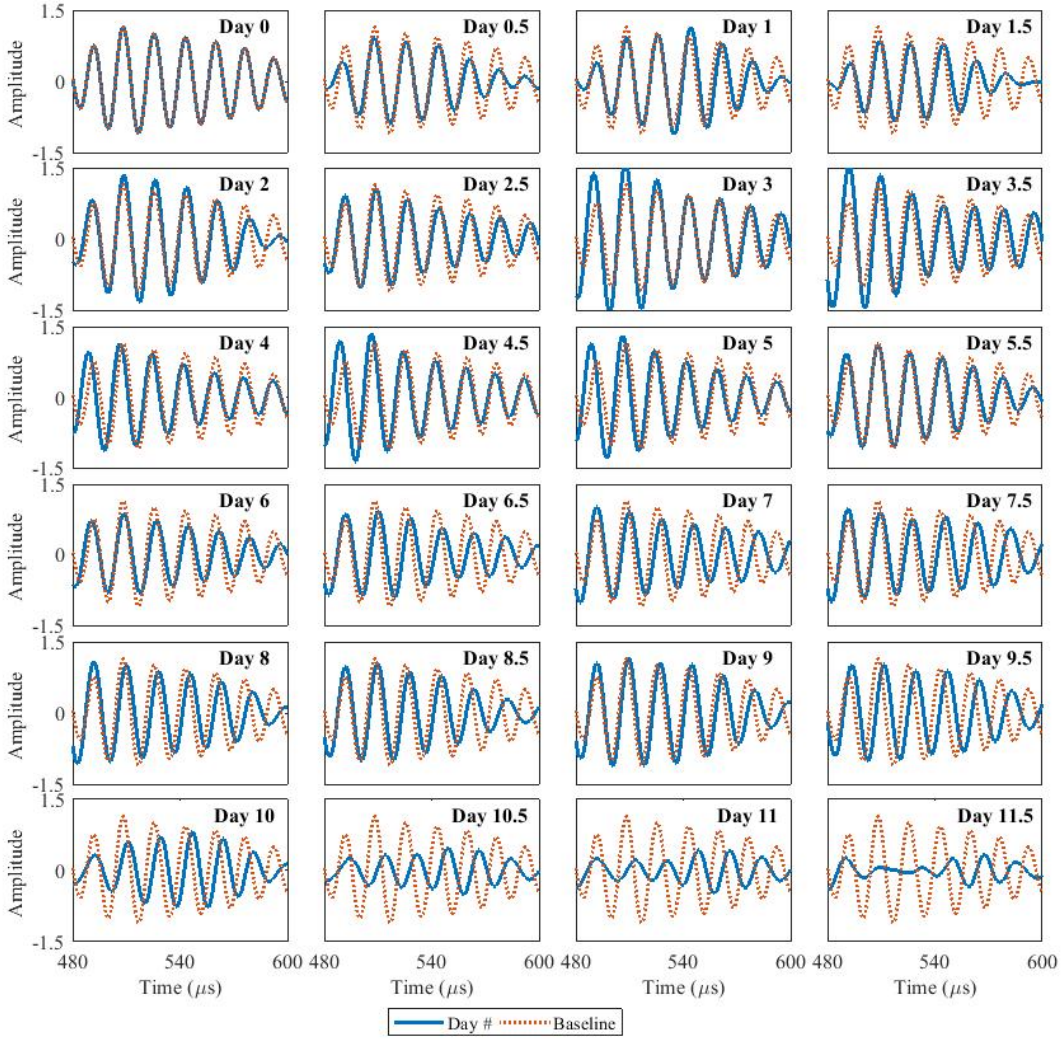

Figure 6.14: Comparison of normalised $L(0,\ 4)$ mode and baseline for various level of corrosion.

time of arrival of a frequency. A continuous-wavelet transform (CWT) was developed to overcome the limitation of the two methods of analysis mentioned above. The CWT has an excellent frequency resolution at lower frequencies and good time resolution at higher frequencies. In this study, Morlet wavelet is used as the mother wavelet, because it has good shape correlation with the input signal, which is a five-cycle pulse. Figure 6.15(a) shows the scalogram of the signal after CWT for the baseline signal, where three peaks are clearly observed corresponding to the dominant modes, $L(0,\ 3)$, $L(0,\ 1)$ and $L(0,\ 4)$. Similarly, the diminishing of the wave modes, $L(0,\ 3)$ and $L(0,\ 4)$, after six days of corrosion is reflected in Figure 6.15(b), while the scalogram of the signal after nine days of corrosion shows that the amplitudes of these two modes increase, in which $L(0,\ 3)$ is amplified significantly (Figure 6.15(c)). Finally, Figure 6.15(d) shows the scalogram on

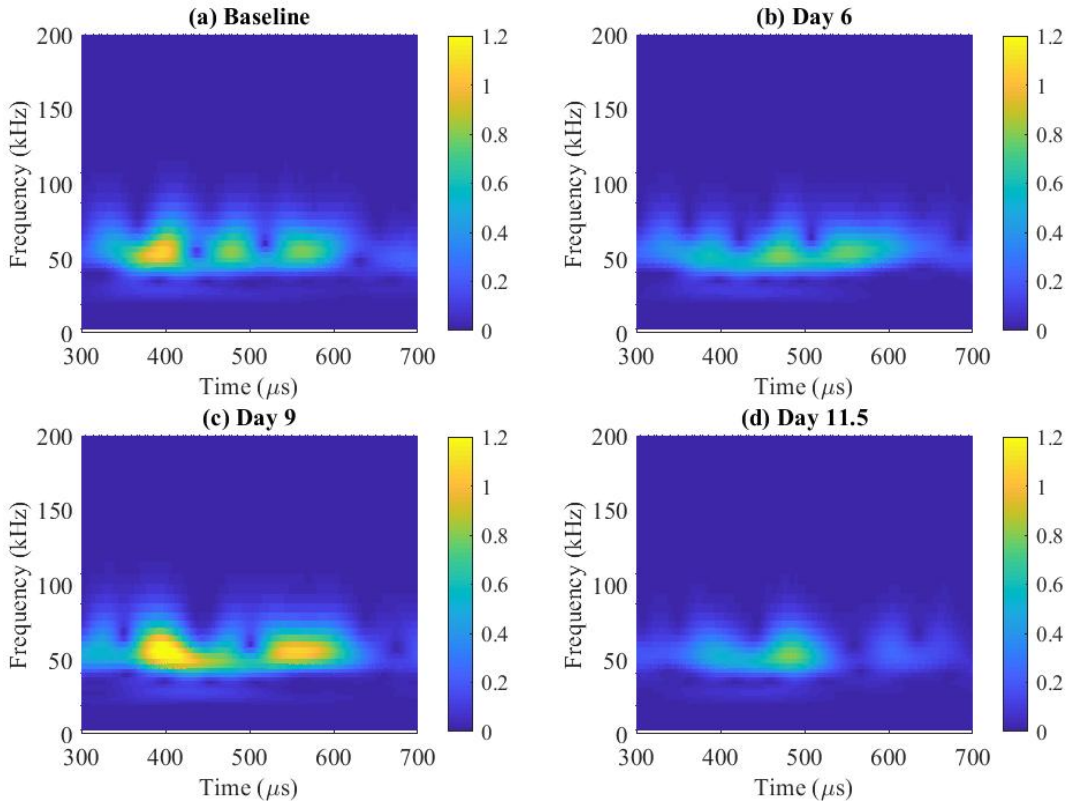

Figure 6.15: Magnitude scalogram of signal on the (a) initial day (baseline), (b) sixth day, (c) ninth day, and (d) twelfth day; showing the CWT amplitude versus time, and the frequency of corroded bars.

the twelfth day of corrosion, in which the amplitude of these two modes drops drastically.

On the basis of the aforementioned observation, the amplitudes of the $L(0,\ 3)$ and $L(0,\ 4)$ modes are tracked continuously using the CWT scalograms of the signals to study the effect of the corrosive environment on the GW signals. To minimise the effect of discrepancies in signal acquisition using CTs, a non-dimensional coefficient, RA, is designed for comparison of the peak amplitudes of the wave modes. It is defined by the

following equation:

$$
\begin{aligned}
Relative\ amplitude(RA) &= \frac{\int_{T_n^-}^{T_n^+} Sdt}{\int_{T_1^-}^{T_1^+} Sdt} \\
T_n^+ = t_n + \frac{\Delta_i}{2} \quad ; \quad T_n^- &= t_n - \frac{\Delta_i}{2} \\
T_1^+ = t_1 + \frac{\Delta_i}{2} \quad ; \quad T_1^- &= t_1 - \frac{\Delta_i}{2}
\end{aligned}
\tag{6.1}
$$

where S is the signal, t_n and t_1 are the arrival times of the peaks of the L(0, n) and $L(0,\ 1)$ modes that were estimated from the CWT scalogram, and Δ_i is the pulse duration of the input signal, which is 83.2 μs for an input of 60 kHz. The difference that occurs in the RA value with the number of days in the corrosive solution is shown in Figure 6.16.

The RA values of the $L(0,\ 3)$ mode show a steady decrease and those of the $L(0,\ 4)$ mode show a considerable increase until four days due to the de-passivation and seepage of the corrosive solution and a rapid decrease from after the fourth day until the sixth day due to the build-up of corrosion pressure. In the debonding phase, which occurs from after six days until the ninth day, the RA values of the $L(0,\ 3)$ mode shows a trend of increase, but those of the $L(0,\ 4)$ mode do not increase much. In the diameter reduction phase, the RA values of both modes decrease rapidly. The dependence of the group velocity of the $L(0,\ 4)$, $L(0,\ 1)$ and $L(0,\ 3)$ modes on the corrosion level is shown Figures 6.17 (a)–(c), respectively. It is found that the group velocity of the $L(0,\ 4)$ mode changes at corrosion initiation and in the diameter reduction phases, while it is not affected much during the debonding phase. The group velocities of the $L(0,\ 1)$ and $L(0,\ 3)$ modes vary in the initiation phase. In the later phases, the variation is not pronounced. The percentage of group velocity variation in debonding and diameter reduction phases is 4.4 per cent and 5.1 per cent for the $L(0,\ 1)$ and $L(0,\ 3)$ modes, respectively. The variation is smaller than that in the $L(0,\ 4)$ mode, which shows a change of 11 per cent.

It is therefore concluded that the RA values and group velocities of various modes can be used to classify and distinguish the phases of corrosion in a corroded RC beam. These features can be used to develop a damage identification algorithm to compare the set of signals that is acquired at appropriately spaced time intervals during the life of the RC

beam, which will enable the identifying of the type of damage.

6.5 Concluding remarks

In this chapter, the importance of continuous monitoring by SHM tools is emphasised by detecting the zero-effect state. This effect is confirmed by the experimental studies on corroded RC beams. The GW modes in RC beam are detected by calculating the dispersion curves using the theoretical model and verified with the help of numerical simulations and experiments. Numerical simulations confirm the state of rebar which includes the loss of diameter and weakening of the bond. The GWs generated by CTs and corrosion was accelerated using an impressed-current method. Theoretical dispersion curves were generated, from which it was found that the four longitudinal modes $L(0,\ 1)$, $L(0,\ 2)$, $L(0,\ 3)$ and $L(0,\ 4)$ occurred at 60 kHz excitation. The amplitude and the group velocity of these waves were studied.

A non-dimensional parameter, RA, was defined to study the amplitude changes with the development of corrosion. They were found to capture effectively the phases of corrosion. In the initiation phase, the RA values of the $L(0,\ 3)$ mode decreased, and the group velocity of the $L(0,\ 3)$ mode increased. In the progression phase, the amplitude of the $L(0,\ 3)$ mode increased. In the diameter reduction phase, the RA values of both the $L(0,\ 3)$ and $L(0,\ 4)$ modes decreased rapidly along with a decrease in the group velocity of the $L(0,\ 4)$ mode. This study can be extended to the implement a damage identification algorithm on corroded RC structures to identify the status of corrosion.

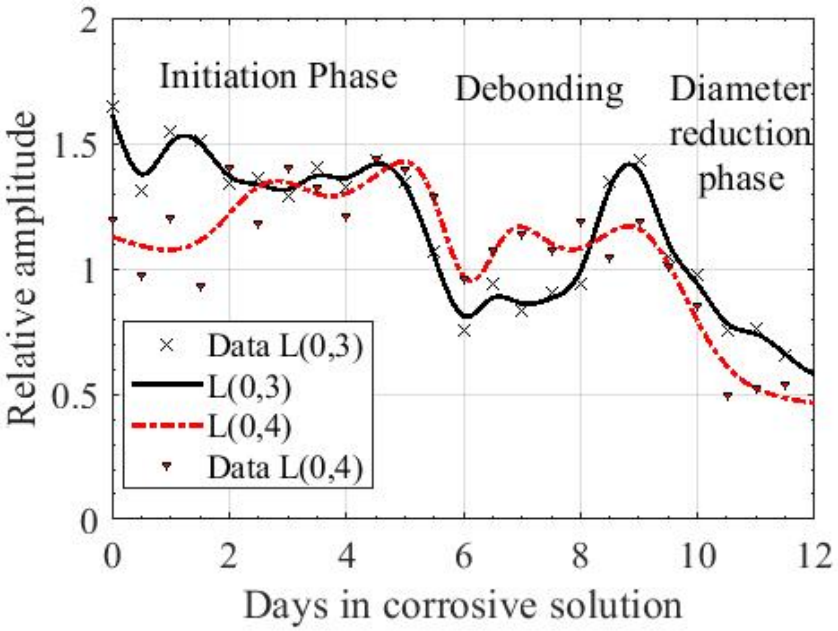

Figure 6.16: Relative amplitude curves of $L(0,\ 3)$ and $L(0,\ 4)$ modes with an increase in corrosion of rebars.

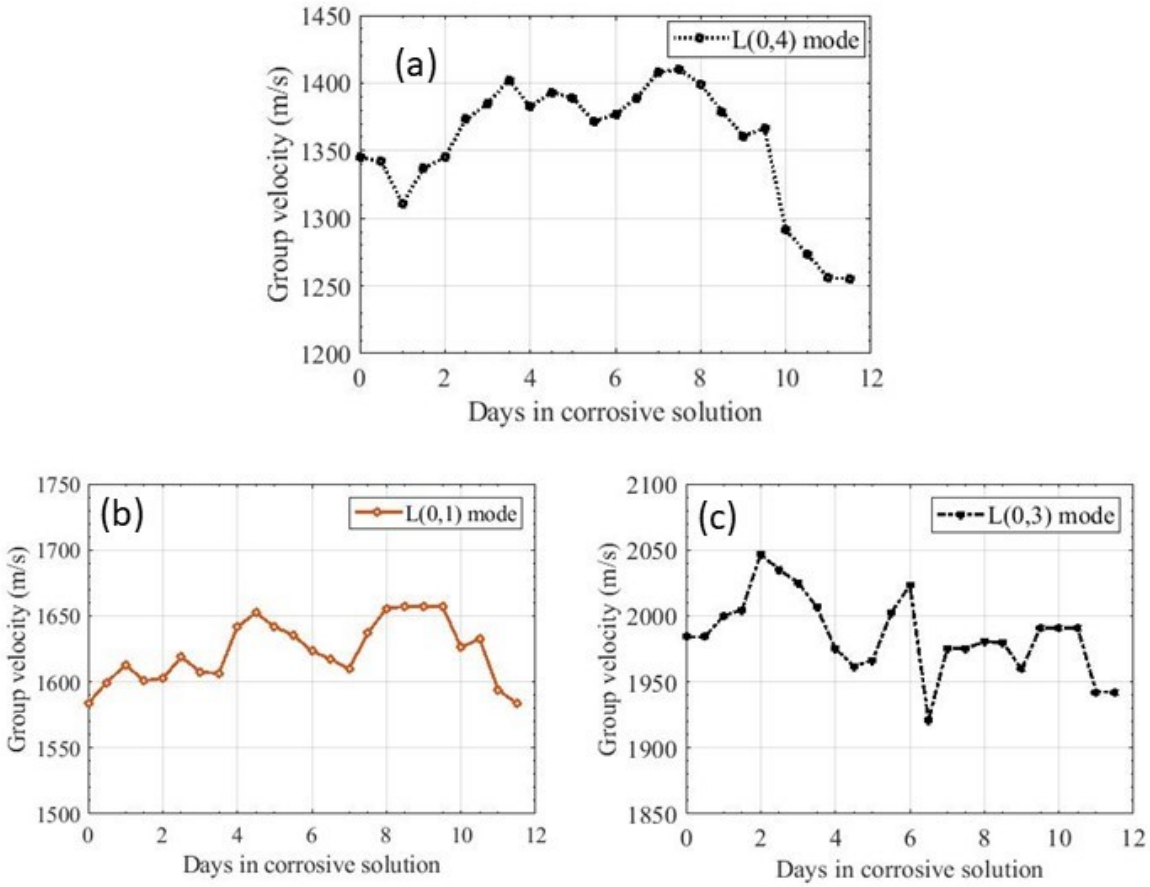

Figure 6.17: Variation of the group velocity of (a) $L(0,\ 4)$ mode, (b) $L(0,\ 1)$ mode and (c) $L(0,\ 3)$ mode with increase in corrosion of rebars.

Chapter 7

Flexural guided waves for detecting the pitting corrosion of rebars

7.1 Introduction

The identification of corrosion and the measuring of its rate remains a major concern in research in civil SHM. Several models have been attempted to correlate the corrosion current to actual corrosion; however, the actual mapping of corrosion in RC is yet to be accomplished. Detectability of corrosion of rebars embedded in cement mortar is for various correlate mass loss examined by researchers [Ervin *et al.*, 2006].Studies have shown that corrosion and debonding have a complementary effect on GW characteristics. Debonding results in an increase in the signal strength, whereas the reduction in diameter, which is caused by corrosion, results in a reduction in the signal strength [Na *et al.*, 2003; Ervin *et al.*, 2009]. Study of accelerated corrosion in rebars has been the focus of research in recent years [Sharma and Mukherjee, 2010]. CTs that are attached at the ends of the rebars are used by researchers to generate GWs in rebar. However, CTs are not field-deployable, because the ends of rebars are generally not available in many locations. Embeddable piezoelectric sensors attached to rebar, which are installed during the construction phase, have proven to be durable and effective tools in assessing the corrosion [Talakokula and Bhalla, 2015].

Pitting corrosion of rebars in RC beam is investigated the using ultrasonic GWs that are generated and acquired by PWTs in the current study. The combined influence of corrosion and debonding on wave characteristics is investigated to establish methods to distinguish and correctly quantify the damage level. A three-dimensional finite element

model of an RC beam is developed in the Abaqus software and the wave propagation in RC beam is studied after including the two effects of corrosion. It is observed that the reduction in diameter would result in the diminishing of the GW amplitude, whereas debonding results in an increase in the GW amplitude. It is found that these two complimentary effects on wave features result in a signal that has the same wave features as undamaged rebar that is surrounded by concrete, which could be termed as the zero-effect state. An accelerated corrosion setup is deployed to restrict the extent of corrosion to a specified length. The response of the beam is monitored continuously to correlate the structural changes to the measurements of the sensor. Wave characteristics from various stages of the corroded rebar are compared to infer the stage of corrosion. The possible mechanism of rebar corrosion process in concrete is proposed on the basis of the signal characteristics of longitudinal and flexural modes of GWs.

7.2 Experimental results

Three concrete specimens each of type 20C1 are tested by using the accelerated corrosion setup that is presented in the section 4.4.2. Tests on two samples are carried out for twelve days, and the test on the third sample is carried out for two days to observe the initiation of corrosion. The rebars are removed at the end of the test and are examined for extent, intensity, and pattern of corrosion. A five-cycle Hanning-windowed pulse at 75 kHz excitation frequency with peak to peak voltage of 30 V is used as an excitation pulse. The GW signal and its envelope are shown in Figure 7.1, in which the $L(0,\ 1)$ and $F(1,\ 1)$ modes can be located, and the flexural mode can be recognised as the predominant mode. To minimise the noise, the recorded signal was averaged over 512 samples by using the inbuilt function in the oscilloscope. Amplitude and velocity, which are features of the signal, were examined, and an attempt was made to recognise the phases of corrosion. Various stages of corrosion that are apparent from the variation in the signal characteristics are presented in this section.

7.2.1 Corrosion initiation phase

Figure 7.2 depicts the corrosion process in the RC structures. Corrosion in the rebars initiates when there is a potential difference between the terminals, which provides the

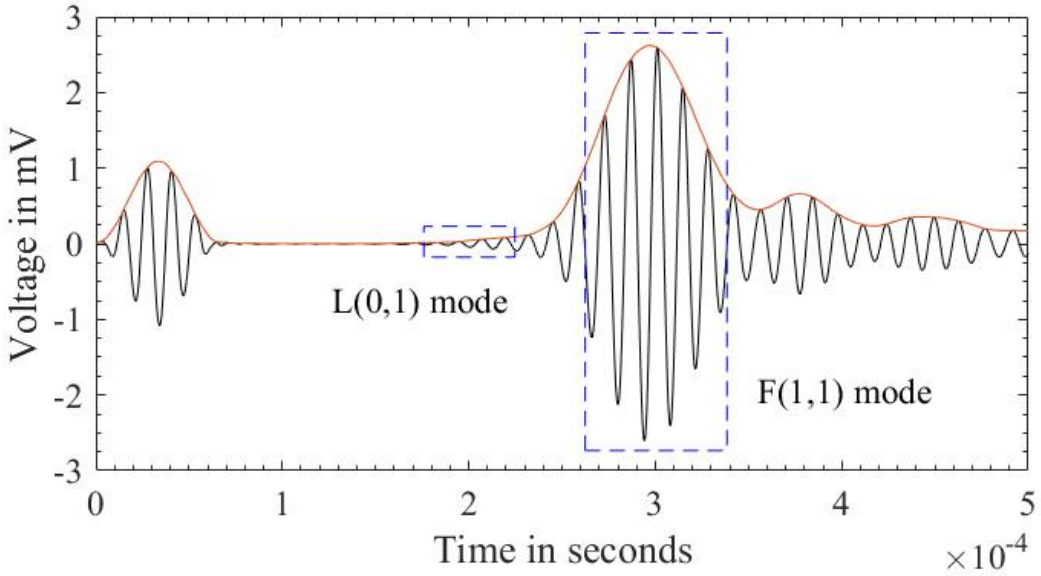

Figure 7.1: Baseline signal obtained from undamaged concrete specimen excited with 5 cycle hanning pulse at 75 kHz.

necessary electrons to dissociate water molecules. The hydroxide ions, in turn, oxidise the iron to form the rust product. In the initial stage of the experiment, the electrolyte seeps into the concrete beam through pores. A gradual increase in the current across the terminals is observed in the power supply. A current of 0.47 Amperes is observed in the constant voltage DC power supply after three days in the electrolyte. The studies have indicated that initiation of corrosion leads to an increase in the diameter of the rebar [Cao and Cheung, 2014]. An increased stress transfer from the rebar to the surface of the concrete is expected in such a case, which causes more energy inside the bar to be dissipated to the surrounding concrete medium. As a result of the phenomenon that is mentioned above, the amplitude of the $F(1,\ 1)$ mode, which shows dominant out-of-plane vibration, reduces in the initial stage. The group velocity of $F(1,\ 1)$ mode increases in the initial 24 hours and decreases later on. The initial increase in velocity confirms the seeping of electrolyte through the pores in the concrete. The decrease in velocity afterwards could be due to the increase in the bond between the rebar and concrete.

Figure 7.3 depicts the change in the GW signal with the progress of corrosion. The measurements are obtained for the same input signal at the end of each day for four consecutive days in the corrosive solution. In order to compare the signals, the energy of the GW signal at various stages of corrosion is plotted in Figure 7.4 by using the Hilbert transform. The sensor measurements indicate that the amplitude of the $F(1,\ 1)$

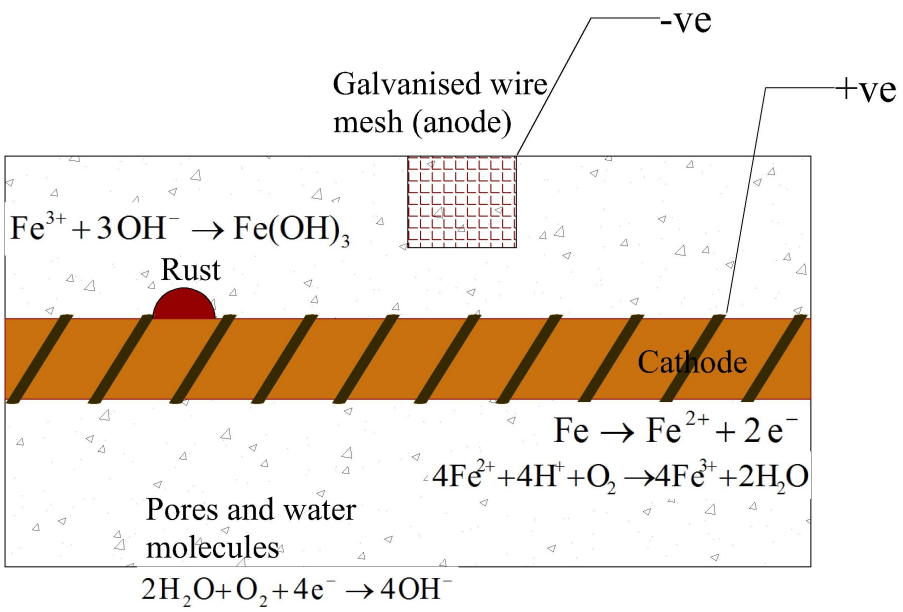

Figure 7.2: Schematic diagram of corrosion in RC structures, triggered by the impressed current.

mode gradually decreases for the initial four days in the corrosive solution, whereas the amplitude of the $L(0,\ 1)$ mode is almost intact. The $L(0,\ 1)$ has dominant in-plane vibration hence it is insensitive to the change in bonding condition due to corrosion initiation. The third sample is opened on day 2 to ascertain this effect, and it has been observed that the changes in the wave properties are caused by increased bonding. The concrete beam is split after the test, as shown in Figure 7.5. On examination, it is observed that the corroded portion of the beam indicates an increased bonding between steel and concrete. Separating the rebar from the concrete becomes difficult when there is slight corrosion in the rebar because the bonding increases with the initial corrosion.

7.2.2 Corrosion progression phase

It has been observed that the energy of both $L(0,\ 1)$ and $F(1,\ 1)$ modes in this phase increase with the progress of corrosion in the rebar. The energy envelope of GW signals is shown in Figure 7.6. The increase in the signal strength is observed for six days, that is, the fifth day to tenth day. The colour of the electrolyte begins to change to brown, which indicates the oozing of the rust product. Studies have indicated that a porous rust is formed when the rebar is allowed to corrode [Caré *et al.*, 2008]. The bond between the concrete and rebar is weakened due to this porous rust, and this effect is termed as

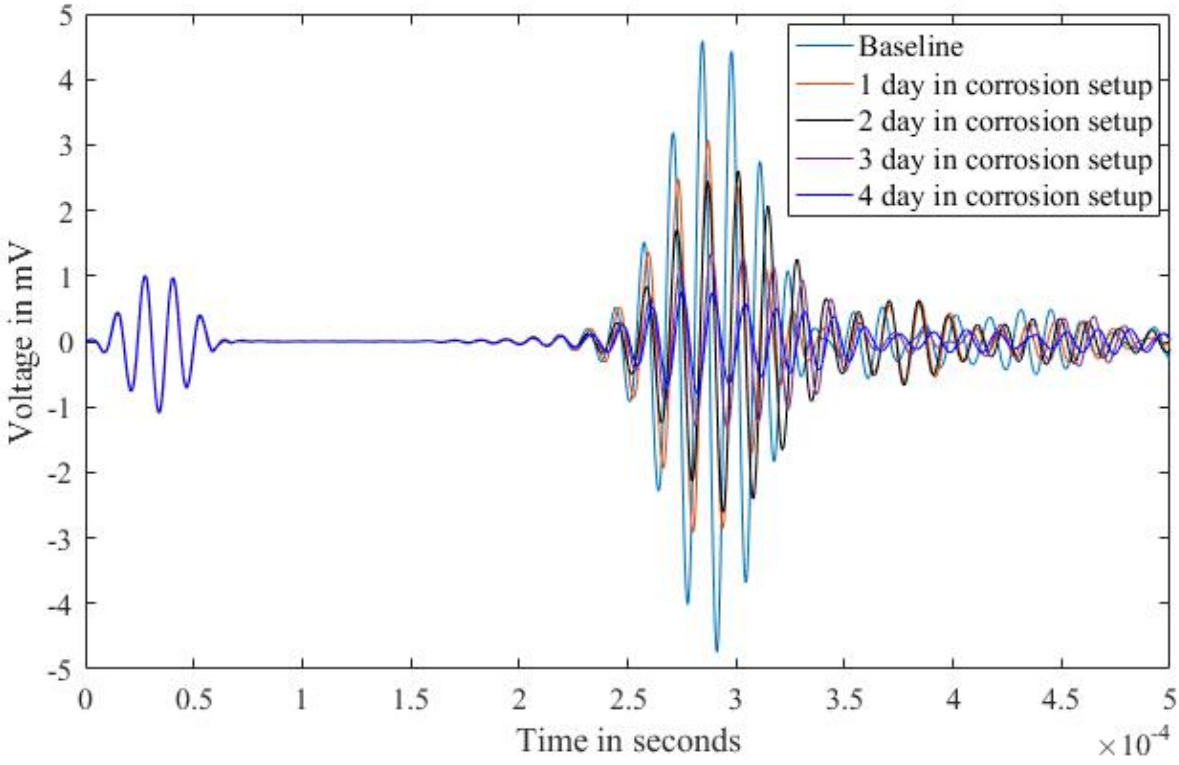

Figure 7.3: GW signals recorded using piezoelectric transducers attached to the rebar after various days in corrosive solution.

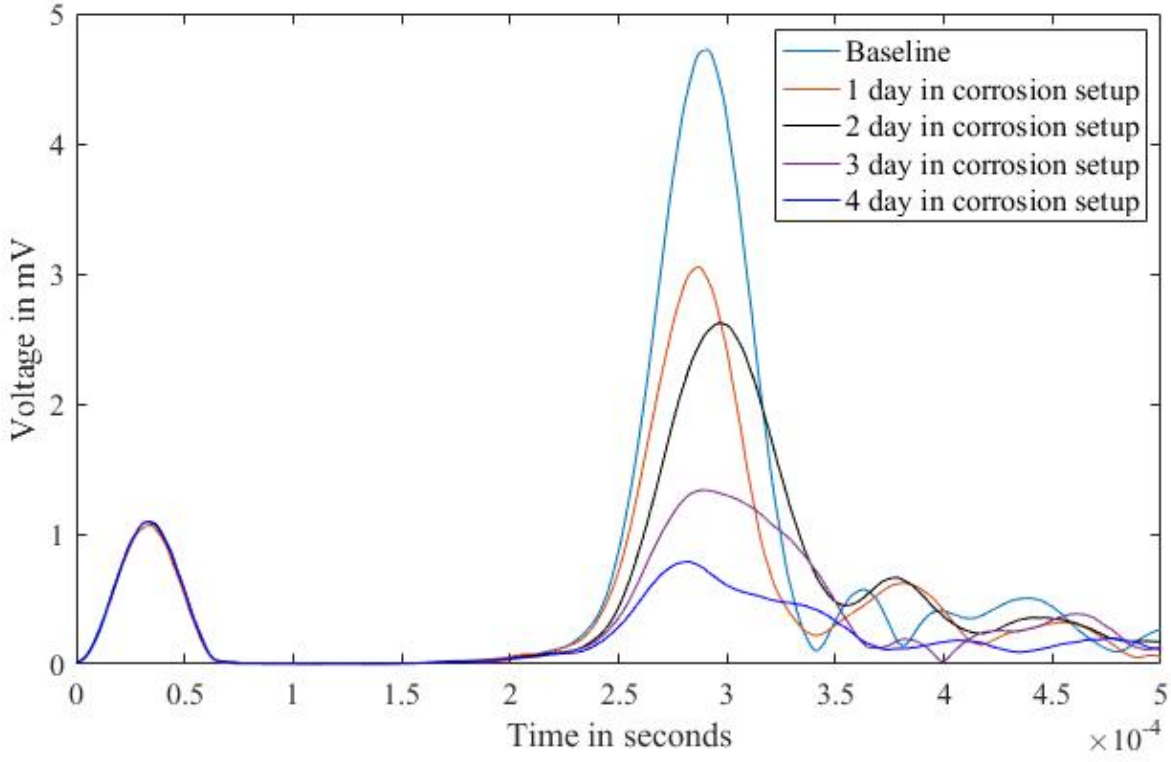

Figure 7.4: Energy envelope of the GW signals recorded using piezoelectric transducers attached to the rebar in the initial phase of corrosion.

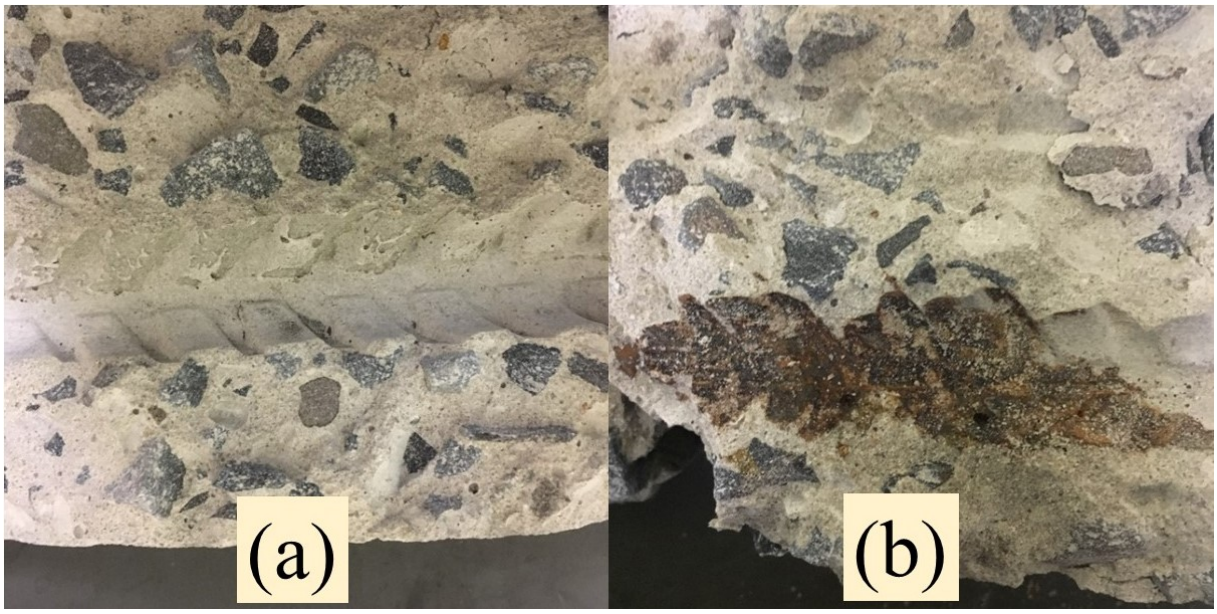

Figure 7.5: Split RCC beam showing the bonding between reinforcement and concrete (a) at the intact portion and, (b) corroded portion.

debonding. Due to debonding, the wave energy during the GW testing is focused inside the core of the rebar with reduced leakage into the surrounding concrete medium. This is the reason for the increase in the signal strength, which was observed for both $L(0,\ 1)$ and $F(1,\ 1)$ modes as the debonding progressed, while $F(1,\ 1)$ shows more sensitivity because it is more sensitive to bonding conditions. Thus, it can be concluded that the predominant effect at this stage is bond loss.

Another important observation from the time series analysis is that the arrival time of the $L(0,\ 1)$ mode is unaffected by the corrosion. Thus, the time of flight of the $L(0,\ 1)$ mode cannot provide significant information in the case of the pitting type of corrosion.

7.2.3 Diameter reduction and concrete cracking phase

The beam is kept in the corrosion setup for a further three days to correlate the visible changes in concrete to the sensor measurements. The test setup limits the corrosive zone to 150 mm. Corrosion occurs predominantly in this zone as the availability of electrolyte is limited to this zone. Figure 7.7 shows the rebars pulled out after the completion of corrosion test. A large corrosion pit is observed in central portion with axial extent of 120 mm. Visible cracks, as shown in Figure 7.7, are aligned along the length of rebar and appear on the surface of the concrete. The corrosion of the reinforcement bar is apparent from the discharge of the rust product from these cracks. The energy envelope of the

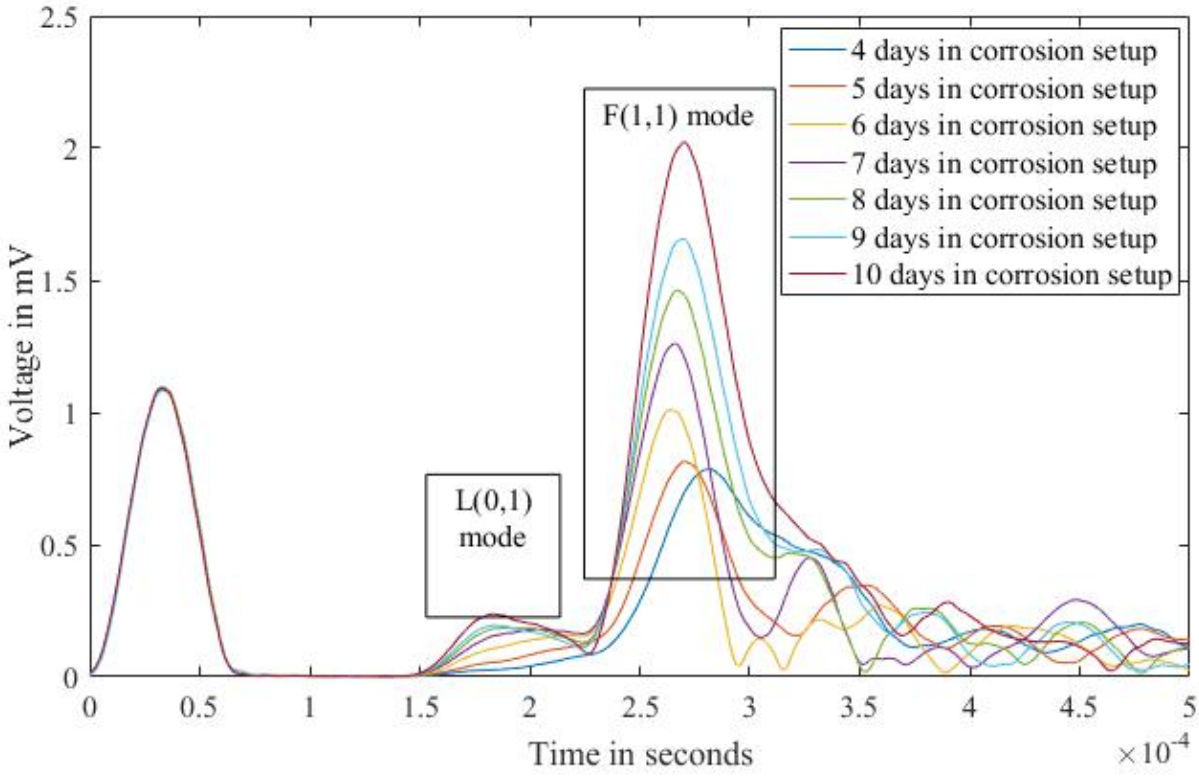

Figure 7.6: Energy envelope of the GW signals recorded using piezoelectric transducers attached to the rebar in the corrosion progression phase.

signal is shown in Figure 7.8. In this phase, a reduction in the amplitude of the $F(1,\ 1)$ mode is observed, while the change in $L(0,\ 1)$ is marginal in GW signals. In previous studies, it is shown that the reduction in the diameter of the rebar results in a reduction in amplitude because of the greater amount of wave reflection in the corrosion region. Since the $L(0,\ 1)$ mode propagation is more concentrated along the rebar, it is less affected by the reduction in the diameter than the $F(1,\ 1)$ mode. As the rebar already debonds from the concrete in the previous phase, the predominant effect in this phase is the reduction in diameter.

7.3 Mechanism of corrosion process

The mechanism of corrosion inside the concrete can be deduced using the pattern of the signal strength measurements. Three phases of corrosion namely initiation phase, progression phase and diameter reduction phase can be identified using the current method of corrosion monitoring. The initiation phase is indicated by the reduction in the amplitude of the $F(1,\ 1)$ mode as the bonding between concrete and steel is strengthened. The

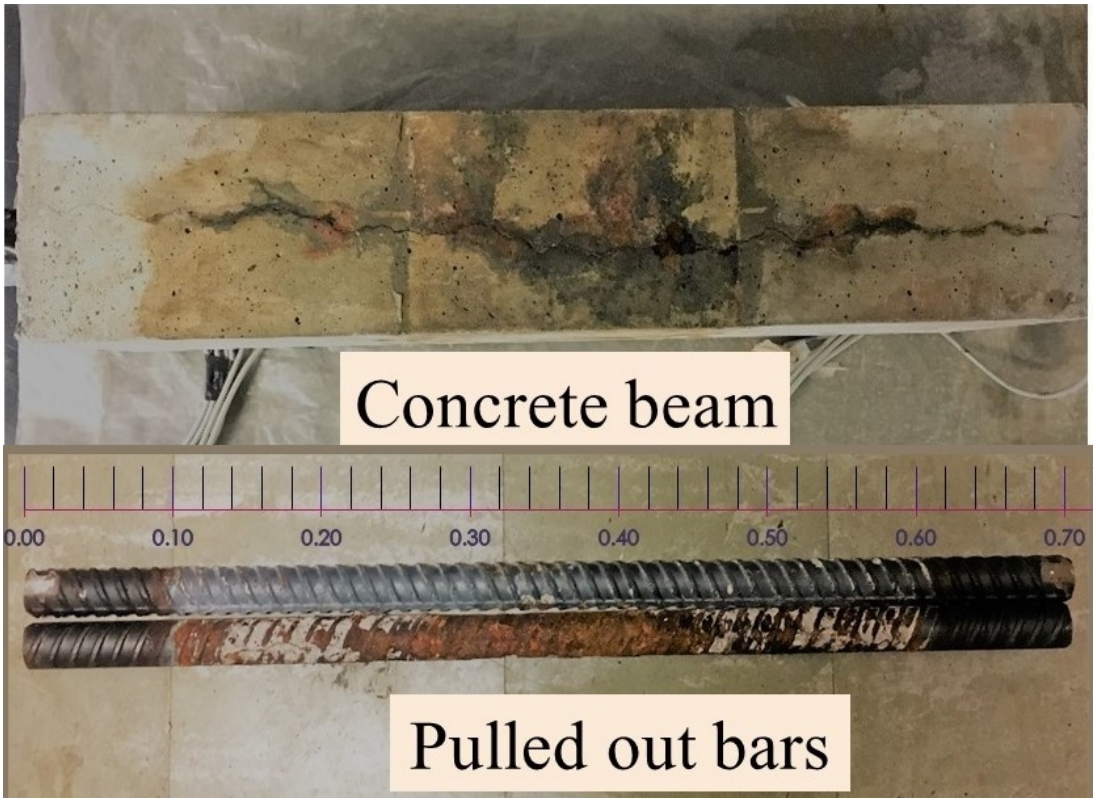

Figure 7.7: Cracked concrete beam and the pulled-out rebars after twelve days of corrosion.

predicted mechanism of corrosion initiation conforms with the previous studies [Pantazopoulou and Papoulia, 2001; Wang and Liu, 2006], which indicate that the bond strength increases in the initial phase of corrosion. In the progression phase, the debonding is dominant; hence, a slight increase in the amplitude can be observed. The effect of debonding on GW features has been studied numerically in the section 6.2.2 has indicated that an increase in the debonding leads to an increase in the GW amplitude. Thus, the corrosion progression phase is predicted to have a predominant debonding damage. In the final phase, a reduction in the diameter is observed in the experiments along with a reduction in the GW amplitude. This phase has been studied numerically by the current authors and it is demonstrated that a reduction in the diameter leads to a reduction in the GW amplitude.

All the phases of corrosion, which are identified from the amplitude measurements, are shown in Figure 7.9. In the absence of continuous monitoring, observing of the signal amplitudes on the third day, eighth day and twelfth day could result in misinterpretation of the condition of the rebar as being healthy although there is considerable corrosion. This observation also proves the zero effect state, which is proposed by the authors. Thus,

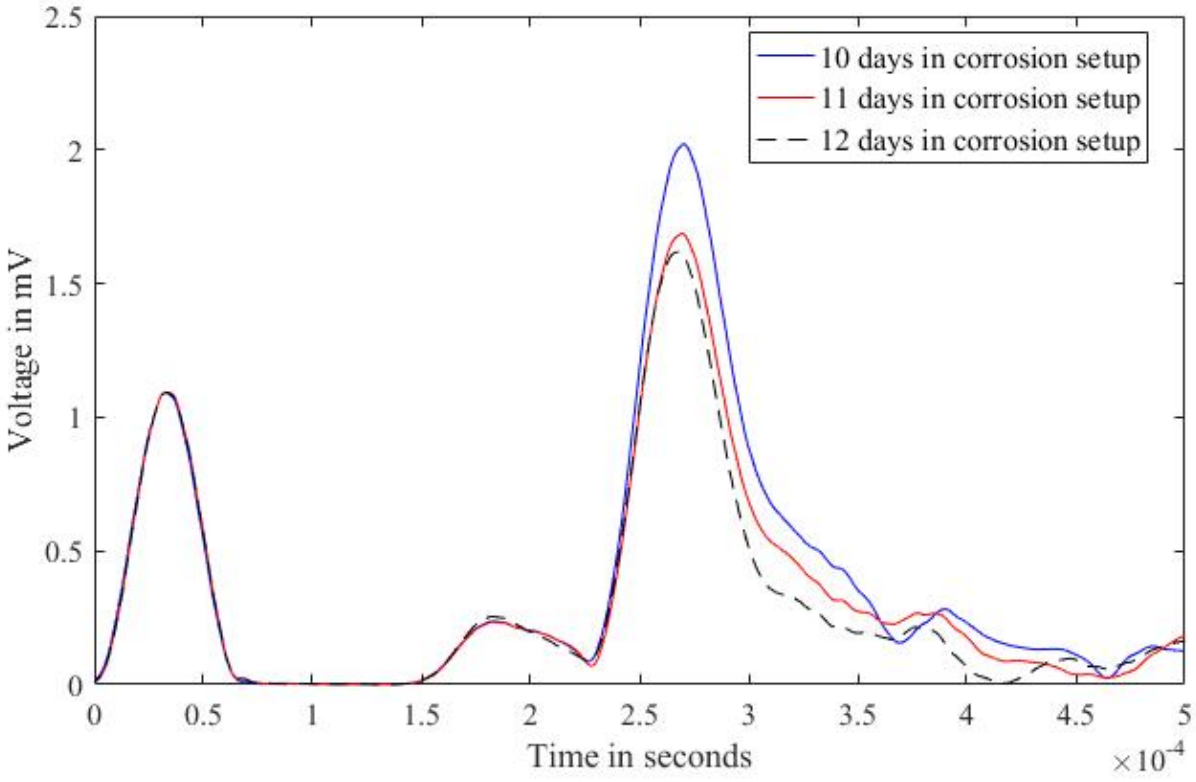

Figure 7.8: Energy envelope of the GW signals recorded using piezoelectric transducers attached to the rebar in the final phase.

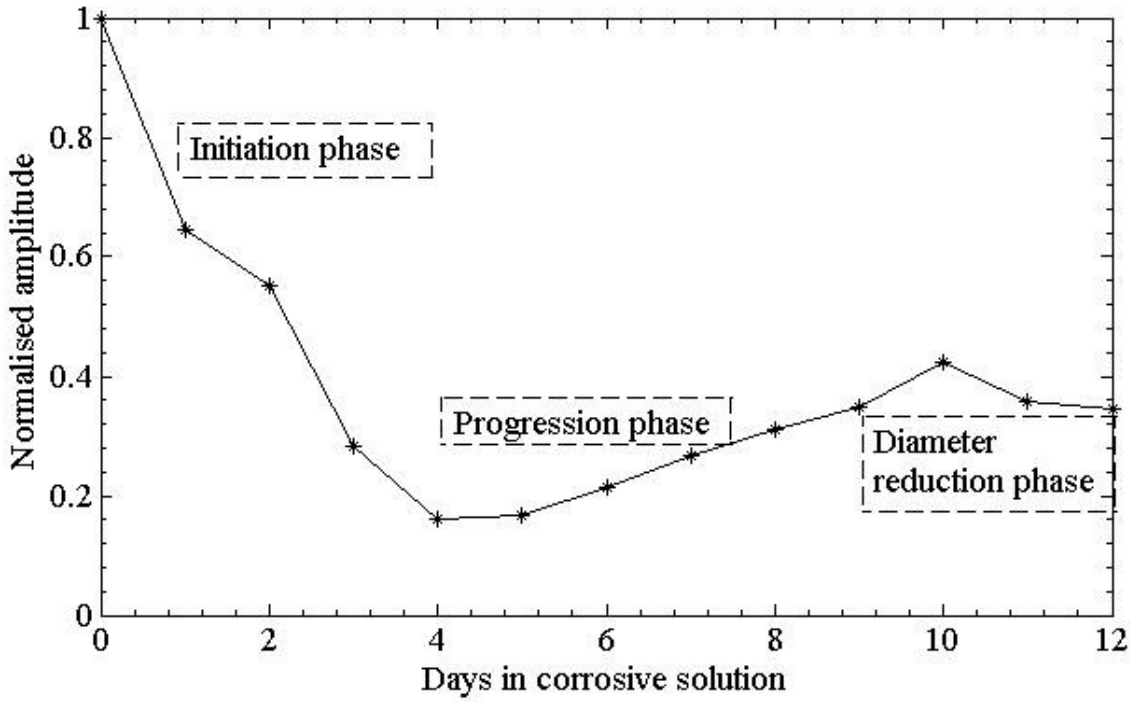

Figure 7.9: Variation in the amplitude of $F(1,\ 1)$ mode with the progress of corrosion.

continuous monitoring of the RC structures is necessary to detect the status of corrosion in rebars. The impressed current in the power supply varies with the corrosion, as shown in Figure 7.10. Initially, the current increases with time as the corrosive solution seeps

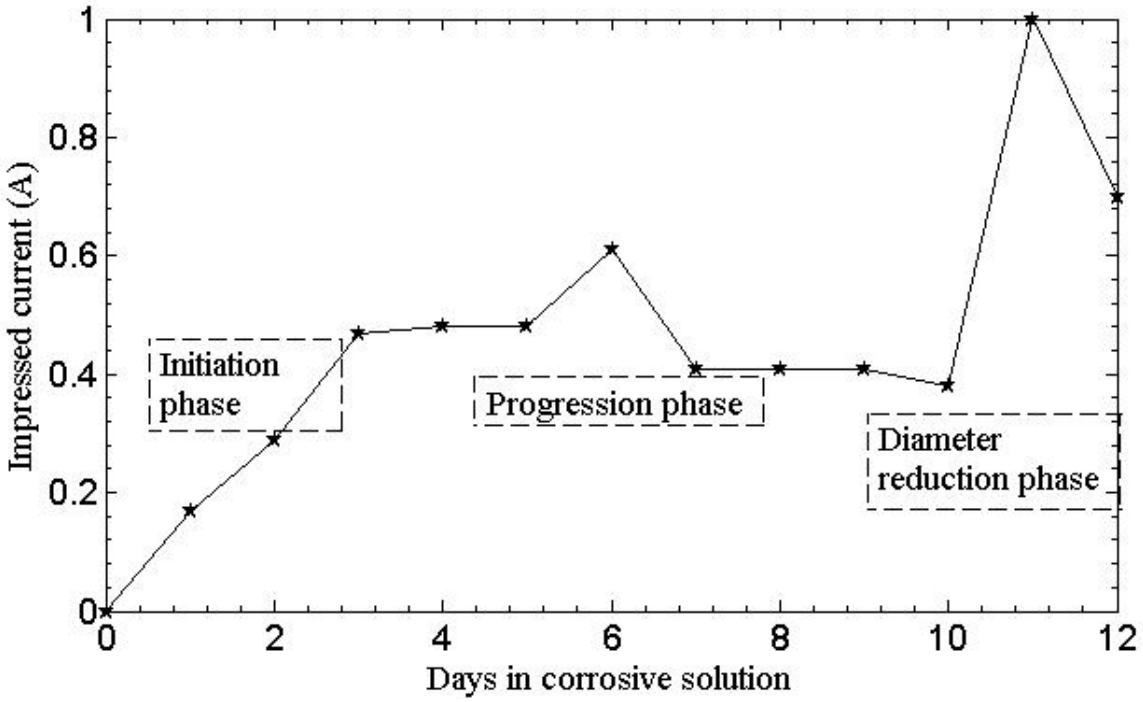

Figure 7.10: Impressed current observed in the power supply for the constant voltage across the terminals.

into the concrete through the pores. The current stabilises in the corrosion progression phase, indicating a constant rate of corrosion. A considerable increase in the current is observed on the eleventh day, which coincides with the appearance of visible cracks in the concrete. This increase in the current is a result of increased availability of the chloride ions that flood the concrete through the cracks.

The mass loss in corrosion setup has a direct correlation with impressed current. Studies have proved that Faraday's law can be applied to estimate the mass loss [El Maaddawy and Soudki, 2003]. The mass loss observed in experiments after two days in corrosion is 0.45 percent which is same as mass loss predicted by the Faraday's law. Monitoring of corrosion progress, especially its initiation, with such a low mass loss in concrete has been successfully achieved by using the PWTs in this study.

The variation of group velocity of $F(1,\ 1)$ mode as the corrosion build up in sample 20C1 is shown in Figure 7.11. The group velocity variation reflects various phases of corrosion that are influenced by by multiple factors such as corrosion pressure, rebar

diameter and bonding. In the corrosion initiation process the electrolyte seeps into the concrete and corrosion process is initiated. During this process the cathodic protection gets de-passivated and the corrosion product is formed. The formation of corrosion product results in the increase of bond strength between concrete and steel. This effect is observed by the decrease in the GW velocity as more energy is leaked into the concrete and its velocity is delayed by the lower Young's modulus of concrete. In the corrosion progression phase, the corrosion product gets debonded from the steel bar. The velocity of the $F(1,\ 1)$ mode is increased in this phase as energy is concentrated inside the core of rebar and wave mainly propagates in steel. The final phase of corrosion is diameter reduction. This phase is like a simple steel bar corrosion as the rebar and concrete are already separated. The group velocity of the $F(1,\ 1)$ mode therefore gets reduced in this phase. The accelerated corrosion experiments are repeated on concrete sample 12C2

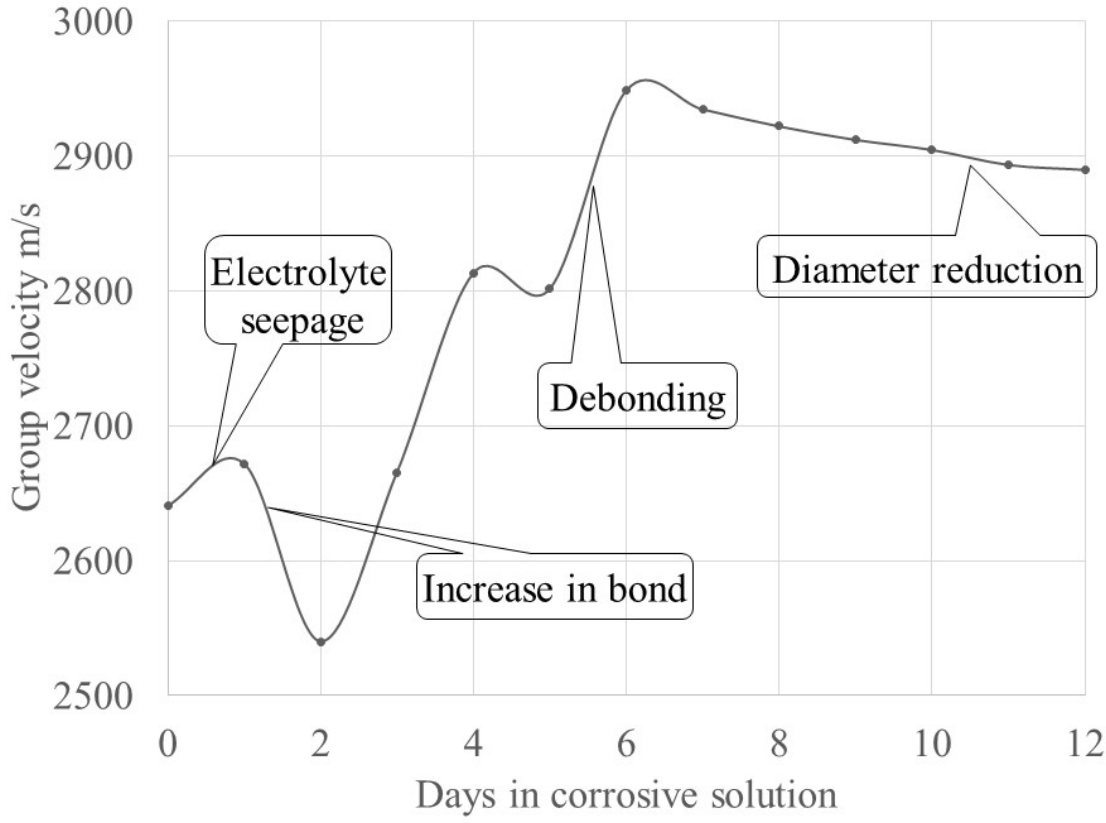

Figure 7.11: Variation of group velocity of flexural mode with the progress of corrosion for sample 20C1

to ensure the universal applicability of PWT based damage detection. The samples are corroded at the corrosion rate equal that of sample 20C1. The amplitude variation curve

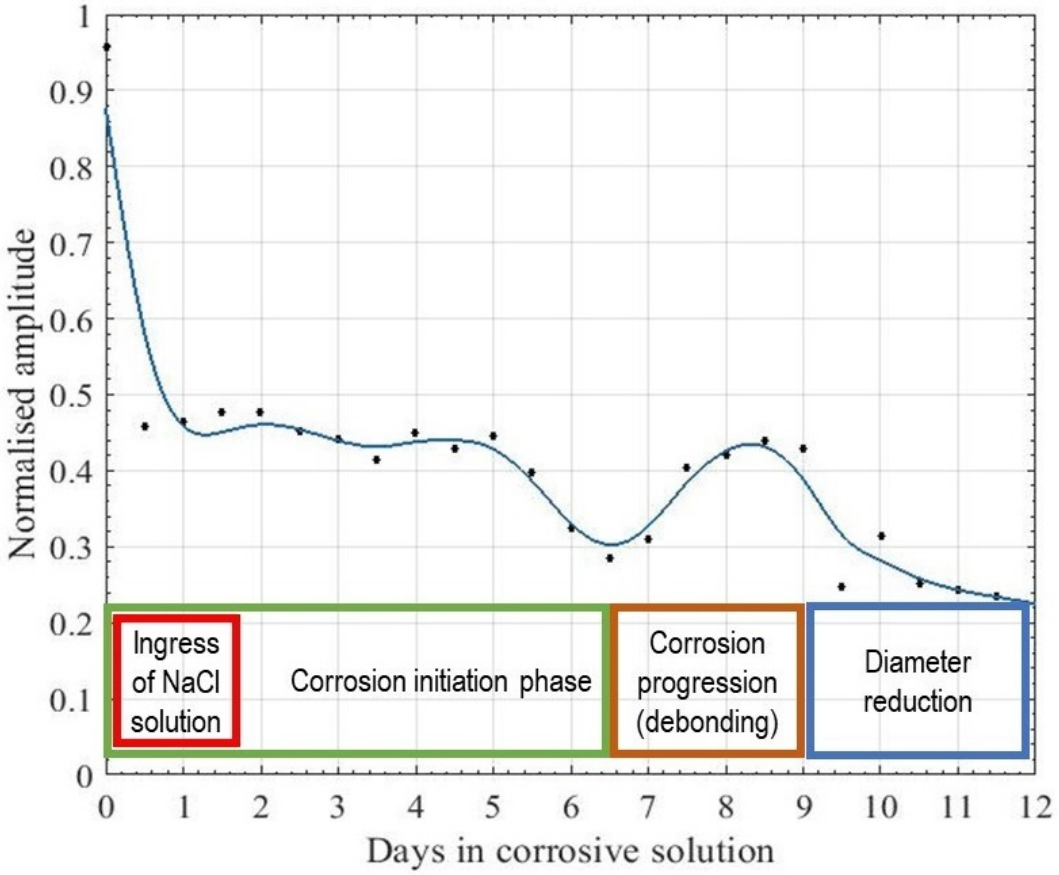

Figure 7.12: Various phases of corrosion recognised from the changes in the amplitude with corrosion of sample 12C2.

is plotted in figure 7.12 in which all the three phases of corrosion can be recognised.

7.4 Damage index for extreme corrosion

A concrete sample of type 12C1 is subjected to extreme corrosion current and the changes in GW signals are observed. The aim of this exercise is to quantify the corrosion in the diameter reduction phase. A corrosion current of 0.4 Ampere is maintained across the terminals in the corrosion setup which corresponds to the current density of 350 mA/cm^2 in a 12 mm-diameter rebar. The rebar is corroded for fifteen days in the corrosion setup. The GW response of embedded rebars in the high corrosive current is analysed to assess the intensity of corrosion. In this experiment, corrosion evolved rapidly owing to the fact that the rate of corrosion induced in the rebars is very high. Previous studies express that the group velocity of the flexural mode show a great sensitivity in the corrosion initiation and progression phases. The extreme corrosion mainly leads to diameter reduction phase

and the contact conditions do not alter in this phase; the rebar is completely detached from the concrete and the length of the pit is very small compared to the length of the rebar thus the group velocities do not alter much. It is noticed that the amplitude of the flexural mode decreases continuously and considerably with corrosion. At the end of fifteen days in corrosive solution, the amplitude falls by over 80 percent where the estimated percentage of corrosion is just 15 percent. Hence, the amplitude serves as a good metric to estimate the severity of pitting corrosion in rebars.

Wavelet analysis of the signals is carried out using CWT and it is observed that the frequency of the signals does not vary much with corrosion. CWT based analysis helps in filtering the high frequency noise and is very helpful to compare the signals at a particular frequency. Wavelet coefficients of the signals are used to define a damage index that is expressed as

$$DI_{RC} = \sqrt{\frac{\int_0^T (wc_i - wc_b)^2 dt}{\int_0^T (wc_b)^2 dt}} \tag{7.1}$$

where, T is the total time of waveform, wc_i is the wavelet coefficient of signal on the i^{th} day, and wc_b is the wavelet coefficient of baseline. The damage index defined by Equation 7.1 is used obtain the value of DI for each corroded state of the rebar and plotted in Figure 7.13. The plot shows that in the initial stages of corrosion the value of DI is low and the value of DI increases with corrosion. This damage index can be effectively used to quantify the state of corrosion in rebars.

Comparing the amplitudes may lead to erroneous results as the contact condition between the rebar and PWT affect these measurements. To account for this, the signal may be normalised by the peak amplitude of flexural mode. The normalisation of the signal with the flexural mode nullifies the variation of $F(1,\ 1)$ amplitude and magnifies the contribution of the other modes. The relative amplitudes of the other modes increase with the corrosion, hence they can be used to quantify the corrosion.

7.5 Concluding remarks

In this chapter, pitting corrosion in rebars is studied using ultrasonic GWs, which are generated using PWTs. Corrosion is accelerated using the impressed current method.

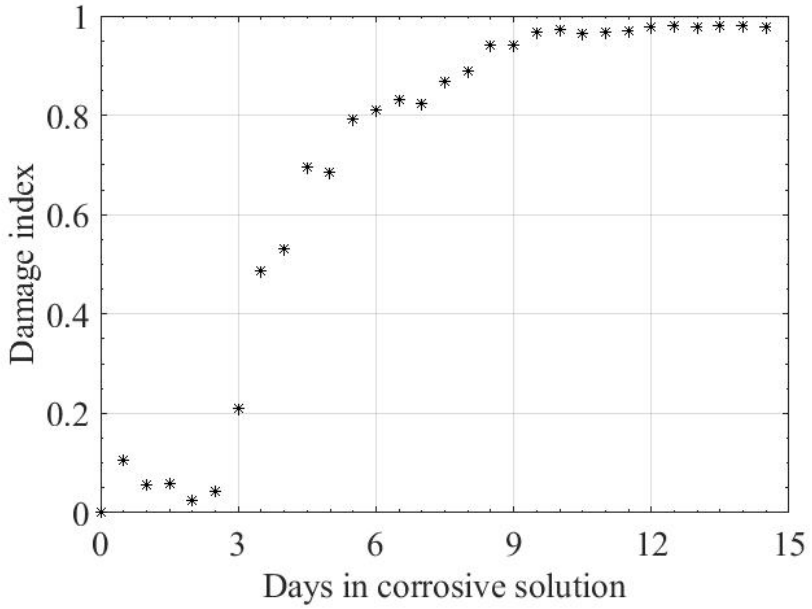

Figure 7.13: Variation in the damage index ($\mathrm{DI}_R C$) with the number of days in corrosive solution.

Localised corrosion is achieved by restricting the availability of the electrolyte to a specific portion of the RC beam. Longitudinal and flexural modes of wave propagation are deployed in the study. The flexural mode of wave propagation shows greater sensitivity to the interface conditions than longitudinal mode and, hence, can be used to detect corrosion initiation. The variation of group velocity gives useful information about the change in the bond between in rebars and concrete. The mechanism of corrosion process is proposed on the basis of the measured signal strength of the flexural mode, $F(1,\ 1)$. The effect of extreme corrosion in rebars on the GW characteristics is studied and a damage identification mechanism is proposed. The changes in relative amplitude of the other modes is evaluated to estimate the corrosion. The damage index defined in this chapter can be used to quantify the severity of pitting corrosion in rebars. Upcoming work may focus on the quantitative correlation between the signal and the actual damage scenarios such as debonding or diameter reduction.

Chapter 8

Summary and conclusions

8.1 Summary of work

Most of the present infrastructure is constructed using reinforced concrete (RC). They are regularly subjected to harsh environment and loading during their operation, that leads to their deterioration. Common damages such as cracks, corrosion and debonding in RC can lead to catastrophic failure if left unattended. Rebar corrosion is a predominant and pernicious damage that poses a significant challenge to the structural health of RC. It occurs due to slow and continuous seepage of acidic agents such as chloride, sulphate and its inception can get accelerated due to carbonation of concrete. Rebar can get corroded in two ways depending on the concentration of corrosion-causing agents, humidity and access to the rebars in the form of pores. These are called uniform corrosion and pitting corrosion, respectively. The latter type of corrosion is more detrimental to structural health as it can rapidly decrease the rebar cross-section in a localised area. The strength of structural member at the site of corrosion is reduced beyond the imposed loads and leads to failure without prior warning. The present methods of corrosion detection are limited in their capability to detect the inception of the damage, which could enable us to arrest the cause and take remedial measures to restore the damaged area. An extensive literature review is carried out to understand the current progress in corrosion detection. It was found that several techniques are developed based electrochemical and electromechanical properties of RC. However, the incipient corrosion is not yet deciphered. GW-based methods are a promising alternative to the current strategies. Ultrasonic guided waves that are generated and sensed with the help of piezoelectric sensors are deployed in these techniques to render the damages with small dimensions.

Initially, pitting corrosion of bare reinforcement bars is examined numerically and experimentally by using longitudinal GWs. The rebars are corroded artificially by chipping the material. It is observed that the direct transmitted signal is not affected much by pitting corrosion; hence, it could not be used to identify the damage, which, however, can be highlighted by various damage-scattered wave modes. A damage index method is thus developed using scattered wave modes. A method is developed by utilising the energy and the time of arrival of scattered wave modes to identify arbitrary pitting corrosion. The arrival time of dominant scattered wave modes is used to trace the front and rear edges of the damage. The factors that affect the scattered energy in corroded rebar are explored by defining a scatter coefficient. It is found that the scatter coefficient gradually increases with the mass loss, and the increment is pronounced when the pitting corrosion is closer to the receiver location. The scatter coefficient, when used in conjunction with the localisation method, is found to be promising in the assessment of pitting corrosion in bare rebar. However, these indices were not suitable for real-life corrosion, as the rebars that are corroded using accelerated corrosion setup did not provide sharp vertical edges, which are seen in artificially corroded rebars. GW signals that are actuated and received using PWTs and CTs are carefully examined to understand the effect of accelerated corrosion. It is found that the amplitude and group velocity of the GWs are sensitive to corrosion.

Numerical simulations are deployed to understand the effect of corrosion on GW properties. The numerical results indicate the existence of the zero-effect state in corroded RC beams. Experiments are thus disposed to confirm this zero-effect state and probe the possible corrosion monitoring strategy. An accelerated corrosion setup by using the impressed current method is designed to corroded the rebars locally. The corrosion is localised by restricting the availability of electrolyte to a specific portion of the RC beam. Longitudinal GWs that are generated by CTs are used to survey corrosion in embedded rebars by using the numerical and experimental models, and they are found to effectively capture the phases of corrosion. Theoretical dispersion curves are generated and it is found that four longitudinal modes, namely, $L(0,\ 1)$, $L(0,\ 2)$, $L(0,\ 3)$ and $L(0,\ 4)$ occur at 60 kHz excitation. The amplitude and group velocity of these waves is studied. A non-dimensional parameter, RA, is defined to study the amplitude. In the initiation phase, the RA values of $L(0,\ 3)$ mode decreases and group velocity of $L(0,\ 3)$ mode increases.

In the progression phase, the amplitude of the $L(0,\ 3)$ mode increases. In the diameter reduction phase, the RA values of both the $L(0,\ 3)$ and $L(0,\ 4)$ modes decreases rapidly along with the decrease in group velocity of $L(0,\ 4)$ mode. The study can be extended to implement a damage identification algorithm on corroded RC structures to identify the status corrosion. Although CTs provide various modes that are efficient in corrosion classification, they are not embeddable. Several researchers have indicated that PWTs can be embedded in concrete. GW signals that are generated by PWTs are used to study the corrosion of rebars embedded in concrete. Flexural mode of wave propagation is more sensitive to the interface conditions. It is shown that the corrosion mechanism could be represented using the GWs captured using PWTs. Mechanism of corrosion process is proposed based on the measured signal strength for flexural mode. The measurements are confirmed by the variation in impressed current in the corrosion setup.

8.2 Conclusions

The extensive on pitting corrosion monitoring by using ultrasonic GW provides the following conclusions:

- Group velocity dispersion curves are generated using theoretical calculations for 20 mm and 12 mm diameter rebars. Dispersion relations of group velocity and frequency are traced with the help of experiments and numerical modelling. Study of GW propagation in bare rebars has provided a clear understanding of scattering of waves by transmission and reflection. The signal confirms that a dominant $L(0,\ 1)$ mode is generated when CT is used for excitation.

- The presence of sharp damage edges in corroded bare rebars result in discrete wave packets that are generated due to the scattering of the GWs by transmission and reflection. These modes are exploited to define a damage index (DI) which is given by $DI(x) = \sqrt{\int_{t_1}^{t_2}(S-B)^2 dt}$. The DI increases with increase in the intensity. The location of the damage is indicated by peaks in damage index plot.

- For a general case of corrosion scatter coefficients are defined by $S_{coeff} = \sqrt{\frac{\int_0^{3T}(S-B)^2 dt}{\int_0^{3T}(B)^2 dt}}$. The S_{coeff} represents the energy scattered due to the damages, which is an excellent tool to quantify anomalies in the rebars. The Scoeff gradually increases with the

mass loss, and the increment is pronounced when the pitting corrosion is closer to the receiver location. The S_{coeff} in conjunction with the localisation method can be used to assess the pitting corrosion in rebars.

- An accelerated corrosion setup is developed to simulate and expedite the natural erosion in rebars. In contrast to artificially corroded rebars, the distinct wave packets do not appear in the fast-tracked real-life corroded rebars. The amplitude and group velocity of the $F(1,\ 1)$ mode, that is actuated and sensed by PWTs, decrease with the increase in the corrosion level, hence it is suitable for quantification of pitting corrosion.

- The zero-effect state is proposed wherein GW signals from a corroded RC specimen are same as that of the uncorroded sample. This hypothesis is authenticated by the numerical and experimental results. The need for engaging structural evaluation systems is further emphasised by the zero-effect state.

- An approximate concrete model that accounts for the finite size of the concrete beam is developed to calculate the dispersion curves. The model that is used in this research can effectively replace the full-scale three-dimensional model in finite element simulation of the RC beam; thus, it is cost-effective.

- Dispersion curves indicate that multiple wave modes exist in embedded rebars. Experiments and FEA calculation confirm the multiple modes.

- It is discovered that four longitudinal modes $L(0,\ 1)$, $L(0,\ 2)$, $L(0,\ 3)$ and $L(0,\ 4)$ occur at 60 kHz excitation when CTs are deployed to study corrosion in RC. Among these, the changes in the higher longitudinal modes $L(0,\ 3)$ and are beneficial to note corrosion. The $L(0,\ 3)$ mode is sensitive to all the three phases of corrosion as the mode shape of this mode shows dominant dispacement in the core of the rebar along with a slight peak in interface region. In contrast, the $L(0,\ 4)$ mode shows dominant displacement only in the core of rebar hence this mode is responsive only to the corrosion inception and diameter reduction phases.

- The RA factor defined in this study is effectual to capture corrosion in its embryonic phase. The RA value is given by the expression $(RA) = \frac{\int_{T_n^-}^{T_n^+} Sdt}{\int_{T_1^-}^{T_1^+} Sdt}$. The RA values

provide the flexibility to identify and distinguish various phases of corrosion without a baseline.

- The RA values of the $L(0,\ 3)$ mode show a decrease in the initiation phase and an increase in the progression phase. The RA values of $L(0,\ 4)$ mode can capture the initial phases of electrolyte seepage and depassivation that occur till the fourth day. In the diameter reduction phase, the RA values of both the $L(0,\ 3)$ and $L(0,\ 4)$ modes decrease rapidly.

- Additionally, corrosion can be quantified by using the group velocity of $L(0,\ 4)$ mode, which shows a change of 11 per cent in the initiation phase and the diameter reduction phase. The group velocity of this mode remains unaltered in the debonding phase.

- PWTs generate both longitudinal and flexural modes in RC, among which flexural modes are dominant. PWTs are field-deployable and worthwhile to perceive the various phases of corrosion in the embedded rebars. The amplitude of flexural mode decreases in the corrosion initiation phase, increases in the debonding phase and decreases in the diameter reduction phase. The group velocity of flexural mode can capture the initial seepage of electrolyte and depassivation. The group velocity shows a substantial change of 11 per cent in the debonding phase, while the change in the diameter reduction phase is insignificant.

- A hybrid-system that evaluates the changes in both the longitudinal and flexural modes is recommended to portray the condition of corroded rebars in RC. The longitudinal modes propagate in the core of rebar; hence, they shall be deployed to assess corrosion initiation and diameter reduction phase. The flexural mode shows greater sensitivity to the interface conditions; thus, they shall be used to monitor the debonding phase.

8.3 Research contribution

The contributions made in this thesis by filling the lacuna in the research are mentioned below:

1. A damage index method is proposed to quantify loss of mass, location and extent of pitting corrosion in bare rebars.

2. The zero-effect state in corroded RC structures is proposed. The existence of this effect is demonstrated through numerical and experimental observations.

3. A method of dispersion curve calculation for embedded rebars is proposed. These curves are useful for identification of GW modes.

4. The approximate concrete beam model used in this study is worthwhile alternative to the full-scale three-dimensional model in finite element simulation of the RC beam.

5. A non-dimensional parameter RA is proposed. This parameter captures the sensitivity of different modes towards each phase of corrosion.

6. Suitability of GWs that are generated and sensed by PWTs and CTs to assess incipient corrosion is established.

8.4 Future work

Further research may be carried out by extending this thesis in the following way:

- Improvements to the numerical model can be done by using various contact models for rebar and concrete interface.

- The proposed mechanism of corrosion can be further confirmed with numerical studies, in particular, for corrosion initiation.

- The realistic properties of rust may be explored in the numerical modelling.

- The proposed damage index method can be tested for the complex geometries of the pitting corrosion and for the rebars embedded in concrete.

- The results of GW technique can be verified with acoustic emission technique or fibre optic sensors.

- Corrosion rate shall be correlated with the sensor measurements by measuring the corrosion rate at various instances of testing using methods such as galvanostatic pulse technique.
- Damage level may be ascertained by identifying the wave modes and by developing an algorithm for various damage scenario.
- The upcoming studies may include the corrosion of multiple rebars embedded in rebars.
- A complete software and hardware package which can be deployed in field may be developed. GW signals can be used for imaging of concrete.

8.5 Publications

Journal

1. Sriramadasu, R. C., Banerjee, S., & Lu, Y. (2019). Detection and assessment of pitting corrosion in rebars using scattering of ultrasonic guided waves. NDT and E International, 101, 53-61. https://doi.org/10.1016/j.ndteint.2018.10.005
2. Sriramadasu, R. C., Lu, Y., & Banerjee, S. (2019). Identification of incipient pitting corrosion in reinforced concrete structures using guided waves and piezoelectric wafer transducers. Structural Health Monitoring, 18(1), 164-171. https://doi.org/10.1177/1475921718809151
3. Sriramadasu, R. C., Banerjee, S., & Lu, Y. (2019). Sensitivity of longitudinal guided wave modes to pitting corrosion of rebars embedded in concrete. (Submitted 2019)
4. Sriramadasu, R. C., Lu, Y., & Banerjee, S. (2019). Evaluation of pitting corrosion in reinforced concrete using ultrasonic guided waves: a review (To be prepared)

Conference

5. Sriramadasu, R. C., Banerjee, S., & Lu, Y. (2018). Quantification of pitting corrosion in rebars embedded in concrete using ultrasonic guided waves. In NDE-2018, Theme Frontiers in NDE Science & Technology, Organized by Indian Society for Non–Destructive Testing (ISNT).

6. Sriramadasu, R. C., Lu, Y., & Banerjee, S. (2018). Identification of pitting corrosion in steel bars and rebars embedded in concrete using ultrasonic guided waves. In Ninth International Conference on Advances in Steel Structures. (ICASS'2018).

7. Rajeshwara, C. S., Banerjee, S., & Lu, Y. (2017). A damage index method for detection of localized corrosion in reinforcement bars using scattering of longitudinal guided waves. In SHMII 2017 - 8th International Conference on Structural Health Monitoring of Intelligent Infrastructure, Proceedings (pp. 549-558).

8. Rajeshwara, C. S., Banerjee, S., & Lu, Y. (2017). Identification of zero effect state in corroded RCC structures using guided waves and embedded piezoelectric wafer transducers (PWT). In 6th Asia Pacific Workshop on Structural Health Monitoring. ((Procedia Engineering; Vol. 188 pp. 209- 216)).
https://doi.org/10.1016/j.proeng.2017.04.476

References

Ahmad, S. (2003). Reinforcement corrosion in concrete structures, its monitoring and service life prediction - A review. *Cement and Concrete Composites*, **25**(4-5 SPEC), 459–471.

Aktan, A. E., Farhey, D. N., Brown, D. L., Dalal, V., Helmicki, A. J., Hunt, V. J., and Shelley, S. J. (1996). Condition assessment for bridge management. *Journal of Infrastructure Systems*, **2**(3), 108–117.

Al-Sulaimani, G. J., Kaleemullah, M., Basunbul, I. A., and Rasheeduzzafar (1990). Influence of corrosion and cracking on bond behavior and strength of reinforced concrete members. *ACI Structural Journal*, **87**(2), 220–231.

Almusallam, A. A. (2001). Effect of degree of corrosion on the properties of reinforcing steel bars. *Construction and Building Materials*, **15**, 361–368.

Almusallam, A. A., Al-Gahtani, A. S., Aziz, A. R., and Rasheeduzzafar (1996). Effect of reinforcement corrosion on bond strength. *Construction and Building Materials*, **10**(2), 123–129.

Amjad, U., Yadav, S. K., and Kundu, T. (2015). Detection and quantification of diameter reduction due to corrosion in reinforcing steel bars. *Structural Health Monitoring*, **14**(5), 532–543.

Auyeung, Y. (2001). *Bond properties of corroded reinforcement with and without confinement.* Phd thesis, New Brunswick Rutgers, The State University of New Jersey.

Barrias, A., Casas, J., and Villalba, S. (2016). A review of distributed optical fiber sensors for civil engineering applications. *Sensors*, **16**(5), 748.

Beard, M. D. (2002). *Guided wave inspection of embedded cylindrical structures.* Ph.D. thesis, Department of Mechanical Engineering, University of London, London.

Beniwal, S. and Ganguli, A. (2015). Defect detection around rebars in concrete using focused ultrasound and reverse time migration. *Ultrasonics*, **62**, 112–125.

Beniwal, S. and Ganguli, A. (2016). Localized condition monitoring rround rebars using focused ultrasonic field and SAFT. *Research in Nondestructive Evaluation*, **27**(1), 48–67.

Bilcik, J. and Holly, I. (2013). Effect of reinforcement corrosion on bond behaviour. *Procedia Engineering*, **65**, 248–253.

Brown, L. F. and Mason, J. L. (1996). Disposable PVDF ultrasonic transducers for nondestructive testing applications. *IEEE Transactions on Ultrasonics, Ferroelectrics, and Frequency Control*, **43**(4), 560–568.

Cabrera, J. G. (1996). Deterioration of concrete due to reinforcement steel corrosion. *Cement and Concrete Composites*, **18**(1), 47–59.

Cao, C. and Cheung, M. M. S. (2014). Non-uniform rust expansion for chloride-induced pitting corrosion in RC structures. *Construction and Building Materials*, **51**, 75–81.

Cao, M. S., Sha, G. G., Gao, Y. F., and Ostachowicz, W. (2017). Structural damage identification using damping: A compendium of uses and features. *Smart Materials and Structures*, **26**(4).

Carandente, R., Lovstad, A., and Cawley, P. (2012). The influence of sharp edges in corrosion profiles on the reflection of guided waves. *NDT and E International*, **52**, 57–68.

Caré, S., Nguyen, Q., L'Hostis, V., and Berthaud, Y. (2008). Mechanical properties of the rust layer induced by impressed current method in reinforced mortar. *Cement and Concrete Research*, **38**(8-9), 1079–1091.

Chaki, S. and Bourse, G. (2009). Guided ultrasonic waves for non-destructive monitoring of the stress levels in prestressed steel strands. *Ultrasonics*, **49**(2), 162–171.

Chang, C. Y. and Yuan, F. G. (2018). Extraction of guided wave dispersion curve in isotropic and anisotropic materials by Matrix Pencil method. *Ultrasonics*, **89**(November 2017), 143–154.

Cheng, C. C., Cheng, T. M., and Chiang, C. H. (2008). Defect detection of concrete structures using both infrared thermography and elastic waves. *Automation in Construction*, **18**(1), 87–92.

Coccia, S., Imperatore, S., and Rinaldi, Z. (2016). Influence of corrosion on the bond strength of steel rebars in concrete. *Materials and Structures/Materiaux et Constructions*, **49**(1-2), 537–551.

Courant, R., Friedrichs, K., and Lewy, H. (1967). On the partial difference equations of mathematical physics. *IBM Journal of Research and Development*, **11**(2), 215–234.

Davis, M., Hoult, N. A., and Scott, A. (2016). Distributed strain sensing to determine the impact of corrosion on bond performance in reinforced concrete. *Construction and Building Materials*, **114**, 481–491.

De Weerdt, K., Lothenbach, B., and Geiker, M. R. (2019). Comparing chloride ingress from seawater and NaCl solution in Portland cement mortar. *Cement and Concrete Research*, **115**, 80–89.

Del Grande, N. K. and Durbin, P. F. (2003). Delamination detection in reinforced concrete using thermal inertia. *Proceeding of SPIE, Nondestructive Evaluation of Bridges and Highways III*, **3587**(February 1999), 186–197.

Demma, A., Cawley, P., Lowe, M., Roosenbrand, A. G., and Pavlakovic, B. (2004). The reflection of guided waves from notches in pipes: A guide for interpreting corrosion measurements. *NDT and E International*, **37**(3), 167–180.

Di Benedetti, M., Loreto, G., Matta, F., and Nanni, A. (2012). Acoustic emission monitoring of reinforced concrete under accelerated corrosion. *Journal of Materials in Civil Engineering*, **25**(8), 1022–1029.

Dumoulin, C., Karaiskos, G., Carette, J., Staquet, S., and Deraemaeker, A. (2012). Monitoring of the ultrasonic P-wave velocity in early-age concrete with embedded piezoelectric transducers. *Smart Materials and Structures*, **21**(4).

Dung, C. V. and Sasaki, E. (2016). Numerical simulation of output response of PVDF sensor attached on a cantilever beam subjected to impact loading. *Sensors (Switzerland)*, **16**(5).

El-Dieb, A. S. and El-Maaddawy, T. A. (2018). Assessment of reinforcement corrosion protection of self-curing concrete. *Journal of Building Engineering*, **20**(June), 72–80.

El Maaddawy, T. A. and Soudki, K. A. (2003). Effectiveness of impressed current technique to simulate corrosion of steel reinforcement in concrete. *Journal of Materials in Civil Engineering*, **15**(1), 41–47.

Ervin, B. L. and Reis, H. (2008). Longitudinal guided waves for monitoring corrosion in reinforced mortar. *Measurement Science and Technology*, **19**(5), 055702.

Ervin, B. L., Bernhard, J. T., Kuchma, D. A., and Reis, H. (2006). Estimation of general corrosion damage to steel reinforced mortar using frequency sweeps of guided mechanical waves. *Insight - Non-Destructive Testing and Condition Monitoring*, **48**(11), 682–692.

Ervin, B. L., Kuchma, D. A., Bernhard, J. T., and Reis, H. (2009). Monitoring corrosion of rebar embedded in mortar using high-frequency guided ultrasonic waves. *Journal of Engineering Mechanics*, **135**(1), 9–19.

Fang, C., Lundgren, K., Chen, L., and Zhu, C. (2004). Corrosion influence on bond in reinforced concrete. *Cement and Concrete Research*, **34**(11), 2159–2167.

Fang, C., Gylltoft, K., Lundgren, K., and Plos, M. (2006). Effect of corrosion on bond in reinforced concrete under cyclic loading. *Cement and Concrete Research*, **36**(1), 548–555.

Feldman, M. (2011). Hilbert transform in vibration analysis. *Mechanical Systems and Signal Processing*, **25**(3), 735–802.

Frankowski, P. K. (2011). Eddy current method for identification and analysis of reinforcement bars in concrete structures. *Electrodynamic and Mechatronic Systems - Proceedings of 2011, 3rd International Students Conference on Electrodynamics and Mechatronics, SCE III*, pages 105–108.

Fu, X. and Chung, D. D. (1997). Effect of corrosion on the bond between concrete and steel rebar. *Cement and Concrete Research*, **27**(12), 1811–1815.

Gaul, L., Sprenger, H., Schaal, C., and Bischoff, S. (2012). Structural health monitoring of cylindrical structures using guided ultrasonic waves. *Acta Mechanica*, **223**(8), 1669–1680.

Gazis, D. C. (1959). Three-dimensional investigation of the propagation of waves in hollow circular cylinders. II. Numerical results. *The Journal of the Acoustical Society of America*, **31**(5), 573–578.

Graff, K. F. (1975). Wave motion in elastic solids. In *Ultrasonics*, pages 235–236. Courier Corporation.

Gu, H., Zhao, Y., and Wang, M. L. (2005). A wireless smart PVDF sensor for structural health monitoring. *Structural Control and Health Monitoring*, **12**(3-4), 329–343.

Guo, J. and Yang, C. (2015). Highly stabilized phase-shifted fiber Bragg grating sensing system for ultrasonic detection. *IEEE Photonics Technology Letters*, **27**(8), 848–851.

Hornbostel, K., Larsen, C. K., and Geiker, M. R. (2013). Relationship between concrete resistivity and corrosion rate–a literature review. *Cement and Concrete Composites*, **39**, 60–72.

Horrigmoe, G., Saether, I., Antonsen, R., and Arntsen, B. (2007). Laboratory investigations of steel bar corrosion in concrete. Technical report, European Commission.

Hosseini, S. M. H., Duczek, S., and Gabbert, U. (2013). Non-reflecting boundary condition for Lamb wave propagation problems in honeycomb and CFRP plates using dashpot elements. *Composites Part B: Engineering*, **54**(1), 1–10.

Hughi, D. and Marzouk, H. (2015). Crack width monitoring system for reinforced concrete beams using piezo-ceramic sensors. *Journal of Civil Structural Health Monitoring*, **5**, 57–66.

Ji, Y. S., Zhao, W., Zhou, M., Ma, H. R., and Zeng, P. (2013). Corrosion current distribution of macrocell and microcell of steel bar in concrete exposed to chloride environments. *Construction and Building Materials*, **47**, 104–110.

Karhunen, K., Seppänen, A., Lehikoinen, A., Monteiro, P. J., and Kaipio, J. P. (2010). Electrical Resistance Tomography imaging of concrete. *Cement and Concrete Research*, **40**(1), 137–145.

Kemp, E. L., Brezny, F., and Unterspan, J. (1968). Effect of rust and scale on the bond characteristcs of deformed reinforcing bars. *ACI Journal Proceedings*, **65**(9), 743–756.

Khan, H., Razmjou, A., Warkiani, M. E., Kottapalli, A., and Asadnia, M. (2018). Sensitive and flexible polymeric strain sensor for accurate human motion monitoring. *Sensors (Switzerland)*, **18**(2).

Kim, S. B. and Sohn, H. (2006). Application of time-reversal guided waves to field bridge testing for baseline-free damage diagnosis. *Proceedings of SPIE*, **6177**, 1–10.

Kim, Y. G., Moon, H. S., Park, K. J., and Lee, J. K. (2011). Generating and detecting torsional guided waves using magnetostrictive sensors of crossed coils. *NDT and E International*, **44**(2), 145–151.

Kim, Y. Y. and Kwon, Y. E. (2015). Review of magnetostrictive patch transducers and applications in ultrasonic nondestructive testing of waveguides. *Ultrasonics*, **62**, 3–19.

Kudela, P., Zak, A., Krawczuk, M., and Ostachowicz, W. (2007). Modelling of wave propagation in composite plates using the time domain spectral element method. *Journal of Sound and Vibration*, **302**(4-5), 728–745.

Kwon, S.-J., Xue, H., Feng, M. Q., and Baek, S. (2011). Nondestructive corrosion detection in concrete through integrated heat induction and IR thermography. *Nondestructive Characterization for Composite Materials, Aerospace Engineering, Civil Infrastructure, and Homeland Security 2011*, **7983**, 79831R.

Kwun, H. and Teller, C. M. (1994). Magnetostrictive generation and detection of longitudinal, torsional, and flexural waves in a steel rod. *The Journal of the Acoustical Society of America*, **96**(2), 1202–1204.

Lamb, H. (1917). On waves in an elastic plate. *Proceedings of the Royal Society of London. Series A, Containing papers of a mathematical and physical character*, pages 114–128.

Lau, K. (2004). Fibre-optic sensors and smart composites for concrete applications. *Magazine of Concrete Research*, **55**(1), 19–34.

Law, D. W., Cairns, J., Millard, S. G., and Bungey, J. H. (2004). Measurement of loss of steel from reinforcing bars in concrete using linear polarisation resistance measurements. *NDT and E International*, **37**(5), 381–388.

Lebrun, B., Jayet, Y., and Baboux, J. C. (1997). Pulsed eddy current signal analysis: application to the experimental detection and characterisation of deep flaws in highly conductive materials. *NDT & E International*, **30**(3), 163–170.

Lee, H. S., Noguchi, T., and Tomosawa, F. (2002). Evaluation of the bond properties between concrete and reinforcement as a function of the degree of reinforcement corrosion. *Cement and Concrete Research*, **32**(8), 1313–1318.

Li, F., Murayama, H., Kageyama, K., and Shirai, T. (2009). Guided wave and damage detection in composite laminates using different fiber optic sensors. *Sensors*, **9**(5), 4005–4021.

Li, J. and Rose, J. L. (2002). Angular-profile tuning of guided waves in hollow cylinders using a circumferential phased array. *IEEE Transactions on Ultrasonics, Ferroelectrics, and Frequency Control*, **49**(12), 1720–1729.

Li, J., Lu, Y., Guan, R., and Qu, W. (2017). Guided waves for debonding identification in CFRP-reinforced concrete beams. *Construction and Building Materials*, **131**, 388–399.

Lu, Y., Li, J., Ye, L., and Wang, D. (2013). Guided waves for damage detection in rebar-reinforced concrete beams. *Construction and Building Materials*, **47**, 370–378.

Lu, Y., Li, J. S., Lyu, H. B., Hong, M., and Su, Z. Q. (2014). The application of guided waves for debonding identification in FRP reinforced civil structures. In *5th Asia-Pacific Workshop on Structural Health Monitoring Conference*.

Luangvilai, K., Punurai, W., Jacobs, L. J., and Asce, M. (2003). Guided Lamb wave propagation in composite plate/concrete component. *Engineering Mechanics*, **128**(12), 1337–1341.

Maaddawy, T. E., Soudki, K., and Topper, T. (2005). Long-term performance of corrosion-damaged reinforced concrete beams. *ACI Structural journal*, **102**(5), 649–656.

Maalej, M., Ahmed, S. F. U., Kuang, K. S. C., and Paramasivam, P. (2004). Fiber optic sensing for monitoring corrosion-induced damage. *Structural Health Monitoring*, **3**(2), 165–176.

Maierhofer, C., Arndt, R., Röllig, M., Rieck, C., Walther, A., Scheel, H., and Hillemeier, B. (2006). Application of impulse-thermography for non-destructive assessment of concrete structures. *Cement and Concrete Composites*, **28**(4), 393–401.

Mangual, J., ElBatanouny, M. K., Velez, W., Ziehl, P., Matta, F., and Gonzalez, M. (2011). Assessment of corrosion rate in prestressed concrete with acoustic emission. *Proceedings of the SPIE - The International Society for Optical Engineering*, **7981**, 1–12.

Mangual, J., ElBatanouny, M. K., Ziehl, P., and Matta, F. (2013). Acoustic-emission-based characterization of corrosion damage in cracked concrete with prestressing strand. *ACI Materials Journal*, **110**(1), 89–98.

Markovic, N., Nestorovic, T., and Stojic, D. (2015). Numerical modeling of damage detection in concrete beams using piezoelectric patches. *Mechanics Research Communications*, **64**, 15–22.

Melle, S. M., Liu, K., and Measures, R. M. (1992). A passive wavelength demodulation system for guided-wave bragg grating sensors. *IEEE Photonics Technology Letters*, **4**(5), 516–518.

Miller, T., Hauser, C. J., and Kundu, T. (2002). Nondestructive inspection of corrosion and delamination at the concrete-steel reinforcement interface. *Nondestructive Evaluation*, **2002**, 121–128.

Miller, T. H., Kundu, T., Huang, J., and Grill, J. Y. (2013). A new guided wave-based technique for corrosion monitoring in reinforced concrete. *Structural Health Monitoring*, **12**(1), 35–47.

Minesawa, G. V. and Sasaki, E. (2014). Eddy current inspection of corrosion defects for concrete embedded steel members. *AIP Conference Proceedings*, **1581**, 781–786.

Mustapha, S., Lu, Y., Li, J., and Ye, L. (2014). Damage detection in rebar-reinforced concrete beams based on time reversal of guided waves. *Structural Health Monitoring*, **13**(4), 347–358.

Na, W. B. and Kund, T. (2003). Inspection of interfaces between corroded steel bars and concrete using the combination of a piezoelectric zirconate-titanate transducer and an electromagnetic acoustic transducer. *Experimental Mechanics*, **43**(1), 24–31.

Na, W.-B., Kundu, T., and Ehsani, M. R. (2003). Lamb waves for detecting delamination between steel bars and concrete. *Computer-Aided Civil and Infrastructure Engineering*, **18**(1), 58–63.

Noorsuhada, M. N. (2016). An overview on fatigue damage assessment of reinforced concrete structures with the aid of acoustic emission technique. *Construction and Building Materials*, **112**, 424–439.

Nurmalia, Nakamura, N., Ogi, H., and Hirao, M. (2017). EMAT pipe inspection technique using higher mode torsional guided wave T(0,2). *NDT and E International*, **87**, 78–84.

Pandey, A. K. and Biswas, M. (1994). Damage detection in structures using changes in flexibility. *Journal of Sound and Vibration*, **169**(1), 3–17.

Pantazopoulou, S. J. and Papoulia, K. D. (2001). Modeling cover-cracking due to reinforcement corrosion in rc structures. *Journal of Engineering Mechanics*, **127**(4), 342–351.

Park, G. and Inman, D. J. (2007). Structural health monitoring using piezoelectric impedance measurements. *Philosophical Transactions of the Royal Society A: Mathematical, Physical and Engineering Sciences*, **365**(1851), 373–392.

Park, H. W., Kim, S. B., and Sohn, H. (2009). Understanding a time reversal process in Lamb wave propagation. *Wave Motion*, **46**(7), 451–467.

Pavlakovic, B. and Lowe, M. J. S. (2005). Disperse Software.

Pradhan, B. and Bhattacharjee, B. (2009). Performance evaluation of rebar in chloride contaminated concrete by corrosion rate. *Construction and Building Materials*, **23**(6), 2346–2356.

Raghavan, A. and Cesnik, C. E. S. (2007). Review of guided-wave structural health monitoring. *The Shock and Vibration Digest*, **39**(2), 91–114.

Rayleigh, L. (1885). On waves propagating along the plane surface of an elastic solid. *Proc. London Math. Soc.*, **7**(1), 4–11.

Razak, H. A. and Choi, F. C. (2001). The effect of corrosion on the natural frequency and modal damping of reinforced concrete beams. *Engineering Structures*, **23**(9), 1126–1133.

Regier, R. and Hoult, N. A. (2015). Concrete deterioration detection using distributed sensors. *Proceedings of the Institution of Civil Engineers - Structures and Buildings*, **168**(2), 118–126.

Reis, H., Ervin, B. L., Kuchma, D. A., and Bernhard, J. T. (2005). Estimation of corrosion damage in steel reinforced mortar using guided waves. *Journal of Pressure Vessel Technology*, **127**(3), 255.

Robinson, D. W., Wright, J., Gupta, S., Mottram, T., Armitage, P., Gower, M., Lodeiro, M., Gelat, P., and Schwarz, C. (2016). A novel non-linear elastic wave acoustic spectroscopy (NEWS) non-destructive inspection (NDI) method for aeronautic and spacecraft materials and components. *CEAS Space Journal*, **8**(1), 35–45.

Rodriguez, J., Ortega, L. M., and Casal, J. (1997). Load carrying capacity of concrete structures with corroded reinforcement. *Construction and Building Materials*, **11**(4), 239–248.

Rose, J. L. (2014). *Ultrasonic guided waves in solid media*, volume 9781107048. Cambridge university press.

Sadowski, L. (2012). New non-destructive method for linear polarisation resistance corrosion rate measurement. *Archives of Civil and Mechanical Engineering*, **10**(2), 109–116.

Seco, F. and Jiménez, A. R. (2012). Modelling the generation and propagation of ultrasonic signals in cylindrical waveguides. In *Ultrasonic Waves*, chapter 1, pages 1–28. Intech Open Access Publisher.

Sharma, A., Sharma, S., Sharma, S., and Mukherjee, A. (2018). Investigation of deterioration in corroding reinforced concrete beams using active and passive techniques. *Construction and Building Materials*, **161**, 555–569.

Sharma, S. and Mukherjee, A. (2010). Longitudinal guided waves for monitoring chloride corrosion in reinforcing bars in concrete. *Structural Health Monitoring*, **9**(6), 555–567.

Sharma, S. and Mukherjee, A. (2013). Nondestructive evaluation of corrosion in varying environments using guided waves. *Research in Nondestructive Evaluation*, **24**(2), 63–88.

Sikdar, S., Banerjee, S., and Ashish, G. (2016). Ultrasonic guided wave propagation and disbond identification in a honeycomb composite sandwich structure using bonded piezoelectric wafer transducers. *Journal of Intelligent Material Systems and Structures*, **27**(13), 1767–1779.

Sinkovics, N., Hoque, S. F., and Sinkovics, R. R. (2016). Rana plaza collapse aftermath: Are CSR compliance and auditing pressures effective? *Accounting, Auditing and Accountability Journal*, **29**(4), 617–649.

Sohn, H., Dutta, D., Yang, J. Y., Park, H. J., DeSimio, M., Olson, S., and Swenson, E. (2011). Delamination detection in composites through guided wave field image processing. *Composites Science and Technology*, **71**(9), 1250–1256.

Song, F., Huang, G. L., Kim, J. H., and Haran, S. (2008). On the study of surface wave propagation in concrete structures using a piezoelectric actuator/sensor system. *Smart Materials and Structures*, **17**(5), 055024.

Song, H. W. and Saraswathy, V. (2007). Corrosion monitoring of reinforced concrete structures - a review. *International Journal of Electrochemical Science*, **2**, 1– 28.

Su, Z. and Ye, L. (2009). *Identification of damage using Lamb waves: From fundamentals to applications*, volume 48. Springer Science & Business Media.

Sun, R., Sevillano, E., and Perera, R. (2015). Debonding detection of FRP strengthened concrete beams by using impedance measurements and an ensemble PSO adaptive spectral model. *Composite Structures*, **125**, 374–387.

Sun, Z., Zhang, L., and Rose, J. L. (2005). Flexural torsional guided Wave mechanics and focusing in pipe. *Journal of Pressure Vessel Technology*, **127**(4), 471.

Talakokula, V. and Bhalla, S. (2015). Reinforcement corrosion assessment capability of surface bonded and embedded piezo sensors for reinforced concrete structures. *Journal of Intelligent Material Systems and Structures*, **26**(17), 2304–2313.

Talakokula, V., Bhalla, S., and Gupta, A. (2014). Corrosion assessment of reinforced concrete structures based on equivalent structural parameters using electro-mechanical impedance technique. *Journal of Intelligent Material Systems and Structures*, **25**(4), 484–500.

Tan, C. H., Shee, Y. G., Yap, B. K., and Adikan, F. R. (2016). Fiber Bragg grating based sensing system: Early corrosion detection for structural health monitoring. *Sensors and Actuators, A: Physical*, **246**, 123–128.

Tang, L. (2002). A study of the polarisation techniques for corrosion rate measurement in a steel-concrete system. *9th International Conference on Durability of Building Materials and Components*, pages 17–20.

Tian, G. Y. and Sophian, A. (2005). Defect classification using a new feature for pulsed eddy current sensors. *NDT and E International*, **38**(1), 77–82.

Tian, G. Y., Sophian, A., Taylor, D., and Rudlin, J. (2005). Multiple sensors on pulsed eddy-current detection for 3-D subsurface crack assessment. *IEEE Sensors Journal*, **5**(1), 90–96.

Treiber, M., Kim, J.-Y., Jacobs, L. J., and Qu, J. (2009). Correction for partial reflection in ultrasonic attenuation measurements using contact transducers. *The Journal of the Acoustical Society of America*, **125**(5), 2946.

Tse, P. W. and Wang, X. (2013). Characterization of pipeline defect in guided-waves based inspection through matching pursuit with the optimized dictionary. *NDT and E International*, **54**, 171–182.

United Nations (2018). The world's cities in 2018—Data booklet. *Department of Economic and Social Affairs, Population Division (2018)*, page ST/ESA/ SER.A/417.

Valipour, M., Shekarchi, M., and Ghods, P. (2014). Comparative studies of experimental and numerical techniques in measurement of corrosion rate and time-to-corrosion-initiation of rebar in concrete in marine environments. *Cement and Concrete Composites*, **48**, 98–107.

Vu, K. A. T. and Stewart, M. G. (2000). Structural reliability of concrete bridges including improved chloride-induced corrosion models. *Structural Safety*, **22**(4), 313–333.

Wahalathantri, B. L., Thambiratnam, D. P., Chan, T. H., and Fawzia, S. (2015). Vibration based baseline updating method to localize crack formation and propagation in reinforced concrete members. *Journal of Sound and Vibration*, **344**, 258–276.

Wandowski, T., Malinowski, P., Ostachowicz, W., Rawski, M., Tomaszewicz, P., Luba, T., and Borowik, G. (2015). Embedded damage localization subsystem based on elastic wave propagation. *Computer-Aided Civil and Infrastructure Engineering*, **30**(8), 654–665.

Wang, X. and Liu, X. (2006). Bond strength modeling for corroded reinforcements. *Construction and Building Materials*, **20**(3), 177–186.

Wang, X., Tse, P. W., Mechefske, C. K., and Hua, M. (2010). Experimental investigation of reflection in guided wave-based inspection for the characterization of pipeline defects. *NDT and E International*, **43**(4), 365–374.

Wang, Y., Zhu, X., Hao, H., and Ou, J. (2009). Guided wave propagation and spectral element method for debonding damage assessment in RC structures. *Journal of Sound and Vibration*, **324**(3-5), 751–772.

Wei-liang, J. and Yu-xi, Z. (2001). Effect of corrosion on bond behavior and bending strength of reinforced concrete beams. *Journal of Zhejiang University*, **2**(3), 298–308.

Wickramasinghe, W. R., Thambiratnam, D. P., Chan, T. H., and Nguyen, T. (2016). Vibration characteristics and damage detection in a suspension bridge. *Journal of Sound and Vibration*, **375**, 254–274.

Willberg, C., Duczek, S., Vivar-Perez, J. M., and Ahmad, Z. A. B. (2015). Simulation methods for guided wave-based structural health monitoring: a review. *Applied Mechanics Reviews*, **67**(1), 01080301–01080320.

Wu, F. and Chang, F. K. (2006a). Debond detection using embedded piezoelectric elements for reinforced concrete structures - Part II: Analysis and algorithm. *Structural Health Monitoring*, **5**(1), 17–28.

Wu, F. and Chang, F.-K. (2006b). Debond detection using embedded piezoelectric elements in reinforced concrete structures-part I: experiment. *Structural Health Monitoring*, **5**(1), 5–15.

Wu, F., Yi, J., and Li, W. J. (2014). Numerical analysis of PZT rebar active sensing system for structural health monitoring of RC structure. *Nondestructive Characterization for Composite Materials, Aerospace Engineering, Civil Infrastructure, and Homeland Security 2014*, **9063**, 906314.

Wu, F., Chan, H.-L., and Chang, F.-K. (2015). Ultrasonic guided wave active sensing for monitoring of split failures in reinforced concrete. *Structural Health Monitoring: An International Journal*, **14**(5), 439–448.

Xu, B., Zhang, T., Song, G., and Gu, H. (2013). Active interface debonding detection of a concrete-filled steel tube with piezoelectric technologies using wavelet packet analysis. *Mechanical Systems and Signal Processing*, **36**(1), 7–17.

Yang, Y., Cascante, G., and Anna Polak, M. (2009). Depth detection of surface-breaking cracks in concrete plates using fundamental Lamb modes. *NDT and E International*, **42**(6), 501–512.

Yang, Y., Zhang, M. Y., Xiao, L., and Qu, W. Z. (2015). A Simulation study of surface breaking crack in concrete beam based on time-reversed theory of surface wave. *Key Engineering Materials*, **665**, 165–168.

Yu, L. and Tian, Z. (2013). Lamb wave structural health monitoring using a hybrid PZT-laser vibrometer approach. *Structural Health Monitoring*, **12**(5-6), 469–483.

Yu, Y., Zhao, X., Wang, Y., and Ou, J. (2013). A study on PVDF sensor using wireless experimental system for bridge structural local monitoring. *Telecommunication Systems*, **52**(4), 2357–2366.

Zaki, A., Chai, H. K., Behnia, A., Aggelis, D. G., Tan, J. Y., and Ibrahim, Z. (2017). Monitoring fracture of steel corroded reinforced concrete members under flexure by acoustic emission technique. *Construction and Building Materials*, **136**, 609–618.

Zhang, Y., Li, D., and Zhou, Z. (2017). Time reversal method for guided waves with multimode and multipath on corrosion defect detection in wire. *Applied Sciences*, **7**(4), 424.

Zhu, H., Liu, X., Tang, D., Jia, C., Qian, Y., and Cao, S. (2016). An experimental study on the corrosion amount in RC structures by eddy current heating. *Proceedings of 2016 IEEE International Conference of Online Analysis and Computing Science, ICOACS 2016*, pages 127–130.

Zhu, J. and Popovics, J. S. (2007). Imaging concrete structures using air-coupled impact-echo. *Journal of Engineering Mechanics*, **133**(6), 628–640.

Rajeshwara Chary Sriramadasu

Structural Engineering Researcher

+91-9590962988

rcsriramadasu@gmail.com

Flat No 306, Harihara house,
Road No 10, Bhandari layout,
Nizampet, Hyderabad,
Telangana, India-500090.

LinkedIn

Google Scholar

Research Gate

ORCiD

Research Interests

- **Non-destructive Evaluation**
- **Finite Element Analysis**
- **Ultrasonic Guided Waves**
- **Piezoelectric Sensors**
- **Damage Prognosis**
- **Corrosion of Reinforcement Bars**
- **Retrofitting of Reinforced Concrete.**

Skills

- **Abaqus** — 9 / 10
- **AutoCAD** — 10 / 10
- **MATLAB** — 9 / 10
- **Latex** — 9 / 10
- **MS Office** — 10 / 10
- **Python** — 8 / 10
- **STAAD Pro** — 10 / 10

CAREER SUMMARY

Structural health monitoring researcher with a long-term goal to build safe, smart and resilient infrastructure. Indo-Australian joint-PhD that resulted in high quality journal and conference publications. Expert in conducting largescale laboratory experiments of pitting corrosion in concrete, finite element simulation of guided wave propagation in composite concrete-rebar system and signal processing. 4 years of industry experience in leading the design and construction of bulk material handling structures of a Mega Thermal Power Project and a 7 MT Steel Plant.

Education

Doctor of philosophy (PhD)

(2015 - 2019)

Joint PhD by Collaboration. Monash University & Indian Institute of Technology Bombay. **(CGPA 9.910/10)**

Bachelor of technology

(2006 – 2010)

Department of Civil Engineering. Indian Institute of Technology Roorkee. **(CGPA 6.902/10)**

Experience

1. **Teaching assistant.** **(**Fall ’15 ’16 and Autumn ’15 ’16 ’18)
   Institution: Indian Institute of Technology Bombay, Mumbai.
2. **Civil Engineer.** (July 2010 to July 2014)
   Company: Bharat Heavy Electricals Limited,
   Industrial Systems Group, Bengaluru.

Leadership activities

1. Mentored dissertation projects of 2 Master’s students and 1 Dual Degree student.
2. Institute Research Scholar Companion (2015-16).
3. Student Representative, IITB-Monash (2015-2017).
4. Student organizer of the sixth International Congress on Computational Mechanics and Simulation (ICCMS2016)